COMPUTATIONAL AND EXPERIMENTAL STUDIES OF THIOPHENE-BASED CONJUGATED POLYMER MORPHOLOGY AND CHARGE CARRIER DYNAMICS

By

HILARY S. MARSH

B. S. University of Dayton, 2010

A thesis submitted to the

Faculty of the Graduate School of the

University of Colorado in partial fulfillment

of the requirement for the degree of

Doctor of Philosophy

Department of Chemical and Biological Engineering

2015

This thesis entitled:

Computational and Experimental Studies of Thiophene-based Conjugated Polymer Morphology and Charge Carrier Dynamics

written by Hilary S. Marsh

has been approved for the Department of Chemical and Biological Engineering

_____

Arthi Jayaraman

_____

Garry Rumbles

Date_____

The final copy of this thesis has been examined by the signatories, and we find that both the content and the form meet acceptable presentation standards of scholarly work in the above mentioned discipline.

Abstract

Marsh, Hilary Susan (Ph.D., Chemical and Biological Engineering)

Computational and Experimental Studies of Thiophene-based Conjugated Polymer Morphology and Charge Carrier Dynamics

Thesis directed by Professor Arthi Jayaraman and Professor Garry Rumbles

Organic photovoltaic device efficiency is strongly influenced by the morphology of the active layer composed of conjugated polythiophenes (electron donors) and fullerene derivatives (electron acceptors). The goal of this thesis is to understand how molecular features affect the morphology and charge carrier dynamics in neat polythiophene and polythiophene-acceptor blends, using simulations and experiments.

We use molecular dynamics simulations with our newly developed intermediate resolution model to study how oligothiophene (eg. poly(3-hexylthiophene), P3HT) and acceptor (eg. [6,6]-phenyl-C_{61}-butyric acid methyl ester, PCBM) architecture and chemistry affect neat and blend morphology. Our coarse-grained model enables observation of molecular-level packing, e.g. the experimentally observed intercalation of acceptor molecules between oligomer side chains, as well as the transition from a disordered initial state to experimentally observed ordered morphologies. With this validated model, we study the impact of alkyl side-chain length and placement along generic oligothiophenes on the order-disorder transition temperature and molecular packing. We also predict the appropriate backbone-acceptor attraction that leads to blend morphologies with increased connectivity and interfacial area, characteristics beneficial for exciton dissociation and charge transport. We also predict additive design that provides a desired

degree of acceptor macrophase separation, and acceptor intercalation. Lastly, in collaboration with Briseño *et al*. at University of Massachusetts, we study monomers and dimers of 2,5-bis(3-alkylthiophen-2-yl)thieno[3,2-b]thiophene (BTTT) mixed with PCBM, and find, in agreement with experimental structural characterization, that the BTTT2-PCBM blends have higher crystallinity than neat BTTT2, and that in blends, PCBMs form rows between alkyl side chains of BTTT2.

To complement the morphological simulation studies, we use Time-Resolved Microwave Conductivity at the National Renewable Energy Laboratory to elucidate how polythiophene crystalline domain sizes, determined using X-Ray Diffraction, affect the yield and lifetime of photogenerated charge carriers in P3HT and poly(2,2′:5′,2″-3,3″-dihexyl-terthiophene) (PTTT) films. We show that polythiophene crystallite size is tuned with casting temperature and that films with larger crystalline domains have longer charge carrier lifetimes in neat films and films with phthalocyanine acceptor molecules. Thus, charge carrier lifetime is modulated by crystallite size both in films with low charge carrier concentrations and in films with higher charge carrier concentrations approaching those in organic electronic devices.

Acknowledgements

First, I would like to than my advisors, Dr. Arthi Jayaraman and Dr. Garry Rumbles for working together so that I could succeed at a doctoral thesis that is composed of simulation and experimental work. I thank both of my advisors for their support, scientific guidance and all of the time and effort invested in making me a better researcher, scientist and communicator. I would also like to thank my thesis committee members: Dr. Charles Musgrave, Dr. Matthew Glaser, and Dr. Andrew Goodwin.

I thank Jayaraman group members past and present for their friendship, scientific guidance and computing help, specifically postdocs Dr. Eric Jankowski and Dr. Dongsheng Zhang, and fellow graduate students Tyler Martin, Carla Estridge, Arezou Seifpour, and Robert Elder. For my experimental work, I give special thanks to Dr. Obadiah Reid who mentored me from my first day in the lab at NREL. I also thank Dr. Nikos Kopidakis, Dr. Andrew Ferguson, Dr. Jaehong Park, and Dr. Rebecca Callahan. My collaborators Dr. Martin Heeney and Dr. Natalie Stingelin from Imperial College, London were also instrumental in my work.

I also thank my funding sources: DOE Early Career Award and NREL LDRD Fund. My super computing resources included NERSC, the Janus Super Computer at CU Boulder and NREL GPU resources.

I thank my roommates Jennie Jorgenson, Morgan Figuers, and Julie Stiver for a great home to return to after each work day and my fiancé Ioan Feier for his love and support during the last five years. Finally, I thank my parents for their love and support though the ups and downs of graduate school and for raising me to be the woman that I am today.

Table of Contents

Tables

Figures

Chapter 1
Introduction

Polythiophenes are widely used in organic electronics because they have conducting properties, and polythiophene architecture and chemistry can be modified to achieve properties desirable for a wide range of applications such organic solar cells, light emitting diodes and field effect transistors. These conjugated polymers are composed of a thiophene backbone with alkyl side chains that increase the solubility of the polythiophenes in solvents used for solution processing. In films, polythiophenes form both crystalline domains of aligned, semi-rigid conjugated backbones and amorphous domains connecting the crystallites. The polythiophene morphology in the active layer strongly influences the efficiency of the organic electronic devices. The polymer film morphology is affected by processing conditions, as well as by the chemical and physical features of the polythiophenes, such as molecular weight and alkyl side chain length, spacing, and orientation on the thiophene backbone. The active layer morphology is also affected by the architecture and chemistry of the fullerene derivative molecules (electron acceptors) blended with polythiophenes (electron donors), especially for bulk heterojunction organic solar cell applications. An understanding of how this large set of donor and acceptor design parameters affects the morphology and the behavior of charge carriers in neat polymer films and in polymer-acceptor molecule blends is critical for designing organic electronic devices with improved efficiency. To achieve this understanding a synergistic effort of computational and experimental studies is needed.

The goal of my thesis research is to determine how molecular-level features of polythiophene electron donors and fullerene derivative and phthalocyanine electron acceptors affect the morphology and charge carrier dynamics of donor-acceptor blends and neat donor (no

acceptors) systems using molecular simulations and experiments. In Chapters 2-6, using molecular dynamics simulations, we predict bulk morphologies of a large library of molecules, and provide guidelines to experimentalists about the physical (e.g. architecture) and chemical (e.g. interactions) features of the molecules that affect morphology. We validate our newly developed coarse-grained model through direct comparisons with published experimental results as well as through collaboration with experimentalists (Briseño *et al.* at University of Massachusetts) who synthesize and characterize the specific oligothiophene molecules we simulate. In Chapters 7 and 8, we conduct experiments probing the charge carrier dynamics of films containing polythiophenes with some of the architectures and chemistries studied in simulation.

In Chapter 2, we use coarse-grained Langevin dynamics simulations of blends of generic thiophene-based, conjugated oligomers and fullerene derivative acceptor molecules to show how architecture (e.g., side chains, backbone flexibility of oligomers) and the pair-wise interactions between the constituents of the blend affect morphology and phase transition. Alkyl side chains on the conjugated oligomer backbones shift the liquid crystal (LC) transition temperature from that of bare conjugated backbones and the direction of the shift depends on backbone–backbone interactions. Rigid backbones and constrained side chains cause a lamellar morphology of conjugated polymers and amorphous acceptors, whereas flexible backbones and unconstrained side chains facilitate highly ordered acceptor arrangement. Strong backbone–backbone attraction shifts LC transition to higher temperatures than weak backbone–backbone attraction, and strong acceptor–acceptor attraction increases acceptor aggregation. Pure macro-phase separated domains form when all pair-wise interactions in the blend are strongly attractive, whereas

interconnected domains form at intermediate acceptor–acceptor attraction and strong polymer–polymer attraction.

In Chapter 3, we transition from simulations run on central processing units (CPUs) to performing simulations on graphics processing units (GPUs), which increases computational efficiency and allows us to simulate larger systems with increased detail, and to improve the coarse-grained model in Chapter 2. We use the results from Chapter 2 to select the backbone-backbone attraction strength that best reproduces experimental data and we validate our model in this chapter with comparisons to experimental results of P3HT and poly(3,4-dihexyl-2,2′-bithiophene) (PDHBT) polymers. We present a high- throughput coarse-grained simulation study that links molecular-level design parameters to features in the assembled morphology of neat polymers and donor−acceptor blends. These models reproduce neat polymer morphologies observed in experiments, such as lamellae, hexagonally packed cylinders, and acceptor intercalation among donor side chains. Furthermore, for blends of conjugated polymers and fullerene derivatives, this study shows how conjugated polymer architecture and acceptor miscibility can be tailored to obtain new blend morphologies, which have features that are known to be optimal for higher efficiency solar cells.

In Chapter 4, we focus on neat oligomer morphology and on the thermodynamics of oligomer ordering using the coarse-grained model refined in Chapter 3. We have performed coarse-grained molecular dynamics simulations of thiophene-based conjugated oligomers to elucidate how the oligomer architecture, specifically the orientation and density of alkyl side chains extending from the thiophene backbones, impacts the order-disorder temperatures and the various ordered morphologies that the oligomers form. We find that the orientation of side chains along the oligomer backbone plays a more significant role than side chain density, side chain-

side chain interactions, or side chain length in determining the thermodynamically stable morphologies and the phase transition temperatures. Oligomers with side chains oriented on both sides of the backbone ("-anti") form lamellae, while oligomers with side chains oriented on one side of the backbone ("-syn") assemble into hexagonally packed cylinders that can undergo a second, lower temperature transition to lamellae or ribbons depending on side chain – side chain interaction strength. The strength of side chain – side chain interactions affects the order-disorder temperature, with oligomers having moderately attractive side chains exhibiting higher transition temperatures than those with weakly attractive side chains. Side chain length modulates the spacing between morphological features, such as cylinders and lamellae, and affects the order – disorder temperature differently depending on oligomer architecture.

In Chapter 5, we study how minority component additives, such as methyl ester additives, diiodooctane, and alkanedithiols, affect oligomer-acceptor blend morphology. Small molecule additives have been shown to increase the device efficiency of conjugated polymer and fullerene derivative based organic solar cells by modifying the morphology of the device active layer. In this work we conduct a systematic study of how additives affect the donor-acceptor morphology using molecular dynamics simulations of blends of thiophene-based oligomers, mimicking poly(3-dodecylthiophene) (P3DDT) or poly(2,2′:5′,2″-3,3″-didocyl-terthiophene) (PTTT), fullerene derivatives, and additives of varying length and chemical functionalization, mimicking experimentally used additives. We find that functionalization of additives with end groups that are attracted to acceptor molecules are necessary to induce increased donor-acceptor macrophase separation. In blends where acceptors intercalate between oligomer alkyl side chains, functionalized additives decrease acceptor intercalation. Functionalized additives with shorter

alkyl segments increase acceptor macrophase separation more than additives with same chemical functionalization but longer alkyl segments.

In Chapter 6, we collaborate with experimentalists (Briseño *et al.* at University of Massachusetts), to study blends of 2,5-bis(3-alkylthiophen-2-yl)thieno[3,2-b]thiophene (BTTT) oligomers and fullerene derivative acceptor molecules used in bulk heterojunction organic solar cells. Our simulation results agree with experimental data of ordered structures of BTTT oligomers and acceptor molecules. Thus, our model is not only validated for predicting morphologies of crystalline domains in polythiophene blends, but also for oligomers used directly in device active layers. We find that acceptors form channels in between BTTT oligomer side chains and that oligomer-acceptor blends have higher oligomer order than that of neat oligomers. This work will lead to future collaboration to investigate the effect of oligomer backbone and alkyl side chain length on morphology.

The second part of the thesis work, Chapters 7 and 8, details our experimental work at the National Renewable Energy Laboratory focused on the morphology and charge carrier dynamics of polythiophenes. The microstructure of neat conjugated polymers is crucial in determining the ultimate morphology and photovoltaic performance of polymer/fullerene blends, yet until recently, little work has focused on controlling the former. In Chapter 7, we demonstrate that both the long-range order along the (100)-direction and the lamellar crystal thickness along the (001)-direction in neat P3HT and PTTT films can be manipulated by varying crystallization temperature. Changes in crystalline domain size impact the yield and dynamics of photogenerated charge carriers. Time-resolved microwave conductivity (TRMC) measurements show that neat polymer films composed of larger crystalline domains have longer photoconductance lifetimes and charge carrier yield decreases with increasing crystallite size for

P3HT. Our results suggest that the classical polymer science description of temperature-dependent crystallization of polymers from solution can be used to understand film formation in neat conjugated polymers, and hence, should be considered when discussing the structural evolution of organic bulk heterojunction organic solar cell active layers.

In Chapter 8, we investigate whether the changes in polythiophene crystalline domain size discovered in Chapter 7 affect charge carrier yield and lifetime when the concentration of charge carriers in the films approaches that used in an organic electronic device, and when charge carriers are generated by acceptor molecules instead of in the polymer domain. In this work, we incorporate phthalocyanine electron accepting molecules into the polymer films in low concentration. Selective excitation of the phthalocyanine generates a higher density of charge carriers than what is generated in neat films. Preliminary results show that changes in polythiophene crystallite size affect charge carrier lifetime in films with phthalocyanine in the same way as in neat polymer films. Future work will involve using [6,6]-phenyl-C_{71}-butyric acid methyl ester ($PC_{71}BM$), a more common electron accepting molecule, in similar experiments and performing control experiments with regiorandom P3HT which is completely amorphous (no crystalline domains).

Chapter 2

Morphological Studies of Blends of Conjugated Polymers and Acceptor Molecules using Langevin Dynamics Simulations

Adapted from: *J. Polym. Sci., Part B: Polym. Phys.* 51 (1) 64-77, **2013**

2.1 INTRODUCTION

Organic solar cells have many advantages over conventional silicon solar cells, such as increased flexibility, lower cost and lighter weight. Despite these advantages, organic solar cells are less used than inorganic solar cells due to low device efficiencies. Efficiency of organic solar cells is strongly dependent on the morphology or spatial organization of the materials within the active layer[1-5]. The active layer is typically made of two materials, an electron donating species (e.g. a conjugated polymer) and an electron accepting species (e.g. a fullerene derivative). When photons are absorbed by the conjugated polymer it creates excitons, which are bound charges with binding energies of 0.3-0.5 eV. Excitons can only travel about 10nm before they recombine and dissipate their energy, lowering device efficiency. If excitons successfully make it to a donor-acceptor interface, they dissociate into electrons in the acceptor material and holes in the donor material, which then travel to their respective electrodes. Thus, an ideal morphology that exhibits high efficiency would be one that has a large interface between donor and acceptor materials, small domains (< 10nm) and continuous pathways to the electrodes[1-5].

The donor-acceptor morphology in the active layer is a function of the chemistry and architecture of the conjugated polymer and acceptor molecules and of the processing conditions e.g. conditions during solvent and thermal annealing[1-6]. Commonly used conjugated polymers

are poly(3-hexylthiophene) (P3HT), poly(3,3'''-didodecylquaterthiophene) (PQT-12) and poly(2,5-bis(3-tetradecylthiophen-2-yl)thieno[3,2-b]thiophene (pBTTT). These various conjugated polymers differ in their architecture, such as the alkyl side chain length and the spacing on the backbone between the side chains. For conjugated polymers, the π-conjugation along the backbone makes the polymer backbones more rigid than the backbones of many flexible polymers like polystyrene. For example, the persistence length of P3HT is about 2.4nm[7] while that of polystyrene is about 1 nm[8]. This increased rigidity gives rise to orientational ordering between conjugated polymer backbones below the melting temperature of these polymers. Commonly used electron acceptor molecules are fullerene derivatives, such as [6,6]-phenyl-C_{61}-butyric acid methyl ester (PCBM) and [6,6]-phenyl-C_{71}-butyric acid methyl ester. Fullerene functionalization improves miscibility of the fullerene, C_{60}, in solvents used during preparation of the active layer such as dichlorobenzene, toluene, and dichloromethane. Functionalization also changes molecular interactions of the fullerene with the conjugated polymer and with other fullerene molecules.

Many experimental studies on blends of the conjugated polymer, P3HT, and PCBM molecules have shown the formation of pure domains of either component, and mixed amorphous regions within the active layer[9-11]. Strong attractive interactions between PCBM and P3HT favor the formation of amorphous regions rather than PCBM crystallites[12]. However, when enough P3HT has crystallized to increase the concentration of PCBM over the solubility limit, the limited solubility of PCBM causes PCBM crystals to form[10]. The morphology of conjugated polymer-acceptor molecule blends is also dependent on the conjugated polymer alkyl side chain length and spacing[6, 13-19]. Studies of the conjugated polymer T8TBT with side chains

and without side chains found that the presence and orientation of side chains affect morphology and thus the decay of charge carriers in the active layer. For example, blends of PCBM and T8TBT with no side chains form purer domains and larger aggregates than do blends of T8TBT with side chains[13].

While the above studies note the various factors that affect blend morphology, they are focused on a relatively narrow range of polymers and acceptors due to extensive synthetic efforts involved in making the materials, and there is a lack of consistency in the morphologies for identical systems in different experiments due to kinetic trapping. It would be useful if one could predict the equilibrium morphology for a variety of conjugated polymer–acceptor blends, and have a systematic study varying the physical and chemical features of the conjugated polymers and acceptor molecules to isolate the role of each feature on the resulting phase behavior and blend morphology. Molecular simulations are ideal for such systematic studies to understand effects of various parameters on equilibrium behavior because they can avoid discrepancies due to variations in experimental protocols, e.g. small variations in parameters like film thickness, solvent type, and annealing time, all of which significantly affect blend morphology. Additionally, simulations can cover a large parameter space, including diverse material architectures and chemistries, without any limitations due to difficult or time consuming synthesis.

There are a few noteworthy coarse-grained simulation studies of blends of P3HT and PCBM focused on the effect of varying blend composition on bulk morphology. One such study was done by Huang *et al*. who developed a coarse-grained model for systems of P3HT and C_{60} where P3HT was represented by three beads per monomer (as done in this paper), and C_{60} (not a

fullerene derivative) was represented by one bead. The interactions between the coarse-grained beads were obtained by mapping the coarse-grained blend structure to the structure obtained using atomistic simulations. They studied blends of P3HT and C_{60} at varying weight ratios at temperatures above the melting point of the polymer[20, 21]. In another study, Lee *et al*. created a coarse-grained model of the P3HT:PCBM system from atomistic simulation, with a P3HT monomer represented by single bead and the PCBM molecule represented by one bead[22].They varied the weight ratio of the blend and studied domain sizes and shapes as well as interfacial characteristics of the blend at 423K. While the above simulation studies are significant, they were either conducted above melting temperature of the polymer [20, 21]. or used a model that was too coarse-grained to be able to study spatial arrangement at the molecular level[22]. Additionally, these past studies focused mainly on the effect of blend composition (e.g. relative volume fractions of P3HT and PCBM) on the morphology.

In this paper we use coarse-grained Langevin dynamics simulations to obtain a fundamental understanding of how physical (e.g. size, flexibility) and chemical (e.g. pair-wise interaction strengths) features of donor (conjugated polymer) and acceptor (fullerene derivative) molecules affect morphology and phase transition in blends of conjugated polymer and acceptors. We model the conjugated polymer using three coarse-grained beads – one backbone bead to represent the thiophene ring, and two side chain beads each representing an alkyl group, similar to the model used by Huang *et al*. [20, 21]. The acceptor molecule is modeled using one large coarse-grained bead to represent a fullerene derivative, with modified pair-wise interactions from that of Huang *et al*. [20, 21]. First, we demonstrate the role of the alkyl side chains of the conjugated polymer on the phase transition and morphology at varying pair-wise interactions

involving the backbone and side chain beads. When the pair-wise interactions involving the coarse-grained side chain beads are stronger than those involving coarse-grained backbone beads (interaction set I), the side chains shift the liquid crystalline transition of polymer-acceptor blends to a higher temperature compared to bare backbones. Also, due to the alkyl side chains i) the rigid conjugated backbones are spaced more closely together compared to systems of bare rigid backbones, ii) the acceptors are less ordered and iii) the acceptors arrange themselves in layers alternating with layers of conjugated polymer instead of a columnar ordering surrounded by bare backbones. Additionally, the side chains also decrease the diffusion of both polymer backbones and the acceptor molecules. When the pair-wise interactions involving the backbone beads are stronger than those involving side chains (interaction set II), the LC transition temperature is higher than with interaction set I. In addition, with interaction set II, the side chains shift the LC transition temperature of the conjugated polymer to lower temperatures than for bare interaction set II backbones, opposite to the trend seen with blends with interaction set I. When all pair-wise interactions involving backbones and side chains are strongly attractive (interaction set III), the LC transition temperatures are the same as those seen for interaction set II, but higher than those with interaction set I (all in presence of side chains), suggesting that the polymer backbone alignment and the LC transition temperature are strongly dependent on the strength of the backbone-backbone attractions.

Next we elucidate the role of the physical features of the conjugated polymer, such as backbone flexibility/rigidity and the constraint of the alkyl side chain (using dihedral and three body angle potentials) on the blend morphology. Blends with polymers having *unconstrained* side chains and *rigid* backbones exhibit similar LC transition temperature and ordering of

backbones and acceptors as that seen with blends containing polymers with *constrained* side chains and *rigid* backbones. Blends with polymers having *constrained* side chains and *flexible* backbones form mixed, disordered layers of conjugated polymer and acceptors, while blends with polymers having *unconstrained* side chains and *flexible* backbones form ordered columns of acceptor molecules. These results suggest that while the side chain constraint plays a smaller role when the backbone is rigid, in case of flexible backbones it dictates the order of the acceptors.

Lastly, we study the role of acceptor molecule chemistry in dictating the morphology in conjugated polymer-acceptor molecule blends. At all blend compositions and pair-wise interaction strengths involving the polymers, increasing acceptor-acceptor attractive interaction strength leads to increasing acceptor aggregation. At weak acceptor-acceptor attraction, *alternating layers* of conjugated polymer and acceptor molecules are seen for all interaction sets. At strong acceptor-acceptor attractions, *pure macrophase separated domains* of acceptor and conjugated polymers are formed when all pair-wise interactions involving backbones and side chains are strongly attractive (interaction set III). At intermediate acceptor-acceptor interaction strength, blends with interaction set III form *interconnected domains* of acceptors and conjugated polymers. These results show how fine tuning the chemistry of the acceptor and polymer can shift the equilibrium morphology from pure phase separated domains to well mixed domains to partially mixed/interconnected domains.

These results connecting physical (e.g. size, flexibility) and chemical (e.g. pair-wise interaction strengths) features of donor (conjugated polymer) and acceptor (fullerene derivative) molecules to observed blend morphology and phase transition should provide a) a molecular-level picture to experimentalists explaining why the specific choice of polymer and acceptor

gives them higher or lower device efficiency, and b) valuable guidelines to synthetic chemists on what chemical and physical features should be incorporated into conjugated polymers and/or acceptors to obtain a specific blend morphology.

This paper is organized as follows. In section II, we discuss the specifics of our model and simulation method, the analysis methods and the parameters varied. In section III, we present results that help explain the role of physical and chemical features of the conjugated polymer as well as role of acceptor molecule chemistry and size in shaping the morphology of blends of conjugated polymer and acceptor molecules. We conclude in section IV with a summary and future outlook.

2.2 APPROACH

2.2.1 Model

We model blends of conjugated polymer and acceptor molecules in a coarse-grained manner in order to simulate these systems on a length scale that is large enough to examine the blend morphology, while retaining necessary molecular-level detail. We model the conjugated polymer using three coarse-grained beads per monomer. The polymer backbone is a rigid[23] chain of coarse-grained beads (B) each representing a thiophene ring. The flexible alkyl side chains attached to each backbone bead are represented using two types of side chain beads (S1 and S2), as shown in Figure 2.1. We model acceptor molecules as a single coarse-grained bead (A), to mimic a fullerene derivative. We determine approximate bead masses from the collective molecular weight of the atoms that each coarse-grained bead represents, assuming P3HT as our model polymer. We normalize each bead's mass to the mass of a backbone bead (B) to obtain dimensionless masses. See Section 2.7.1 for the dimensionless masses of each bead. We obtain

the bonded interaction potentials (bonded, dihedral angle, and three body angle potentials) for the conjugated polymers by fitting the potentials obtained for the similarly coarse-grained P3HT polymer model (derived by mapping the coarse-grained model to atomistically detailed simulations conducted above the melting temperature of P3HT) by Huang *et al.*[20, 21] (Section 2.7.1). We model the non-bonded interactions using Lennard Jones (LJ) potentials[24] for the non-bonded pairs of beads in the conjugated polymer, and between conjugated polymer beads and acceptor bead. Table V in Section 2.7.1 lists the values for the dimensionless LJ parameters, ε_{ij} and σ_{ij}, also adapted from the non-bonded potentials calculated by Huang *et al*. [20, 21] (values were non-dimensionalized in relation to the values of ε and σ for B-S1 interactions). We vary the chemistry of the backbone beads and side chain beads by tuning $\varepsilon_{B\text{-}j}$, $\varepsilon_{S1\text{-}j}$, and $\varepsilon_{S2\text{-}j}$, the interaction well depths between B or S1 or S2 beads and another j^{th} type bead in the system, with *j* being B, S1, S2 or A. Additional details of the interactions are provided in the Section 2.7.1. To model the varying acceptor molecule solubility in an implicit organic solvent, we vary the well depth of the acceptor-acceptor interactions, dimensionless $\varepsilon_{A\text{-}A}$, from 2 to 4. If the acceptor molecule was a fullerene molecule with no functionalization, the dimensionless $\varepsilon_{A\text{-}A}$ between two C_{60} molecules would approximately be 6[20, 21].

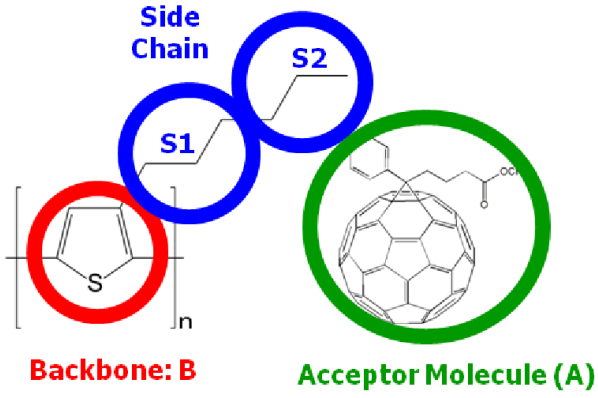

FIGURE 2.1: Coarse-grained model of conjugated polymer with backbone beads (B) and side chain beads (S1 and S2), and acceptor molecule (A).

Here are some implications of the choice of our model. First, while the level of detail we have chosen in the coarse-grained model is appropriate to capture the effects of backbone beads and alkyl side chains beads separately, it limits us to studying oligomers instead of polymers. To simulate long polymers one would have to choose coarse-grained models where each bead represents a Kuhn segment or a group of monomers, thus obscuring all of the molecular details we wish to retain. Second, for the majority of the study, we assume that the polymer backbone is perfectly rigid. While long polymers do have some flexibility in the backbone, assuming a perfectly rigid backbone is a good assumption for oligomers based on past work. The conjugation length of P3HT in solution is shown to be 6 monomers[7] and past experiments with P3HT have assumed that the P3HT backbone is completely planar with a molecular weight of 5 kDa (~19 monomers)[25]. We note that this model which is based on P3HT mostly, can reproduce faithfully the backbone-backbone distance of approximately 16 Å found in crystallographic data for P3HT layer-lyer spacing[26, 27] shown in Section 2.7.1. By assuming rigidity and simulating short polymers, this model can better capture local ordering in small crystalline domains and the effect of side chains on local morphology. By studying oligomers with rigid backbones, we expect not to capture the amorphous polymer domains found in blends of longer conjugated polymers. To overcome this limitation, we do report results from simulations using flexible polymer backbones as well, but not as extensively as we have for blends with rigid backbones.

2.2.2 Simulation Method

We use Langevin dynamics simulations[24] (via LAMMPS Molecular Dynamics Simulator[28]) to simulate these blends of conjugated polymers and acceptor molecules in implicit

solvent in the NVT ensemble. Every system is cooled from a high temperature, T^*_{high}, to a low temperature, T^*_{low}, where T^*_{high} is selected as the temperature at which the system is completely disordered and T^*_{low} is selected as the temperature at which the system has ordered. The cooling schedule is $T_{n+1}=T_n(0.95)$ and at each temperature the system is equilibrated for $5x10^6$ to $25x10^6$ time steps. We choose this cooling schedule after extensive tests to ensure that the observed morphology is not a function of the cooling schedule, and as a result is the true equilibrium morphology. We note that all temperatures are dimensionless by normalizing with ε/k_b, where k_b is the Boltzmann constant and ε is $\varepsilon_{B\text{-}S1}$ from interaction set 1 (Section 2.7.1).

2.2.3 Analysis

To understand phase behavior of the conjugated polymer-acceptor molecule blends, we quantify orientational and positional order among the various components of the blend as a function of temperature.

Since the conjugated oligomers have rigid backbones, we expect that as the system is cooled, a transition from a relatively isotropic arrangement at high temperatures to an orientationally aligned state with nematic or smectic order at low temperatures. To identify this liquid crystalline like transition (denoted as LC transition throughout this paper), we calculate orientational order parameter, S_2[29], for the polymer backbone at various temperatures. S_2 is equal to the largest Eigen value of the ordering tensor, Q, defined as:

$$Q = \frac{1}{N}\sum_{i=1}^{N}\left[\frac{3}{2}(\hat{u}_i)_\alpha(\hat{u}_i)_\beta - \frac{1}{2}\delta_{\alpha\beta}\right] \quad (1)$$

where N is the number of polymer backbones in the system, $\hat{u}_i$ is the unit vector of the i^{th} chain and α and β take values x, y, and z[29].

Since $S_2 = 0$ for a disordered isotropic system and $S_2 = 1$ for a perfectly orientationally aligned system, the LC transition temperature is identified as the temperature where there is an abrupt increase in the value of S_2. The S_2 value at each temperature is an ensemble average over the equilibrium state at each temperature and error bar magnitude is calculated from three trials of representative systems. While S_2 characterizes a global orientational order, to quantify how backbones align with each other, both locally and as a function of backbone-backbone distance, we calculate a second orientational order parameter $P_2(r)$[30] as a function of backbone-backbone distance r. In some systems, we observe multiple domains where the backbones are orientationally aligned with other backbones *within* that domain, but the domains themselves might not be aligned to each other. A domain is a collection of backbones where every pair of backbones within a distance of 2.0σ (arbitrarily chosen) of each other and are aligned with a P_2 greater than 0.9 (chosen after several tests). A distance of 2σ was chosen because σ is the closest possible spacing of two backbone beads and 2.0σ encompasses all close backbones. For a few select systems, the individual domains are identified and the alignment and spatial distribution of each species within each domain are calculated.

We also calculate radial distribution functions, $g_{ij}(r)$[24] between backbone-backbone centers of mass denoted by $g_{BB}(r)$, acceptor bead-acceptor bead, $g_{AA}(r)$, and acceptor bead-backbone bead, $g_{AB}(r)$. To quantify acceptor order and crystallinity, we calculate the number of nearest acceptor neighbors, a neighbor being defined as a particle within a distance $r_q = 1.2\ \sigma$[31, 32]. Histograms of acceptor neighbors are then created by plotting the fraction of acceptors having a specific number of neighbors (0, 1, 2, 3, etc.). We also calculate the global bond order parameter Q_6[31, 32]:

$$Q_l = \left(\frac{4\pi}{2 \cdot l + 1} \sum_{m=-l}^{l} \left| Q_{lm}^2 \right| \right)^{0.5} \tag{2}$$

$$Q_{lm} = \frac{\sum_{i=1}^{N} \sum_{j=1}^{N_b(i)} Y_{lm}(\hat{r}_{ij}) a(r_{ij})}{\sum_{i=1}^{N} \sum_{j=1}^{N_b(i)} a(r_{ij})} \quad , \quad a(r_{ij}) = (r_{ij} - r_q)^2 \qquad \text{and } l = 6. \tag{3}$$

$N_b(i)$ is the number of neighbors of acceptor i that are a distance of r_q from acceptor i. j are all acceptors within radius r_q from acceptor i and N is the total number of acceptors in the system. $Y_{lm}(r_{ij}) = Y_{lm}(\theta_{ij}, \phi_{ij})$ are spherical harmonics where $r_{ij,}$ $\theta_{ij,}$ and ϕ_{ij} are the coordinates of the vector between beads i and j in spherical coordinates. $a(r_{ij})$ is a weight function that approaches zero at r_q. Amorphous spheres have a Q_6 value of zero, while for FCC packed spheres, $Q_6 = 0.57452$[32]. We calculate Q_6 only for blends that show significant acceptor ordering or aggregation and include only those acceptors that have two or more acceptor neighbors.

Finally, in order to quantify the mobility of each species with time, we calculate the mean square displacement (MSD) of each species[24]:

$$MSD = \left\langle r^2(t) \right\rangle = \left\langle \frac{1}{N} \sum_{i=0}^{N} \left(r_i(t + \delta t) - r_i(t) \right)^2 \right\rangle \tag{4}$$

where N is the number of molecules of that species and $r_i(t+\delta t)$-$r_i(t)$ is the distance between the center of mass of a molecule at time t and at time $t+\delta t$. The average displacement at each time increment: δt, $2\delta t$, $3\delta t$ etc. is averaged for each molecule type. The diffusion coefficient is calculated from the slope of the diffusive portion of the MSD curve.

2.2.4 Parameters Varied

The conjugated polymer chains are of length 10 monomers throughout this study. We conduct simulations for overall volume fraction, η, of 0.1, 0.2, and 0.3, with acceptor molecule volume fractions ϕ varied from 0 to 0.6. For brevity we only present results for blends where η = 0.2 because the trends observed at η = 0.2 are similar at other η as well. Section 2.7.4 presents results at η = 0.1. To isolate the role of each of the pair-wise interactions on observed morphology, we simulate blends of polymers and acceptors using several sets of non-bonded pair-wise interactions, $\varepsilon_{B\text{-}j}$, $\varepsilon_{S1\text{-}j}$ and $\varepsilon_{S2\text{-}j}$, involving the conjugated polymer beads. See Section 2.7.1 for the Lennard Jones parameters for each of these sets. For interaction set I we have adapted the potentials from the P3HT:C_{60} model of Huang et al. [20, 21], while lowering their acceptor-acceptor attractive well depths to mimic the increased solubility of fullerene derivatives compared to C_{60}. In interaction set II, pair-wise interactions involving backbone (B) are stronger than the interactions involving the side chain beads. In interaction set III, the pair-wise interactions involving backbone and involving the side chain beads are all strong. The acceptor-acceptor attractive well depth, $\varepsilon_{A\text{-}A}$, is varied from 2-4 to model various acceptor molecule chemistries. Acceptor molecule diameter is also varied from d = 2 in the original model to d = 2.6. Increasing d would mimic incorporation of large functional groups on the C_{60} for molecules such as bis-$PC_{61}BM$, methano fullerenes, indene fullerenes, and dihydronaphthyl fullerenes.

2.3 RESULTS

2.3.1 Role of Conjugated Polymer Side Chains

To better understand the role of the conjugated polymer side chains in blend morphology, we first present the morphology of blends containing bare backbones (without side chains) and

acceptor molecules, and then contrast that to results observed with side chains. Our discussion in this section is focused on one total packing fraction, $\eta = 0.2$, while Section 2.7.4 shows results for $\eta = 0.1$ systems. To characterize the morphology at various polymer-acceptor blend compositions, we present visual snapshots, plots of orientational order among the polymer backbones as a function of temperature, pair-wise radial distribution functions, and histograms of neighbors per acceptor.

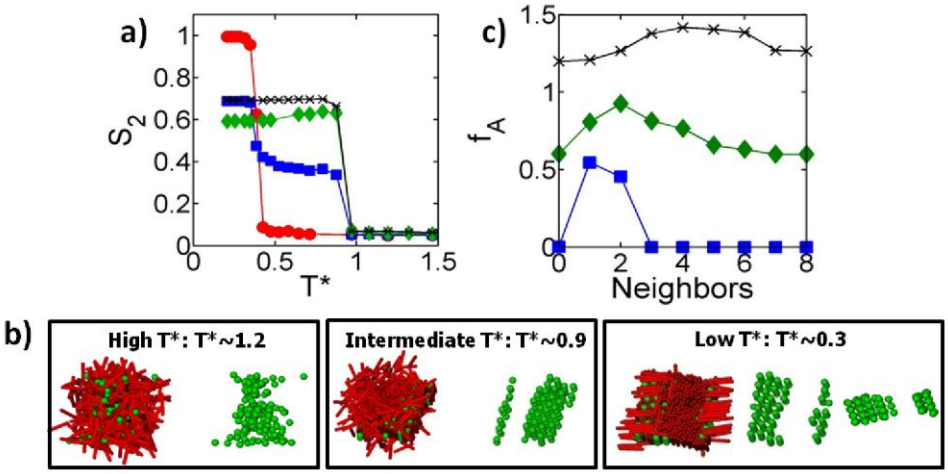

FIGURE 2.2: a) Order parameter, S_2, as a function of reduced temperature, T*, for blends of conjugated polymer backbones and acceptors with interaction set I in the absence of side chains at a total blend volume fraction $\eta = 0.2$ and acceptor volume fraction $\phi = 0$ (red circles), 0.2 (blue squares), 0.4 (green diamonds), and 0.6 (black X). b) Simulation snapshots of the $\eta = 0.2$ $\phi = 0.2$ blend at high (T* ~ 1.2), intermediate (T* ~ 0.9), and low (T* ~ 0.3) temperatures. c) Histogram of acceptor neighbors at T* = 0.208 for blends of conjugated polymer backbones and acceptor molecules with interaction set I in the absence of side chains at total volume fraction $\eta = 0.2$ and varying acceptor volume fraction $\phi = 0.2$ (blue squares), 0.4 (green diamonds), and 0.6 (black X); curves are offset by 0.6 units along the y-axis for clarity.

Figure 2.2a shows the plot of S_2 for bare polymer backbones as a function of reduced temperature, T*, for pure polymer backbones (acceptor volume fraction $\phi = 0$), and for blends with increasing acceptor volume fraction $\phi = 0.2$-0.6. All curves in Figure 2.2 exhibit a liquid crystalline (LC) transition denoted by an abrupt/gradual increase in S_2 value. While $S_2 = 1$

denotes perfect orientational order (nematic or smectic), in many of our systems, S_2 does not reach 1, yet visual analyses (e.g. snapshots in Figure 2.2) confirm good backbone-backbone alignment. Careful inspection shows that an S_2 value of less than 1 in these blends occurs either due the presence of multiple domains that are not aligned with each other but have excellent backbone-backbone alignment within each domain, or due to the presence of a few unaligned backbones. See Section 2.7.2 for domain analysis of the $\eta = 0.2$ $\phi = 0.2$ blend showing that while the overall S_2 is less than 1, S_2 within domains is near 1 indicating good backbone alignment. Thus, we focus our discussions mainly on the LC transition temperature, and less on the value of S_2 below the LC transition temperature. Error bars for each data point, as calculated from three trials of representative systems, are approximately the size of the symbol (Section 2.7.2). Figure 2.2a shows that upon adding acceptors to pure conjugated polymer, the LC transition of the bare polymer backbones shifts to a higher T*. Past studies of spheres and rods with only hard-sphere interactions have shown that adding spheres induces rod alignment to maximize the free volume in the system and in turn increase translational entropy[30, 33]. In the blends studied here there are additional attractive enthalpic backbone-backbone, backbone-acceptor and acceptor-acceptor interactions (with acceptor-acceptor attraction being the strongest) that favor polymer backbone alignment. Thus, ordering of the backbone and acceptor species is favored enthalpically and entropically.

At low acceptor molecule volume fraction ($\phi = 0.2$), we see a two-step transition in S_2, while at high acceptor volume fractions we see a single sharp transition in S_2. This can be explained with a visual analysis of the blend. Figure 2.2b shows single snapshots representative of the $\eta = 0.2$ $\phi = 0.2$ blend at various temperatures. When an initially disordered $\eta = 0.2$ $\phi = 0.2$

blend of bare polymer backbones and acceptors is cooled, first the acceptors aggregate at high T*. Then at intermediate T*, polymer backbones penetrate the acceptor aggregate and align (increase in S_2) in order to maximize both attractive acceptor-acceptor interactions (dominant), and attractive acceptor-backbone (moderate) and backbone-backbone interactions (weak). At this stage, we see acceptors arrange into columns between these backbones. We note that the results presented in Figure 2.2 are in the absence of polymer side chains As the blend is cooled further, excess backbones align, causing the second increase in S_2 and forming a pure backbone domain. The histogram of acceptor neighbors for the $\eta = 0.2$ $\phi = 0.2$ blend as a function of temperature shows the progression from disperse to aggregated acceptors to columnar acceptor order as temperature is lowered (Section 2.7.2). As temperature is lowered, the number of neighbors of an acceptor increases from 0 (dispersed state at T*=1.463) to the 1-2 neighbors at the lowest temperature as expected in a highly ordered columnar arrangement where acceptors on the ends of columns have 1 neighbor and those in the centers of columns have 2. At high ϕ ($\phi \geq 0.4$), there are sufficient acceptors in the blend that after the acceptors have aggregated, most of the polymer backbones enter the acceptor aggregate and align, leaving no unaligned backbones to align at the lowest T*. Thus, high ϕ systems exhibit only one transition in S_2. In addition, at high ϕ, acceptor molecules gain more neighbors (Figure 2.2c) because there are more acceptors in these systems than can align in columns between backbones and thus neat columns are not formed. We also characterize the mobility of the various species in the blend by plotting the diffusion coefficient as a function of temperature. The diffusion coefficient for acceptors and polymer backbones at varying ϕ (Section 2.7.3) shows that the diffusion is higher for backbones than for acceptors because acceptors, such as fullerene derivatives, have a larger mass than do

backbone beads (e.g. thiophene ring). As ϕ increases, acceptor diffusion decreases because the higher number of acceptor molecules lead to larger aggregates, impeding acceptor diffusion within the large aggregates. In case of backbones, below the LC transition T*, as ϕ increases backbone diffusion decreases. This is because at high ϕ most of the polymer backbones in the blend are within the acceptor aggregates (below the LC transition T*) and thus, have lower diffusion compared to the unaligned and mobile backbones present at low ϕ at the same temperatures.

Having understood the effect of acceptor molecules on bare polymer backbones *without* side chains, we next present how *presence of alkyl side chains* changes these trends. In Figure 2.3a we see that in the presence of side chains, the LC transition temperature of polymer backbones shifts to higher temperatures both for pure polymer ($\phi = 0$) as well as for blends with acceptor molecules ($\phi > 0$). This is because in the presence of side chains, the attractive side chain-side chain interactions drive the polymers in the blend to aggregate, and as a result cause the backbone-backbone alignment (and LC transition) to occur at higher temperatures than in the absence of side chains. Interestingly, in the presence of side chains, with addition of acceptor molecules we shift the LC transition slightly to *lower* temperatures (Figure 2.3b) as compared to the more drastic shift to *higher* temperature upon adding acceptors to bare polymer backbones (Figure 2.2a). This is because in the presence of side chains, when conjugated polymer molecules are disordered, acceptors are able to have favorable contacts with flexible side chains and also maintain higher translational entropy, shifting the LC transition to lower temperatures. Our observation of lower LC transition is in agreement with experimental observation of lower melting temperature for P3HT/PCBM blends as compared to pure P3HT because PCBM serves

as an impurity that disrupts order[34]. In the presence of side chains, acceptors in these blends lack crystalline order and locate themselves between conjugated polymer layers. Visual analysis, acceptor-acceptor radial distribution function $g_{AA}(r)$ and histogram of acceptor neighbors (Section 2.7.2) confirm this. Q_6 values (Section 2.7.5) for $\eta = 0.2$ $\phi = 0.2$ and 0.3 blends containing polymers *with* side chains are lower (decreased order) than those of $\eta = 0.2$ $\phi = 0.2$ and 0.3 blends containing polymers *without* side chains. Additionally, in blends with side chains, polymer backbones are pressed closer together than in blends without side chains as indicated by a shift in the first peak position in the backbone-backbone radial distribution function, $g_{BB}(r)$, to shorter backbone center of mass-backbone center of mass distances (Figure 2.3c). Since the above results are with a set of interactions where the side chain-side chain attraction is stronger than backbone-backbone attraction, we believe the enthalpic gain from bringing side chains close to each other drives backbones to be closer together.

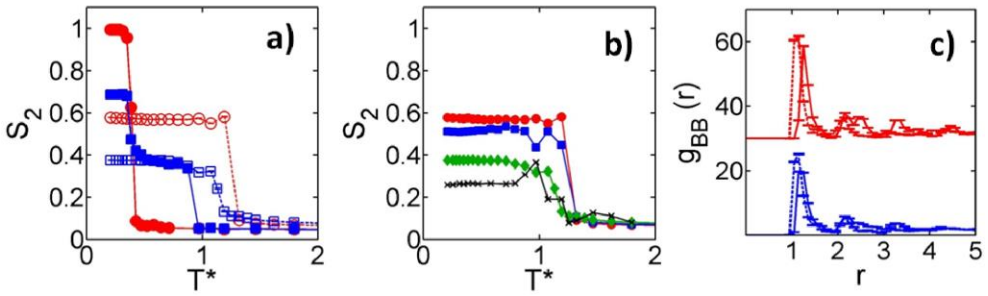

FIGURE 2.3: a) Order parameter, S_2, as a function of reduced temperature, T*, for $\eta = 0.2$ blends of acceptors and conjugated polymers with interaction set I, with (open symbol) and without (solid symbol) alkyl side chains at acceptor volume fraction $\phi = 0$ (red circles) and $\phi = 0.2$ (blue squares). b) Order parameter, S_2, as a function of reduced temperature, T*, for $\eta = 0.2$ blends of acceptors and conjugated polymers with interaction set I, with side chains at acceptor volume fraction $\phi = 0$ (red circles), 0.1 (blue squares), 0.2 (green diamonds), and 0.3 (black X). c) Backbone-backbone radial distribution function, $g_{BB}(r)$, as a function of distance between backbone centers of mass, r, for $\eta = 0.2$ blends of conjugated polymers with interaction set I, with (dashed lines) and without (solid lines) alkyl side chains and acceptor volume fraction $\phi = 0$ (red) and $\phi = 0.2$ (blue) at T* = 0.208; curves for the $\phi = 0$ systems are shifted up by 30 units along the y-axis for clarity.

In the presence of side chains, backbone diffusion is lower than in the absence of side chains, because the polymer molecules become bulkier when side chain beads are added to the backbone (Section 2.7.3). In systems with side chains, attractive interactions of side chains with side chains on other backbones cause the blend to aggregate at higher temperatures, further lowering backbone diffusion as compared to systems without side chains. Adding acceptors to conjugated polymers with side chains further lowers backbone and acceptor diffusion because acceptors are attracted to conjugated polymer side chains and the entire blend aggregates strongly. Acceptor diffusion decreases when polymer backbones have side chains and as acceptor volume fraction ϕ increases.

In summary, when pair-wise interactions involving side chains are more attractive than those involving backbones (interaction set I), the role of side chains is to a) increase the LC transition temperature of the blend, b) facilitate conjugated polymer and acceptors to order into a layer-by-layer morphology with the acceptor molecules arranging amorphously in between conjugated polymer layers, and c) lower the diffusion of the conjugated polymer backbones in the blends.

To understand how the above results are affected by the choice of pair-wise interactions between side chain, backbone, and acceptor beads, we systematically vary the strength of attraction between the various pairs in the blend in the next section.

2.3.2 Role of Chemical Interactions within the Blends

For clarity we denote the interactions used in the previous section as interaction set I. We first interchange the non-bonded pair-wise interactions involving side chain beads (S1) with the non-bonded pair-wise interactions involving backbone beads (B) from *interaction set I*, and

denote this new set of interactions as interaction set II. Thus, in *interaction set II* the backbone-acceptor and backbone-backbone interactions are more strongly attractive than side chain-acceptor and side chain-side chain intereactions in contrast to interaction set I (results shown so far) where the backbone-acceptor and backbone-backbone interactions are less attractive than side chain-acceptor and side chain-side chain intereactions. In *interaction set III*, all pair-wise interactions, backbone-acceptor, backbone-backbone, side chain-acceptor and side chain-side chain, are strongly attracting. Section 2.7.1 lists the Lennard Jones parameters for all interaction sets.

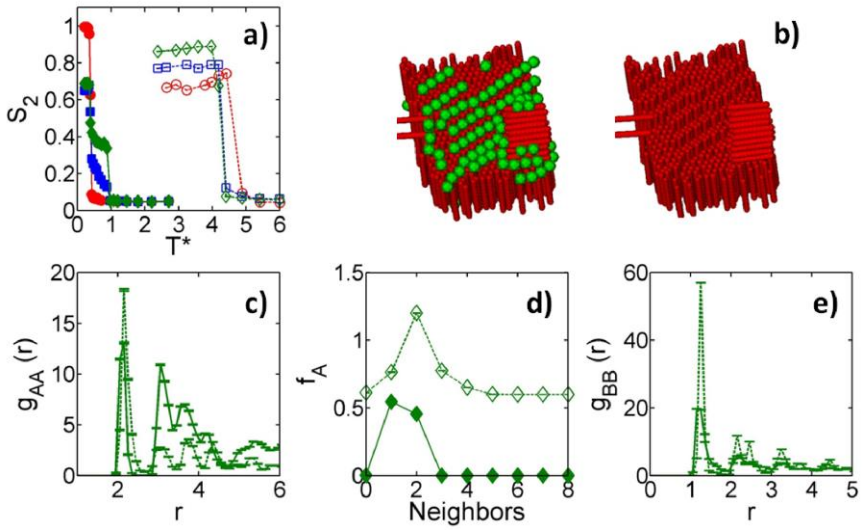

FIGURE 2.4: a) Order parameter, S2, as a function of reduced temperature, T*, for η = 0.2 blends of conjugated polymer backbones without side chains with interaction set I (solid lines) and interaction set II or III (dashed lines) at acceptor volume fraction ϕ = 0 (red circles), 0.1 (blue squares), and 0.2 (green diamonds). b) Snapshot of the η = 0.2 ϕ = 0.2 blend of conjugated polymer backbones (without side chains) with interaction set II at T* = 0.213, pictured with and without acceptors (green spheres). c) Acceptor-acceptor radial distribution function, gAA(r), as a function of distance between acceptor centers of mass, r, for the η = 0.2 ϕ = 0.2 blend with interaction set I at T* = 0.208 (solid lines) and interaction set II or III at T* = 0.213 (dashed lines), both without side chains. d) Histogram of acceptor neighbors with curves offset along y-axis by 0.6 units, for the η = 0.2 ϕ = 0.2 blend with interaction set I at T*=0.208 (solid green diamonds) and interaction set II at T* = 0.213 (open green diamonds), both without polymer side chains. e) Backbone-backbone radial distribution function, gBB(r), as a function of distance between backbone centers of mass, r, for the η = 0.2 ϕ = 0.2 blend with interaction set I at T* =

0.208 (solid lines) and interaction set II or III at T* = 0.213 (dashed lines), both without side chains.

In the absence of side chains, the polymer backbones undergo LC transition at a higher temperature with interaction set II (dashed lines in Figure 2.4a) than with interaction set I (solid lines in Figure 2.4a). Since backbone-backbone and backbone-acceptor attractive interactions are stronger in interaction set II compared to interaction set I, there is a higher enthalpic driving force for backbone alignment in interaction set II than in interaction set I, in addition to similar entropic reasons for ordering in both interaction sets (discussed in the previous section). Blends of acceptors and polymers with interaction set II (no side chains) have lower LC transition temperatures compared to that of pure polymers with interaction set II (no side chains). Interestingly, this trend is the opposite of that seen in blends with interaction set I (no side chains), where the addition of acceptors causes the LC transition to occur at higher temperatures than in systems without acceptors. This is because in interaction set I, backbone alignment is facilitated by acceptor aggregation, which happens at higher temperatures than the temperature of backbone alignment. In contrast, in interaction set II, backbone alignment occurs at a temperature higher than that of acceptor aggregation and acceptors impede backbone ordering and are expelled from the backbone domain. Thus, the LC transition in blends occurs at a lower temperature than with pure polymer backbones in interaction set II. In both interaction sets I and II, acceptor volume fraction does not affect the LC transition temperature significantly (Figure 2.4a).

With interaction set II, acceptors organize in rows at the edges of backbone domains to maximize the acceptor–backbone contacts (Figure 2.4b) and the enthalpic gain from favorable acceptor-backbone, backbone-backbone, and acceptor-acceptor contacts. This difference in

ordering is also seen in the acceptor-acceptor radial distribution function, $g_{AA}(r)$, (Figure 2.4c) which shows that a higher number of acceptors are in close proximity to each other in blends with interaction set II than in blends with interaction set I. The histogram of acceptor neighbors (Figure 2.4d) shows that the majority of acceptors have 2 neighbors with interaction set II, compared to 1-2 neighbors for interaction set I, because the majority of acceptors are in within a long row in systems with interaction set II, while with interaction set I, acceptors are in columns that are only as long as the backbone lengths, leading to a higher number of acceptors at the ends of columns that have only 1 neighbor. Because of the absence of acceptors between the backbones in the aligned backbone domain, there are more backbones at the closest backbone-backbone spacing in blends with interaction set II than in blends with interaction set I (Figure 2.4e). Note that in the absence of side chains, interaction set III and II are identical.

In the presence of side chains, comparing pure polymers and blends of acceptors and polymer with interaction set I, interaction set II and interaction set III, we see that i) blends of conjugated polymer and acceptors form layers of conjugated polymer with acceptors in between for all three sets of interactions, and ii) the LC transition temperature is the same for interaction sets II and III but higher than that for interaction set I (Figure 2.5a). Since the gain in backbone translational entropy from backbone alignment is the same in interaction set I, II and III, the similar LC transition temperature for interaction sets II and III (and higher than interaction set I) is purely due to the higher enthalpic gain from backbone alignment arising from stronger backbone-backbone attractions for interaction sets II and III.

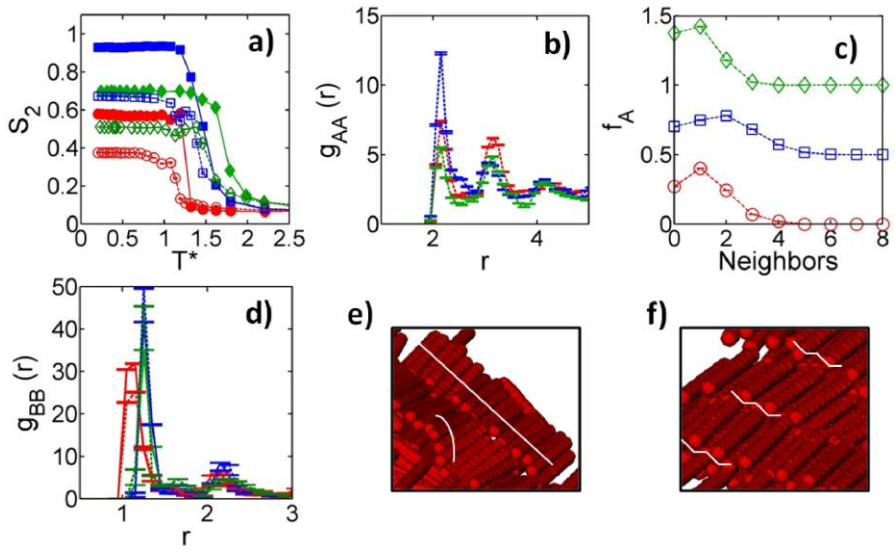

FIGURE 2.5: a) Order parameter, S_2, as a function of reduced temperature, T*, for pure polymer with side chains at η = 0.2 (solid symbols) and η = 0.2 ϕ = 0.2 blends of polymers and acceptors (open symbols), with interaction set I (red circles), interaction set II (blue squares) and interaction set III (green diamonds). b) Acceptor-acceptor radial distribution function, $g_{AA}(r)$, as a function of distance between acceptor centers of mass, r, for η = 0.2 ϕ = 0.2 blends with interaction set I (red) at T* = 0.208 , interaction set II (blue) at T* = 0.208 and interaction set III (green) at T* = 0.23. c) Histogram of acceptor neighbors for η = 0.2 ϕ = 0.2 blends of polymers with side chains and acceptors with interaction set I (red circles) at T* = 0.208, interaction set II (blue squares) at T* = 0.208 and interaction set III (green diamonds) at T* = 0.23; curves are offset by 0.5 units for clarity. d) Backbone-backbone radial distribution function, $g_{BB}(r)$, as a function of distance between backbone centers of mass, r, for pure polymer with side chains at η = 0.2 (solid lines) and interaction set I at T* = 0 .208 (red), interaction set II at T* = 0.208 (blue), and interaction set III at T* = 0.242 (green) and η = 0.2 ϕ = 0.2 blends (dashed lines) with interaction set I (red) at T* = 0.208 , interaction set II (blue) at T* = 0.208 and interaction set III (green) at T* = 0.23. e) Section of simulation snapshot showing only backbones of the pure polymer, η = 0.2 ϕ = 0, with side chains and interaction set I at T* = 0.208 and f) the pure polymer, η = 0.2 ϕ = 0, with side chains with interaction set II at T* = 0.208.

Comparing blends with and without side chains for interaction set II and III, we find that the LC transition temperature in the presence of side chains is lower than the corresponding polymer blends in the absence of side chains (dashed lines Figure 2.4a). This trend is opposite of that seen with interaction set I (comparing dashed with solid lines in Figure 2.3a). This is because for interaction set II and III, both for blends and pure polymers, the side chains impede

the strongly attracting backbones from aligning, decreasing the LC transition temperature from that of systems without side chains. In contrast, with interaction set I, strongly attracting side chains bring the weakly interacting backbones together, facilitating alignment, compared to systems without side chains where backbones are weakly interacting.

There is higher extent of acceptor aggregation (Figure 2.5b) with the acceptor molecules having more neighbors (Figure 2.5c) with interaction set II than with interaction sets I and III. This is because with interaction sets I and III, acceptors are strongly attracted to the side chains which disrupts acceptor aggregation. With interaction set II, acceptors interact more weakly with the side chains, making acceptor-acceptor interactions, and in turn acceptor aggregation, more dominant. Additionally, with interaction set II, acceptors have more neighbors (Figure 2.5c) but remain relatively disordered as evidenced by lower Q_6 values (Section 2.7.5). Interestingly, center of masses of the polymer backbones are spaced further apart with interaction sets II and III compared to those in interaction set I, as shown by the backbone-backbone radial distribution (Figure 2.5d). This is not driven by increased acceptor-backbone attractive interaction, as evidenced by the backbones being closer together both at $\phi = 0$ and $\phi = 0.2$. This increased backbone-backbone spacing is better explained through visual analysis of sections of the pure polymer, $\eta = 0.2$ $\phi = 0$, (shown with side chains hidden for clarity) with interaction set I (Figure 2.5e) and interaction set II (Figure 2.5f). Backbone layers are more planar (see white lines in Figure 2.5e) with backbone centers of mass lying on the same flat/curved plane because the strong side chain-side chain interactions in interaction set I align the backbones to maximize side chain-side chain contacts. The backbone layers show a zig-zag (see zig-zag white lines in Figure 2.5f) arrangement with interaction sets II and III because strong backbone-backbone attractions

cause each backbone to lie in the groove of two other backbones in order to make contacts with higher number of neighboring backbones than they would if they were aligned next to one another in a plane (as seen in interaction set I).

In summary, when pair-wise interactions involving backbones are strongly attractive (interaction set II and III) a) the role of side chains is to decrease the LC transition temperature of the blend as compared to bare backbones, and b) in the presence of side chains, the LC transition temperature shifts to higher temperatures as compared to when pair-wise interactions involving backbones are weakly attractive. Lastly, while all three interaction sets show similar overall layer-by-layer morphology, weak side chain attractions and strong backbone attractions (interaction set II) allow acceptor molecules to be more aggregated due to reduced acceptor-side chain attraction strength.

2.3.4 Role of Physical Features of Conjugated Polymers

While the discussion so far has been for blends where the conjugated polymer has a perfectly rigid backbone, resulting in liquid crystalline polymer domains, in order to understand and isolate the effect of the conjugated backbone rigidity and constrained side chains (in the form of dihedral angle and three-body angle potentials), we present effects on morphology by systematically removing backbone rigidity and the constraints on the side chain beads for blends with interaction set I (Figure 2.6). Since the layer-by-layer *morphology* of the polymers and acceptors (Figure 2.7a) was largely similar for all three interaction sets in the above section, we present results here only for interaction set I.

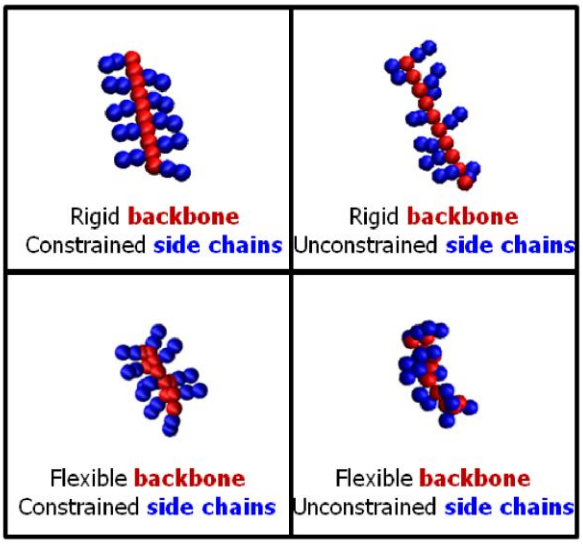

FIGURE 2.6: Schematic of physical changes made to the conjugated polymer model in this study.

First, we remove constraints on the alkyl side chains while maintaining a rigid backbone. Figure 2.7b shows snapshots at T* = 0.208 for pure polymer ($\phi = 0$) and for $\phi = 0.2$ blends with rigid backbones and unconstrained side chains. Snapshots show visually the similarity in the order within the blend and pure polymers with that seen with rigid backbone and constrained side chains (Figure 2.7a). Additionally, both in the absence and presence of acceptors, the conjugated polymers with rigid backbones and unconstrained side chains exhibit similar LC transition temperature, backbone-backbone layer spacing and acceptor order below LC transition, as that of the analogous system with side chain constraints intact (Section 2.7.2).

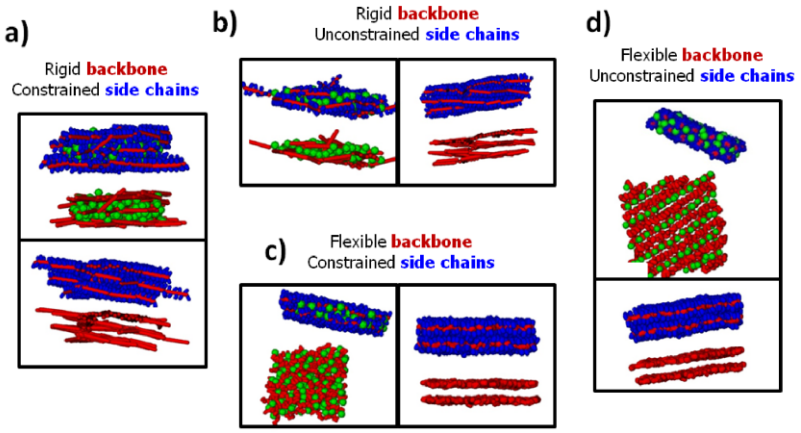

FIGURE 2.7: Simulation snapshots at T* = 0.208 of blends of acceptors and polymers with a) rigid backbone and constrained side chains for η = 0.2 ϕ = 0.2 (above) and η = 0.2 ϕ = 0 (below), b) rigid backbone and unconstrained side chains for η = 0.2 ϕ = 0.2 (left) and η = 0.2 ϕ = 0 (right), c) flexible backbone and constrained side chains η = 0.175 ϕ = 0.2 (left) and η = 0.2 ϕ = 0 (right), and d) flexible backbone and unconstrained side chains for η = 0.2 ϕ = 0.2 (above) and η = 0.2 ϕ = 0 (below) all for interaction set I. The upper image of each section shows all components in the system (backbone, side chain and acceptors), while lower section shows the same snapshot with side chains removed for clarity.

Next, we make backbones completely flexible while constraining side chains. The visual analysis (Figure 2.7c) shows that in blends of flexible polymers and acceptors, there is a higher extent of mixing between the components, as compared to blends containing rigid polymers. Also, since flexible polymer backbones show no alignment, S_2 is not meaningful. The acceptor-acceptor radial distribution function (Figure 2.8a) and histogram of acceptor neighbors (Figure 2.8b) show that by only introducing flexibility in polymer backbone, while maintaining constrained side chains, one cannot change the acceptor order from that seen for rigid backbones and constrained side chains; acceptors remain amorphous with mostly 1 or 0 neighbors and low Q_6.

When backbones are *flexible* and the side chains are *unconstrained*, the acceptors organize themselves to maximize acceptor-acceptor and acceptor-side chain interactions. Snapshots (Figure 2.7d) show the polymer domains being amorphous and the acceptor domains being

ordered. The acceptor-acceptor radial distribution shows that there are more acceptors at the closest acceptor-acceptor distance when backbones are flexible and side chains are unconstrained (Figure 2.8a) than with rigid backbones and constrained or unconstrained side chains. Furthermore, a higher Q_6 and the histogram of acceptor neighbors peaking at two neighbors (Figure 2.8b) confirm a higher order when the polymer backbone is flexible and the side chains are unconstrained. In the blends previously discussed (rigid backbone/constrained side chains, rigid backbone/unconstrained side chains, and flexible backbone/constrained side chains), the side chain beads constrained to particular angles and/or restricted to particular positions or orientations due to rigidity of the backbone deter acceptors from ordering.

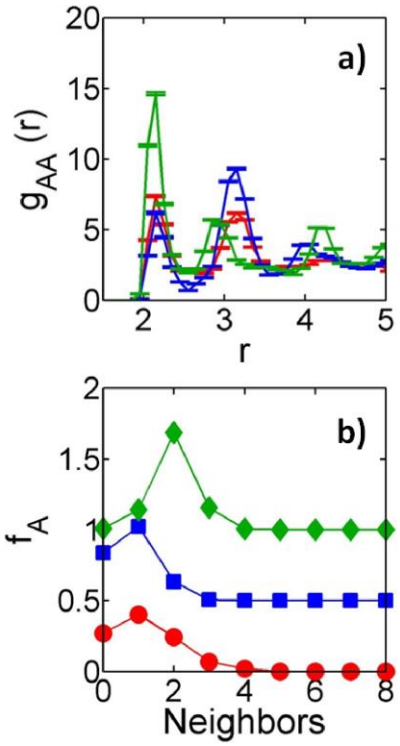

FIGURE 2.8: a) Acceptor-acceptor radial distribution function, $g_{AA}(r)$, as a function of distance between acceptor centers of mass, r, and b) histogram of acceptor neighbors (with curves offset in y-axis by 0.5 units for clarity) at T* = 0.208 for $\eta = 0.2$ $\phi = 0.2$ blends with rigid backbone and constrained side chains (red), flexible backbone and constrained side chains (blue) and flexible backbone and unconstrained side chains (green).

In summary, without constraints on the rigidity of the backbone and on the angular position of the side chains, in blends of acceptors and polymers with flexible backbone and unconstrained side chains, the acceptors exhibit higher order.

2.3.5 Role of Acceptor Molecule - Acceptor Molecule Interactions

So far the results and discussion have focused on effects of chemical and physical features of conjugated polymer at constant acceptor-acceptor interactions at dimensionless $\varepsilon_{A\text{-}A} = 2$. Since significant synthetic effort in the field of bulk heterojunction materials revolves around varying functionalization of fullerene, we shift our focus in this section to effects of varying acceptor chemistry (dimensionless $\varepsilon_{A\text{-}A} = 2$, 3 and 4) on morphology and phase transition in blends of conjugated polymers and acceptors. Varying the acceptor-acceptor attraction can mimic changing chemical functionalization on fullerenes, as well as changing effective solvent-acceptor interactions.

For blends of acceptors and conjugated polymers (rigid backbone and side chain constraints intact) with interaction set I, in the absence of side chains, as $\varepsilon_{A\text{-}A}$ increases, the LC transition temperature increases slightly for both $\eta = 0.2$ $\phi = 0.2$ and $\eta = 0.2$ $\phi = 0.3$ blends (Section 2.7.6). This is because the propensity of acceptor aggregation is increased with increasing $\varepsilon_{A\text{-}A}$. As a result, acceptor aggregation occurs at a higher temperature, the backbones penetrate the acceptor domain at a higher temperature and the LC transition temperature shifts to higher values. As $\varepsilon_{A\text{-}A}$ increases, we observe higher contact peaks in $g_{AA}(r)$, higher number of neighbors per acceptor molecule (as many as 8 neighbors at $\varepsilon_{A\text{-}A} = 4$), and larger acceptor domains that remain fairly disordered with low Q_6.

In the presence of side chains, the LC transition temperature remains unaffected by increasing $\varepsilon_{A\text{-}A}$ (Figure 2.9a), in contrast to the small shift seen in the absence of side chains. This is because with interaction set I, the strong attraction of polymer side chain beads with acceptors and strong side chain-side chain interactions cause the entire blend to aggregate regardless of $\varepsilon_{A\text{-}A}$. Thus, the acceptor-acceptor interactions do not play a role in dictating backbone alignment or LC transition temperature. The plot of the backbone-backbone radial distribution function (Figure 2.9b) also shows that $\varepsilon_{A\text{-}A}$ does not significantly affect the backbone-backbone ordering. The acceptor-acceptor radial distribution function (Figure 2.9c) and histogram of acceptor neighbors (Figure 2.9d) show that with increasing $\varepsilon_{A\text{-}A}$, acceptors have more nearest neighbors, confirming increased aggregation. These trends are more pronounced at higher volume fraction of acceptors in the blend (See results for the $\eta = 0.2$ $\phi = 0.3$ blend in Section 2.7.6). Similarly, the LC transition in blends with interaction sets II and III is minimally affected by increasing $\varepsilon_{A\text{-}A}$ (Figure 2.10a and Section 2.7.6). The histograms of acceptor neighbors for $\varepsilon_{A\text{-}A} = 2$ blends are shown in Figure 2.5c, and those for $\varepsilon_{A\text{-}A} = 4$ blends are shown in Figure 2.10b. At $\varepsilon_{A\text{-}A} = 2$, many acceptors have 0 or 1 neighbors and thus form small mixed domains. At $\varepsilon_{A\text{-}A} = 4$, acceptors have more neighbors and the number of neighbors increases going from interaction set I to II to III, indicating that larger domains are formed at $\varepsilon_{A.A} = 4$ with all interaction sets and the largest domains are formed with interaction set III. Radial distribution functions, shown in Section 2.7.6, show that for interaction set III, the number of acceptors at contact distance greatly increases at $\varepsilon_{A\text{-}A} = 4$ compared to $\varepsilon_{A\text{-}A} = 2$ and compared to interaction sets I and II, while the $g_{AB}(r)$ curve decreases in magnitude for interaction set III and $\varepsilon_{A\text{-}A} = 4$

because larger, purer acceptor domains are formed with interaction set III and $\varepsilon_{A\text{-}A} = 4$ compared to systems with other interaction sets.

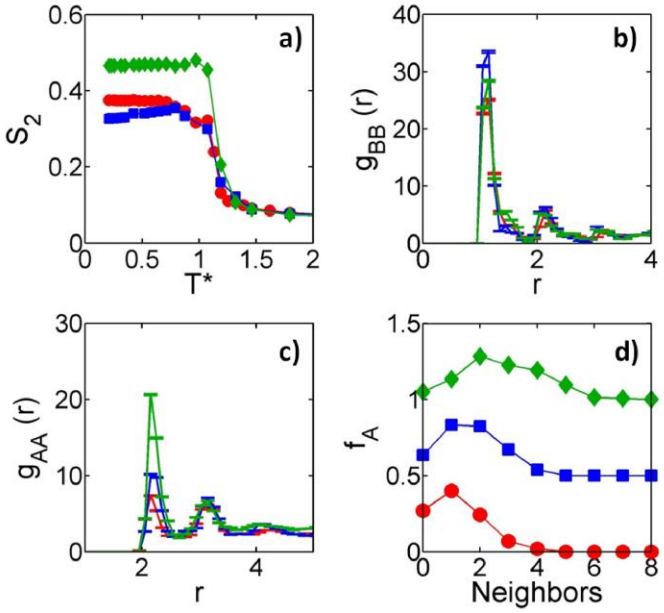

FIGURE 2.9: a) Order parameter, S_2, as a function of reduced temperature, T*, for $\eta = 0.2$ $\phi = 0.2$ blends with side chains for varying values of acceptor-acceptor interaction $\varepsilon_{A\text{-}A} = 2$ (red circles), 3 (blue squares), and 4 (green diamonds) kT. b) Backbone-backbone radial distribution function, $g_{BB}(r)$, as a function of distance between backbone centers of mass, r, c) acceptor-acceptor radial distribution function, $g_{AA}(r)$, as a function of distance between acceptor centers of mass, r, and d) histogram of acceptor neighbors (with curves offset along y-axis for clarity by 0.5 units) for $\eta = 0.2$ $\phi = 0.2$ blends at T* = 0.208 with side chains for varying values of attractive well depth of acceptor-acceptor interaction $\varepsilon_{A\text{-}A} = 2$ (red), 3 (blue), and 4 (green) kT.

Visual analysis confirms that with interaction set III and $\varepsilon_{A\text{-}A} = 4$kT, pure acceptor domains and pure conjugated polymer domains are formed (Figure 2.10c), unlike the morphology seen with interaction sets I and II where acceptor molecules mix/form layers with conjugated polymer for all $\varepsilon_{A\text{-}A}$. With interaction set III and $\varepsilon_{A\text{-}A} = 4$kT, since all like-bead pair-wise interactions (backbone-backbone, side chain-side chain, and acceptor-acceptor) are strongly attractive, there is a strong enthalpic driving force for macroscopic de-mixing. Polymers with

strongly interacting backbones and side chains align with each other and the more strongly interacting acceptors aggregate in a separate domain. Figure 2.10c shows a snapshot of this demixed blend formed for interaction set III and $\varepsilon_{A-A} = 4kT$. Figure 10d shows the mixed blend formed for interaction set I and $\varepsilon_{A-A} = 4kT$, where acceptors are in between layers of conjugated polymers. Interestingly, for interaction set III blends, with intermediate ε_{A-A} ($\varepsilon_{A-A} = 3$), interconnecting domains are formed (Figure 2.10e) where pure acceptor and polymer domains are connected through mixed regions of acceptor and polymers. This is in contrast to the macro-phase separation found with $\varepsilon_{A-A} = 4$ and the mixed blends found with $\varepsilon_{A-A} = 2$. We also performed simulations of $\eta = 0.2$ $\phi = 0.3$ and $\eta = 0.2$ $\phi = 0.4$ blends and found that those systems also showed interconnecting ($\varepsilon_{A-A} = 3$) and phase separated ($\varepsilon_{A-A} = 4$) domains at interaction set III.

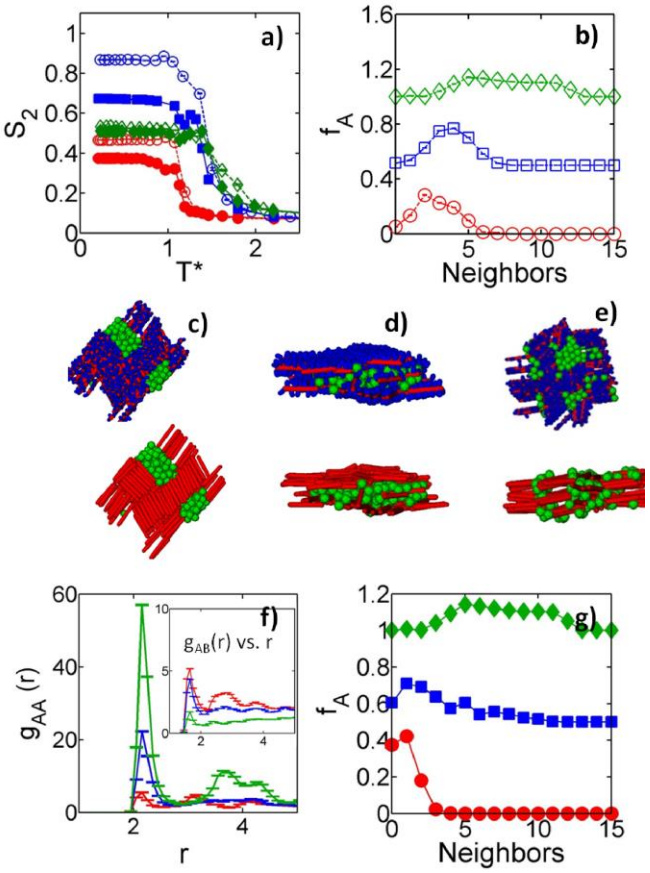

FIGURE 2.10: a) Order parameter, S_2, as a function of reduced temperature, T*, for $\eta = 0.2$ $\phi = 0.2$ blends of acceptors and conjugated polymer backbones with side chains at $\varepsilon_{A\text{-}A} = 2$ (solid symbol) and $\varepsilon_{A\text{-}A} = 4$ (open symbol) kT and interaction set I (red circles), interaction set II (blue squares), and interaction set III (green diamonds). b) Histogram of acceptor neighbors for $\eta = 0.2$ $\phi = 0.2$ blends of acceptors and conjugated polymer backbones with alkyl side chains at $\varepsilon_{A\text{-}A} = 4$ kT, with interaction set I at T* = 0.208 (red circles), interaction set II at T* = 0.23 (blue squares), and interaction set III at T* = 0.23 (green diamonds). Simulation snapshots of the $\eta = 0.2$ $\phi = 0.2$ blend with c) interaction set III and $\varepsilon_{A\text{-}A} = 4$ at T* = 0.23, d) interaction set I and $\varepsilon_{A\text{-}A} = 4$ at T* = 0.208 and e) interaction set III and $\varepsilon_{A\text{-}A} = 3$ at T*=0.242, shown with and without side chains for clarity. f) Acceptor-acceptor radial distribution function, $g_{AA}(r)$, as a function of distance between acceptor centers of mass, r, and acceptor-backbone radial distribution function, $g_{AB}(r)$, as a function of distance between acceptor and backbone bead centers of mass, r, of the $\eta = 0.2$ $\phi = 0.2$ blend with interaction set III and g) histogram of acceptor neighbors for $\eta = 0.2$ $\phi = 0.2$ blends with interaction set II with varying values of attractive well depth of acceptor-acceptor interaction $\varepsilon_{A\text{-}A} = 2$ at T* = 0.23 (red), 3 at T* = 0.24 (blue), and 4 kT at T* = 0.23 (green).

When comparing $\varepsilon_{A\text{-}A} = 3$ and $\varepsilon_{A\text{-}A} = 4$ at interaction set III, the acceptor-acceptor radial distribution (Figure 2.10f) shows less acceptor aggregation and less long range order

(demonstrated by the absence of peaks in the $g_{AA}(r)$ plot at large values of r that are seen for $\varepsilon_{A.A} = 4$). The backbone-acceptor radial distribution shows that the number of acceptor and backbone beads at closest contact decreases from $\varepsilon_{A\text{-}A} = 2$ to 3 to 4 because the blend becomes less and less mixed. The histogram of acceptor neighbors (Figure 2.10g) shows the differences in acceptor domains between the three levels of $\varepsilon_{A.A}$. At $\varepsilon_{A.A} = 2$, acceptors have 0, 1 or 2 neighbors (only 22 percent of acceptors have 3 or greater neighbors and no acceptors have 5 or greater neighbors), indicating that there is little aggregation and pure acceptor domains are not formed. At $\varepsilon_{A.A} = 3$, about 50 percent of acceptors have few neighbors (0, 1, or 2 neighbors) and 50 percent of acceptors have 3 or greater neighbors, indicating the presence of both large domains and dispersed acceptors. Furthermore, in this blend, 28.5 percent of acceptors have five or greater neighbors. At $\varepsilon_{A.A} = 4$, 99.1 percent of acceptors have 3 or greater neighbors and 85.8 percent have 5 or greater neighbors indicating that the majority of acceptors are in large, segregated domains. In contrast, with interaction set I, the $\eta = 0.2$ $\phi = 0.2$ $\varepsilon_{A.A} = 3$ blend (Figure 2.9d) has 21 percent of acceptors with three or greater neighbors and 0 acceptors with greater than 5 neighbors.

In summary, acceptor-acceptor attraction does not affect the LC transition temperature of blends with side chains, but with strongly interacting conjugated polymers (interaction set III) and $\varepsilon_{A.A} = 3$ and 4, blends with interconnecting domains and pure domains, respectively, are formed. Recent experimental work on blends of polymers and acceptor molecules for bulk heterojunction solar cells similarly underlines the importance of the relative mixing of domains in the blend[35, 36]. The conjugated polymer and acceptor molecules must have partial miscibility to create percolation pathways for electrons and holes to travel to the electrodes[35]. Completely

segregated or completely mixed blends do not form these pathways and active layer efficiency is decreased.

We also investigate the effect of acceptor size on morphological development for interaction sets I, II and III and $\varepsilon_{A.A} = 2$ (Section 2.7.7). We increase the acceptor diameter from 2 to 2.6 while keeping the number of acceptor and polymer molecules constant. We find that the acceptor size only minimally affects the LC transition temperature and acceptor molecule ordering for blends with interaction sets I, II and III. Plots of the acceptor-acceptor radial distribution function show that acceptor order is slightly higher for d = 2 than for larger acceptor diameters, indicating that increasing acceptor diameter decreases acceptor order (Section 2.7.7).

2.4 CONCLUSION

We have conducted Langevin dynamics simulations of blends of conjugated polymers and acceptor molecules to isolate the effects of various physical (side chains, flexibility) and chemical features (pair-wise interactions) of the conjugated polymer and acceptor molecule on the blend morphology and phase transition.

When the pair-wise interactions involving side chains are more attractive than those involving backbones (interaction set I), the role of side chains is to a) increase the LC transition temperature of the blend, b) facilitate conjugated polymer and acceptors to order into a layer-by-layer morphology with the acceptor molecules arranging amorphously in between conjugated polymer layers, and c) lower the diffusion of the conjugated polymer backbones in the blends. When the pair-wise interactions involving backbones are strongly attractive (interaction set II and III), a) the role of side chains is to decrease the LC transition temperature of the blend as compared to bare backbones, and b) in the presence of side chains, the LC transition temperature

shifts to higher temperatures compared to when pair-wise interactions involving backbones are weakly attractive. Lastly, while all three interaction sets show similar overall layer-by-layer morphology, weak side chain attractions and strong backbone attractions allow acceptor molecules to be more aggregated due to reduced acceptor-side chain attraction strength.

Blends of acceptors and conjugated polymers with rigid backbones and unconstrained side chains have the same LC transition temperature and molecular ordering as with rigid backbones and constrained side chains, suggesting the backbone rigidity rather than side chain constraints drives backbone alignment. Blends with flexible backbones and constrained side chains form mixed, disordered layers, while blends with flexible backbones and unconstrained side chains form a morphology with acceptors exhibiting higher order in their arrangement. Therefore, the presence of side chain constraints and the rigidity of the backbone reduce overall acceptor order.

Increasing acceptor-acceptor attraction strength increases acceptor aggregation significantly but does not affect the LC transition temperature. When pair-wise interactions involving the side chains are stronger than those involving the backbone or pair-wise interactions involving the backbone are stronger than those involving the side chains, alternating layers of conjugated polymer and acceptors are formed and acceptor aggregation increases with acceptor–acceptor attraction. When all pair-wise attractions are strong, pure domains of conjugated polymer and acceptors are formed at high acceptor-acceptor attraction, while interconnected domains of conjugated polymer and acceptors are formed at intermediate acceptor-acceptor attraction.

Since morphology plays a significant role in determining the device efficiency of organic solar cells, a large number of experimental studies have been looking for synthetic guidelines to control a) the composition of conjugated polymer and acceptor domains at equilibrium, such as mixed amorphous domains versus pure crystalline domains, and b) the crystallinity of conjugated polymers, characterized in this work through backbone alignment. By isolating the effect of each parameter on the structure and thermodynamics of these conjugated polymer-acceptor blends, we have provided design principles for synthetic chemists on which physical and chemical features to incorporate in the conjugated polymer and acceptor to achieve a target morphology.

2.5 ACKNOWLEDGEMENTS

This work was supported by Department of Energy Early Career Award under grant number DE-SC0003912. This work was conducted on supercomputing resources of the (NERSC) National Energy Research Scientific Computing Center supported by the Office of Science of the U.S. Department of Energy under Contract No. DE-AC02-05CH11231, and on Janus supercomputer supported by the National Science Foundation (award number CNS-0821794) and the University of Colorado Boulder. H. S. Marsh acknowledges technical help given by D. Zhang during the early stages of this work.

2.6 REFERENCES

1. Slota, J. E.; He, X. M.; Huck, W. T. S. *Nano Today* **2010,** 5, (3), 231-242.
2. Ruderer, M. A.; Muller-Buschbaum, P. *Soft Matter* **2011,** 7, (12), 5482-5493.
3. Brady, M. A.; Su, G. M.; Chabinyc, M. L. *Soft Matter* **2011,** 7, (23), 11065-11077.
4. Topham, P. D.; Parnell, A. J.; Hiorns, R. C. *Journal of Polymer Science Part B-Polymer Physics* **2011,** 49, (16), 1131-1156.

5. Deibel, C.; Dyakonov, V. *Reports on Progress in Physics* **2010,** 73, (9), 39.

6. Zhou, H. X.; Yang, L. Q.; You, W. *Macromolecules* **2012,** 45, (2), 607-632.

7. Heffner, G. W.; Pearson, D. S. *Macromolecules* **1991,** 24, (23), 6295-6299.

8. Wignall, G. D.; Ballard, D. G. H.; Schelten, J. *European Polymer Journal* **1974,** 10, (9), 861-865.

9. Yin, W.; Dadmun, M. *Acs Nano* **2011,** 5, (6), 4756-4768.

10. Kozub, D. R.; Vakhshouri, K.; Orme, L. M.; Wang, C.; Hexemer, A.; Gomez, E. D. *Macromolecules* **2011,** 44, (14), 5722-5726.

11. Pfannmoller, M.; Flugge, H.; Benner, G.; Wacker, I.; Sommer, C.; Hanselmann, M.; Schmale, S.; Schmidt, H.; Hamprecht, F. A.; Rabe, T.; Kowalsky, W.; Schroder, R. R. *Nano Letters* **2011,** 11, (8), 3099-3107.

12. Schmidt-Hansberg, B.; Sanyal, M.; Klein, M. F. G.; Pfaff, M.; Schnabel, N.; Jaiser, S.; Vorobiev, A.; Muller, E.; Colsmann, A.; Scharfer, P.; Gerthsen, D.; Lemmer, U.; Barrena, E.; Schabel, W. *Acs Nano* **2011,** 5, (11), 8579-8590.

13. Massip, S.; Oberhumer, P. M.; Tu, G.; Albert-Seifried, S.; Huck, W. T. S.; Friend, R. H.; Greenham, N. C. *Journal of Physical Chemistry C* **2011,** 115, (50), 25046-25055.

14. Yang, L. Q.; Zhou, H. X.; You, W. *Journal of Physical Chemistry C* **2010,** 114, (39), 16793-16800.

15. Carbonnier, B.; Egbe, D. A. M.; Birckner, E.; Grummt, U. W.; Pakula, T. *Macromolecules* **2005,** 38, (18), 7546-7554.

16. Gadisa, A.; Oosterbaan, W. D.; Vandewal, K.; Bolsee, J. C.; Bertho, S.; D'Haen, J.; Lutsen, L.; Vanderzande, D.; Manca, J. V. *Advanced Functional Materials* **2009,** 19, (20), 3300-3306.

17. Sista, P.; Xue, B. F.; Wilson, M.; Holmes, N.; Kularatne, R. S.; Nguyen, H.; Dastoor, P. C.; Belcher, W.; Poole, K.; Janesko, B. G.; Biewer, M. C.; Stefan, M. C. *Macromolecules* **2012,** 45, (2), 772-780.

18. Cates, N. C.; Gysel, R.; Dahl, J. E. P.; Sellinger, A.; McGehee, M. D. *Chemistry of Materials* **2010,** 22, (11), 3543-3548.

19. Miller, N. C.; Gysel, R.; Miller, C. E.; Verploegen, E.; Beiley, Z.; Heeney, M.; McCulloch, I.; Bao, Z. N.; Toney, M. F.; McGehee, M. D. *Journal of Polymer Science Part B-Polymer Physics* **2011,** 49, (7), 499-503.

20. Huang, D. M.; Moule, A. J.; Faller, R. *Fluid Phase Equilibria* **2011,** 302, (1-2), 21-25.

21. Huang, D. M.; Faller, R.; Do, K.; Moule, A. J. *Journal of Chemical Theory and Computation* **2010,** 6, (2), 526-537.

22. Lee, C. K.; Pao, C. W.; Chu, C. W. *Energy & Environmental Science* **2011,** 4, (10), 4124-4132.

23. Kamberaj, H.; Low, R. J.; Neal, M. P. *Journal of Chemical Physics* **2005,** 122, (22).

24. Leach, A. E., *Molecular Modelling: Principles and Applications* 1ed.; Longman: Essex, 1996.

25. Scharsich, C.; Lohwasser, R.; Sommer, M.; Asawapirom, U.; Scherf, U.; Thelakkat, M.; Neher, D.; Kohler, A. *Journal of Polymer Science Part B: Polymer Physics* **2011,** 50, (6), 442-453.

26. Dag, S.; Wang, L. W. *Journal of Physical Chemistry B* **2010,** 114, (18), 5997-6000.

27. Prosa, T. J.; Winokur, M. J.; Moulton, J.; Smith, P.; Heeger, A. J. *Macromolecules* **1992,** 25, (17), 4364-4372.

28. Plimpton, S. *Journal of Computational Physics* **1995,** 117, (1), 1-19.

29. Zhang, Z.; Guo, H. *The Journal of chemical physics* **2010,** 133, (14), 144911-144911.

30. Urakami, N.; Imai, M. *The Journal of Chemical Physics* **2003,** 119, (4), 2463-2463.

31. Steinhardt, P. J.; Nelson, D. R.; Ronchetti, M. *Physical Review B* **1983,** 28, (2), 784-805.

32. Yiannourakou, M.; Economou, I. G.; Bitsanis, I. A. *Journal of Chemical Physics* **2010,** 133, (22).

33. Adams, M.; Dogic, Z.; Keller, S. L.; Fraden, S. *Nature* **1998,** 393, (6683), 349-352.

34. Malgas, G. F.; Motaung, D. E.; Arendse, C. J. *Journal of Materials Science* **2012,** 47, (10), 4282-4289.

35. Vakhshouri, K.; Kozub, D. R.; Wang, C. C.; Salleo, A.; Gomez, E. D. *Physical Review Letters* **2012,** 108, (2), 5.

36. Chu, T.; Lu, J.; Beaupre, S.; Zhang, Y.; Pouliot, J.; Jiayun, Z.; Najari, A.; Leclerc, M.; Tao, Y. *Adv*. *Funct*. *Mater*. **2012,** 22, (11), 2345-2351.

2.7 SUPPORTING INFORMATION

2.7.1 Additional Details of the Model

Bead masses and angle potentials

TABLE 2.1: Approximate bead masses determined from the molecular weight of the atoms that make up each bead for the P3HT and acceptor molecule system, normalized to the backbone bead mass (B) to obtain dimensionless values. S1 and S2 are the inner and outer side chain beads respectively and A is the acceptor bead (Figure 2.1).

B	S1	S2	A
1	0.5	0.5	11

TABLE 2.2: Dimensionless parameters used in bonded potentials of the form

$$U_{bond}=K_2(r-r_o)^2+ K_3(r-r_o)^3+ K_4(r-r_o)^4 \quad (1)$$

between beads i and j for coarse-grained simulations of conjugated polymer and acceptor molecules where K_2, K_3, and K_4 are constants and r_o is the equilibrium bond distance. Values are normalized to the values of ε and σ for B-S1 interactions for dimensionless values.

i	j	r_o	K_2	K_3	K_4
B	B	0.826	2659.97	17801.77	46303.3
B	S1	0.788	1629.77	26489.91	124401.9
S1	S2	0.722	1081.31	-1170.1	0

TABLE 2.3: Dimensionless parameters used in the dihedral angle potential between beads S1-B-B-S1 of adjacent molecules of the form

$$U_{Dihedral} = \sum_{n=1-5} A_n \cos^{n-1}(\phi) \quad (2)$$

for coarse-grained simulations of conjugated polymer and acceptor molecules where A_1-A_5 are constants. Values are normalized to the values of ε and σ for B-S1 interactions.

A_1	A_2	A_3	A_4	A_5
0.994	0.696	0.942	0.0784	-1.229

TABLE 2.4: Dimensionless parameters used in three-body angle potentials of the form

$$U_{Angle}=K_2(\theta - \theta_o)^2+ K_3(\theta- \theta_o)^3+ K_4(\theta - \theta_o)^4 \quad (3)$$

between beads i, j, and k for coarse-grained simulations of conjugated polymer and acceptor molecules where K_2, K_3, and K_4 are constants and θ_o is the equilibrium angle. Values are normalized to the values of ε and σ for B-S1 interactions.

i	j	k	θ_o	K_2	K_3	K_4
B	S1	S2	180	0.178	-2.80	-0.63
B	B	S1	122.32	13.05	4.43	4.24
S1	B	B	82.97	29.43	-7.54	19.55

Lennard Jones non-bonded interaction potentials for interaction sets I, II and III

TABLE 2.5: Lennard Jones attraction parameters, σ_{ij} and ε_{ij}, for non-bonded interactions between beads i and j in interaction sets I, II and III. Values are normalized to the values of ε and σ for B-S1 interactions. B is the backbone bead, S1 and S2 are side chain beads and A is the acceptor molecule bead. Interaction set I uses non-bonded interaction potentials adapted from work by Huang et al.[20, 21]. For interaction set II, we give backbone beads the interaction potentials of the most strongly interacting side chain bead S1 and the side chain beads the interaction strengths of backbone beads. For interaction set III, we give all beads the strong interaction strengths of the S1 beads.

i	**J**	σ_{ij}	ε_{ij} **(I)**	ε_{ij} **(II)**	ε_{ij} **(III)**
B	B	*1.135*	0.079	0.91	0.91
B	S1	*1.000*	1.000	1.000	0.91
B	S2	*1.115*	0.093	1.000	0.91
S1	S1	*1.058*	0.91	0.079	0.91
S1	S2	*1.058*	0.366	0.079	0.91
S2	S2	*1.115*	0.331	0.079	0.91
B	A	*1.500*	1.028	1.65	1.65
S1	A	*1.462*	1.65	1.028	1.65
S2	A	*1.519*	1.271	1.028	1.65
A	A	*1.962*	2-4	2-4	2-4

Interaction set I uses non-bonded interaction potentials adapted from work by Huang et al.[1,2]. The procedure of adaptation from the work by Huang et al.[1,2] was as follows. The values for the non-bonded interaction potentials calculated by Huang et al.[1,2] were plotted as a function of r. The value where the potential, U(r), is equal to ε is R_m. Sigma was calculated from the following formula: $R_m=2^{1/6}\sigma$. $R_m = 2^{1/6} \cdot \sigma$

And, for the bonded and angle potentials, the potentials of Huang et al.[1,2] were fit with functions of the same form consisting 3 terms (5 terms in the case of the dihedral angle potential). Function coefficients and values for ε and σ were then normalized using the ε and σ values for B-S1 interactions.

In interaction set II, we assigned values so that the B-B interaction potentials are (equal to S1-S1 of interaction set I) and more strongly attractive than S1-S1, S1-S2 and S2-S2 (all equal to B-B of interaction set I), and same order of magnitude as B-S1 and B-S2.

In interaction set III, we assigned values so that the all pair-wise attraction strengths in the polymer are the same magnitude as S1-S1 of interaction set I.

Reproduction of P3HT crystallographic data for polymer layer spacing

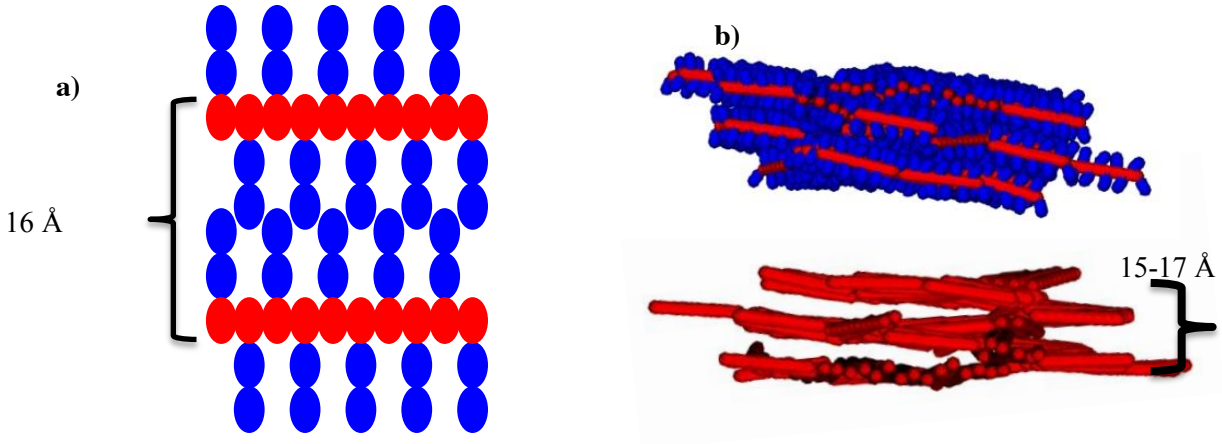

FIGURE 2.11: a) Schematic of P3HT layer spacing and b) single snapshot from coarse grained simulation of the pure polymer, $\eta = 0.2$ $\phi = 0$ at $T^* = 0.208$, showing similar layer spacing. Our model faithfully reproduces experimentally and computationally determined conjugated polymer layer spacing of about 16Å[26, 27].

2.7.2 Additional Analysis of $\eta = 0.2$ $\phi = 0.2$ Blend

Domain analysis (without side chains) of $\eta = 0.2$ $\phi = 0.2$ blend

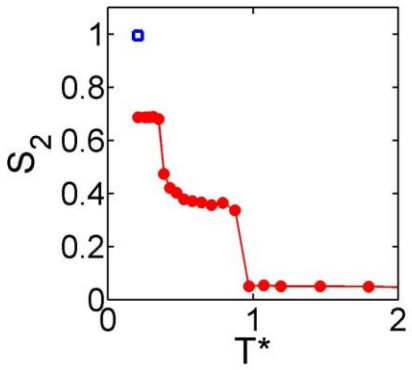

FIGURE 2.12: Order parameter, S_2, as a function of reduced temperature, T*, for the $\eta = 0.2$ $\phi = 0.2$ blend without side chains (red circles), and the S_2 value for the blend calculated as the average S_2 value for domains consisting of ≥ 10 backbones at T* = 0.208 (blue open square).

The blend has three domains of ≥10 backbones and 99.3% of the backbones are in a domain. Backbones are well aligned with each other within each domain but S_2 does not reach one in this blend because the domains themselves are not aligned with each other. Thus, we focus on LC transition temperature rather than the exact value of S_2.

Method for evaluating averages

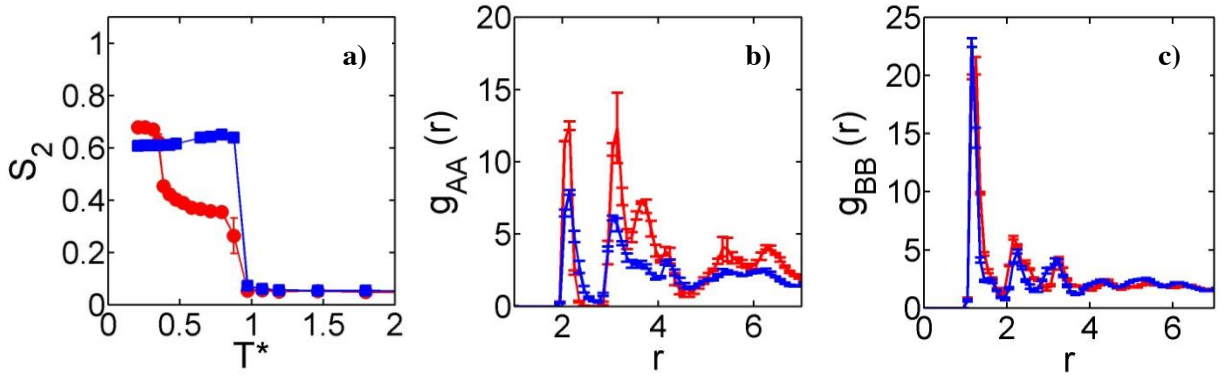

FIGURE 2.13: a) Average order parameter, S_2, as a function of reduced temperature, T*, b) average acceptor-acceptor radial distribution function as a function of distance between acceptor centers of mass, r, and c) average backbone-backbone radial distribution function as a function of distance between backbone centers of mass, r, at T* = 0.208 averaged over three trials with error bars calculated from the three trials for blends without alkyl side chains for the $\eta = 0.2$ $\phi = 0.2$ (red) and $\eta = 0.2$ $\phi = 0.4$ (blue) blends. Error bars are no larger than the size of the data symbols for most points.

Histogram of acceptor neighbors for the $\eta = 0.2$ $\phi = 0.2$ blend without side chains at varying T*

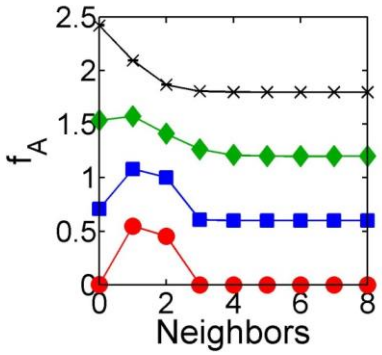

FIGURE 2.14: Histogram of acceptor neighbors for the η = 0.2 ϕ = 0.2 blend without side chains, with curves offset for clarity along y-axis by 0.6 units, at T* = 0.208 (red circles), T* = 0.922 (blue squares), T* = 0.971 (green diamonds), and T* = 1.463 (black X).

At high temperatures (T* = 1.463), most acceptors have no neighbors, indicating that the blend is well mixed. The number of neighbors per acceptor increases as temperature is lowered (T* = 0.971) indicating that acceptors aggregate. At intermediate temperatures (T* = 0.922) acceptors arrange in columns as backbones penetrate the acceptor domain and align as indicated by the peak in the neighbor plot at 1 and 2 neighbors. At low T* (T* = 0.208), there is little change in the neighbor plot because acceptors maintain the same order found at intermediate T*.

Domain analysis for η = 0.2 ϕ = 0.2 blends with side chains

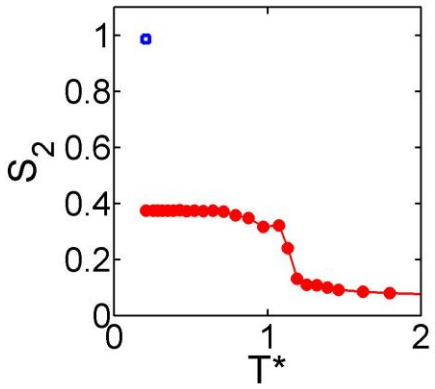

FIGURE 2.15: Order parameter, S_2, as a function of reduced temperature, T*, for the η = 0.2 ϕ = 0.2 blend with side chains (red circles), and the S_2 value for the blend calculated as the average S_2 value for domains consisting of ≥ 10 backbones at T* = 0.208 (blue open square).

The blend has four domains of ≥ 10 backbones with 46% of backbones in a domain. Backbones are well aligned with each other in each domain because average domain S_2 value is near 1. S_2 is reduced both due to backbones in domains < 10 backbones and because the domains do not align with each other. Because of the multiple factors that cause S_2 to decrease, we focus only on the LC transition temperature and not on the exact value of S_2.

Acceptor-acceptor radial distribution function and histogram of acceptor neighbors for η = 0.2 ϕ = 0.2 blends with and without side chains

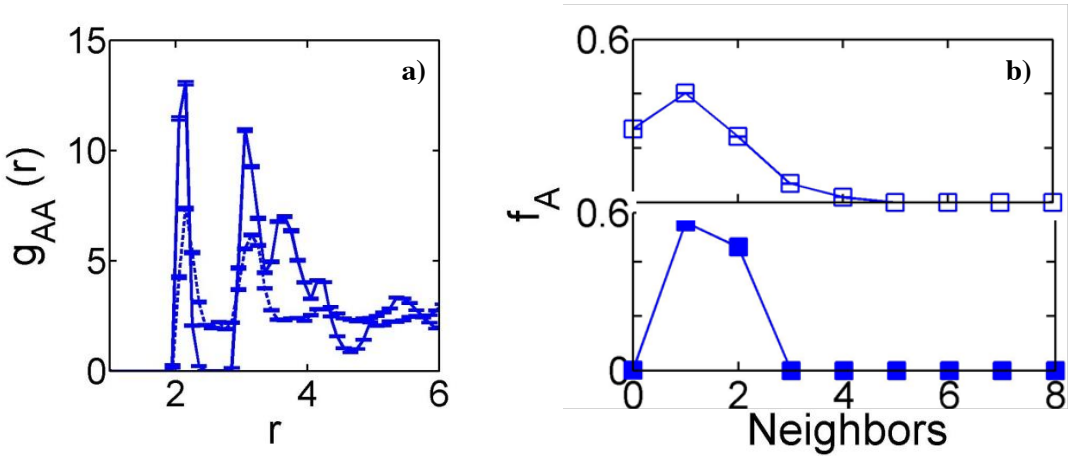

FIGURE 2.16: a) Acceptor-acceptor radial distribution function as a function of distance between acceptor centers of mass, r, and b) histogram of acceptor neighbors for the η = 0.2 ϕ = 0.2 blends with (blue square open symbol) and without (blue square solid symbol) alkyl side chains at T* = 0.208.

The blend without side chains has a larger peak in the acceptor-acceptor radial distribution function at the lowest value of r than does the blend with side chains and shows periodic acceptor spacing. The acceptor molecules in blends without side chains have 1 or 2 neighbors which is indicative of columnar ordering. However, with side chains, most acceptors have 0 or 1 neighbor, while less have 2 or 3 neighbors, indicating disorder. These trends indicate that blends without side chains have a higher degree of acceptor order than those with side chains.

Order parameter, S_2, radial distribution functions and histogram of acceptor neighbors for $\eta = 0.2$ $\phi = 0.2$ blends with a rigid backbone with both constrained and unconstrained side chains

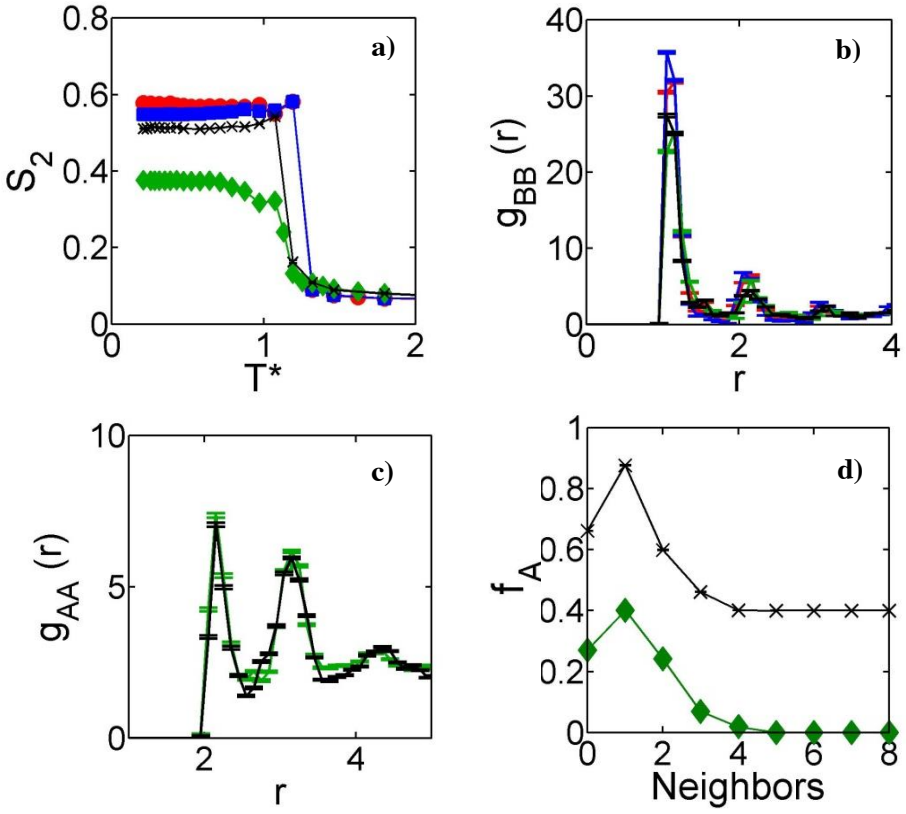

FIGURE 2.17: a) Order parameter, S_2, as a function of reduced temperature, T*, b) backbone-backbone radial distribution function as a function of distance between backbone centers of mass, r, at T* = 0.208, and c) acceptor-acceptor radial distribution function as a function of distance between acceptor centers of mass, r, at T* = 0.208, and d) histogram of acceptor neighbors at T *= 0.208 with curves offset for clarity by 0.4 units for pure polymer, $\eta = 0.2$ $\phi = 0$, with side chains and interaction set I with rigid backbone and constrained side chains (red circles) and with rigid backbone and unconstrained side chains (blue squares). Curves for $\eta = 0.2$ $\phi = 0.2$ blends with side chains and interaction set I are also shown with rigid backbone and constrained side chains (green diamonds) and with rigid backbone and unconstrained side chains (black X).

The LC transition temperatures remain the same for both the pure polymer, $\eta = 0.2$ $\phi = 0$, and the $\eta = 0.2$ $\phi = 0.2$ blend with a rigid backbone and unconstrained side chains compared to the full model. Thus, polymer molecules form ordered domains whether or not side chains are

constrained. Additionally, Figures 2.9b and 2.9c show that backbones and acceptors maintain similar ordering below the LC transition temperature, respectively. The Q_6 value is low and the histogram of acceptor neighbors shows that acceptors most likely have one or zero neighbors. Thus, acceptors in these blends are fairly disordered

2.7.3 Diffusion Coefficient of Backbones and Acceptors for η = 0.2 Blends

Backbone and acceptor molecule diffusion coefficients for η = 0.2 blends without side chains

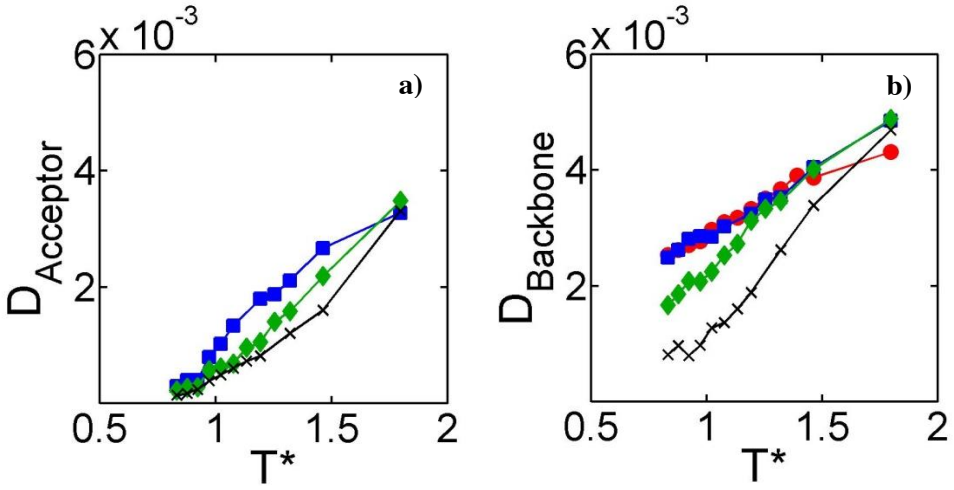

FIGURE 2.18: Diffusion coefficient of a) acceptors and b) conjugated polymer backbones without side chains as a function of reduced temperature, T*, for total packing fraction of η = 0.2 and at varying volume fraction of acceptors: ϕ = 0 (red circles), 0.2 (blue squares), 0.4 (green diamonds) and 0.6 (black X).

Acceptor diffusion is lower than backbone diffusion because acceptor molecules are more massive. As ϕ increases, acceptor diffusion decreases because acceptors form larger and thus more massive aggregates which diffuse more slowly. In case of backbones, below the high temperature LC transition T*, as the acceptor volume fraction increases backbone diffusion decreases. At high ϕ, most backbones are within the acceptor aggregate and thus have lower

diffusion compared to the unaligned and mobile backbones present at low ϕ at the same temperatures.

Backbone and acceptor molecule diffusion coefficients for η = 0.2 blends with side chains

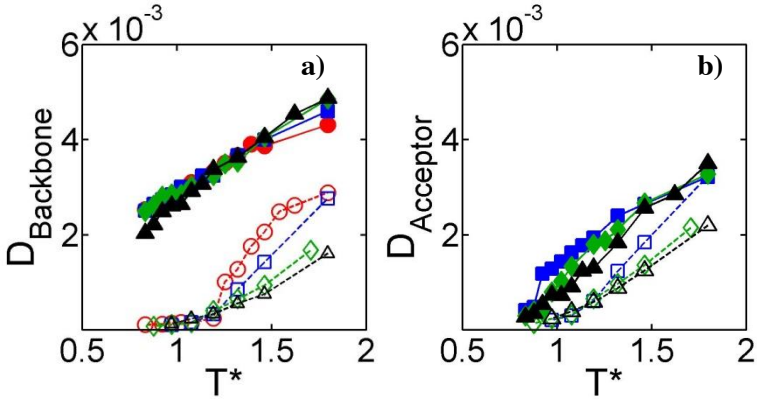

FIGURE 2.19: Diffusion coefficient as a function of reduced temperature, T*, for a) conjugated polymer backbones and b) acceptors for η = 0.2 blends of conjugated polymer backbones with (open symbol) and without (solid symbol) alkyl side chains with acceptor volume fraction ϕ = 0 (red circles), ϕ = 0.1 (blue squares), ϕ = 0.2 (green diamonds), and ϕ = 0.3 (black triangles).

Diffusion of both backbones and acceptors is lower for blends with alkyl side chains compared to blends without side chains due to increased blend aggregation. In blends with side chains, backbone diffusion is decreased with the addition of acceptor molecules because acceptor molecules increase blend aggregation due to strong acceptor-side chain and acceptor-acceptor interactions.

2.7.4 Analysis of η = 0.1 Blends

Order parameter, S_2, for η = 0.1 blends without side chains

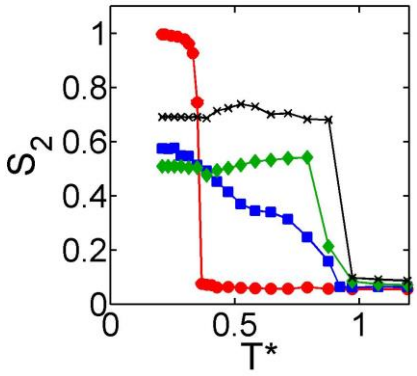

FIGURE 2.20: Order parameter, S_2, as a function of reduced temperature, T*, for η = 0.1 blends of conjugated polymer backbones without side chains at varying volume fraction of acceptors ϕ = 0 (red circles), 0.2 (blue squares), 0.4 (green diamonds), and 0.6 (black X). The η = 0.1 blends show the same trends as do the η = 0.2 blends: the LC transition T* increases with the addition of acceptors, ϕ does not significantly affect the LC transition T*, and there are two LC transitions for low ϕ blends (eg. ϕ = 0.2, blue squares).

Order parameter, S_2, and radial distribution functions for η = 0.1 blends with and without side chains

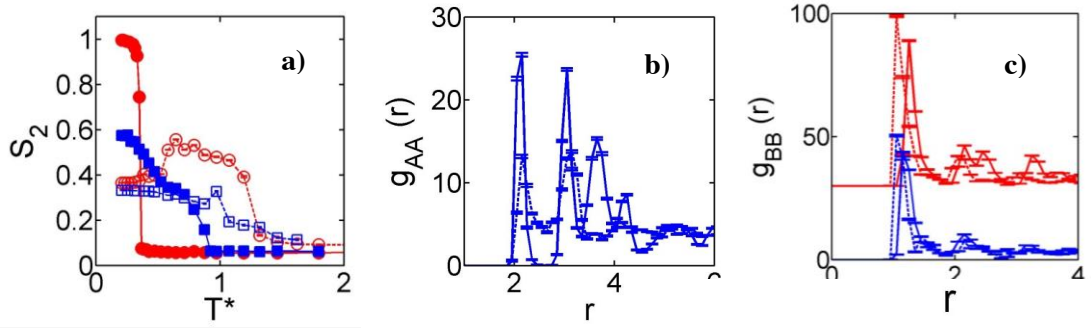

FIGURE 2.21: a) Order parameter, S_2, as a function of reduced temperature, T*, for η = 0.1 blends at acceptor volume fraction ϕ = 0 (red circles) and ϕ = 0.2 (blue squares) for blends with (open symbol) and without (solid symbol) alkyl side chains. b) Acceptor-acceptor radial distribution function as a function of distance between acceptor centers of mass, r, and c) backbone-backbone radial distribution function as a function of distance between backbone centers of mass, r, for the η = 0.1 blend at acceptor volume fractions ϕ = 0 (red) and ϕ = 0.2 (blue) for blends with (dashed lines) and without (solid lines) alkyl side chains T* = 0.208. In the $g_{BB}(r)$ plot, curves for the ϕ = 0 blends are shifted up by 30 units for clarity.

The η = 0.1 blends show the same trends as do the η = 0.2 blends: the LC transition occurs at higher temperatures for blends with side chains than for blends without side chains, adding acceptor molecules slightly decreases the LC transition T* for blends with side chains, the $g_{AA}(r)$ plot indicates that acceptors are less ordered in blends with side chains compared to blends without side chains, and the strong attractions of side chains with side chains on other conjugated polymer molecules draw backbones closer together and thus $g_{BB}(r)$ exhibits a peak at a lower value of r with side chains compared to without side chains.

Comparison of backbone and acceptor diffusion coefficients for η = 0.1 blends with and without alkyl side chains

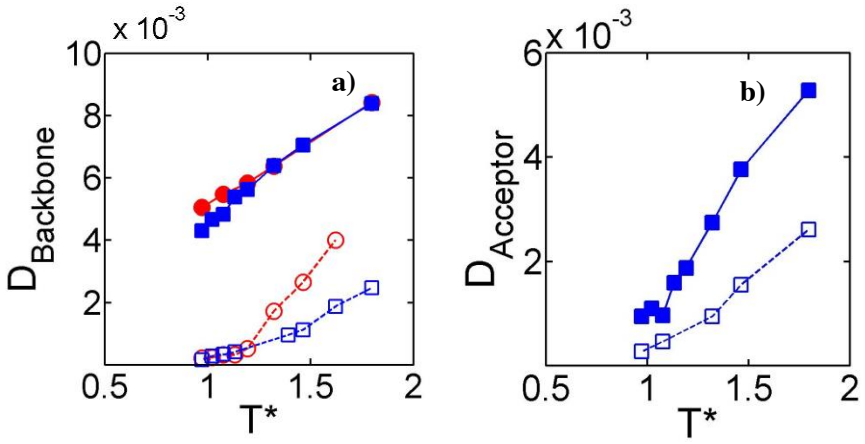

FIGURE 2.22: Diffusion coefficient as a function of temperature, T*, for a) polymer backbones and b) acceptors for η = 0.1 blends with ϕ = 0 (red circles) and ϕ = 0.2 (blue squares) with (open symbol) and without (solid symbol) alkyl side chains. The η = 0.1 blends show the same trends as do the η = 0.2 blends.

Both backbone and acceptor diffusion are reduced with the introduction of alkyl side chains because of increased blend aggregation. Adding acceptors to pure conjugated polymers with side chains decreases backbone diffusion because strong acceptor-side chain and acceptor-acceptor interactions further increase blend aggregation.

2.7.5 Table of Q_6 Values for Conjugated Polymer-Acceptor Molecule Blends

TABLE 2.6: Overall bond order parameter, Q_6, for conjugated polymer and acceptor blends a) with and b) without alkyl side chains for interaction sets I-III, $\varepsilon_{A\text{-}A}$ = 2-4 and acceptor diameter d = 2-2.6.

a) Without Side chains

η	ϕ	$\varepsilon_{A\text{-}A}$	Q_6
0.2	0.1	2	0.987
0.2	0.2	2	0.988
0.2	0.3	2	0.986
0.2	0.4	2	0.811
0.2	0.6	2	0.657
0.2	0.2	4	0.494
0.2	0.3	4	0.146

Interaction Set II

η	ϕ	$\varepsilon_{A\text{-}A}$	Q_6
0.2	0.1	2	0.463
0.2	0.2	2	0.611
0.2	0.2	4	0.602

b) With side chains

η	ϕ	$\varepsilon_{A\text{-}A}$	Q_6
0.2	0.2	2	0.130
0.2	0.3	2	0.099
0.2	0.2	4	0.141
0.2	0.3	4	0.078

Interaction Set II

η	ϕ	$\varepsilon_{A\text{-}A}$	Q_6
0.2	0.1	2	0.349
0.2	0.2	2	0.109
0.2	0.2	4	0.137

Interaction Set III

η	ϕ	$\varepsilon_{A\text{-}A}$	Q_6
0.2	0.2	2	0.178
0.2	0.2	4	0.073

Fully Flexible

η	ϕ	$\varepsilon_{A\text{-}A}$	Q_6
0.2	0.2	2	0.736

Rigid backbone, unconstrained SC

η	ϕ	$\varepsilon_{A\text{-}A}$	Q_6
0.2	0.2	2	0.211

Flexible backbone, constrained SC

η	ϕ	$\varepsilon_{A\text{-}A}$	Q_6
0.2	0.2	2	0.202

Acceptor size

η	ϕ	$\varepsilon_{A\text{-}A}$	d	Q_6
0.2	0.2	2	2.2	0.134
0.2	0.2	2	2.4	0.119
0.2	0.2	2	2.6	0.122

2.7.6 Varying Acceptor-Acceptor Interactions

Orientational order parameter, S_2, acceptor-acceptor radial distribution function and histogram of acceptor neighbors for $\eta = 0.2$ $\phi = 0.2$ blends without side chains for $\varepsilon_{A\text{-}A} = 2\text{-}4$

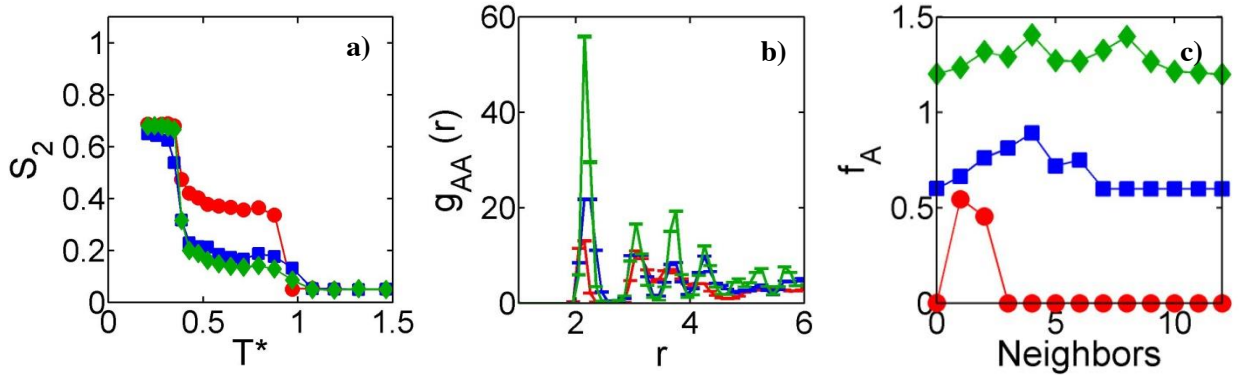

FIGURE 2.23: a) Order parameter, S_2, as a function of reduced temperature, T*, b) acceptor-acceptor radial distribution function as a function of distance between acceptor centers of mass, r, at T* = 0.208, and c) histogram of acceptor neighbors at T* = 0.208 with curves offset for clarity by 0.6 units for $\eta = 0.2$ $\phi = 0.2$ blends of conjugated polymer backbones without side chains with varying values of attractive well depth of acceptor-acceptor interaction $\varepsilon_{A\text{-}A} = 2$ (red circles), 3 (blue squares), and 4 (green diamonds) kT.

Figure 2.23a shows that increasing $\varepsilon_{A\text{-}A}$ slightly increases the LC transition temperature. In Figure 2.213b, the acceptor-acceptor radial distribution shows that acceptor aggregation increases with $\varepsilon_{A\text{-}A}$ and acceptors have more neighbors as shown in Figure 2.23c.

Orientational order parameter, S_2, acceptor-acceptor radial distribution function and histogram of acceptor neighbors for $\eta = 0.2$ $\phi = 0.3$ blends without side chains for $\varepsilon_{A\text{-}A} = 2$-4

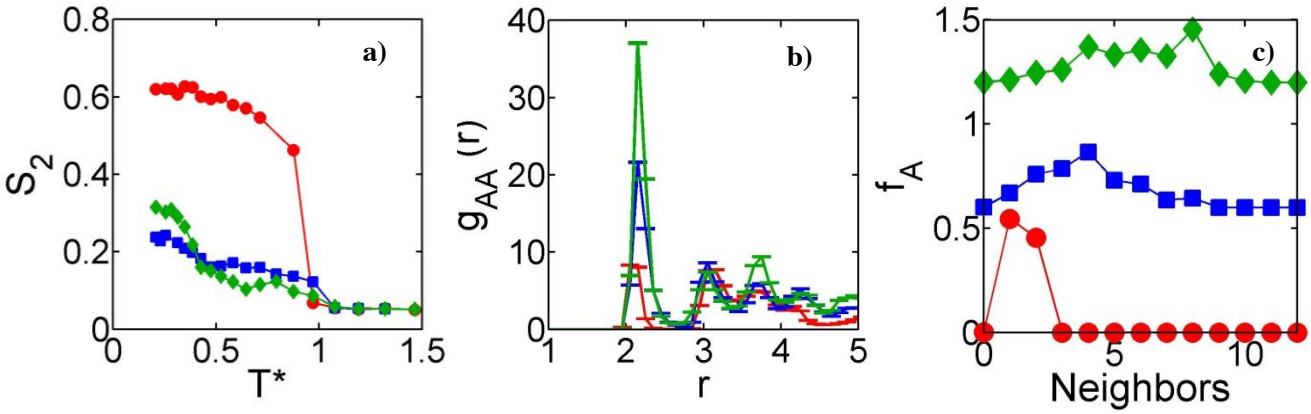

FIGURE 2.24: a) Order parameter, S_2, as a function of reduced temperature, T*, for $\eta = 0.2$ $\phi = 0.3$ blends without side chains for varying values of attractive well depth of acceptor-acceptor interaction $\varepsilon_{A\text{-}A} = 2$ (red circles), 3 (blue squares), and 4 (green diamonds) kT. b) Acceptor radial distribution function as a function of distance between acceptor centers of mass, r, at T* = 0.208 and c) histogram of acceptor neighbors with curves offset by 0.4 units for clarity at T* = 0.208 for $\eta = 0.2$ $\phi = 0.3$ blends without side chains for varying values of attractive well depth of acceptor-acceptor interaction $\varepsilon_{A\text{-}A} = 2$ (red circles), 3 (blue squares), and 4 (green diamonds) kT. Figures 2.24a-c show similar trends to the $\eta = 0.2$ $\phi = 0.2$ blends (Figures 2.23a-c).

Like for the $\eta = 0.2$ $\phi = 0.2$ blends, the LC transition occurs at a slightly higher temperature with increased $\varepsilon_{A\text{-}A}$ because acceptor aggregation and thus backbone alignment occurs at higher temperatures with increasing $\varepsilon_{A\text{-}A}$. There is only one LC transition for $\eta = 0.2$ $\phi = 0.3$ blends because the acceptor domain is large enough for the majority of backbones to enter the domain and align. As $\varepsilon_{A\text{-}A}$ increases, acceptors are more aggregated and have more neighbors as shown by Figures 2.24b and 2.24c.

Orientational order parameter, S_2, radial distribution functions and histogram of acceptor neighbors for $\eta = 0.2$ $\phi = 0.3$ blends with side chains for $\varepsilon_{A\text{-}A} = 2$-4

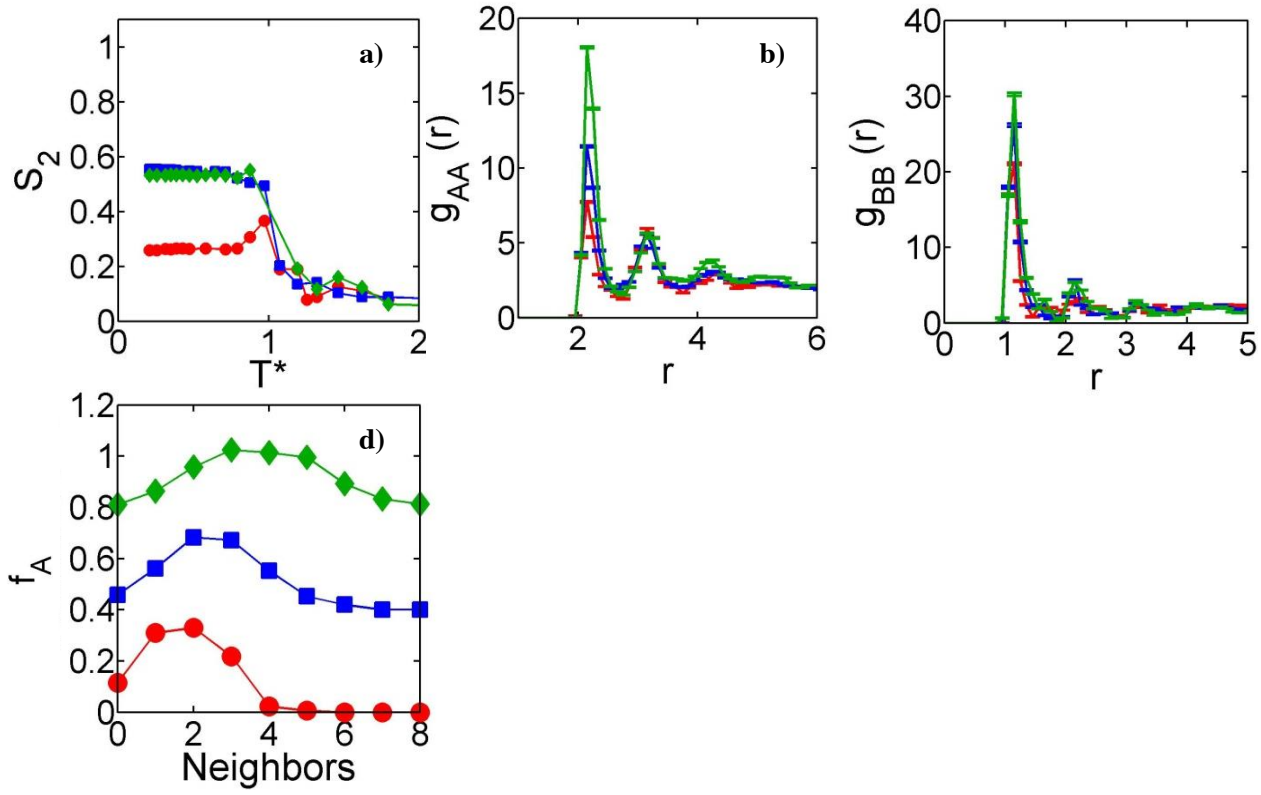

FIGURE 2.25: a) Order parameter, S_2, as a function of reduced temperature, T*, for $\eta = 0.2$ $\phi = 0.3$ blends with side chains for varying values of attractive well depth of acceptor-acceptor interaction $\varepsilon_{A\text{-}A} = 2$ (red circles), 3 (blue squares), and 4 (green diamonds) kT. b) Acceptor-acceptor radial distribution function as a function of distance between acceptor centers of mass, r, and c) backbone-backbone radial distribution function as a function of distance between backbone centers of mass, r, at T* = 0.208 for $\eta = 0.2$ $\phi = 0.3$ blends with side chains for varying values of attractive well depth of acceptor-acceptor interaction $\varepsilon_{A\text{-}A} = 2$ (red), 3 (blue), and 4 (green) kT. d) Histogram of acceptor neighbors with curves offset for clarity by 0.4 units at T* = 0.208 for $\eta = 0.2$ $\phi = 0.3$ blends with side chains for varying values of attractive well depth of acceptor-acceptor interaction $\varepsilon_{A\text{-}A} = 2$ (red circles), 3 (blue squares), and 4 (green diamonds) kT.

Like in the $\eta = 0.2$ $\phi = 0.2$ blends with side chains, $\varepsilon_{A\text{-}A}$ does not affect the liquid crystal transition temperature for $\eta = 0.2$ $\phi = 0.3$ blends. Acceptor-acceptor aggregation is increased with increasing $\varepsilon_{A\text{-}A}$ because of increased enthalpic gain for close acceptor proximity. Increasing $\varepsilon_{A\text{-}A}$ increases backbone ordering as shown by the increasing peak height in the backbone-

backbone radial distribution function at contact. This trend occurs because acceptors are more aggregated with each other instead of with polymer side chains and are thus less disruptive of polymer backbone ordering.

Backbone-backbone, acceptor-backbone, and acceptor-acceptor radial distribution functions for $\eta = 0.2$, $\phi = 0.2$ blends with side chains and interaction sets I, II, and III for $\varepsilon_{A\text{-}A} = 2$ and 4kT

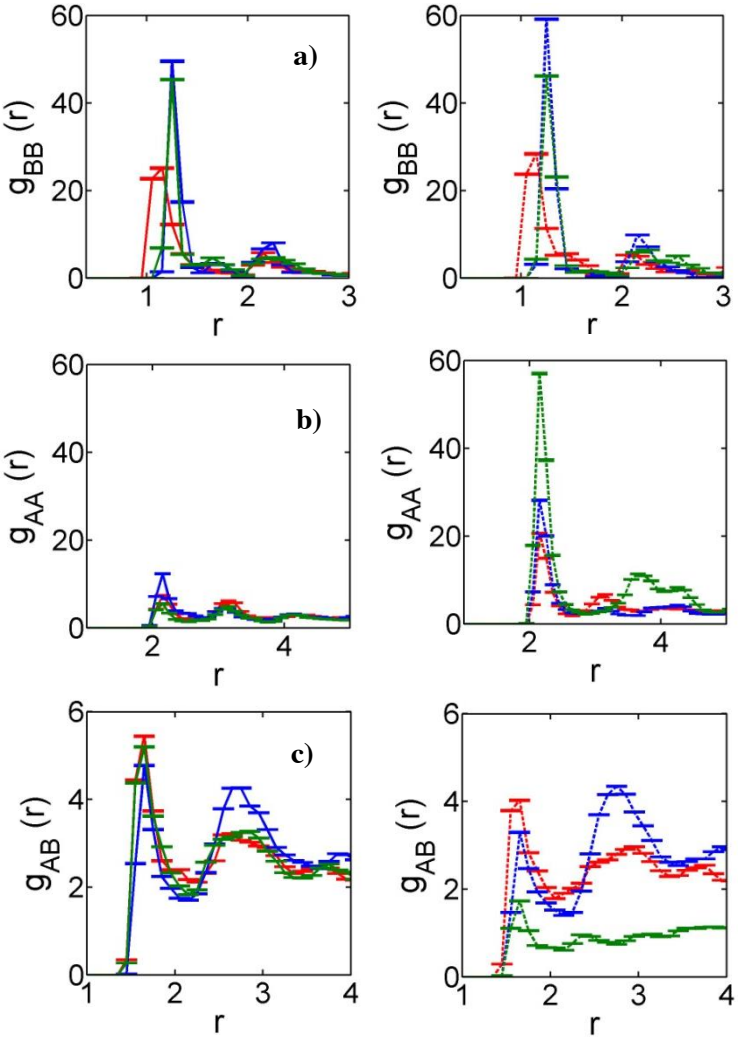

FIGURE 2.26: a) Backbone-backbone radial distribution function as a function of distance between backbone centers of mass, r, b) acceptor-acceptor radial distribution function as a function of distance between acceptor centers of mass, r, and c) acceptor-acceptor radial distribution function as a function of distance between backbone and acceptor bead centers, r, for $\eta = 0.2$, $\phi = 0.2$ blends with side chains for $\varepsilon_{A\text{-}A} = 2$ (solid lines, left column) and $\varepsilon_{A\text{-}A} = 4$ (dashed lines, right column) with interaction set I at T* = 0.208 (red), interaction set II at T* = 0.23 (blue), and interaction set III at T* = 0.23 (green).

The $g_{BB}(r)$ plots (Figure 2.26a) show backbone-backbone order does not significantly change when $\varepsilon_{A\text{-}A}$ is increased to 4kT for interaction sets I and III. Backbone order is higher for interaction set II with $\varepsilon_{A\text{-}A} = 4$ because increased acceptor aggregation causes fewer acceptors to interfere with backbone ordering. In interaction set I, acceptors are weakly attracted to backbones and in interaction set III, when all interactions are strong, acceptors are strongly attracted to side chains as well as backbones. Thus, acceptors do not interfere with backbone ordering as much in interaction sets I and III and so backbone order changes significantly at $\varepsilon_{A\text{-}A} = 4$ only with interaction set II. Figure 2.26b shows that more acceptors are at contact distance for all interaction sets with increased $\varepsilon_{A\text{-}A}$, indicating increased acceptor aggregation. The increase is the most dramatic for interaction set III because at $\varepsilon_{A\text{-}A} = 4$, the blend macrophase separates. The $g_{AB}(r)$ plots (Figure 2.26c) show that the interaction set III blend at $e_{A\text{-}A} = 4$ is less mixed than the other blends because the curve for interaction set III has a much lower peak at A-B contact. Thus, acceptor domains increase in size with $\varepsilon_{A\text{-}A} = 4$ and for $\varepsilon_{A\text{-}A} = 4$ and interaction set III, the blend is phase separated with larger, more pure domains.

Order parameter, S_2, for interaction set III blends with side chains where $\eta = 0.2$, $\phi = 0.2\text{-}0.4$, and $\varepsilon_{A\text{-}A} = 2\text{-}4$

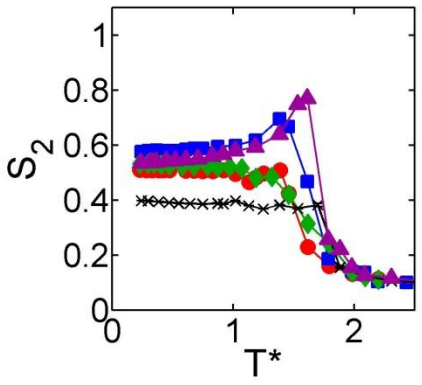

FIGURE 2.27: Order parameter, S_2, as a function of reduced temperature, T*, for interaction set III η = 0.2 blends with side chains where ϕ = 0.2 and ε_{A-A} = 2 (red circles), ϕ = 0.2 and ε_{A-A} = 3 (blue squares), ϕ = 0.2 and ε_{A-A} = 4 (green diamonds), ϕ = 0.3 and ε_{A-A} = 4 (black X), and ϕ = 0.4 and ε_{A-A} = 4 (purple triangles). The LC transition temperature is not significantly affected by ε_{A-A} at varying values of ϕ.

2.7.7 Varying Acceptor Molecule Size

Order parameter, S_2, for acceptor molecule diameter = 2-2.6 and interaction sets I, II, and III

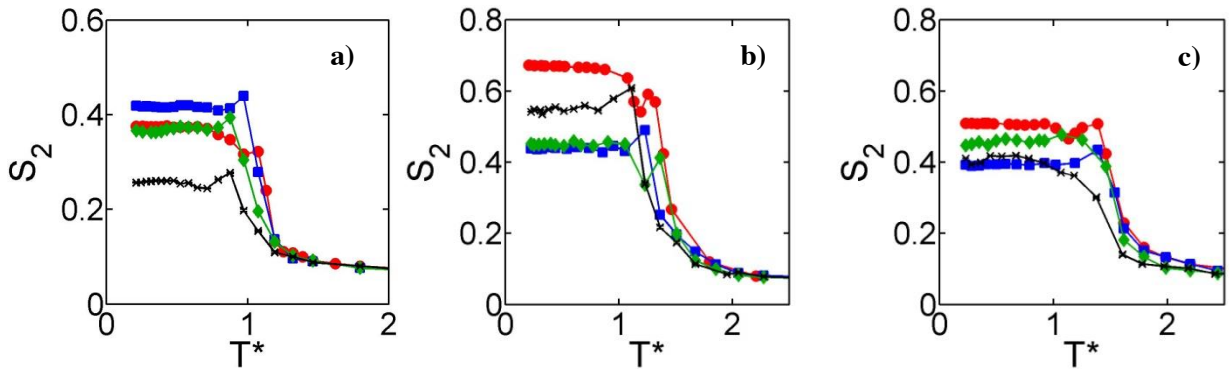

FIGURE 2.28: a) Order parameter, S_2, as a function of reduced temperature, T*, for η = 0.2 ϕ = 0.2 blends with side chains with a) interaction set I, b) interaction set II and c) interaction set III with acceptor diameter d = 2 (red circles), d = 2.2 (blue squares), d = 2 .4 (green diamonds), and d = 2 .6 (black X). Acceptor molecule size does not significantly affect LC transition temperature for blends with side chains and interaction sets I, II, or III.

Backbone-backbone, acceptor-acceptor, and acceptor-backbone, radial distribution functions for η = 0.2, ϕ = 0.2 blends with side chains and interaction sets I, II and III for d = 2-2.6

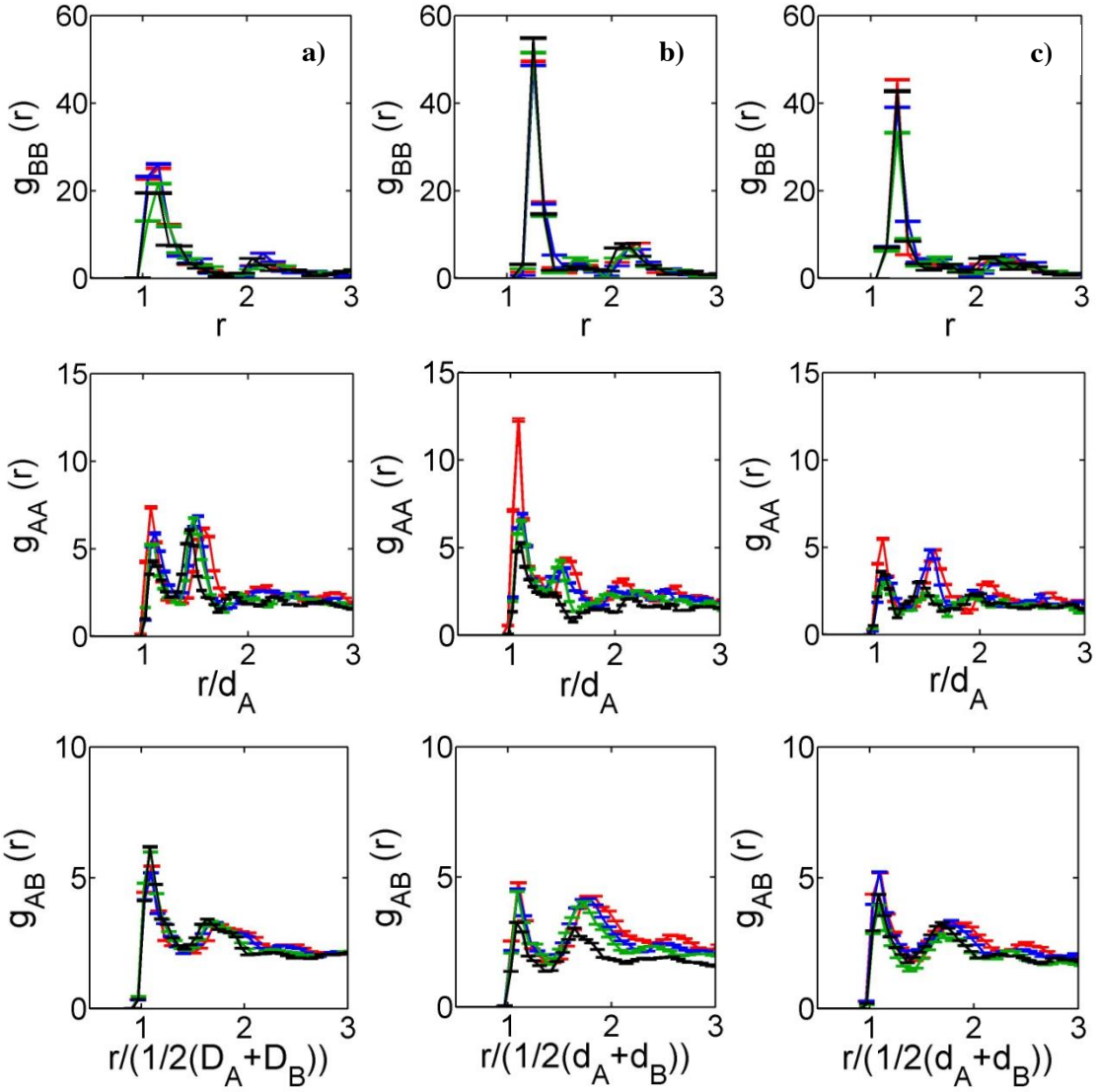

3

FIGURE 2.29: Backbone-backbone radial distribution function (top row) as a function of distance between backbone centers of mass, r, acceptor-acceptor radial distribution function as a function of distance between acceptor centers of mass, r (middle row), and acceptor-backbone radial distribution function as a function of distance between backbone and acceptor bead centers, r (bottom row), for η = 0.2, ϕ = 0.2 blends with side chains for a) interaction set I at T* = 0.208, b) interaction set II at T* = 0.23 and c) interaction set III at T* = 0.23, where d = 2 (red), d = 2.2 (blue), d =2 .4 (green), and d =2 .6 (black).

Acceptor molecule size does not significantly affect backbone-backbone or acceptor-backbone order as shown by the $g_{BB}(r)$ and $g_{AB}(r)$ plots.

Chapter 3

Computationally linking molecular features of conjugated polymers and fullerene derivatives to bulk heterojunction morphology

Adapted from: *Macromolecules*, 46 (14), 5775-5784, **2013.**

3.1 INTRODUCTION

Organic photovoltaic device efficiency is strongly dependent on the morphology or spatial organization of the electron donor and acceptor materials within the active layer. Ideal active layer morphologies have high interfacial area between donor and acceptor materials to facilitate exciton dissociation into free electrons and holes. Additionally, the presence of small donor domains (< 10 nm) can reduce exciton recombination, and continuous pathways within each domain to its respective electrode are needed for charge transport. The donor-acceptor morphology in the active layer is a function of the chemistry and architecture of both donors and acceptors, and of the processing conditions, including solvent evaporation rate and thermal annealing temperature [1-5]. Conjugated polymer electron donors such as poly(3-hexylthiophene) (P3HT), poly(2,2′:5′,2″-3,3″-dihexyl-terthiophene) (PTTT or C6-TT) , and poly(3,4-dihexyl-2,2′-bithiophene) (PDHBT), differ in the architecture of alkyl side chains along their π-conjugated backbones. Commonly used electron acceptor molecules are fullerene derivatives, such as [6,6]-phenyl-C_{61}-butyric acid methyl ester (PCBM) and [6,6]-phenyl-C_{71}-butyric acid methyl ester, where fullerene functionalization is used to tune its miscibility in solvents and donor molecules[6,7-9].

Experimental studies of blends of conjugated polymers and fullerene derivatives have shown the formation of pure domains of the conjugated polymer and fullerene derivatives, and

mixed amorphous regions[10-13]. Molecular features, such as the length and spacing of the alkyl side chains of the conjugated polymers can further influence packing both within the pure polymer domains and within the mixed polymer-fullerene derivative domains[5, 14-19]. Studies of poly(2,5-bis(3-alkylthiophen-2-yl)thieno[3,2-b]thiophene) (pBTTT) and fullerene derivatives have demonstrated intercalation of the fullerene between the alkyl side chains of PBTTT, which have greater spacing along the polymer backbone compared to the side chains of P3HT, which shows no intercalation[20, 21]. There is also evidence for fullerene intercalation in PTTT and PQT polymers[21]. In addition, conjugated polymer-acceptor miscibility has been shown to be a key factor in tuning active layer morphology, and thus solar cell performance[6-9, 22, 23].

The above studies clearly demonstrate the important role that the molecular features of the conjugated polymers and fullerene derivatives play in dictating active layer morphology and device efficiency. Therefore, it would valuable if one could explore the many state points in the large design space of polymer chemistries, fullerene derivatives, blend compositions, and processing conditions to predict the features that could lead to morphologies that are optimal for high device efficiency. Due to the extensive effort involving materials synthesis and characterization needed for a systematic exploration of this vast design space, there is a critical need for *in silico* methods that can link molecular features of the conjugated polymers and fullerene derivatives to their blend morphology. Molecular simulations facilitate such an exploration by providing a way to perform controlled, systematic studies of structure as a function of the molecular features of the system components without the time and material limitations of bench-scale synthesis[24-27].

A central challenge in molecular simulations of donor–acceptor blends is choosing an appropriate model that includes sufficient chemical and physical detail to mimic faithfully the

conjugated polymer and fullerene derivatives, while not being too detailed so as to prevent sufficient sampling at length and time scales that are relevant to experiments. With current hardware and software capabilities, atomistically detailed models of a few dozen chains permit hundreds of picoseconds to a few nanoseconds of simulation[28-31]. In contrast, with highly coarse-grained (CG) simulations, where one or more monomers are grouped together into one CG bead, one can achieve larger time scales but miss important packing considerations, such as intercalation of fullerene derivative between the side chains of the conjugated polymer. [25, 32-36]. Recent CG simulation studies of P3HT and C_{60} use models that are intermediate in detail to atomistic and heavily coarse-grained models, with interaction potentials informed by atomistic simulations, and achieve hundreds of nanoseconds of simulation[32, 33, 37]. However, even these time scales are not sufficient to achieve orientational alignment among the polymers below their melting temperature, where the polymer relaxation times tend to be longer**.** These past simulation studies of donor-acceptor blends motivate the need for advanced computational approaches that use cutting-edge hardware, sufficiently detailed models and can access long equilibration times. Our ability to access sufficiently long simulation time scales with reasonably detailed molecular models has recently been advanced by simulation software utilizing graphics processing units (GPUs), where parallelizable computations can be performed at nearly $4x10^{12}$ FLOPS on the newest cards at the time of publication[38-43], enabling high-throughput approaches[44].

In this paper, we perform high-throughput molecular dynamics simulations of 110 donor-acceptor blends using realistic coarse-grained models on graphics processing units using HOOMD-Blue[38, 39]. The morphology obtained using our approach for neat (no acceptors) systems of polymers mimicking P3HT and PDBHT are in agreement with experimental

measurements[45, 46]. We find that the order-disorder transition (ODT) of neat conjugated polymers depends on side chain density and orientation along the polymer backbone. We study blends of acceptors and polymers while systematically varying polymer architecture, acceptor miscibility, and blend composition to elucidate the effect of these physical and chemical features of acceptors and donors on polymer-acceptor blend morphology. Immiscible acceptors do not significantly change the morphology of blends compared to the neat polymer but increase the ODT of the blend compared to that in the neat case. The ODT of blends with miscible acceptors is dependent on the complicated interplay between entropy and enthalpy governing self-assembly**.** With our realistic, generic coarse-grained models implemented on GPU hardware, we are able to observe for the first time in simulations, the self-assembly of morphologies where strongly miscible acceptors intercalate between alkyl side chains of layered donor molecules when both the side chain spacing along the polymer backbone and the acceptor miscibility facilitate intercalation. Finally, we explore blends of acceptors with strong attraction to the donor backbone and find previously unseen active layer morphologies with desirable characteristics including continuous pathways for charge transport and increased donor-acceptor interfacial area for exciton dissociation.

This paper is organized as follows. In the Approach section we describe the model, simulation methods, and analysis techniques. In the Results section we first describe the effect of polymer architecture on neat polymer (no acceptor) morphologies, followed by a description of the effect of polymer architecture and acceptor miscibility on blend morphology. We conclude this paper with a brief overview of the key conclusions, limitations and strengths of this work.

3.2 APPROACH

3.2.1 Model

In this work we conduct molecular dynamics simulations of organic photovoltaic blends using coarse-grained models in order to generate thermodynamically stable morphologies at experimentally relevant length scales. We simplify the atomistically derived, coarse-grained models of Huang *et. al.* [32-34] to model generic thiophene-based conjugated oligomers and fullerene-derived electron acceptors. The three oligomers (15 monomers in length in this study), denoted by P1, P2, and P3 in Figure 3.1a, differ in the alkyl chain placement along the backbone, and *qualitatively mimic* P3HT, PTTT, and PDHBT, respectively. As in Ref. [32-34] we represent each thiophene ring with one coarse-grained bead (red B in Figure 3.1a), and each alkyl side chain with two coarse-grained beads (blue S in Figure 3.1a). We use harmonic bond, angle, and dihedral intramolecular potentials to define and enforce the connectivity and relative positions of the coarse-grained beads in each oligomer. Our intramolecular potentials match those in Ref. 34 to a first-order approximation, though our backbone angle spring constant $30\varepsilon/\sigma^2$ gives backbone persistence lengths of 12.5 to 20 monomers between T* = 2.5 and T* = 1.5, respectively. These persistence lengths are appropriate for the regioregular P3HT modeled here, which is expected to have significantly longer persistence lengths than the 6 to 8 monomer persistence lengths of regiorandom P3HT[47]. Full specifications of the bond, angle, and dihedral constraints are included in Section 3.7. The Lennard-Jones potential models non-bonded attractions between bead species *i* and *j* with well depth ε_{ij}[48]. Excluded-volume interactions between bead species *i* and *j* are denoted by $\varepsilon_{ij} = 0$, and are modeled by the Weeks-Chandler-Andersen potential[49]. Backbone beads (red *B* beads in Figure 3.1a) are attractive, with $\varepsilon_{BB} = 2.0$, side chain beads (blue *S* beads in Figure 3.1a) are attractive with $\varepsilon_{SS} = 1.0$, and backbone/side

chain interactions are purely excluded volume interactions with $\varepsilon_{BS} = 0$ (Table 3.1). Our potentials qualitatively fit the atomistically derived coarse-grained potentials of Ref. [34], which include effective electrostatic interactions implicitly. We note that our energy unit ε = 2.7e-21 J is slightly larger than the 2.4e-21 J we calculate from the coarse-grained thiophene-thiophene well depth of Ref. [34]. We choose $\varepsilon_{BB}/\varepsilon_{SS} = 2.0$ as backbone aggregation is a stronger driving force for ordering of the thiophene polymers than side chain aggregation because of the conjugated nature of the polymer backbone. This gives our thiophene beads stronger relative attractions than in Ref. [34]. We choose $\varepsilon_{BS} = 0$, unlike Ref. [34], to simplify our generic model. The other fundamental units used in our model are distance σ = 3e-10 m, and mass M = 1.4e-25 kg. The derived time unit $\tau = (M\sigma^2/\varepsilon)^{0.5}$ = 2.16 e-12 s, and pressure unit $P^* = \varepsilon/\sigma^3$ = 987 atm. The dimensionless temperatures $k_BT/\varepsilon = T^*$ = 1.5, 1.75, 2.0, 2.25, and 2.5 correspond to T = 20, 69, 118, 167 and 216 °C, respectively. Our model correctly predicts the density of P3HT at 25°C and 1 atm (1.1 g/cm^3), corresponding to simulated volume fraction η = 0.18, but over-predicts the coefficient of thermal expansion. We therefore perform simulations at P^* = 0.1 = 98.7 atm to access experimentally relevant volume fractions between η = 0.10 at T^* = 2.5 to η = 0.30 at T^* = 1.5.

Fullerene-derived acceptor molecules are modeled as rigid bodies composed of 13 *A* beads arranged into a filled icosahedron (Figure 3.1b) of diameter 3σ. The rigid-body model is chosen for computational efficiency relative to single-sphere models that require large intermolecular potential cutoffs, resulting in a greater number of nearest neighbors per particle, and significantly slower simulations. The functionalization of the fullerene is modeled through non-bonded interactions that represent immiscible acceptors A1, weakly miscible acceptors A2,

and strongly miscible acceptors A3 (Table 3.1). The miscibility of the acceptors with the polymer can be experimentally tuned by functionalizing fullerenes with varying derivatives[7].

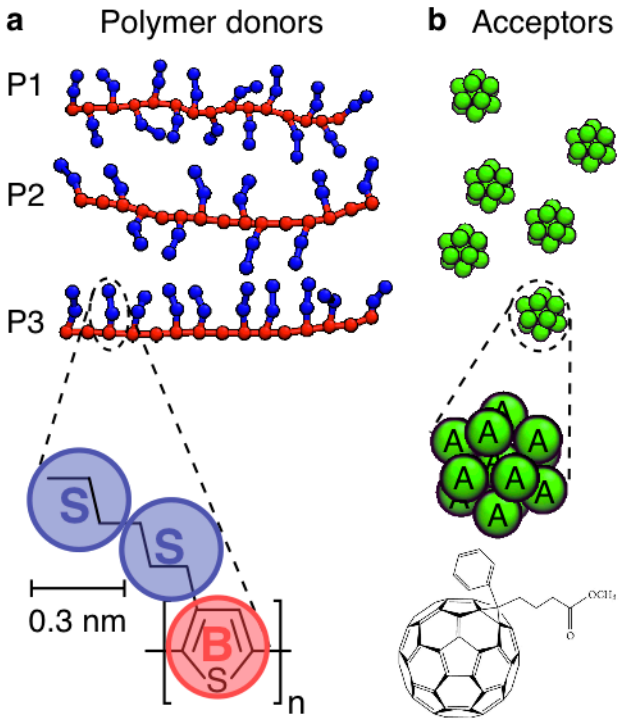

FIGURE 3.1: **a)** Model conjugated oligomers P1, P2, and P3, with coarse-grained beads representing multiple atoms of the alkyl side chains (blue S) and backbones (red B). **b)** Model acceptors such as fullerene derivatives (e.g. PCBM shown) are modeled by a collection of 13 coarse-grained A beads (green).

TABLE 3.1: Lennard-Jones interaction parameters ε_{ij} (acceptor-backbone (ε_{AB}), acceptor-side chain (ε_{AS}) and acceptor-acceptor (ε_{AA})) for three acceptor types A1, A2, and A3. '0' indicates Weeks-Chandler-Andersen interactions.

	ε_{AB}	ε_{AS}	ε_{AA}
A1	0	0	0.5
A2	1.0	0.1	0.5
A3	1.0	0.1	0.1

3.2.2 Simulation Method

Molecular dynamics simulations are performed with HOOMD-blue v0.11.0-65-ga39e1f8 on NVIDIA c2050 or c2090 graphics cards driven by a single core of a 2.67 GHz Nehalem or 2.8 GHz Westmere CPU, respectively. Initially disordered configurations of 250 oligomer chains are

equilibrated in the isothermal-isobaric (constant NPT) ensemble at a dimensionless temperature $k_BT/\varepsilon = T^* = 2.5$ (216˚C) and $P^* = 0.1$ (98.7 atm) with time step $dt = 0.00035\tau$ (0.76 fs). Each system is cooled at constant pressure to $T^* = 1.5$ (20˚C) in 0.25 increments, with sufficient sampling at each temperature to ensure equilibration (see Section 3.7 for details). Equilibration times depend upon the system and temperature. On average $2.9\text{x}10^8$ +/- $1.6\text{x}10^8$ time steps (~219 ns) are required to achieve the 52 +/- 12 statistically independent configurations, as measured by the potential energy autocorrelation function, which are used for calculating ensemble average properties. The slowest system to relax requires $2.21\text{x}10^9$ steps (1.7 μs), taking 357 hours on an NVIDIA c2050 GPU. Equilibrating and sampling the 110 state points studied here required about 780 GPU-days spread over two months on 14 GPUs.

3.2.3 Analysis

To quantify orientational ordering among donor oligomer thiophene backbones, we calculate the local orientational order parameter S_2. We calculate the orientation vectors $o_i = r_{i,end} - r_{i,start}$, where $r_{i,end}$ is the unwrapped position of the end bead and $r_{i,start}$ is the unwrapped position of the first bead for each donor molecule i. Then, for each donor molecule i, its local alignment a_i is the largest eigenvalue of the order tensor

$$Q_i = \frac{1}{N}\sum_{j=1}^{N}\left[\frac{3}{2}(\hat{o}_i)_\alpha(\hat{o}_j)_\beta - \frac{1}{2}\delta_{\alpha\beta}\right]$$

where the index j is over the N neighbors who have at least one backbone bead within 1.6σ of a backbone bead of donor molecule i, $\hat{o}_i$ is the unit orientation vector for donor molecule i, and $\delta_{\alpha\beta}$ is the Kroeneker delta function for Cartesian coordinate indices α and β. The overall S_2 for a snapshot is the average a_i over all donor oligomers, and the average S_2 for a trajectory is the S_2 averaged over the independent snapshots. The value of S_2 is near zero for a disordered system

and approaches a value of one for a perfectly ordered system[50]. In our work, systems with $S_2 <$ 0.6 visually appear disordered and display no diffraction peaks, while systems with $S_2 > 0.9$ look ordered in visual snapshot, and display peaks in simulated scattering experiments with intensities greater than 1.5 times the mean intensity value.

While S_2 quantifies orientational order, we use radial distribution functions ($g_{ij}(r)$)[51] to quantify positional order among the donor and acceptor molecules. The radial distribution function $g_{BB}(r)$ is calculated between backbone beads, excluding those in the same molecule. The acceptor-backbone $g_{AB}(r)$ is calculated between acceptor centers of mass and backbone beads, and the acceptor-acceptor $g_{AA}(r)$ is calculated between acceptor centers of mass. The first peak in the radial distribution function represents the degree to which beads are correlated at their contact distance, and peaks at larger values of arise from long range ordering. Quantification of the structural periodicities of conjugated polymer backbone beads is done using simulated diffraction experiments. To calculate diffraction patterns for a simulation snapshot we select an orientation of the simulation box, replace each backbone bead with a symmetric 2D Gaussian (intensity 5.0 and width 1.0) in the x-y plane, and sum the intensities projected onto a 512 x 512 grid (into the page). These real-space intensities are converted into the frequency domain via the 2D Fourier transform. The magnitudes of the resulting complex-valued matrix are converted to an image using the "jet" color mapping, which is cropped to show the upper left quadrant or upper half of the diffraction pattern. The real-space length scale l of a physical feature corresponding to a diffraction peak is calculated from $q = 2\pi/l$.

A high donor-acceptor interfacial area is important for high efficiency in organic photovoltaic devices to facilitate exciton dissociation along the interface[1-5]. We quantify two aspects of the interface between donor and acceptor molecules. We use the magnitude of the

first peak of $g_{AB}(r)$ as a proxy for the *donor-acceptor contact surface area*, with larger peak values corresponding to greater donor-acceptor interfacial area. We also calculate the *roughness of acceptor domain surfaces* as an independent metric of the interfacial area. Acceptor domain surface roughness is calculated by counting the number of "probe" beads that can sit adjacent to the acceptor surface without overlapping any acceptor beads. We select a spherical probe bead radius $s_{rad} = 2.0\sigma$ and generate 100 points uniformly $s_{rad} + 0.5\sigma$ away from each acceptor bead center. For each of these points we check whether the probe bead centered on the point overlaps with any other acceptor beads. If a probe bead can be placed at a point without overlap, a differential volume $dA = \pi/4$ (corresponding to $1/100^{th}$ of the surface area of a sphere of radius 2.5σ) is added to the total surface roughness. The value $s_{rad} = 2.0\sigma$ is chosen to minimize the contribution of probe molecules from within the bulk acceptor domain while providing sufficient resolution of surface roughness. The acceptor domain surface roughness values presented here are normalized by the number of acceptor molecules and do not consider donor-acceptor contacts. The acceptor domain surface roughness values are also only comparable between similar acceptor domain morphologies, for example, between two cylinders of acceptors phase separated from donors, or two slabs of acceptors, but not between a slab and a cylinder.

All visualization is performed using scripts written for the Visual Molecular Dynamics (VMD) v1.9.1 package[52]. Analysis routines (e.g. S_2, g(r), angle and dihedral angle distributions, widths/spacing in morphology, and surface roughness) are written as Tcl scripts for VMD or as stand-alone Python routines (scattering analysis and potential energy autocorrelation).

3.3 RESULTS

In this section we present the results from our molecular dynamics simulations in the following order. First, we detail the thermodynamics of neat oligomers (oligomers without acceptors), specifically the order-disorder transition, followed by a description of the structures observed for neat oligomers below the order-disorder transition temperature (ODT). Second, we describe the thermodynamics of oligomer-acceptor blends, comparing the ODT for each blend against those observed for neat polymers. Third, we describe the morphologies observed for oligomer-acceptor blends below their ODT. Fourth, we discuss the blend of miscible acceptors A3 with P2, the only blend where intercalation of acceptors among donor side chains is observed. Finally, we present and discuss the results of exploratory simulations leading to novel morphologies with strongly miscible acceptors A5 with the three types of oligomers.

3.3.1 Neat Oligomers (no acceptors)

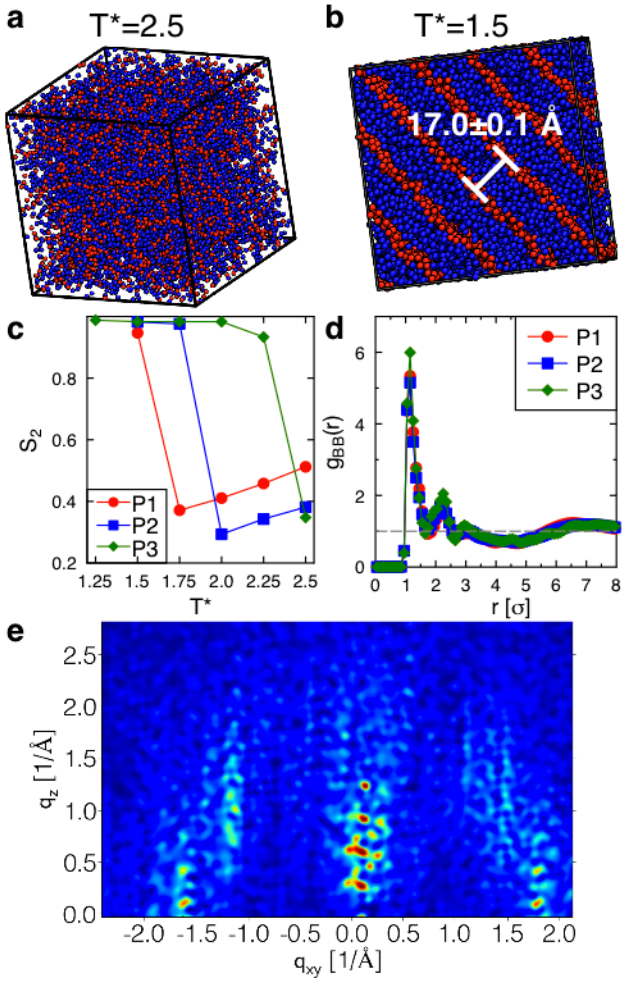

FIGURE 3.2: a) Disordered configurations representative of neat P1, P2, and P3 at high temperatures. **b)** Representative snapshot of layers formed upon cooling to low temperatures for P1, P2, and P3. Layer spacing for P1 is shown. **c)** Orientational order parameter, S_2, as a function of reduced temperature, T*, for neat polymer P1, P2, and P3. **d)** Backbone-backbone radial distribution function as a function of distance between backbone beads, r, for neat polymer P1, P2, and P3 at T* = 1.5. **e)** Diffraction pattern calculated from simulation data for P1 at T* =1.5.

Neat Oligomer (No Acceptors) Thermodynamics

Simulations of P1, P2, and P3 demonstrate that the spacing, orientation, and number of side chains along the oligomer backbone influences the order-disorder transition temperatures (ODT) of the neat oligomers. At high temperature T* = 2.5, all three oligomer melts are disordered (Figure 3.2a), with orientational order parameter $S_2 < 0.6$. We define the order-

disorder transition temperature as the temperature at which the S_2 value abruptly increases, with $S_2 > 0.9$ denoting an ordered state, such as lamellae (Figure 3.2b) or hexagonally packed cylinders, as described in the analysis section. Figure 3.2c shows a plot of the orientational order parameter S_2 as a function of temperature for neat oligomers P1, P2, and P3, which have ODTs around $T^* \approx 1.5$, 1.75 and 2.25 respectively. The ODT is higher for oligomers with more "exposed" backbone (P3>P2>P1). This trend is expected because the Lennard-Jones attraction $\varepsilon_{BB} = 2.0$ between thiophene beads is the strongest enthalpic driving force in these systems, facilitating alignment of backbones. P1 has the least exposed backbone due to the side chains extending from every thiophene ring along the backbone, and consequently P1 has the lowest ODT. P3 has the most exposed backbone with all side chains on one side of the backbone, further facilitating backbone alignment. In an oligomer of 15 monomers, P2 has the same number of side chains as P3, but less exposed backbone because of the alternating side chain orientations. The link between oligomer side chain placement, and resulting backbone exposure and oligomer ordering, is also evidenced by the backbone-backbone radial distribution function $g_{BB}(r)$ for each oligomer at $T^* = 1.5$ (Figure 3.2d). P3 is more ordered than P1 or P2 at $T^* = 1.5$, as shown by increased magnitude and sharpness of the first two $g_{BB}(r)$ peaks (Figure 3.2d).

Neat Oligomer Morphology

At temperatures at and below the ODT, the neat oligomers self-assemble into lamellae or hexagonally packed cylinders. P1 and P2 both form lamellae with high orientational alignment between the oligomer backbones in the ordered state (Figure 3.2b). The layer spacings of 17 Å measured from the diffraction patterns of P1 in Figure 3.2e and Figure 3.3a are consistent with the 16.8 Å spacing measured in experiments[45, 46]. The imperfect lamellae in Figure 3.3a are observed before equilibration, at 142 ns of a 612 ns simulation, and show broader (n,0,0) peaks

and a sharper (0,1,0) peak compared to the perfect lamellae in Figure 3.2e. The closer resemblance of the imperfect lamellar diffraction pattern to the experimental diffraction pattern is expected because of the distribution of crystal grain sizes and orientations in experiments. The (0,1,0) peak is less pronounced in simulations of P1, and shifted to larger q, but matches experimental measurements qualitatively. In contrast to P1 and P2 oligomers, P3 oligomers form hexagonally packed cylinders around T* ≈ 2.25 (Figure 3.3b) and lamellae similar to Figure 3.2b around T* ≈ 2.0. The hexagonal symmetries in the simulation snapshot, simulated diffraction pattern from the snapshot, and experimental diffraction pattern are evident (Figure 3.3b). The average center-to-center distance between hexagonally-packed cylinders of P3 is calculated to be 18.6 Å, smaller than the 22.5 Å measured in diffraction experiments of PDHBT[46]. The hexagonally packed cylinders, unique to P3 in both simulation and experiment[46], are not observed for P1 or P2 in simulation or experiment because their alternating side chain orientations inhibit cylindrical packing. These results demonstrate that our coarse-grained model for generic conjugated polymers can reproduce experimental diffraction patterns and major trends in morphology based on changes in conjugated polymer architecture.

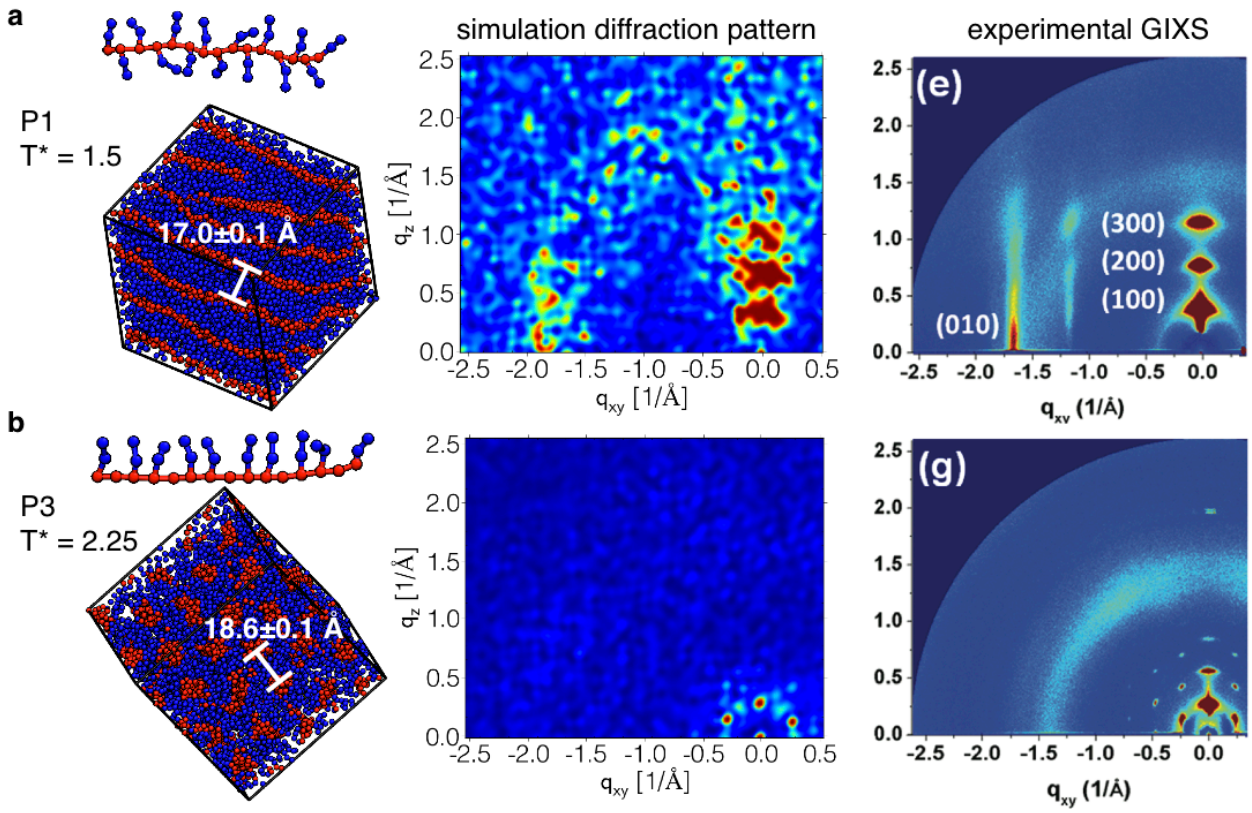

FIGURE 3.3: **a)** Imperfect lamellar P1 (left), diffraction pattern calculated from simulation data (center), and GIXS data from annealed P3HT (right). **b)** P3 in hexagonally packed cylinders at T* = 2.25 (left), diffraction pattern calculated from simulation data (center) and GIXS data from annealed PDHBT (right). Experimental diffraction patterns adapted with permission from *Controlled Conjugated Backbone Twisting for an Increased Open- Circuit Voltage while Having a High Short-Circuit Current in Poly(hexylthiophene) Derivative*s, S. Ko, ET Hoke, L. Pandey, S. Hong, R Mondal, C. Risko, Y Yi, R Noriega, MD. McGehee, JL Bredas, A. Salleo, and Z. Bao, Journal of the American Chemical Society 2012, 134, 5222-5232, Copyright 2012 American Chemical Society.

3.3.2 Oligomer-Acceptor Blends

We now shift focus from neat oligomers to blends of conjugated oligomers (donors) with fullerene derivatives (acceptors) to understand the effects of donor-acceptor miscibility on blend morphology and thermodynamics as a function of blend composition. Rather than focus on how a specific functional group links to specific polymer miscibility, the focus of this work is to show how varying miscibility affects the bulk morphology, and if increasing acceptor-polymer miscibility brings about new and previously unseen morphologies.

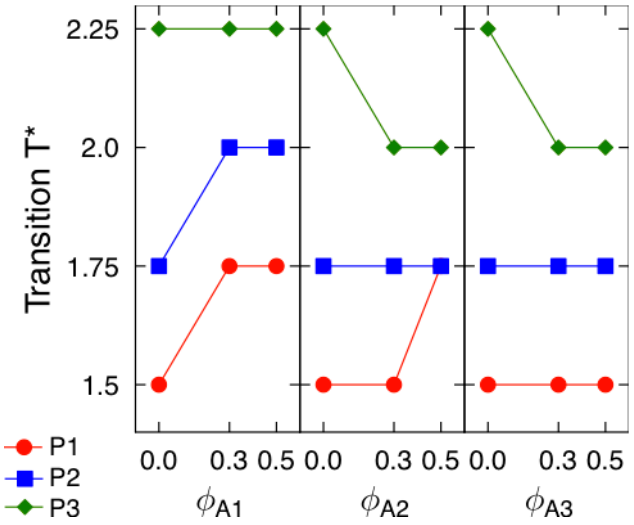

FIGURE 3.4: Order-disorder transition temperatures (ODT) of P1, P2, and P3 as a function of acceptor volume fraction and acceptor miscibility (blends with A1, A2, and A3).

Oligomer-Acceptor Blend Thermodynamics

We study blends of P1, P2, and P3 oligomers mixed with acceptors, at volume fractions of acceptors, $\phi = 0.3$ and $\phi = 0.5$. Figure 3.4 summarizes the approximate ODT for each oligomer, as determined by the temperature around which S_2 abruptly increases from $S_2 < 0.6$ to $S_2 > 0.9$, as a function of the volume fraction of each acceptor. Plots of S_2 as a function of T* for each blend are included in Figure 3.10. Figure 3.4 demonstrates that by adding acceptors, the ODT for the conjugated polymers can shift to higher or lower temperatures, or remain unchanged, depending on the polymer architecture and acceptor miscibility. We hypothesize that the trends in Figure 3.4 are due to a complicated interplay between entropy and enthalpy governing self-assembly, which we explain below.

Immiscible acceptors A1: The higher ODT for P1 and P2 blends with immiscible acceptor A1 compared to neat systems is attributed to a confinement effect; the interface between acceptor and donor molecules that arises from their immiscibility provides a packing constraint, giving rise to an entropic drive for the alignment of the donor molecule backbones that are confined between these interfaces[53]. The ODT of the P3-A1 is the same as for neat P3 oligomers (T* =

2.25), which we hypothesize is due to the shielding of the donor backbones by the side chains surrounding the cylinders, reducing the confinement effect.

Miscible acceptors A2 and A3: The miscibility of the acceptors (lower ε_{AA} and/or higher ε_{AB} leads to higher miscibility of acceptor and donors) and their volume fraction dictate whether oligomer alignment or acceptor aggregation drives the ordering of the system. As noted above for A1, aggregated acceptors provide confinement that can facilitate oligomer alignment as in the case of P1-A1 and P2-A1 blends. A2 acceptors are more miscible than, and remain miscible at lower temperatures than the A1 acceptors. Thus, A2 acceptors only increase the P1 ODT when present in sufficient amount ($\phi = 0.5$). A2 acceptors do not increase the P2 ODT because A2 acceptors do not phase separate at $T^* = 2.0$. A3 acceptors are even more miscible than A2, and are not observed to alter the ODT of P1 at volume fractions of $\phi = 0.3$ or $\phi = 0.5$. The lower ODT of P3 blends with miscible acceptors A2 and A3 as compared to neat P3 oligomer is an enthalpic effect; the increased attraction between donors and acceptors provides an enthalpic driving force for P3 oligomers to mix with A2 or A3 at $T^* = 2.25$, disrupting the hexagonally-packed cylinders in which would be formed by neat P3 or blends of P3 with immiscible acceptors A1. Similar enthalpically driven mixing has been seen in past studies where the miscibility within a polymer nanocomposite has been shown to increase with increasing attraction between polymer and spherical nanoparticles[54]. We hypothesize that this shift to lower approximate ODT upon the addition of weakly miscible (A2) and strongly miscible (A3) acceptors occurs only for P3 oligomers because P3 has more exposed backbone compared to P1 or P2 oligomers and thus a higher driving force for mixing with the miscible acceptors.

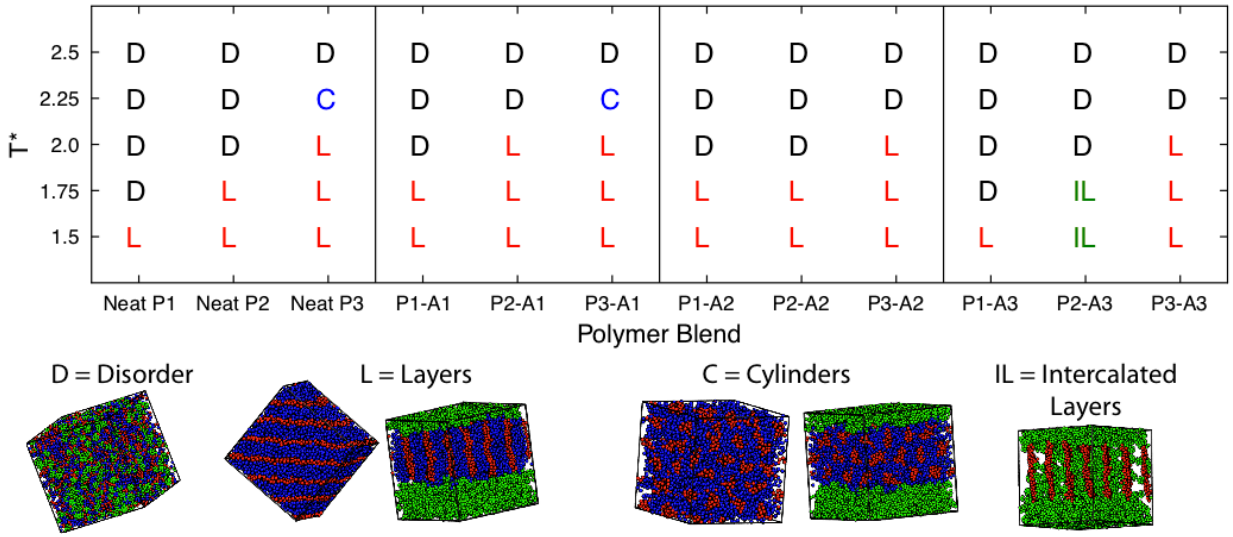

FIGURE 3.5: Phase diagram of blend morphology for P1, P2, and P3 neat polymer and ϕ = 0.5 blends with acceptors A1, A2, and A3. Shown below are representative snapshots of the morphologies in the phase diagram.

Oligomer-Acceptor Blend Morphology

In this section we describe donor-acceptor morphology for each blend. Figure 3.5 summarizes all of the ordered morphologies arising from our high-throughput screening of donor-acceptor blends. Figure 3.6 shows snapshots and radial distribution functions of select blends. We focus on blends of donor oligomers and acceptors at ϕ = 0.5 in the main manuscript for brevity because ϕ = 0.3 blends have oligomer domain morphologies similar to the ϕ = 0.5 blends. Acceptor aggregates in ϕ = 0.3 blends are also similar to those in ϕ = 0.5 blends except that aggregates form cylinders for ϕ = 0.3 blends compared to slabs for ϕ = 0.5 blends because there are fewer acceptors in ϕ = 0.3 blends. Radial distribution functions quantifying the similarities between ϕ = 0.3 and ϕ = 0.5 blend components are included in Section 3.7: Figures 3.11-3.13.

Immiscible acceptors A1: For all three donors (P1, P2 and P3), blends of oligomers and immiscible acceptors (A1) macrophase separate and the oligomer domain has structure similar to

its neat counterpart (compare Figures 6a and 6b with Figures 2b and 3b, respectively). Backbone-backbone positional order is higher in A1 blends than is the case for all neat oligomers P1, P2, and P3 (compare Figure 3.11 with Figure 3.2d) because oligomers are confined between acceptor slabs in A1 blends, facilitating oligomer backbone order[53].

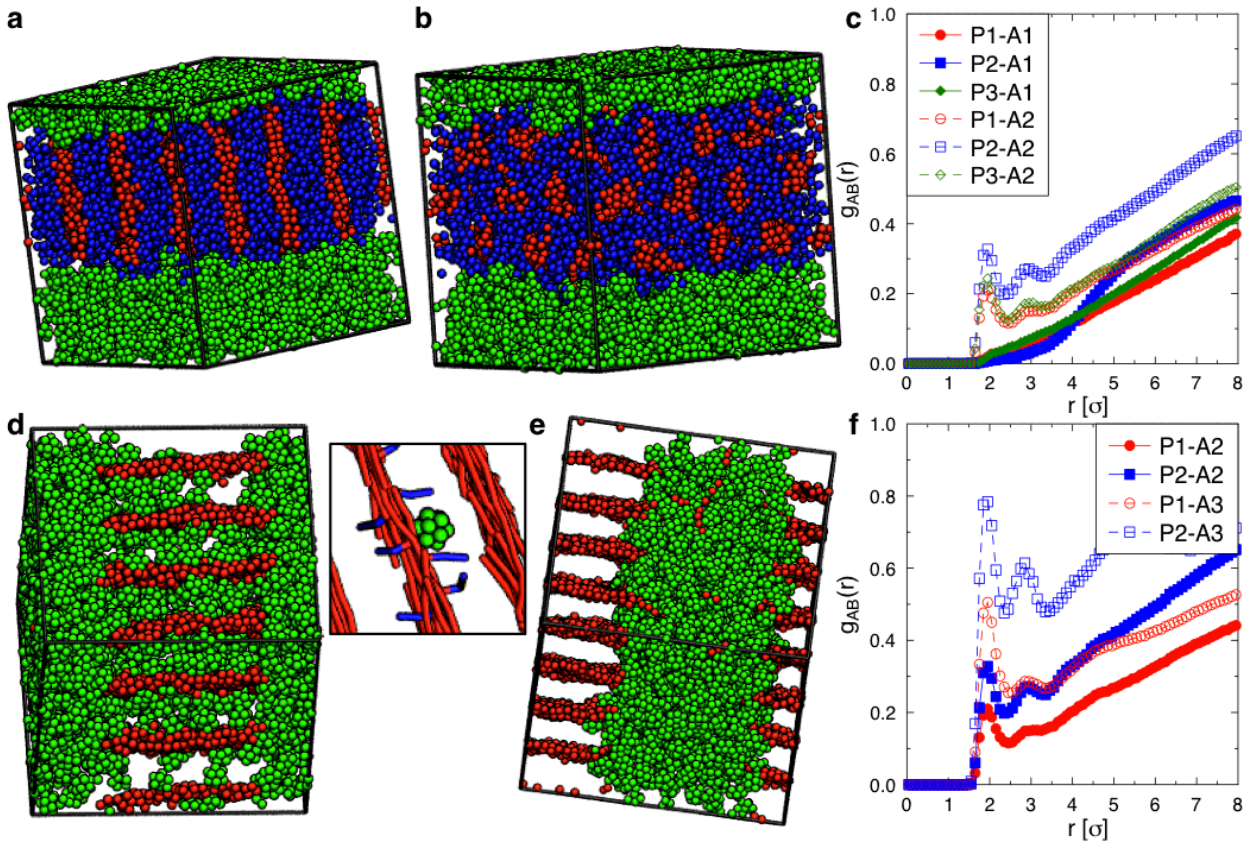

FIGURE 3.6: **a)** Acceptors macrophase separate from the lamellae of conjugated polymers in the P3-A1 ϕ = 0.5 blend at T* = 2.0. **b)** At T* = 2.25, acceptors macrophase separate from hexagonally packed cylinders of conjugated polymers in the P3-A1 ϕ = 0.5 blend. **c)** The acceptor-backbone radial distribution function shows increased acceptor-backbone correlations for A2 relative to A1 at T* = 1.5, for all three polymers. **d)** Acceptors A3 intercalate with P2 layers in the P2-A3 ϕ = 0.5 blend at T* = 1.5 (intercalation detail, right). **e)** Acceptors do not intercalate in P1-A3 ϕ = 0.5 blends at T* = 1.5. **f**) Acceptor-backbone correlation functions for P1 and P2 blends with A2 and A3 at T* = 1.5.

Weakly Miscible Acceptors A2: Weakly miscible acceptors A2 disrupt the hexagonally packed cylinders observed for neat P3 at T* = 2.25 (making the P3 blend disordered at T* = 2.25), but do not alter the morphology of P2 or P1 or the morphology of P3 at T* ≤ 2.0. At T* = 1.5,

lamellae remain the thermodynamically stable structure for all three donors at acceptor volume fractions $\phi = 0.3$ and $\phi = 0.5$ for blends with acceptors A1, A2. Compared to A1 blends, A2 blends result in increased acceptor-backbone spatial correlations and higher acceptor-backbone interfacial area, which is expected due to the higher miscibility (Figure 3.6c). Comparisons of $g_{AA}(r)$ and $g_{BB}(r)$ for these blends are included in Section 3.7: Figure 3.14, showing slightly lower acceptor-acceptor correlations in A2 blends compared to A1 blends, and no difference in the backbone-backbone correlations between A2 and A1 blends. P3 oligomer backbones with more exposed backbone than P1 or P2 give rise to higher $g_{BB}(r)$ in P3-A2 blends relative to P1-A2 or P2-A2 blends, as was the case in A1 blends (compare Section 3.7: Figure 3.11 with 3.12).

Strongly Miscible Acceptors A3: Comparing the heights of the first ($r = 3.0\sigma$) peak in the acceptor-acceptor radial distribution function $g_{AA}(r)$ between A1, A2, and A3 blends (Section 3.7: Figures S.11, S.12 and S.13 respectively) we find acceptor aggregation degreases as acceptor miscibility increases, going from A1 to A2 to A3. Strongly miscible acceptors A3 disrupt the hexagonally packed cylinders observed for neat P3 at $T^* = 2.25$, which is expected because weakly miscible acceptors A2 also disrupted the cylinders. A3 acceptors do not significantly alter morphology of P1 blends or the morphology of P3 blends at $T^* \leq 2.0$. One small difference is the observation that oligomer chains extend into the bulk acceptor domain in A3 blends of P1, P2, and P3 at intermediate temperatures, which is qualitatively consistent with the experimentally hypothesized amorphous region between crystalline domains of pure components[10-13]. A snapshot of the P3-A3 blend at $T^* = 2.0$ demonstrating the extension of oligomer chains into the bulk acceptor phase is included in Section 3.7: Figure 3.15. The disordered polymer chains retract into the ordered lamellae at low temperature ($T^* = 1.5$). Acceptor-acceptor positional order, as measured by the first peak of $g_{AA}(r)$ at 3.0σ in Section 3.7:

Figure 3.13, does not vary significantly between A3 blends of P1, P2, or P3. As is the case for neat oligomers and blends of A1 and A2 acceptors, P3 oligomers have higher backbone positional order because P3 oligomers have more exposed backbone than do P1 and P2 oligomers (Section 3.7: Figure 3.13).

Acceptor Intercalation: In P2-A3 blends we observe the self-assembly of acceptors intercalated among the side chains of layered donor molecules, matching experimental observations[20, 21]. This is the first observation of the self-assembly of intercalated morphologies in simulations, as previously the only simulations that report intercalated configurations either began the simulation with an intercalated initial configuration[55], or observed intercalation among non-layered donor molecules[36]. Intercalation is unique to P2 blends with strongly miscible acceptors A3 (Figure 3.6d). Neither blends of A3 with P1 (Figure 3.6e) or A3 with P3 demonstrate intercalation, in agreement with experiments[20]. Zooming in on a representative acceptor molecule with high backbone correlation (Figure 3.6d, inset) it is clear that the acceptor intercalates in the space between pairs of side chains extending from P2. The strong acceptor-backbone spatial correlation in P2 relative to P1 or P3 is confirmed quantitatively by the acceptor-backbone radial distribution function $g_{AB}(r)$ and demonstrates that the intercalated P2-A3 blend has higher acceptor-backbone interfacial area than do non-intercalated blends (Figure 3.6f). Intercalation does not significantly affect backbone-backbone positional order, as measured by the first peak height of $g_{BB}(r)$ (comparing Section 3.7: Figure 3.12 and 3.13 $g_{BB}(r)$). A complete set of radial distribution function comparisons and snapshots showing that intercalation also occurs in $\phi = 0.3$ blends are included in Section 3.7: Figures 3.13 and 3.14.

Appropriate spacing of donor molecule side chains relative to the size of the acceptor is a necessary condition for intercalation. As in experiments, acceptor molecules do not intercalate if

there is insufficient spacing between polymer side chains[20, 21]. In P1 and P3, the one-monomer gaps between side chains extending in the same direction are too small (1.8σ) to accommodate an acceptor molecule (3.0σ) without significantly bending the side chains or backbone, both of which are energetically unfavorable, explaining why intercalation is not observed for these two oligomers. In contrast, in the case of P2, there is sufficient space in the 4.6σ gap between side chains for acceptors to intercalate. For P2, intercalation also depends crucially on the strength of attraction between the acceptors $\varepsilon_{AA,}$ and the strength of attraction between acceptors and donor backbones ε_{AB}. In other words, the functionalization of the fullerene that affects these interactions can be tuned to drive or deter intercalation. A simulation of the $\phi = 0.5$ P2 blend with acceptor A4 ($\varepsilon_{AB} = 0.1$, $\varepsilon_{AS} = 0.1$, and $\varepsilon_{AA} = 0.1$), which is identical to A3 except for its weaker acceptor-backbone attraction, demonstrates that acceptors with weak acceptor-backbone attraction phase separate from the donors and do not intercalate. In addition, simulations of weakly miscible acceptor A2 ($\varepsilon_{AA} = 0.5$) blends with P2 demonstrate that acceptors with sufficiently strong self-attraction do not intercalate because of the enthalpic drive to macrophase separate. Section 3.7: Figure 3.17 shows snapshots of the P2-A4 and P2-A2 $\phi = 0.5$ blends which do not have intercalated acceptors. Radial distribution functions for the P2-A2, P2-A3, and P2-A4 blends are compared in Section 3.7: Figure 3.18, showing very few acceptor molecules in close contact with backbone beads in the non-intercalated P2-A2 and P2-A4 blends compared to in the intercalated P2-A3 blend. Similarly, simulations of immiscible acceptor A1, where $\varepsilon_{AA} = 0.5$, $\varepsilon_{AB} = 0$, and $\varepsilon_{AS} = 0$ show no intercalation. Our observations of intercalation requiring a balance of acceptor-donor miscibility and donor side chain architecture are consistent with experimental studies, which suggest fullerene-backbone van der Waals attraction facilitates intercalation in PBTTT-C14:PCBM-C70 blends[20, 55].

Donor-Acceptor Interfacial Area: As mentioned above, the strong acceptor-backbone correlation ($g_{AB}(r)$ ~0.8 in Figure 3.6f) shows that the intercalated P2-A3 blend has higher acceptor- donor backbone interfacial area than any of the other P1, P2, or P3 blends with A1, A2, or A3. To further investigate the donor-acceptor interface we quantify acceptor domain surface roughness (Section 3.7: Table 3.4). The intercalated P2-A3 blend has a higher surface roughness (≈ 0.6) in comparison to the non-intercalated blends (surface roughness ≈ 0.2-0.4). Trends in acceptor domain surface roughness for $\phi = 0.3$ blends (Section 3.7: Table 3.5) are less clear and are not compared to $\phi = 0.5$ blends because acceptors form cylindrical domains rather than slabs-like domains.

New Morphologies

In addition to reproducing morphological features that have been observed in experiments, we predict additional conditions and parameters that lead to new blend morphologies, which have not yet been observed in experiments, with characteristics that could give rise to improved photoconversion (Figure 3.7). With the strong acceptor-backbone attractive acceptors A5 ($\varepsilon_{AB} = 2.0$, $\varepsilon_{AS} = 0.1$, and $\varepsilon_{AA} = 0.5$), we find the P2 blend with $\phi_{A5} = 0.3$ equilibrates into a new structural motif in which cylinders of side chain beads are packed hexagonally at about T* = 2.0 (Figure 3.7a). The P2 donor backbones orient to form planes that arrange into a kagome lattice, with the A5 acceptors at the triangular sites of the lattice. The six-fold symmetry and layer spacing (19.4 Å) of the kagome lattice is evident in the diffraction pattern (Figure7a). Blends of P3 with $\phi_{A5} = 0.5$ form alternating layers of acceptors and polymer backbones at about T* = 2.25. From the diffraction pattern of the $\phi_{A5} = 0.5$ P3-A5 blends at T* = 1.5, the four-fold symmetry of square-packed backbones around acceptor molecules is evident (Figure 3.7b). Blends of P3-A5 with $\phi_{A5} = 0.3$ form a third new morphology (Figure 3.7c)

wherein cylinders of polymer backbones are filled with a 1D arrangement of acceptors at about T* = 2.25; with a few acceptors found outside the cylinders. The six-fold symmetry of the backbone-bead diffraction pattern reveals the long-range hexagonal ordering of the backbone cylinders. When this $\phi_{A5} = 0.3$ P3-A5 blend is cooled to T* = 1.5 the cylinders merge together to form alternating layers of oligomer backbones and acceptor molecules (Figure 3.7d). Thus, the morphology of the P3-A5 blends can be tuned with temperature and with acceptor molecule volume fraction. Additional simulations at lower volume fraction of acceptors ($\phi_{A5} = 0.2$) confirm that nearly all acceptors assemble within P3 backbone cylinders when there are fewer excess acceptors. The P2-A5 $\phi_{A5} = 0.3$, P3-A5 $\phi_{A5} = 0.5$ and P3-A5 $\phi_{A5} = 0.3$ blends have ordered donor domains with high interfacial area between acceptors and backbone beads as shown by a significant increase in first peak height in $g_{AB}(r) \approx 4.5$ (Figure 3.7e) compared to A2 and A3 blends where the first peak height of $g_{AB}(r) \approx 0.8$ (Figure 3.6c and f). Comparisons of acceptor domain surface roughness are not applicable between these A5 blends because the shapes of the acceptor aggregates vary too widely between structures to make the comparison meaningful. Acceptor domain surface roughness values are for these blends are included for completeness in Section 3.7.3 Table 3.6.

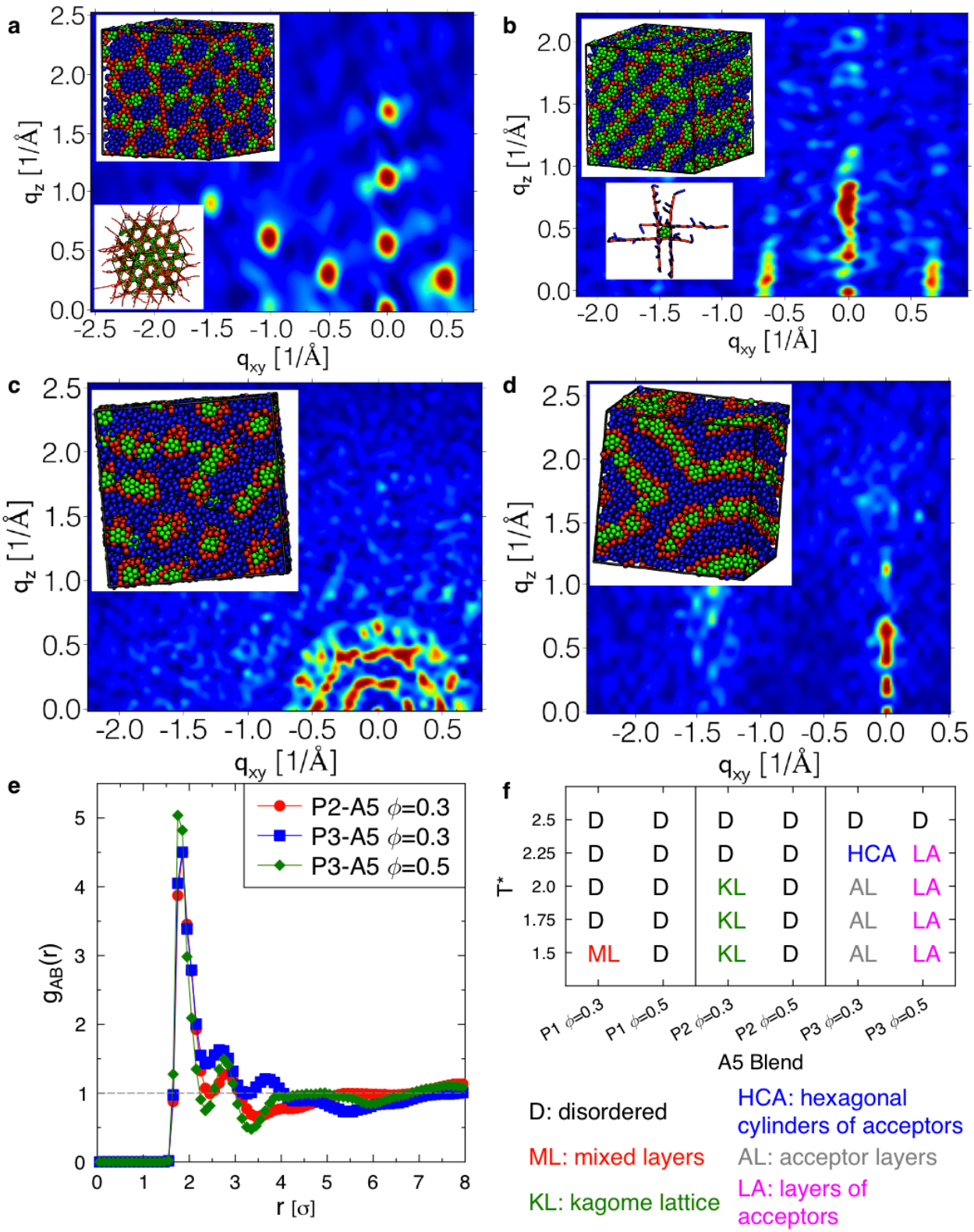
a
b
c
d
e
f
q_z [1/Å]
q_{xy} [1/Å]
$g_{AB}(r)$
r [σ]
P2-A5 ϕ=0.3
P3-A5 ϕ=0.3
P3-A5 ϕ=0.5
T*
A5 Blend
P1 ϕ=0.3
P1 ϕ=0.5
P2 ϕ=0.3
P2 ϕ=0.5
P3 ϕ=0.3
P3 ϕ=0.5
D: disordered
ML: mixed layers
KL: kagome lattice
HCA: hexagonal cylinders of acceptors
AL: acceptor layers
LA: layers of acceptors

FIGURE 3.7: a) Diffraction pattern of kagome lattice formed by planes of aligned conjugated backbones in P2-A5 $\phi = 0.3$ at T* = 2.0 (snapshot, inset top) and with side chains removed for clarity (inset bottom). **b)** Diffraction pattern of square-lattice backbones among layers of acceptors in P3-A5 at T* =1.5 (snapshot, inset, top). **c)** Diffraction pattern of hexagonally packed donor-acceptor cylinders with the acceptors filling the polymer backbone cylinders in the P3-A5 $\phi = 0.3$ blend at T* = 2.25 (snapshot, inset). **d)** Diffraction pattern of layers formed when the hexagonally packed cylinders from (c) merge at T* = 1.5 (snapshot, inset). **e)** Acceptor-backbone radial distribution function as a function of distance between acceptor centers of mass and backbone beads, r, for P2-A5 $\phi = 0.3$, P3-A5 $\phi = 0.3$, and P3-A5 $\phi = 0.5$ blends at T* = 1.5. **f)** Phase diagram for A5 blends with P1, P2, and P3.

Large interfacial area blends, such as the A5 blends presented here, could improve organic solar cell performance if the high interfacial areas are matched with large connected domains of both acceptor and donor molecules[1-5]. Section 3.7: Figure 3.19 shows $g_{BB}(r)$ and $g_{AA}(r)$ at T* = 1.5 for these A5 blends. The P2-A5 $\phi_{A5} = 0.3$ and P3-A5 $\phi_{A5} = 0.5$ blends demonstrate relatively low acceptor aggregation, as evidenced by the lack of distinct peaks in $g_{AA}(r)$, because acceptors are interspersed in a lattice of backbones in both cases. Acceptor order is higher for the P3-A5 $\phi_{A5} = 0.3$ at T* = 1.5 because acceptors are arranged in layers surrounded by backbones. Backbone-backbone positional order is similar between the P2-A5 $\phi_{A5} = 0.3$, P3-A5 $\phi_{A5} = 0.5$ and P3-A5 $\phi_{A5} = 0.3$ blends at T* = 1.5 and lower than that of blends with A1, A2, and A3 acceptors because these A5 blends do not have large acceptor aggregates to confine the polymer and facilitate backbone order. Nevertheless, all of the A5 blend structures presented here have backbone domains that span at least one dimension of the periodic box, and should therefore satisfy the connectivity (and in turn continuous charge transport) constraint. Of all of the morphologies observed in this work, the P3-A5 $\phi_{A5} = 0.3$ morphologies at T* = 2.25 and T* = 1.5 best fulfill the desirable combination of high interfacial area between donors and acceptors coupled with highly connected domains or continuous pathways.

3.4 CONCLUSIONS

In this paper, we have performed coarse-grained molecular dynamics simulations of conjugated polymer-fullerene derivative blends using realistic coarse-grained models on graphics processing units using HOOMD-Blue. The morphologies obtained using our approach for neat systems (no acceptors) of polymers mimicking P3HT and PDBHT are in agreement with experimental measurements[45,46]. We have systematically studied a large set of blends of acceptors and polymers by varying polymer architecture, acceptor miscibility, and blend composition and demonstrated the effect of these parameters on polymer-acceptor blend morphology.

We find that neat polymers can self-assemble to form lamellae or a hexagonally-packed cylinders, which is consistent with experiments[46]. The order-disorder transition temperature (ODT) of the neat polymer systems depends on side chain spacing and orientation on the polymer backbone. Adding immiscible acceptors (A1) shifts the order-disorder transition of the polymers to a higher temperature and increases backbone-backbone positional order compared to neat polymer due to confinement effects. Immiscible acceptors (A1) do not significantly change oligomer morphologies from those observed in the neat case. The ODT of blends with miscible acceptors (A2 and A3) is dependent on the complicated interplay between entropy and enthalpy governing self-assembly**.** Weakly miscible acceptors (A2) disrupt the cylindrical order found for P3 and increase acceptor-backbone correlation but otherwise do not significantly change polymer morphology from the cases of neat polymer and immiscible acceptors. In blends of strongly miscible acceptors (A3) we see acceptor intercalation between side chains of conjugated polymer molecules (P2) if there is sufficient space between adjacent side chains to allow for the presence of an acceptor molecule and sufficient acceptor-backbone attraction which is in

agreement with experiments[20, 55]. Intercalated blends (P2-A3) have increased acceptor-backbone interfacial area compared to non-intercalated blends. At intermediate temperatures, blends with strongly miscible acceptors (A3) have some disordered polymer chains within the acceptor domains while blends with weakly miscible and immiscible acceptors do not. High acceptor-backbone attraction (A5) allows for the formation of novel blend morphologies such as cylinders of acceptors surrounded by backbones and a lattice of polymer backbones, depending on polymer architecture and acceptor volume fraction. The P3-A5 $\phi = 0.3$ blends shows both high interfacial area and high levels of acceptor-acceptor and backbone-backbone correlations which could be beneficial for organic photovoltaic photoconversion[1-5].

Limitations: While computationally efficient and successful in capturing the morphology of acceptor-donor blends, this work is limited to chain lengths in the oligomer regime. Molecular weights or chain lengths much longer than the 15-monomer oligomers are experimentally relevant and are expected to fold into long, ribbon-like fibrils[56,57], or form entangled amorphous regions between crystalline domains[58]. For the oligomers studied here, the persistence lengths of 12.5 to 20 monomers are on the order of the length of the backbone, and it is possible that structure and thermodynamics may differ for fully flexible chains. The increase in packing fraction that occurs as temperature is decreased in this work is qualitatively analogous to the compression that occurs during solvent evaporation in the synthesis of some active layers, but future work mapping solvent evaporation schedules to temperature and pressure schedules is warranted. This work does not provide detailed analysis of how changing overall packing fractions may shift phase transition boundaries, but our preliminary results suggest the morphologies observed here are relatively insensitive to changes in volume fraction of 20% and changes in pressure by a factor of 100.

Strengths: The ability of our coarse-grained model to reproduce complex self-assembled structures observed in experiments demonstrates that atomistic simulations are not always necessary, especially if the goal is to identify trends in how donors and acceptors self-assemble into ordered active-layer morphology for a wide range of physical and chemical features of the donor and acceptors. More importantly, the capability to perform simulations over a wide range of conditions is essential for creating universal design rules and guiding synthesis of donors and acceptors to achieve optimal morphology. Our work here highlights molecular features (acceptor-backbone attractions and side chain orientation of donor polymers) that produce the high interfacial area and continuous pathways in the active layer that is accepted to be optimal for bulk heterojunction device efficiency. The GPU hardware used here, and newer, faster hardware are exciting for their ability to simulate larger systems or systems with additional details (e.g., adding coarse-grained beads representing the shapes and interactions of the fullerene functional groups, or beads representing chemical and physical features of substrates/electrode surfaces), and helps shorten the design-build-test cycle between theory and experiment. Computationally aided materials design, as done in this paper, accelerates engineering of improved organic solar materials and other advanced materials, thus positively impacting cleaner energy applications.

3.5 ACKNOLEDGEMENTS

This work was supported by Department of Energy under Grant No. DE-SC0003912. Portions of this research used resources of the National Energy Research Scientific Computing Center, which is supported by the Office of Science of the U.S. Department of Energy under Contract No. DE-AC02-05CH11231. Portions of this work utilized the Janus supercomputer, which is supported by the National Science Foundation (award number CNS-0821794) and the

University of Colorado Boulder. The Janus supercomputer is a joint effort of the University of Colorado Boulder, the University of Colorado Denver and the National Center for Atmospheric Research. Janus is operated by the University of Colorado Boulder. We also thank Michael Engel, whose visualization software provided the basis for our diffraction pattern routines.

3.6 REFERENCES

1. Slota, J. E.; He, X. M.; Huck, W. T. S. *Nano Today* **2010,** 5, (3), 231-242.

2. Ruderer, M. A.; Muller-Buschbaum, P. *Soft Matter* **2011,** 7, (12), 5482-5493.

3. Brady, M. A.; Su, G. M.; Chabinyc, M. L. *Soft Matter* **2011,** 7, (23), 11065-11077.

4. Deibel, C.; Dyakonov, V. *Reports on Progress in Physics* **2010,** 73, (9), 39.

5. Zhou, H. X.; Yang, L. Q.; You, W. *Macromolecules* **2012,** 45, (2), 607-632.

6. Treat, N. D.; Varotto, A.; Takacs, C. J.; Batara, N.; Al-Hashimi, M.; Heeney, M. J.; Heeger, A. J.; Wudl, F.; Hawker, C. J.; Chabinyc, M. L. *Journal of the American Chemical Society* **2012,** 134, (38), 15869-15879.

7. Kim, K. H.; Kang, H.; Kim, H. J.; Kim, P. S.; Yoon, S. C.; Kim, B. J. *Chemistry of Materials* **2012,** 24, (12), 2373-2381.

8. Shin, W. S.; Lee, J. C.; Kim, J. R.; Lee, H. Y.; Lee, S. K.; Yoon, S. C.; Moon, S. J. *Journal of Materials Chemistry* **2011,** 21, (4), 960-967.

9. Kastner, C.; Susarova, D. K.; Jadhav, R.; Ulbricht, C.; Egbe, D. A. M.; Rathgeber, S.; Troshin, P. A.; Hoppe, H. *Journal of Materials Chemistry* **2012,** 22, (31), 15987-15997.

10. Yin, W.; Dadmun, M. *Acs Nano* **2011,** 5, (6), 4756-4768.

11. Kozub, D. R.; Vakhshouri, K.; Orme, L. M.; Wang, C.; Hexemer, A.; Gomez, E. D. *Macromolecules* **2011,** 44, (14), 5722-5726.

12. Pfannmoller, M.; Flugge, H.; Benner, G.; Wacker, I.; Sommer, C.; Hanselmann, M.; Schmale, S.; Schmidt, H.; Hamprecht, F. A.; Rabe, T.; Kowalsky, W.; Schroder, R. R. *Nano Letters* **2011,** 11, (8), 3099-3107.

13. Schmidt-Hansberg, B.; Sanyal, M.; Klein, M. F. G.; Pfaff, M.; Schnabel, N.; Jaiser, S.; Vorobiev, A.; Muller, E.; Colsmann, A.; Scharfer, P.; Gerthsen, D.; Lemmer, U.; Barrena, E.; Schabel, W. *Acs Nano* **2011,** 5, (11), 8579-8590.

14. Carbonnier, B.; Egbe, D. A. M.; Birckner, E.; Grummt, U. W.; Pakula, T. *Macromolecules* **2005,** 38, (18), 7546-7554.

15. Gadisa, A.; Oosterbaan, W. D.; Vandewal, K.; Bolsee, J. C.; Bertho, S.; D'Haen, J.; Lutsen, L.; Vanderzande, D.; Manca, J. V. *Advanced Functional Materials* **2009,** 19, (20), 3300-3306.

16. Sista, P.; Xue, B. F.; Wilson, M.; Holmes, N.; Kularatne, R. S.; Nguyen, H.; Dastoor, P. C.; Belcher, W.; Poole, K.; Janesko, B. G.; Biewer, M. C.; Stefan, M. C. *Macromolecules* **2012,** 45, (2), 772-780.

17. Ren, G. Q.; Wu, P. T.; Jenekhe, S. A. *Chemistry of Materials* **2010,** 22, (6), 2020-2026.

18. Wu, P. T.; Ren, G. Q.; Jenekhe, S. A. *Macromolecules* **2010,** 43, (7), 3306-3313.

19. Ho, V.; Boudouris, B. W.; Segalman, R. A. *Macromolecules* **2010,** 43, (19), 7895-7899.

20. Miller, N. C.; Cho, E.; Gysel, R.; Risko, C.; Coropceanu, V.; Miller, C. E.; Sweetnam, S.; Sellinger, A.; Heeney, M.; McCulloch, I.; Bredas, J. L.; Toney, M. F.; McGehee, M. D. *Advanced Energy Materials* **2012,** 2, (10), 1208-1217.

21. Mayer, a. C.; Toney, M. F.; Scully, S. R.; Rivnay, J.; Brabec, C. J.; Scharber, M.; Koppe, M.; Heeney, M.; McCulloch, I.; McGehee, M. D. *Advanced Functional Materials* **2009,** 19, (8), 1173-1179.

22. Vakhshouri, K.; Kozub, D. R.; Wang, C. C.; Salleo, A.; Gomez, E. D. *Physical Review Letters* **2012,** 108, (2), 5.

23. Cates, N. C.; Gysel, R.; Dahl, J. E. P.; Sellinger, A.; McGehee, M. D. *Chemistry of Materials* **2010,** 22, (11), 3543-3548.

24. Agarwal, U.; Escobedo, F. A. *Nature Materials* **2011,** 10, (3), 230-235.

25. Lee, C. K.; Pao, C. W.; Chu, C. W. *Energy & Environmental Science* **2011,** 4, (10), 4124-4132.

26. Haji-Akbari, A.; Engel, M.; Keys, A. S.; Zheng, X. Y.; Petschek, R. G.; Palffy-Muhoray, P.; Glotzer, S. C. *Nature* **2009,** 462, (7274), 773-U91.

27. Glotzer, S. C.; Solomon, M. J. *Nature Materials* **2007,** 6, (8), 557-562.

28. Cheung, D. L.; McMahon, D. P.; Troisi, A. *Journal of Physical Chemistry B* **2009,** 113, (28), 9393-9401.

29. Saba, M. I.; Melis, C.; Colombo, L.; Malloci, G.; Mattoni, A. *Journal of Physical Chemistry C* **2011,** 115, (19), 9651-9655.

30. Melis, C.; Colombo, L.; Mattoni, A. *Journal of Physical Chemistry C* **2011,** 115, (2), 576-581.

31. Meredig, B.; Salleo, A.; Gee, R. *Acs Nano* **2009,** 3, (10), 2881-2886.

32. Huang, D. M.; Faller, R.; Do, K.; Moule, A. J. *Journal of Chemical Theory and Computation* **2010,** 6, (2), 526-537.

33. Huang, D. M.; Moule, A. J.; Faller, R. *Fluid Phase Equilibria* **2011,** 302, (1-2), 21-25.

34. Schwarz, K. N.; Kee, T. W.; Huang, D. M. *Nanoscale* **2013**.

35. Lee, C. K.; Hua, C. C.; Chen, S. A. *Macromolecules* **2013,** 46, (5), 1932-1938.

36. Lee, C. K.; Pao, C. W. *Journal of Physical Chemistry C* **2012,** 116, (23), 12455-12461.

37. Marsh, H. S.; Jayaraman, A. *Journal of Polymer Science Part B: Polymer Physics* **2013,** 51, 64-77.

38. Anderson, J. A.; Lorenz, C. D.; Travesset, A. *Journal of Computational Physics* **2008,** 227, (10), 5342-5359.

39. Nguyen, T. D.; Phillips, C. L.; Anderson, J. A.; Glotzer, S. C. *Computer Physics Communications* **2011,** 182, (11), 2307-2313.

40. Brown, W. M.; Wang, P.; Plimpton, S. J.; Tharrington, A. N. *Computer Physics Communications* **2011,** 182, (4), 898-911.

41. Anderson, J.; Jankowski, E.; Grubb, T.; Engel, M.; Glotzer, S. **2012**.

42. Gotz, A. W.; Williamson, M. J.; Xu, D.; Poole, D.; Le Grand, S.; Walker, R. C. *Journal of Chemical Theory and Computation* **2012,** 8, (5), 1542-1555.

43. Stone, J. E.; Phillips, J. C.; Freddolino, P. L.; Hardy, D. J.; Trabuco, L. G.; Schulten, K. *Journal of Computational Chemistry* **2007,** 28, (16), 2618-2640.

44. Curtarolo, S.; Hart, G.; Nardelli, M.; Mingo, N.; Sanvito, S.; Levy, O. *Nature Materials* **2013,** 12, 191-201.

45. Prosa, T. J.; Winokur, M. J.; Moulton, J.; Smith, P.; Heeger, A. J. *Macromolecules* **1992,** 25, (17), 4364-4372.

46. Ko, S. W.; Hoke, E. T.; Pandey, L.; Hong, S. H.; Mondal, R.; Risko, C.; Yi, Y. P.; Noriega, R.; McGehee, M. D.; Bredas, J. L.; Salleo, A.; Bao, Z. A. *Journal of the American Chemical Society* **2012,** 134, (11), 5222-5232.

47. Kline, R. J.; McGehee, M. D.; Kadnikova, E. N.; Liu, J. S.; Frechet, J. M. J.; Toney, M. F. *Macromolecules* **2005,** 38, (8), 3312-3319.

48. Verlet, L. *Physical Review* **1967,** 159, (1), 98-&.

49. Weeks, J. D.; Chandler, D.; Andersen, H. C. *Journal of Chemical Physics* **1971,** 54, (12), 5237-+.

50. Zhang, Z.; Guo, H. *The Journal of chemical physics* **2010,** 133, (14), 144911-144911.

51. Leach, A. E., *Molecular Modelling: Principles and Applications* 1ed.; Longman: Essex, 1996.

52. Humphrey, W.; Dalke, A.; Schulten, K. *Journal of Molecular Graphics & Modelling* **1996,** 14, (1), 33-38.

53. Triplett, D. A.; Fichthorn, K. A. *Physical Review E* **2008,** 77, (1).

54. Hooper, J. B.; Schweizer, K. S. *Macromolecules* **2006,** 39, (15), 5133-5142.

55. Miller, N. C.; Cho, E.; Junk, M. J. N.; Gysel, R.; Risko, C.; Kim, D.; Sweetnam, S.; Miller, C. E.; Richter, L. J.; Kline, R. J.; Heeney, M.; McCulloch, I.; Amassian, A.; Acevedo-Feliz, D.; Knox, C.; Hansen, M. R.; Dudenko, D.; Chmelka, B. F.; Toney, M. F.; Bredas, J. L.; McGehee, M. D. *Advanced Materials* **2012,** 24, (45), 6071-+.

56. Mena-Osteritz, E.; Meyer, A.; Langeveld-Voss, B. M. W.; Janssen, R. A. J.; Meijer, E. W.; Bäuerle, P. *Angewandte Chemie* **2000,** 112, (15), 2791-2796.

57. Liu, J. H.; Arif, M.; Zou, J. H.; Khondaker, S. I.; Zhai, L. *Macromolecules* **2009,** 42, (24), 9390-9393.

58. Brinkmann, M.; Rannou, P. *Macromolecules* **2009,** 42, (4), 1125-1130.

3.7 SUPPORTING INFORMATION

3.7.1 Model and Simulation

Three polymer architectures are created through the different connection of backbone (red) and side-chain (blue) beads (Figure 3.8). Harmonic potentials are used to model bond stretching constraints ($U_{bond} = k_{bond}(l - l_0)^2$), angle bending constraints ($U_{angle} = k_{angle}(\theta - \theta_0)^2$), and dihedral angle twisting constraints ($U_{di} = k_{di}(\phi - \phi_0)^2$). The harmonic bond spring constant is $k_{bond} = 50\ \varepsilon/\sigma^2$ for all bonded pairs. Three different angle constraints with equilibrium angles $\alpha = 3.14$, $\beta = 2.13$, and $\gamma = 1.45$ are used to enforce backbone straightness and side-chain extension angle (Figure 3.S.0). The spring constants for all angle constraints is $k_{angle} = 6\ \varepsilon/\text{radian}^2$, except the constraint among three backbone beads, which is $30\ \varepsilon/\text{radian}^2$.

The three polymers differ in the harmonic dihedral angle potentials constraining neighboring side-chains (Figure 3.S.0). Polymer 1 is constrained only with dihedral angle A, which has equilibrium angle 3.14 and spring constant $10\ \varepsilon/\text{radian}^2$. Polymer 2 is constrained by

dihedral angles B (equilibrium angle 0, spring constant 50 ε/radian^2) and C (equilibrium angle 3.14, spring constant 50 ε/radian^2). Polymer 3 is constrained by dihedral angle D (equilibrium angle 0, spring constant 10 ε/radian^2).

Acceptor molecules are modeled by 13 spherical beads held together as a rigid body, with relative [X, Y, Z] coordinates:

[-0.9651261 0.00682599 2.84218764]

[-2.95201588 0.07019005 0.53969657]

[2.97152662 -0.09280338 -0.41340506]

[1.61092079 -1.56430364 1.9922123]

[-1.26122427 -2.50876784 1.06083286]

[1.24921405 2.4505167 -1.20179749]

[1.13477838 -2.6238873 -0.91519409]

[1.68328679 1.5256567 1.96217287]

[0.99170464 -0.16791122 -2.82807803]

[-1.52378225 1.46814334 -2.12860489]

[-1.67226791 -1.61901844 -1.89550781]

[-1.2243228 2.6015029 0.86137301]

[0. 0. 0.]

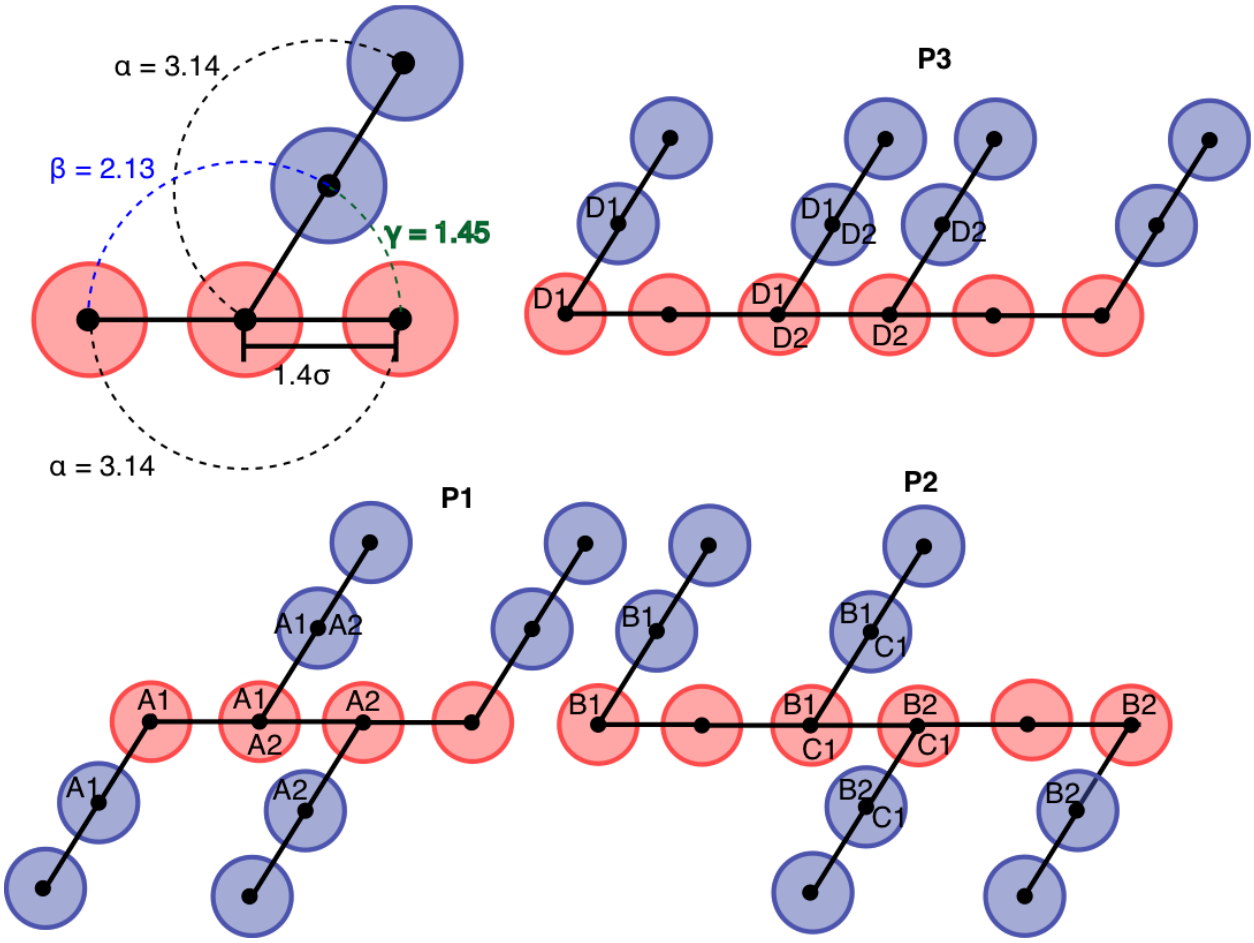

FIGURE 3.8: Polymer architecture details.

Backbone beads are colored red, side-chain beads are colored blue, and bonds between beads are denoted by black lines. All three polymers share the same bond lengths (1.4σ, upper left) between connected beads. The angle constraints are also the same for all three polymers (α = 3.14, β = 2.13, and γ =1.45, upper left). Angle α spans three neighboring backbone beads and is also used for two side-chain beads and their connecting backbone bead. Angle β is between the first bead of a side-chain, its backbone connection, and the backbone bead with the next-lowest index. Angle γ is between a side-chain, its backbone connection, and the backbone bead with the next-highest index. Quadruplets of particles comprising a dihedral angle constraint are

marked with the same labels (A1, B2, etc). The letter denotes the dihedral type (A, B, C, or D), and the number distinguishes separate dihedrals of the same type on the same polymer.

The five acceptor molecule types are distinguished by their Lennard-Jones (LJ) interaction well depths. The well depth between acceptor beads (A), backbone beads (B), and side-chain beads (S) are denoted by ε_{ij} where i and j indicate two bead species, and are expressed in units of ε (Table 3.2). The LJ potential is truncated and shifted to zero at $r_{cut} = 2.5$, and the force is smoothed to zero at r_{cut}. An epsilon $\varepsilon_{ij} = 0$ indicates species i and j interact via the Weeks-Chandler-Andersen (WCA) potential, which models excluded volume only (no attraction).

TABLE 3.2: Lennard-Jones well depths for different acceptor types

	ε_{AA}	ε_{AB}	ε_{AS}
A1 – immiscible	0.5	0	0
A2 - weakly miscible	0.5	1.0	0.1
A3 - miscible	0.1	1.0	0.1
A4 - weak backbone attraction	0.1	0.1	0.1
A5 – strong backbone attraction	0.5	2.0	0.1

TABLE 3.3: Lennard-Jones well depths for donor molecule constituents

	B	S
B	$\varepsilon_{BB} = 2.0$	$\varepsilon_{BS} = 0$
S	$\varepsilon_{BS} = 0$	$\varepsilon_{SS} = 0.1$

Simulations are initialized by placing 250 donor molecule chains randomly in a cubic simulation box with side length L = 300, along with the appropriate number of acceptor molecules. The donor chains are initially wrapped in a spiral to help with placement, so initial randomization of all degrees of freedom is accomplished by performing 1e7 steps in which the interactions between each bead species is the WCA potential at T* = 2.5 and P* = 0.1. The Nose-Hoover thermostat and Anderson barostat are used to maintain temperature and pressure. The velocity Verlet algorithm is used to update particle positions and velocities between time steps. A step-size dt = 0.00035τ is used, corresponding to 0.79 femtoseconds. Note that for blends of P3-A3, a step size of dt = 0.0004τ is used.

3.7.2 Measuring equilibration

In practice it is easy to show that a sequence of configurations from a molecular dynamics or Monte Carlo simulation do not represent an equilibrium distribution, but it is more difficult to prove that an ensemble of configurations is indeed the equilibrium distribution. Here we use a heuristic to select a portion of the simulation trajectory with a stable average potential energy and at least twenty statistically independent configurations as measured by the potential energy autocorrelation function. We output thermodynamic observables including potential energy, kinetic energy, temperature, pressure, and volume with a frequency of once every 1e5 time steps. To select the portion of the trajectory over which the autocorrelation function is calculated, we define a sample window size W, and average W of the last potential energy samples. We then check the previous window of W samples; it is included if its average and standard deviation overlap with the first sample. This process is repeated until a window whose average and standard deviation do not lie within the average and standard deviation of the first window sampled, or until the entire trajectory is included. We check the windowing operation

for window sizes W = {5, 10, 20, 50, 100}. If at least three window sizes do not agree on the length of the sampling window, we consider the system unequilibrated and continue running. Once a window into the potential energy time series is selected, we calculate the correlation time by finding the first lag dt at which the correlation function

$$C(dt) = \frac{\left\langle \left(PE(t) - \overline{PE}\right)\left(PE(t+dt) - \overline{PE}\right) \right\rangle}{\sigma^2}$$

is less than or equal to zero. Here, σ^2 is the variance of the window into the potential energy time series PE(t). The number of samples in the window divided by the correlation time yields the number of independent samples that can be included in an ensemble average.

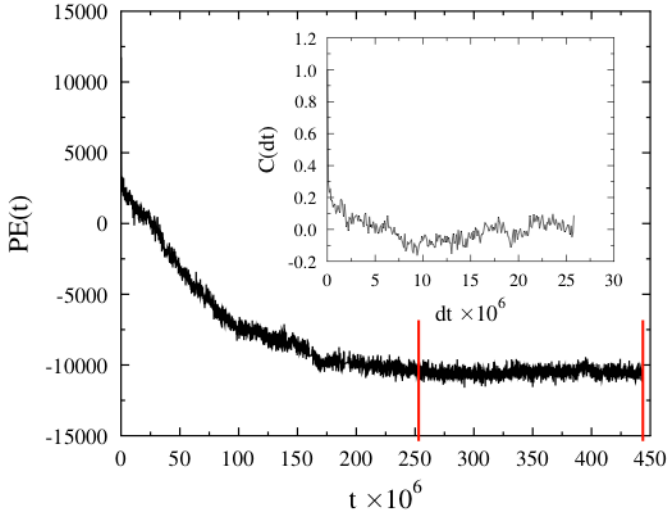

FIGURE 3.9: Potential energy time series, with equilibrated window indicated by red lines. Potential energy autocorrelation function for the indicated time window is inset. Units of time are time steps.

3.7.3 Additional Results

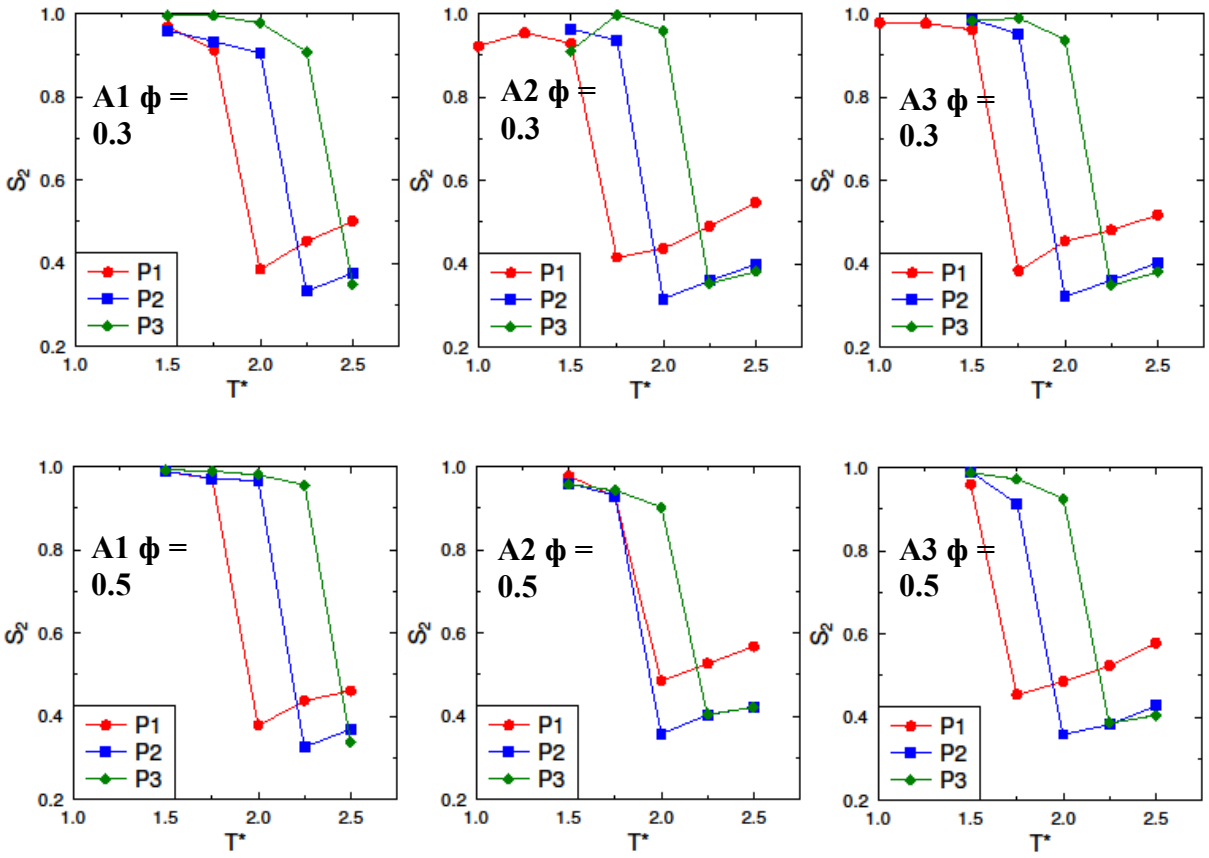

FIGURE 3.10: Orientational order parameter, S_2, as a function of reduced temperature, T*, for blends with acceptors A1 (left), A2 (center), and A3 (right) and ϕ = 0.3 (top) and 0.5 (bottom).

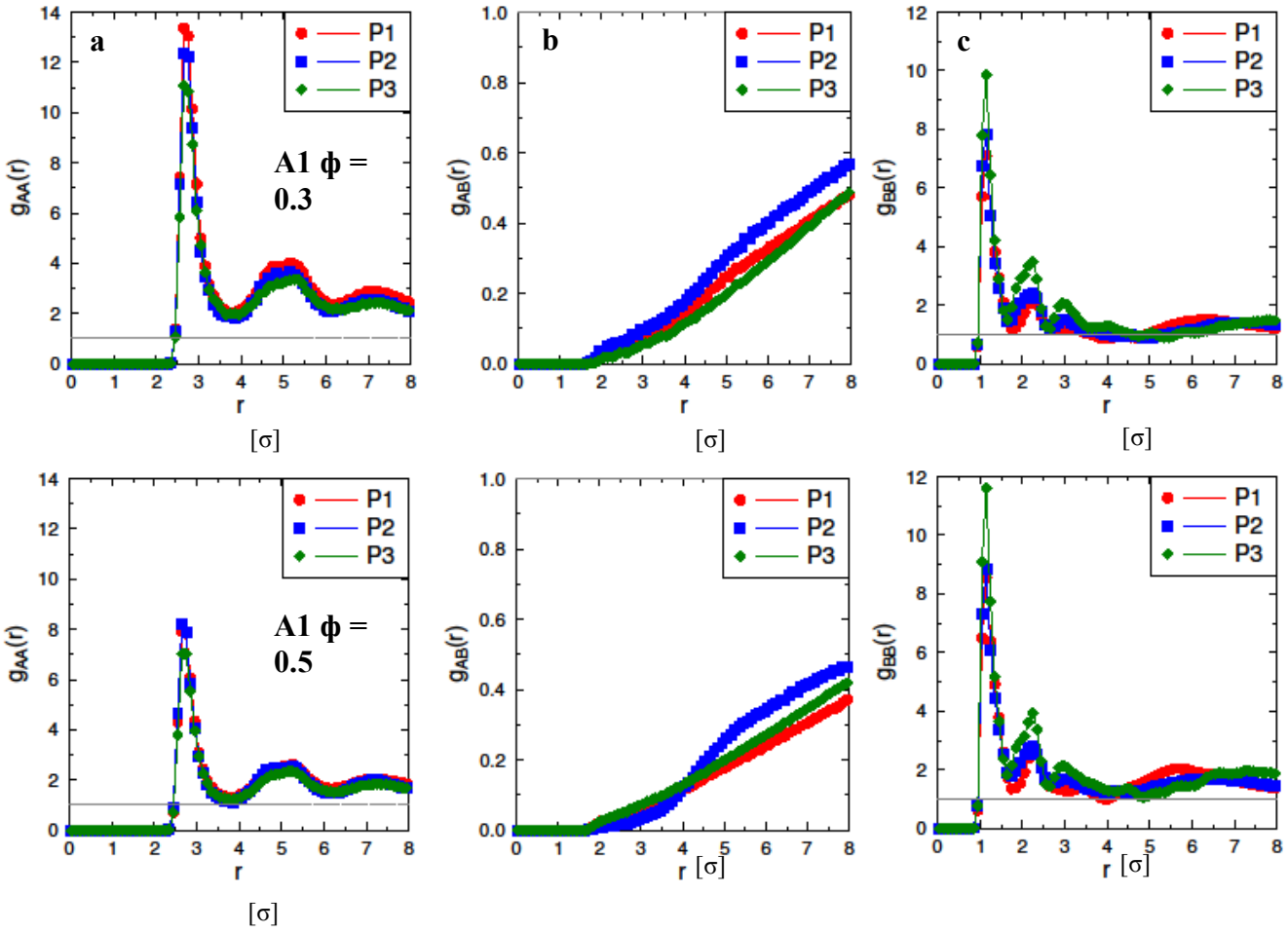

FIGURE 3.11: **a)** Acceptor-acceptor radial distribution function as a function of distance between acceptor centers of mass, r, **b)** acceptor-backbone radial distribution function as a function of distance between acceptor centers of mass and backbone beads, r, and **c)** backbone-backbone radial distribution function as a function of distance between backbone beads, r, for ϕ = 0.3 (top) and ϕ = 0.5 (bottom) blends with immiscible acceptors, A1, at T* = 1.5.

The $g_{AA}(r)$ and $g_{AB}(r)$ plots show that acceptor aggregation and acceptor-backbone correlation do not change with polymer architecture. Backbone correlation is higher for P3 blends because P3 side chains are all on one side of the backbone, facilitating alignment. Comparing ϕ = 0.3 and ϕ = 0.5 blends, trends are similar but acceptor aggregation is higher for ϕ = 0.3 blends because of packing within the aggregate. Acceptors pack more tightly on the surface of aggregates and ϕ = 0.3 blends have a higher ratio of acceptors on the aggregate

surface to acceptors in the aggregate bulk than do ϕ = 0.5 blends, leading to higher $g_{AA}(r)$ values for ϕ = 0.3 blends. Backbones are more ordered in ϕ = 0.5 blends than in ϕ = 0.3 blends because the larger acceptor aggregate in ϕ = 0.5 blends imposes a higher packing constraint on the backbones, facilitating alignment.

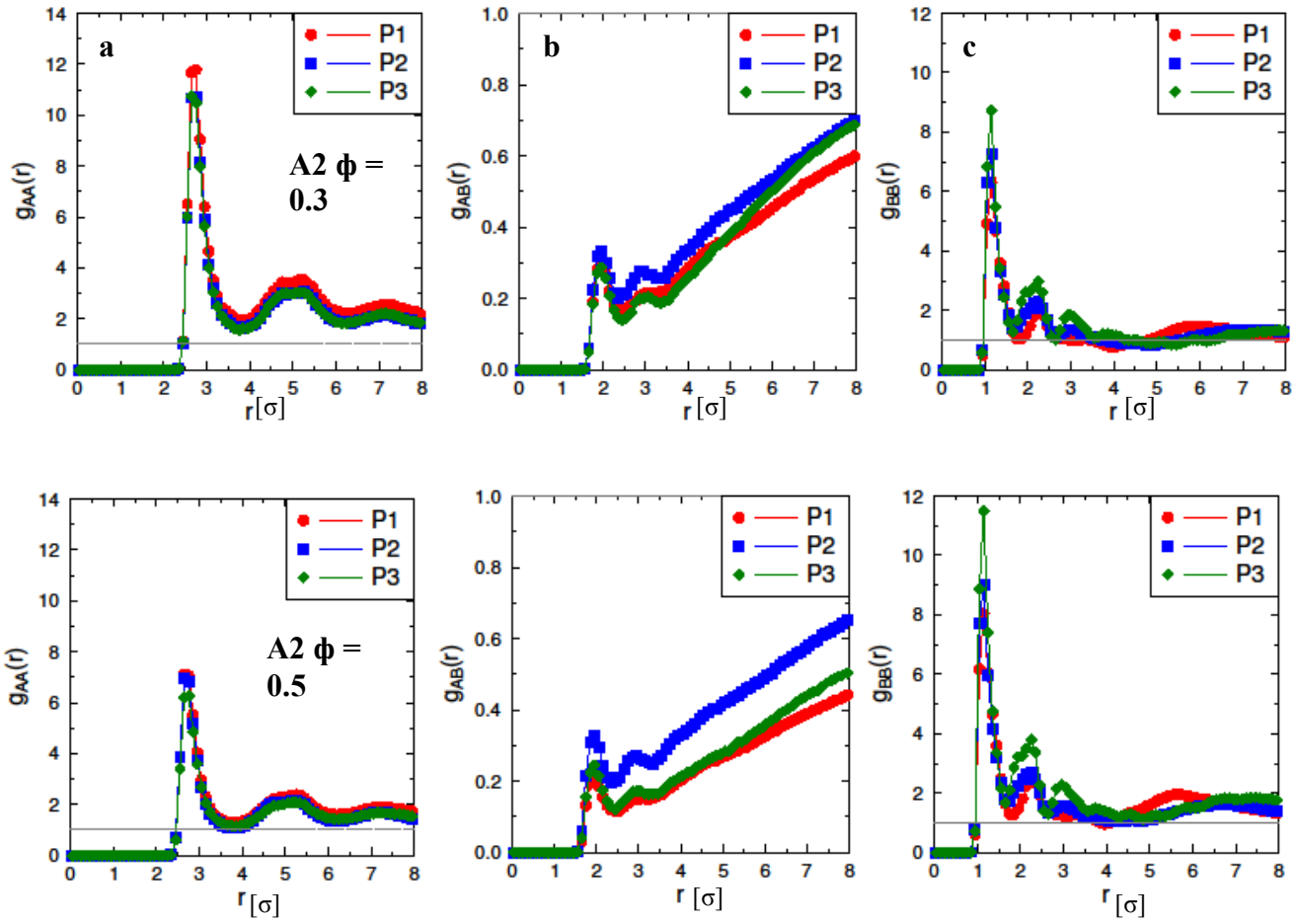

FIGURE 3.12: **a)** Acceptor-acceptor radial distribution function as a function of distance between acceptor centers of mass, r, **b)** acceptor-backbone radial distribution function as a function of distance between acceptor centers of mass and backbone beads, r, and **c)** backbone-backbone radial distribution function as a function of distance between backbone beads, r, for ϕ = 0.3 (top) and ϕ = 0.5 (bottom) blends with acceptors A2 at T* = 1.5.

The $g_{AA}(r)$ and $g_{AB}(r)$ plots show that acceptor aggregation and acceptor-backbone correlation do not change with polymer architecture. Backbone correlation is higher for P3

blends because P3 side chains are all on one side of the backbone, facilitating alignment. Acceptor aggregation is similar for A1 and A2 blends because at low temperatures, A2 molecules form large aggregates similar to in the case of A1 blends. ϕ = 0.3 and ϕ = 0.5 show the same trends, but acceptor aggregation is higher and backbone positional order is lower for ϕ = 0.3 blends than in ϕ = 0.5 blends as discussed in Figure 3.11.

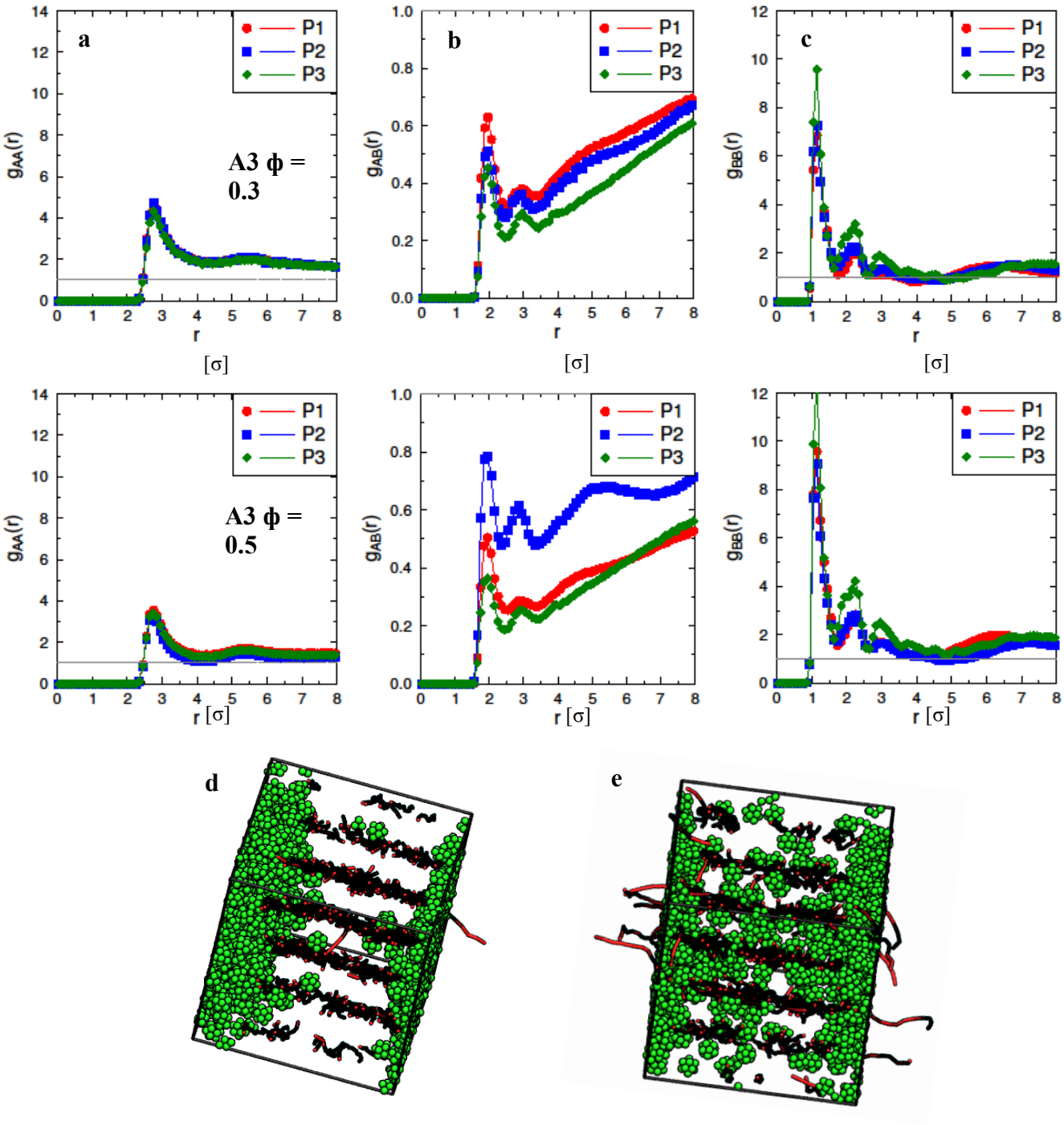

FIGURE 3.13: **a)** Acceptor-acceptor radial distribution function as a function of distance between acceptor centers of mass, r, **b)** acceptor-backbone radial distribution function as a function of distance between acceptor centers of mass and backbone beads, r, and **c)** backbone-backbone radial distribution function as a function of distance between backbone beads, r, for ϕ = 0.3 (top) and ϕ = 0.5 (bottom) blends with immiscible acceptors A3 at T* = 1.5. Snapshots of **d)** P2-A3 ϕ = 0.3 blend at T* = 1.5 showing that there is limited intercalation at low temperature for this blend and **e)** P2-A3 ϕ = 0.3 blend at T* = 1.75 showing that there are more acceptors intercalated at this temperature compared to T* = 1.5. Side chains are hidden for clarity.

The $g_{AB}(r)$ plots show evidence for limited intercalation in the P2-A3 ϕ = 0.3 because of low AB correlation. The AB correlation is much higher in the P2-A3 ϕ = 0.5 blend at T* = 1.5. The $g_{AA}(r)$ plots show that acceptor aggregation and acceptor-backbone correlation do not change with polymer architecture. Acceptor aggregation is lower for A3 blends then for blends with A1 (Figure 3.11) and A2 (Figure 3.12) because of decreased acceptor-acceptor attraction (ε_{AA} = 0.1 for A3 and ε_{AA} = 0.5 for A1 and A2). Backbone correlation is higher for P3 because P3 side chains are all on one side of the backbone, facilitating alignment. Backbone positional order is slightly higher for A3 blends than for A1 (Figure 3.11) and A2 (Figure 3.12) blends because acceptors are less tightly packed in A3 blends, creating a larger aggregate and more confinement for polymer backbones.

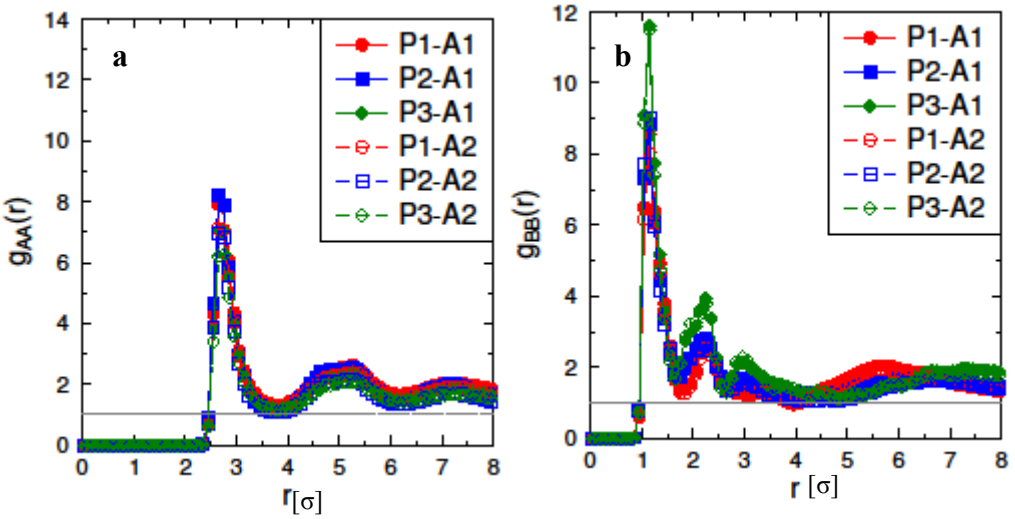

FIGURE 3.14: **a)** Acceptor-acceptor radial distribution function as a function of distance between acceptor centers of mass, r, and **b)** backbone-backbone radial distribution function as a function of distance between backbone beads, r, for ϕ = 0.5 blends of P1 and P2 and P3 with acceptors A1 and A2 at T* = 1.5.

The acceptor-backbone radial distribution function is shown in Figure 3.6 of the main text. Acceptor-acceptor aggregation and backbone positional order do not change significantly between A1 and A2 blends. Acceptors form a large aggregate at low temperature in both cases.

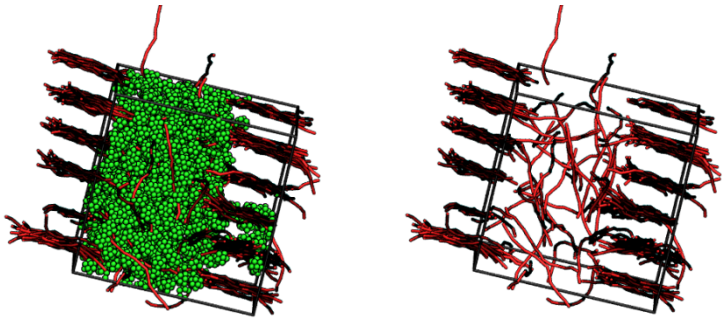

FIGURE 3.15: Snapshot of P3-A3 blend at T* = 2.0 with side chains hidden for clarity showing disordered regions in the oligomers (right), and as a result, a mixed, amorphous domain of polymer and acceptor (left) forming in A3 blends. Side chains are hidden for clarity.

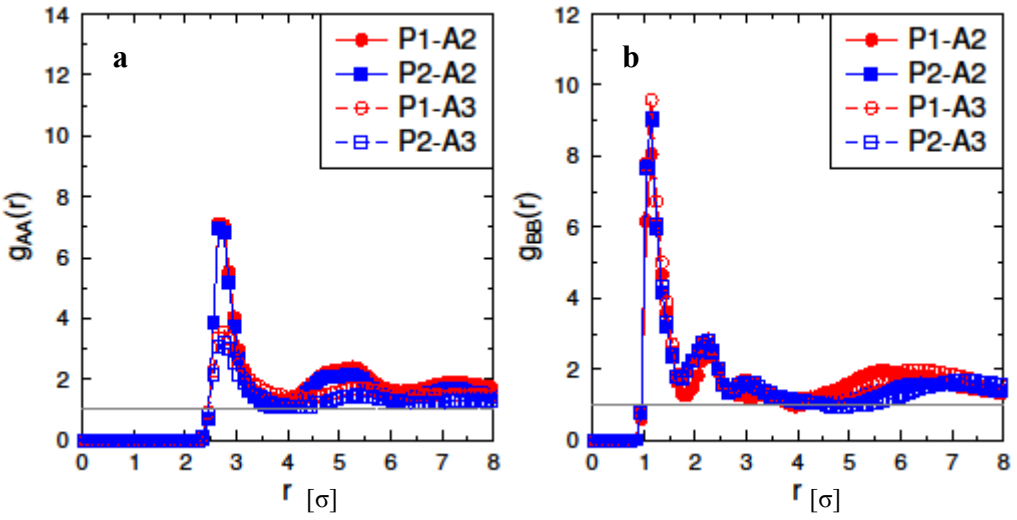

FIGURE 3.16: **a)** Acceptor-acceptor radial distribution function as a function of distance between acceptor centers of mass, r, and **b)** backbone-backbone radial distribution function as a function of distance between backbone beads, r, for ϕ = 0.5 blends of P1 and P2 with acceptors A2 and A3 at T* = 1.5.

The acceptor-backbone radial distribution function is shown in Figure 3.6 of the main text. Acceptor-acceptor aggregation is lower for A3 blends than for A2 blends because A3 acceptors have lower acceptor-acceptor attraction (ε_{AA} = 0.1 for A3 and ε_{AA} = 0.5 for A2). Backbone positional order does not change significantly between A2 and A3 blends.

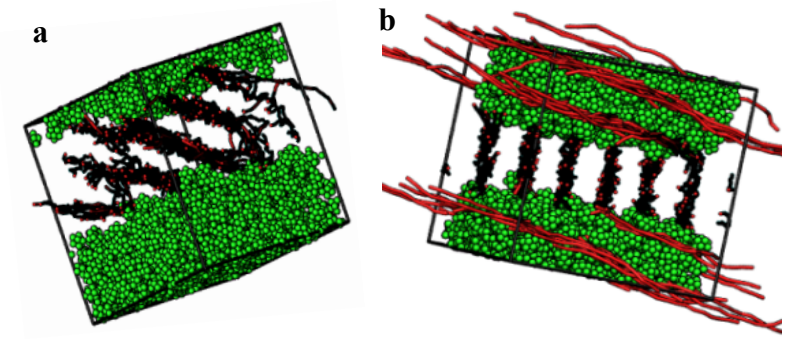

FIGURE 3.17: **a)** P2-A4 ϕ = 0.5 blend at T* = 1.5 where acceptors do not intercalate because of weak acceptor-backbone interactions. **b)** P2-A2 ϕ = 0.5 blend at T* = 1.5 where acceptors do not intercalate because of strong acceptor-acceptor interactions. Side chains are hidden for clarity.

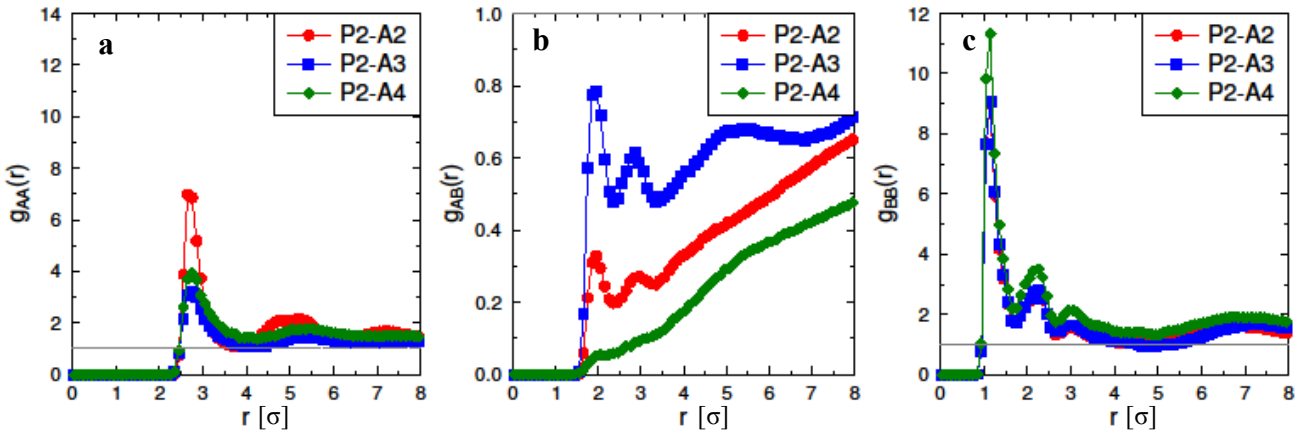

FIGURE 3.18: **a)** Acceptor-acceptor radial distribution function as a function of distance between acceptor centers of mass, r, **b)** acceptor-backbone radial distribution function as a function of distance between acceptor centers of mass and backbone beads, r, and **c)** backbone-backbone radial distribution function as a function of distance between backbone beads, r, for P2-A2, P2-A3, and P2-A4 blends at T* = 1.5.

Acceptor aggregation is higher for the A2 blend compared to the A3 and A4 blends because A2 acceptors are more strongly self-attractive ($\varepsilon_{AA} = 0.5$) than are A3 and A4 acceptors ($\varepsilon_{AA} = 0.1$). The acceptor-backbone radial distribution function shows that acceptor-backbone correlation is higher for the P2-A3 intercalated blend than for the P2-A2 and P2-A4 blends which show no intercalation. Backbone-backbone correlation is higher for P2-A4 blends compared to P2-A2 and P2-A3 blends because the larger P2-A4 acceptor aggregate imposes more confinement, facilitating alignment. P2-A2 and P2-A3 aggregates are smaller because for P2-A2 blends, acceptors are tightly packed because of increased acceptor-acceptor attraction ($\varepsilon_{AA} = 0.5$) and for P2-A3, some acceptors are intercalated reducing the aggregate size compared to P2-A4.

TABLE 3.4: Acceptor domain surface roughness for $\phi = 0.5$ blends of acceptors A1-A3 at T* = 1.5

	A1		**A2**		**A3**	
	Value	**+/- Err**	**Value**	**+/- Err**	**Value**	**+/- Err**
P1	0.31	0.0002	0.266	0.0001	0.312	0.0002
P2	0.27	0.0001	0.442	0.0006	**0.572**	0.0005
P3	0.315	0.0001	0.29	0.0001	0.36	0.0001

The intercalated P2-A5 blend shows higher surface roughness (≈ 0.6) in comparison to non-intercalated blends with surface roughness ≈ 0.2-0.4.

TABLE 3.5: Acceptor domain surface roughness for ϕ = 0.3 blends of acceptors A1-A3 at T* = 1.5

	A1		A2		A3	
	Value	**+/- Err**	**Value**	**+/- Err**	**Value**	**+/- Err**
P1	0.548	0.0005	0.652	0.0004	0.94	0.0005
P2	0.553	0.0006	0.618	0.0003	0.896	0.0011
P3	0.675	0.0006	0.719	0.0002	0.624	0.0006

Trends in surface roughness are more complicated for ϕ = 0.3 blends than for ϕ = 0.5 blends because of the formation of cylindrical acceptor domains for some ϕ = 0.3 blends, making comparison between blends difficult. We refrain from drawing conclusions here, but include the values for completeness.

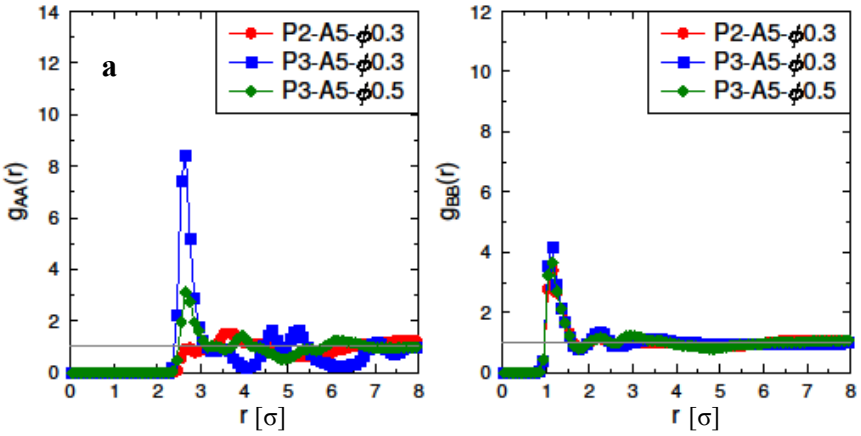

FIGURE 3.19: **a)** Acceptor-acceptor radial distribution function as a function of distance between acceptor centers of mass, r, and **b)** backbone-backbone radial distribution function as a function of distance between backbone beads, r, for P2-A5 ϕ = 0.3, P3-A5 ϕ = 0.3, and P3-A5 ϕ = 0.5 blends at T* = 1.5.

Acceptor-acceptor correlation is low for the P2-A5 ϕ = 0.3 and P3-A5 ϕ = 0.5 blends because acceptors are dispersed in a lattice of backbones at T* = 1.5. The P3-A5 ϕ = 0.3 blend has higher acceptor order and aggregation because acceptors form layers surrounded by backbones at T* = 1.5. Backbone correlation is lower for these A5 blends than for blends with

A1, A2, or A3 because acceptors do not form large aggregates to facilitate alignment. The acceptor-backbone radial distribution function is shown in Figure 7 of the main text.

TABLE 3.6: Acceptor domain surface roughness for P2-A5 and P3-A5 blends T* = 1.5

	Value	**+/- Err**
P2-A5, ϕ = 0.3	0.885	0.0003
P3-A5, ϕ = 0.3	1.398	0.0009
P3-A5. ϕ = 0.5	0.049	0.0001

Comparisons of A5 blend surface roughness with the A1, A2, and A3 blends are not applicable because the A5 acceptors do not form slab-like or cylindrical aggregates

Chapter 4

Controlling the morphology of model conjugated thiophene oligomers through alkyl side chain length, placement and interactions

Adapted from: *Macromolecules*, *47* (8), 2736–2747, 2014.

4.1 INTRODUCTION

Thiophene-based polymers are used in organic electronic materials due to their conjugated backbones and desirable charge carrier mobilities[1-3]. Since the charge carrier mobility depends upon polymer morphology[1-4], the ability to control the morphology of thiophene-based materials is desired for engineering new and improved organic electronic devices. One particularly relevant application of conjugated thiophenes is in organic photovoltaics, where the generation of excitons, separation of excitons to holes and electrons, recombination of holes and electrons, and transport of holes and electrons, which impact overall device efficiency, are determined largely by the active layer morphology[5-9]. In principle, the morphology of the donor domains comprised of conjugated thiophene polymers can be tuned through the selection of polymer features and processing conditions that promote the self-assembly of desired morphologies. Features of the conjugated thiophene polymers that affect morphology are the molecular weight or chain length of the conjugated polymer, the chemistry of the side chains extending from the thiophene rings in the conjugated polymer backbone, the side chain density along the backbone (or number of side chains per thiophene ring), and the side chain length and orientation relative to the backbone. Common thiophene-based conjugated polymers are poly(3-alkylthiophene)s (P3AT), poly(2,2′:5′,2″-3,3″-dialkyl-terthiophene)s (PTTT-CA or CA-TT), poly(3,4-dialkyl-2,2′-bithiophene)s (PDABT), poly(2,5-bis(3-alkylthiophen-2-yl)thieno[3,2-

b]thiophene)s (PBTTT-CA), and poly(3,3‴-alkylquaterthiophene)s (PQT), which differ in the density, orientation, and length of alkyl side chains extending from the π-conjugated backbone. Lamellar morphologies are observed in systems of P3ATs, and the spacing between lamellae depends on the length of alkyl side chain[10-12]. For conjugated thiophenes that have lower side chain density than P3ATs, including PTTT, PBTTT, and PQT, lamellar morphologies with reduced lamellar spacing are observed[3, 13, 14]. The reduced spacing is attributed to side chain interdigitation permitted by the reduced side chain density. The side chains of P3HT are typically not interdigitated[13], but interdigitated polymorphs of P3HT can be formed through proper processing[15-18], and additional work has used interdigitation to explain lamellar spacing in P3ATs with longer alkyl chains, for example, 8 or 12 alkyl carbons per side chain[12]. Experiments have shown that PDHBT, with side chains all on one side of the polymer backbone (termed as –*syn* arrangement in this paper), in contrast to the –*anti* arrangement of side chains of P3HT, PTTT, PBTTT and PQT, where side chains are on both sides of the polymer backbone, form hexagonally-packed and lamellar morphologies and that the assembled morphologies depend crucially on how the polymer is processed[19]. Field theory approaches show microphase separation of comb copolymers is facilitated by increased side chain density[20], and the competition between hexagonally-packed cylinders and lamellae is shown to depend on side chain length, density, and relative side chain – backbone miscibility for hairy-rod and comb copolymers [21, 22]. Side chain length also impacts the melting temperature of conjugated polymers[1,12, 23-26], with experiments showing that longer alkyl side chains lower the melting temperatures of P3ATs[12, 23-25].

In order to systematically elucidate how each side chain feature affects the order-disorder transition temperatures (ODTs), order-order transition temperatures, and the thermodynamically

stable morphologies of conjugated thiophene-based melts, it is necessary to use molecular simulations that circumvent the extensive time and effort involved in synthesis, and allow the effect of each feature on the physics governing conjugated thiophene self-assembly to be isolated. The primary factor limiting molecular simulation studies of conjugated thiophenes is the trade-off between the maintaining chemical detail in the system and the computational cost paid for simulating systems with the long relaxation time scales to observe equilibration[27-31]. The cost of simulating full atomistic detail is exemplified in recent work by Alexiandis *et al*., which shows that the twisting of thiophene rings matters in the packing of P3HT oligomers, but does not access sufficiently long time scales to demonstrate the self-assembly of 64 disordered 20-mer chains into lamellae[32]. At the opposite end of the spectrum of molecular detail is recent work by Carrillo *et al*., where P3HT is modeled with one coarse – grained bead per monomer, which demonstrates the impressively large simulation volumes of $(128nm)^3$, that could be accessed by running molecular dynamics simulations on one of the most powerful supercomputers[30]. The phase separation of P3HT and PCBM, [6,6]-phenyl-C_{61}-butyric acid methyl ester, a common electron-acceptor molecule, is observed during the course of simulations hundreds of nanoseconds long, but due to the highly coarse-grained nature of the P3HT molecules, key morphological features, such as polymer crystallization or side chain interdigitation, are missing in the simulations. Our previous work employed a coarse-grained model intermediate in molecular detail to the aforementioned extremes[31]. We simulated system sizes that permit access to thermodynamically stable configurations in fewer than 15 days of simulation time per trial while retaining enough chemical detail to obtain molecular-level information about the local packing[31]. Our work showed how acceptor miscibility in conjunction with conjugated thiophene oligomer architecture determine self-assembled blend morphology, including intercalation of

fullerenes among the thiophene side chains, for over 100 different state points[31]. In the case of low acceptor miscibility we observed that the conjugated thiophene oligomers macrophase separate from acceptors, and that the conjugated oligomer domain morphologies are the same as those seen in neat systems of thiophene oligomers (without acceptors). In the case of high acceptor miscibility we observed new blend morphologies with interconnected oligomer and acceptor domains.

In this work we employ coarse-grained molecular simulations using the model in Ref. [31] to focus solely on the neat conjugated oligomer systems (no acceptors) and systematically study how side chain characteristics impact the structure and thermodynamics of model conjugated thiophene oligomers. We identify a hierarchy of molecular features that govern order-disorder thermodynamics and explain why specific neat oligomer morphologies are thermodynamically stable at various temperatures. We find that the oligomer ODT is determined primarily by the amount of exposed strongly interacting oligomer backbone beads, followed by side chain- side chain interactions. Oligomers with moderately attractive side chains have higher ODTs than those with weakly attractive side chains. We show that *–anti* oligomers form lamellae, while *–syn* oligomers assemble into hexagonally packed cylinders which reconfigure into lamellae or ribbons at lower temperatures. For *–syn* oligomers, the side chain – side chain interaction strength determines whether or not this secondary order – order transition occurs. Side chain length has a varying effect on ODT, with longer side chains giving rise to larger lamellar and cylinder spacing, and partially disrupting lamellar ordering.

The paper is structured as follows: in the Approach section we describe our conjugated thiophene model, and the GPU-accelerated methods for performing and analyzing molecular dynamics simulations. Following that, we provide a brief description of the thermodynamic

driving forces for ordering in melts of conjugated thiophenes. In the results section we first discuss order disorder transition temperatures, followed by a discussion of the thermodynamically stable structures we observe and detailed analysis explaining the molecular features governing assembly. We conclude with an overview of key results.

4.2 APPROACH

4.2.1 Model

Our coarse-grained model of conjugated thiophene-based oligomers inspired by Refs. [29, 33, 34] and used in Ref. [31] represents each thiophene ring with a single spherical "backbone bead" (red *B* in Figure 4.1a) and each group of three alkyl carbons with a single "side chain bead" (blue *S* in Figure 4.1a). All backbone and side chain coarse-grained beads have unit diameter σ, corresponding to 3×10^{-10} m. The choice of length, energy, and mass units as well as the resulting derived units (*e.g.*, time and pressure) for this model, are explained in detail in Ref. [31], where simulated structures using this model were found to be in agreement with experimental structure of P3HT and PDHBT films[19]. For brevity, we only present the most essential features of the model in this section of this paper.

The architectures denoted by P1 and P2 have side chains arranged on both sides of the backbone, which we refer to as *–anti* architectures, while the architectures denoted by P3 and P4 have side chains arranged on one side of the backbone, which we refer to as *–syn* architectures. P1 and P4 oligomers have side chains on every thiophene ring while P2 and P3 have a lower density of side chains, with side chains on two out of every three backbone thiophene rings. The architectures denoted by P1, P2 and P3 qualitatively mimic P3HT, PTTT, and PDHBT respectively. Oligomers have either "short" (two coarse – grained bead) or "long" (four coarse - grained bead) side chains to model hexyl and dodecyl side chains, respectively. The molecular

structures of the different conjugated thiophenes shown in Figure 4.1b are modeled using different topologies of harmonic bond, angle, and dihedral potentials between pairs, triplets, and quadruplets of simulation beads, respectively. The equilibrium bond distance between neighboring beads is 1.4 σ with harmonic spring constant 50 ε/σ^2. Details of the angle and dihedral potentials differentiating the oligomer types are included in Supporting Information section 1. The equilibrium bond distances, bead sizes, and three and four body angles values are taken from the atomistically derived coarse-grain model of Ref. [29].

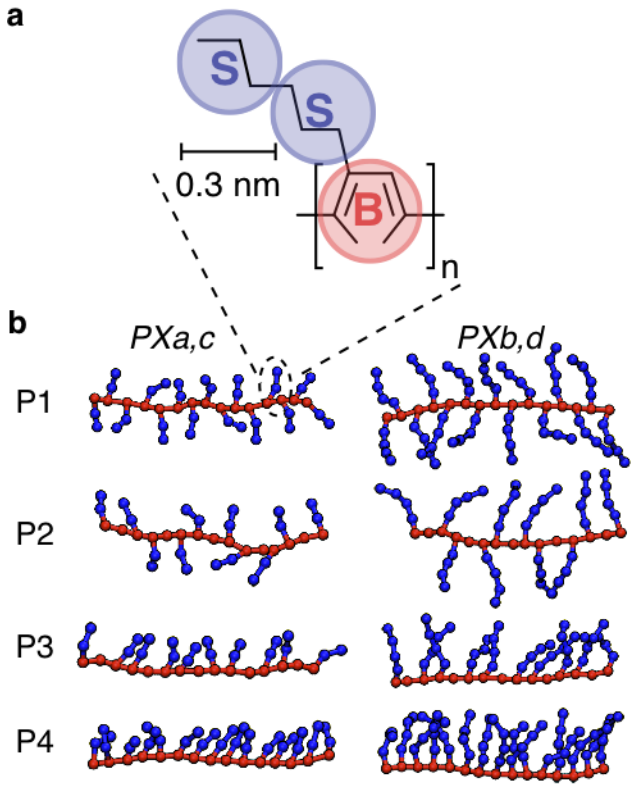

FIGURE 4.1: (a) Coarse-grained model of conjugated thiophene oligomers where thiophene rings are represented by a single coarse-grained "backbone" bead (red B) and groups of three alkyl carbons are represented by a "side chain" bead (blue S). (b) Oligomer architectures for –anti (P1 and P2) and –syn (P3 and P4) oligomers with hexyl side chains (side chain types PXa and PXc) or dodecyl side chains (side chain types PXb and PXd), where X ∈ [1,2,3,4]. Types a and b refer to side chains with moderate (ε_{SS} = 1.0) side chain attraction, and c and d refer to side chains with weak (ε_{SS} = 0.1) attraction, as listed in Table 4.1.

Non-bonded interactions between pairs of beads are defined by the Lennard-Jones (LJ) potential[35], where ε_{ij} determines the well depth of the LJ potential between bead types *i* and *j* in terms of the energy unit $\varepsilon = 2.7 \times 10^{-21}$ J. Each oligomer is comprised of 15 backbone beads and have a backbone – backbone bead attraction $\varepsilon_{BB} = 2.0\ \varepsilon$, which is the most strongly attractive pair-wise non-bonded interaction in this work. This captures the dominant π-π stacking interaction between the conjugated thiophene rings in the oligomer backbones. Interactions between backbone beads and the chemically dissimilar side chains are modeled by the Weeks-Chandler-Andersen potential[36], which we denote with $\varepsilon_{SS} = 0.0$. We specify the alkyl side chain type by *a, b, c,* or *d*, with *a* referring to short (2-bead) side chains with moderate ($\varepsilon_{SS} = 1.0$) side chain attraction, *b* referring to long (4-bead) side chains with moderate ($\varepsilon_{SS} = 1.0$) attraction, *c* referring to short (2-bead) side chains with weak ($\varepsilon_{SS} = 0.1$) attraction, and *d* referring to long (4-bead) side chains with weak ($\varepsilon_{SS} = 0.1$) attraction. In experiments, side chain interaction can be tuned by choice of solvent[37, 38] or by side chain functionalization[39]. For example, weak side chain attraction can be achieved with hexane, which is a good solvent for P3HT side chains and a poor solvent for the thiophene backbone. Hexane has been used to control morphology in P3HT nanowires formed in solution by varying the volume fraction of hexane in chloroform solvent[38], which could be another route to tune side chain attraction. Synthetic methods have been developed for functionalization of P3HT side chains, with for example, ester or hydroxyl groups, and these functionalizations can affect side chain attraction, and thus morphology[39].

TABLE 4.1: Table of model parameters for oligomers PX, where X ∈ [1,2,3,4], for side chain types a, b, c, and d. Lennard Jones well depths for backbone – backbone (ε_{BB}), backbone – side chain (ε_{BS}), and side chain - side chain (ε_{SS}) interactions in units of ε, the energy scale which corresponds to ε = 2.7 x 10^{-21} J for P3HT. The right-most column gives the number of coarse-grained beads in the side chains of each oligomer.

	$\varepsilon_{BB}\,[\varepsilon]$	$\varepsilon_{BS}\,[\varepsilon]$	$\varepsilon_{SS}\,[\varepsilon]$	Side chain beads
PXa	2.0	0	1.0	2
PXb	2.0	0	1.0	4
PXc	2.0	0	0.1	2
PXd	2.0	0	0.1	4

4.2.2 Method

The primary simulations for each of the sixteen oligomer types consist of a sequence of molecular dynamics simulations using HOOMD-Blue[40] performed in a cubic box with periodic boundary conditions in the isothermal-isobaric (NPT) ensemble at a pressure of 0.1 ε/σ^3 and dimensionless temperature T* ranging from 2.5 to 1.5. Simulations of systems with short side chains (*a* and *c*) are performed with 250 oligomer chains and systems with long side chains (*b* and *d*) are performed with 150 oligomer chains to maintain the approximate number of coarse grained beads (*N*). The initial T* is equal to 2.5 for all systems, where an isotropically disordered melt is observed to be the equilibrated structure for all oligomers. After the simulation has reached equilibrium at that temperature (see Supporting Information section 1 for criteria used to establish equilibrium), and has generated at least 20 statistically independent snapshots, an instantaneous quench lowering the temperature by 0.25 dimensionless temperature units is performed and equilibrated, as in Ref [31]. These steps are repeated until we have reached the

lowest T*, which for P2, P3, P4, and P1a,b is T* = 1.5, and for P1c and P1d is T* = 1.25 because P1c and P1d oligomers are disordered at T* = 1.5 but form ordered lamellae at T* = 1.25. Secondary simulations are performed to ensure that the structural features observed for each of the equilibrated systems are not artifacts of the size or the *cubic* shape of the simulation box (see Supporting Information for more details). In these secondary simulations, the final snapshot from each of the primary simulations is used as the initial configuration for a molecular dynamics simulation in which the periodic box axes are scaled independently while their relative orthogonality is maintained.

4.2.3 Analysis

In order to quantify the structural characteristics of our simulations as they progress towards and achieve equilibration we employ correlation functions to measure spatial structure, relaxation times, and length scales of periodic structural features. Radial distribution functions, $g_{i,j}(r)$, are used to quantify spatial correlations for coarse-grained beads of type *i* with beads of type *j*. Because the ordered morphologies we observe in this work consist of regions rich in backbone beads and regions rich in side chain beads, the radial distribution functions $g_{BB}(r)$ and $g_{SS}(r)$ provide useful metrics for packing and order in these regions, respectively. The $g_{BS}(r)$ radial distribution function is also used to quantify backbone – side chain bead structure. In particular, the first "contact" peak of $\rho g_{i,j}(r)$ indicates the average number of nearest neighbors or bead – bead contacts for beads of type *i* with beads of type *j* in a system with number density ρ. Reported radial distributions functions are averages from at least 20 statistically independent snapshots, where standard errors for each data point are smaller than the symbol size.

Diffraction patterns are generated by simulated scattering as done in Ref [31] *via* a plugin written for VMD[41] using the techniques in Ref. [42], and are used to identify the symmetry

groups for periodic structures and their feature spacing. Calculation of diffraction patterns allows comparison with experimental work, and does not assume spherical symmetry as is assumed in transforming radial distribution functions to structure factors[43]. Briefly, the coordinates for each backbone bead are projected onto a 512 x 512 2D grid perpendicular to the z-axis after the rotation matrix generating the view in VMD and periodic boundary conditions are applied. Each cell of the grid is updated with the number of backbone bead centers that are projected onto it, and the 2D Fourier transform of this array is convoluted with the Fourier transform of a 2D Gaussian whose amplitude and peak width are 2.0 and 1.0 σ, respectively. The simulated diffraction pattern is the square of the absolute value of the convoluted Fourier transform. The real space distance corresponding to the frequency-space distance between a feature peak and the origin is used to calculate the average center-to-center spacing between features (for example, layers in a lamellar morphology, or cylinders in a cylindrical morphology). For lamellar morphologies, the backbone lamellar thickness is calculated by calculating the average deviation of a selection of backbone beads from the plane perpendicular to the largest eigenvector of their moment of inertia tensor. The reported feature spacing and lamellar width measurements are averaged from 5 statistically independent snapshots and their reported uncertainties are the standard deviations of these 5 measurements.

We quantify the amount of exposed backbone for an oligomer by the backbone surface area accessible to a probe bead of diameter 2 σ, which depends upon its instantaneous configuration. Here, 100 uniformly distributed points on a sphere of radius 1.5 σ centered at each backbone bead are checked to see if a sphere of diameter 2 σ centered on each point overlaps with any of the backbone or side chain beads belonging to the same chain. Each point that does not overlap contributes a surface area of $9\pi\sigma^2/25$ to the total exposed backbone for a chain. The average

amount of exposed backbone for different chain architectures correlates with the average ODT, for oligomers with that architecture, as we show in the Results Section.

4.2.4 Thermodynamic Driving Forces for Oligomer Assembly

In this section we briefly review thermodynamics of assembly of these conjugated thiophene oligomers, providing context for how energy and entropy impact assembly in the work that follows. The thermodynamically stable morphology for a system of oligomers at a given temperature T and pressure P is dictated by the competition between energy and entropy in the minimization of the Gibb's free energy $G(N,P,T) = U + PV - TS$ *or* $H - TS$, where U is the total energy from bonded and non-bonded interactions, H is the system enthalpy, S is system entropy, P is system pressure, and V is system volume. A system of oligomers transitions from one morphology to another morphology (e.g. disorder to order or order to order) if the change in free energy (ΔG) is negative. This favorable change in free energy, and thus assembly could be driven a) energetically (ΔH is negative, while $T\Delta S$ is negative or negligible), b) entropically (ΔH is positive or negligible while $T\Delta S$ is positive) or c) by both (ΔH is negative and $T\Delta S$ is positive). In polymers and other soft materials such entropic[44-46], and energetic[47, 48] driving forces have been shown to control the formation of ordered morphologies. The balance/competition between change in energy versus change in entropy on the resulting change in free energy is governed by the (prefactor) temperature. In this study, we observe temperature-dependent transitions between disorder and ordered phases as well as between ordered phases, such as cylinders and lamellae, and link these structural transitions to thermodynamic driving forces. For example, we present evidence that the entropic contributions to the free energy make the cylindrical phase more thermodynamically stable than the lamellae at high temperatures and the energetic contributions to the free energy make the lamellar phase more stable at low temperatures.

The non-bonded interactions contributing to U are dictated by the attractions defined by the Lennard-Jones potential between certain pairs of bead types. The larger the attraction $\varepsilon_{i,j}$ between bead types i and j, the stronger the energetic drive to form morphologies where those coarse-grained beads aggregate. The Lennard-Jones attraction is the strongest between backbone beads (ε_{BB} = 2.0) so backbone-backbone interactions are expected to drive transitions into morphologies where the backbone coarse-grained beads aggregate. The side chain - side chain attraction (weak to moderate), while not as strong as backbone-backbone interactions, also impacts the morphologies formed by dictating the thermodynamic driving force to form morphologies where the side-chain aggregation is high.

The bonded interactions, specifically the angle potential between backbone beads has a larger bending penalty ($k = 30\varepsilon/\sigma^2$) compared to the side chains ($k = 6\varepsilon/\sigma^2$). This large bending penalty for the backbone drives alignment and orientational order among the oligomer conjugated backbones. The relatively lower bending penalty for the side chains gives the side chains more flexibility than the chain of backbone beads. Thus the side chains contribute more to the overall conformational entropy than the backbones because side chains are able to sample more conformations than backbones. Thus, energy aside, the morphologies where the side chains are able to sample more conformations (e.g. cylinders) are entropically favored than ones where the side chains are restricted to a relatively smaller volume (e.g. lamellae).

4.3 RESULTS

The primary results of our molecular dynamics simulations are the equilibrated configurations of model thiophene oligomers where we see that the morphology depends upon architecture (P1, P2, P3, or P4), side chain attraction (ε_{SS} = 1.0 or ε_{SS} = 0.1), and side chain length (short, 2 beads or long, 4 beads, corresponding to hexyl and dodecyl chains, respectively).

In the following subsections we first report the order-disorder transition temperatures (ODT) observed for the sixteen different oligomer systems, and discuss the observed hierarchy of molecular features that govern the ODT. Second, we report the thermodynamically stable, self-assembled morphologies and compare their features to experimental measurements, where available. Finally, we present the results of additional simulations and detailed structural analyses, which are used to explain differences in morphology and ODT for the different oligomers.

4.3.1 Trends in Order-Disorder Transitions

Figure 4.2 presents a phase diagram for melts of oligomers P1, P3, P3 and P4, with side chain types *a*, *b*, *c*, and *d*, along with the simulation snapshots and simulated diffraction patterns for each type of morphology: D-disordered, L-lamellae, P-perforated lamellae, C-cylinders, or R-ribbons. Lamellar morphologies have alternating layers of backbones and side chains. Cylindrical morphologies are characterized by the formation of cylinders of backbones surrounded by side chains. Ribbon morphologies have features of lamellar and cylindrical morphologies, and are essentially flattened cylinders. Details of these morphologies are discussed in Section B, and snapshots and diffraction patterns for these morphologies are shown in Figure 4.2 b-f.

In this work, we cool the oligomer melts in steps of $T^* = 0.25$ and define the approximate order disorder transition temperature (ODT) as the temperature where the oligomer melt system changes from a disordered state to one of the ordered states: L, P, C, or R. The phase diagram shows that the average ODT for P1 oligomers is lower than the average ODT for P2, followed by P4 and P3. For each oligomer architecture, the systems with moderately attractive side chains (PXa,b) always have ODTs equal to or greater than their weakly attractive counterparts (PXc,d).

For the oligomers with moderately attractive side chains (PXa,b), those with longer side chains (PXb) have equal or higher ODTs than those with shorter side chains (PXa), while for oligomers with weakly attractive side chains (PXc,d), those with longer side chains have equal or lower ODT than those with short side chains.

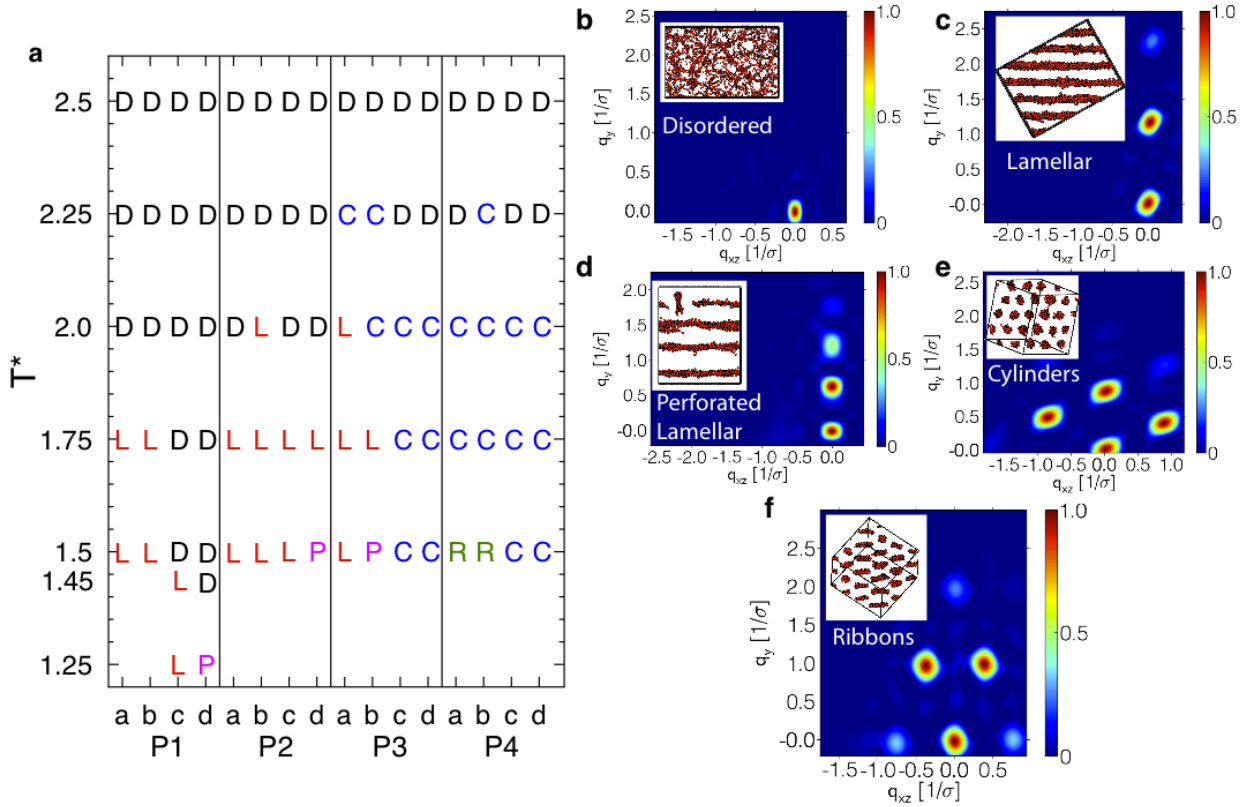

FIGURE 4.2: (a) Phase diagram of thermodynamically stable morphologies for oligomers P1, P2, P3, and P4 with side chain types a, b, c, and d at reduced temperature T* = 1.25 to T* = 2.5. Representative diffraction patterns with snapshots inset for: (b) D = disordered, (c) L = lamellar, (d) P = perforated lamellar, (e) C = cylindrical, and (f) R = ribbon-like morphologies corresponding to the symbols in the phase diagram.

Oligomer architecture affects ODT because backbone beads are the species with the strongest enthalpic driving force for aggregation, and the different architectures (P1, P2, P3 and P4) permit different amounts of backbone bead exposure. Average exposed backbone areas at T* = 1.5 and average ODTs for the four oligomer architectures are compared in Figure 4.3a, and

show a strong correlation between exposed backbone area and ODT. The average ODT for each oligomer, T^*_{ODT}, is calculated by averaging the ODTs for the four side chain types *a*, *b*, *c*, and *d* for each oligomer. The exposed backbone area of a given oligomer is the area accessible to a probe bead averaged over 20 snapshots for each side chain type *a*, *b*, *c*, and *d*. The average exposed backbone areas, A_E, plotted in Figure 4.3 are the average of the exposed backbone areas of the four side chain types, *a*, *b*, *c*, and *d*, for each oligomer. Values for each of the sixteen oligomer types at T* = 1.5 are included in Table 4.4.

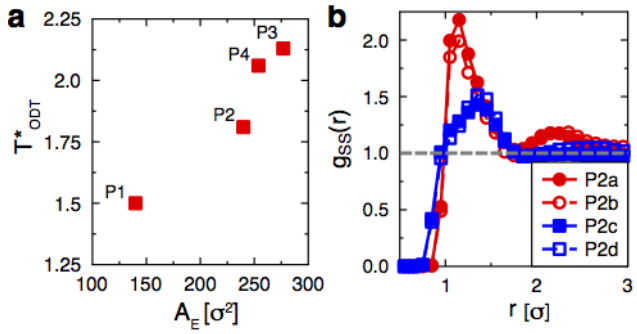

FIGURE 4.3: (a) The average ODTs, T^*_{ODT}, calculated by averaging the ODTs for the four side chain types a, b, c, and d for each oligomer architecture, are correlated with average exposed backbone area, A_E, calculated at T* = 1.5 for oligomers P1, P2, P3, and P4. (b) Side chain radial distribution functions, $g_{SS}(r)$, for P2 oligomers at T* = 1.5 demonstrate that moderately attractive side chains, types a and b, (ε_{SS} = 1.0, red circles) pack more closely than weakly attractive side chains, types c and d (ε_{SS} = 0.1, blue squares) irrespective of side chain length.

P1 has the lowest ODT and the least exposed backbone area because side chains extend from every backbone bead in the *–anti* arrangement. P2 also has *–anti* arranged side chains, but has a higher ODT than P1 because it has more exposed backbone area due to lower side chain density compared to P1. The ODTs of the *–syn* arranged P3 and P4 are higher than those of P1 and P2, because the *–syn* oligomers have significantly more exposed backbone area.

Moderate side chain attraction is expected to give rise to higher ODTs than weak side chain attraction because the stronger attraction favors higher side chain aggregation, quantified using pair correlation functions. For example, higher side chain coordination for P2 oligomers

with moderate side chain attraction (P2a,b) compared to P2 oligomers with weak side chain attraction (P2c,d) is shown by the side chain – side chain radial distribution functions $g_{SS}(r)$ in Figure 4.3b. P2a and P2b have contact peaks that are higher in magnitude than those of P2c and P2d, indicating that P2a and P2b lamellar morphologies have more side chain – side chain contacts than do their weakly attractive counterparts. The length scale of the side chain contact peak for P2a and P2b is $r \sim= 1.15\ \sigma$, which is consistent with the separation distance at the Lennard-Jones potential minimum. For the weakly attractive side chains P2c and P2d, the contact $g_{SS}(r)$ peak is located at $r \sim= 1.4\ \sigma$, which is consistent with the equilibrium bond length between side chain beads of $1.4\ \sigma$, demonstrating that there is negligible side chain aggregation due to non-bonded attractive interactions. Oligomers P1, P3, and P4 have the same structural dependence on side chain attraction as P2: at a given temperature, moderately attractive side chains show high aggregation at $r \sim= 1.15\ \sigma$ and weakly attractive side chains show relatively less coordination at $r \sim= 1.4\ \sigma$ (Figure 4.9).

For the oligomers studied here, increasing the side chain length from a hexyl group to a dodecyl group increases or decreases the ODT, or leaves the ODT unchanged, depending on the oligomer architecture and side chain – side chain attraction strength. The complicated dependence of ODT on side chain length observed in this work reproduces some experimental results of thiophene-based conjugated polymer melting temperatures as well as identifies trends that could in principle be achieved through proper solvent choice or side chain chemistry. Experiments comparing the melting points of P3ATs with hexyl side chains (P3HT) and dodecyl side chains (P3DDT) show that polymers with longer side chains have lower melting temperatures[23]. The same phenomenon is observed for our oligomers P1c and P1d, with the long, dodecyl side chains of P1d preventing order at $T^* = 1.45$, whereas P1c can self-assemble

into lamellae at T* = 1.45. Conversely, for oligomers with moderately attractive side chains (P2a,b and P4a,b), the ODT is higher for the oligomers with longer side chains than for oligomers with shorter side chains. Their weakly attractive counterparts (P2c,d and P4c,d) have ODTs that are equal for the two side chain lengths, within the resolution of the different temperature trials performed here. The ability of our model oligomer P1 to reproduce the chain length dependence of P3AT melting temperatures with weakly attractive side chains suggests the weak attractions provide a faithful representation of alkyl side chain interactions in P3AT melts. However, due to lack of experimental ODT findings that relate alkyl side chain length to ODT for the other oligomer architectures (P2, P3 and P4), we are unable to compare our predictions to experiments for polymers qualitatively similar to our oligomers P2, P3, and P4.

4.3.2 Trends in Ordered Morphologies

In this section we describe the equilibrated morphologies observed in our simulations and compare them to morphologies found in experiments for the few systems where experimental results are available. Representative snapshots and corresponding diffraction patterns for disordered, lamellar, perforated lamellar, cylindrical, and ribbon morphologies are presented in Figure 4.2b-f. Lamellar morphologies are characterized by alternating layers of backbones and side chains. Oligomers with *–anti* oriented side chains, P1 and P2 *a*, *b*, *c*, and *d*, form lamellae at $T^* \leq T^*_{ODT}$ as do P3HT and PTTT experimentally, which are the molecules mimicked by oligomers P1 and P2 [14, 19, 49]. Lamellar morphologies with imperfections including misaligned or broken layers are referred to as perforated lamellae (Figure 4.2d). These perforated lamellae are shown to be thermodynamically stable by transforming, for example, P1b into P1d, by starting with an equilibrated snapshot of P1b at T* = 1.5 and making the side chains weakly attractive, $\varepsilon_{SS} = 0.1$, as for side chain type *d*. The lamellar P1b morphology is observed to rearrange into

perforated lamellae with weak side chain attraction at T* = 1.25. (Figure 4.10). The cylindrical morphologies observed for the *–syn* architectures P3 and P4, and are characterized by six-fold symmetric diffraction peaks indicating a hexagonal packing of parallel cylinders (Figure 4.2e). Ribbon morphologies have features of both lamellar and cylinder morphologies; backbone-rich domains that span the simulation box along one axis assemble parallel to one another (like cylinders), but with flat, non-circularly-symmetric cross-sections (like lamellae). Diffraction patterns for ribbons are similar to cylinders, but show multiple correlation length scales arising from the anisotropic ribbon cross-sections (Figure 4.2f).

The average feature spacing corresponding to the ordered morphologies summarized in Figure 4.2 are presented in Figure 4.4. The feature spacing, calculated from a simulated diffraction pattern, is defined by the length scale corresponding to the maximum of a diffraction peak, and measures the average center-to-center distances between periodic backbone-rich regions such as lamellae and cylinders. Ribbons and cylinders display periodicities along multiple axes, giving rise to larger uncertainties in average feature spacing when these periodicities have different length scales. The lamellar spacing for P1a, mimicking P3HT, of d = 5.5 +/- 0.018 σ or about 16.5 Å at T* = 1.5 agrees with experimentally measured lamellar spacings of approximately 16.6-16.8 Å for P3HT[10, 19, 50, 51]. Increasing the side chain length from hexyl (P1a) to dodecyl (P1b) increases the lamellar spacing to d = 8.8 +- 0.055 σ or about 26.4 Å, which is in good agreement with d = 25.1 - 26.2 Å found in experiments for P3DDT[10-12]. In general, experiments show that lamellar spacing increases with increasing polythiophene side chain length[10-12], and we observe the same behavior for all four simulated oligomers P1, P2, P3, and P4, for both weak and moderate side chain attraction. That is, PXb has larger lamellar spacing than PXa, and PXd has larger lamellar spacing than PXc for X ∈ [1,2,3,4]. In terms of

side chain interactions, the moderate side chain attraction of PXa,b results in smaller lamellar spacings than PXc,d, which is consistent with the intuition that the stronger attractions would pull side chains in closer contact, decreasing the size of the side chain domains.

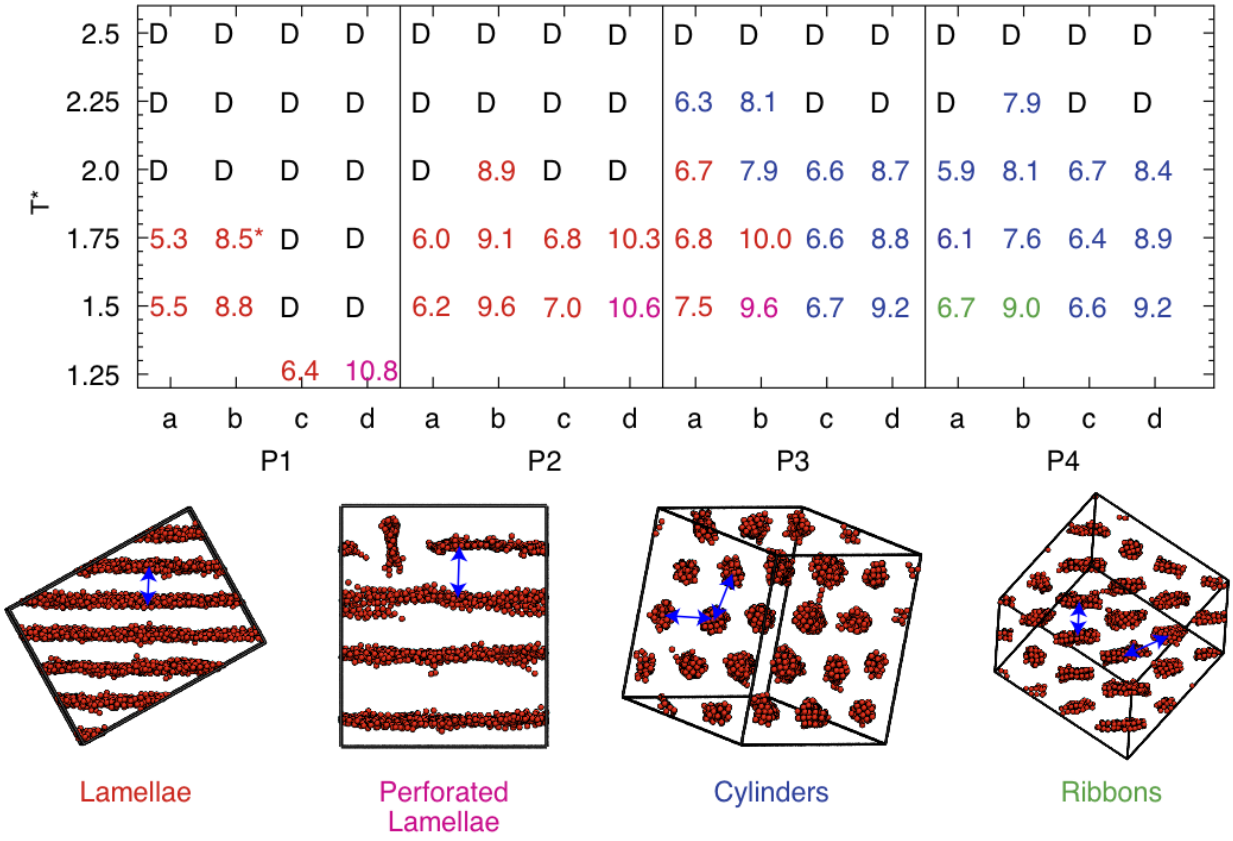

FIGURE 4.4: Average feature spacing of the self-assembled morphologies for each oligomer type at reduced temperatures, T*, between 1.25 and 2.5. Disordered systems with no periodic length scale are labeled "D". Feature spacings for lamellae are shown in red text, perforated lamellae in pink text, cylinders in blue text, and ribbons in green text. The average standard deviation for feature spacing is 0.05 σ for P1, 0.09 σ for P2, 0.2 σ for P3, and 0.27 σ for P4. The largest standard deviation is 0.67 σ for P4 ribbons. The lamellar spacing for P1b at T* = 1.75 is marked with an asterisk to indicate its feature size varied from 7.9 to 8.9 σ, depending on the length of the shortest box axis.

Oligomers with –*syn* arranged side chains (P3 and P4) are observed to form cylindrical, lamellar, or ribbon morphologies (Figure 4.2). The occurrence of cylindrical phases for P3 and P4 oligomers qualitatively matches experimental results for the polymer PDHBT, a conjugated polythiophene with side chains in the -*syn* arrangement, which has been shown to form

hexagonally packed morphologies upon annealing and disordered lamellae when cast[19]. Our results show that P3a and P3b, which have –*syn* oriented side chains and moderate side chain – side chain attraction, form cylinders at the ODT at high temperature (T* = 2.25) and transition to lamellae at lower temperatures (T* = 2.0 or T* = 1.75, respectively). Oligomers P4a and P4b also form cylinders at high temperatures (T* = 2.0 or T* = 2.25, respectively), but transform into ribbons rather than lamellae at low temperature (T* = 1.5). The P4 oligomers differ from P3 oligomers only in side chain density, suggesting that the relatively higher side chain density of P4 inhibits lamellae formation. The prevalence of cylinders at high temperature and lamellae or ribbons at low temperatures for P3a,b and P4a,b suggests higher conformational entropy is associated with cylinder formation relative to lamellae and ribbons, and lower potential energy is associated with lamellae and ribbons relative to cylinders. This is consistent with our observation that lamellae are not observed to assemble in –*syn* architectures with weak side chain attraction (P3c,d and P4c,d), and shows that lamellae formation requires an energetic thermodynamic driving force.

Reduced lamellar spacing is measured in experiments for polythiophenes with lower side chain density on the backbone compared to those with a higher side chain density. The reduced lamellar spacing for PTTT, PQT, and PBTTT, which have lower side chain density than P3HT, is attributed to interdigitation of the alkyl side chains[3, 13, 14, 49, 52]. In contrast to the experimental observations, our simulations show that lamellar spacing increases with a decrease in side chain density. For example, the lamellar spacing for P1 oligomers is smaller than the lamellar spacing for P2 oligomers with the same side chain type at the same temperature, even though P2 has lower side chain density than P1 (Figure 4.4). Specifically, at T* = 1.5, P1a has a lamellar spacing of 5.5 σ while P2a has a lamellar spacing of 6.2 σ. We observe the backbone rich

regions are thicker in systems of P2 oligomers compared to P1 oligomers (SI Table 4.5), which partially explains the increased lamellar spacing for P2 oligomers. We attribute the discrepancy between these simulation results and experimental decrease in lamellar spacing to the coarse-grained representation of thiophene rings, which would π-stack in experiments, but hexagonally close-pack due to spherical representation in our model (one of the limitations of our coarse-grained model), especially in lower side chain density oligomers. While π-stacked thiophene rings could cause the side chains to interdigitate at lower side chain density per thiophene ring, in our model the hexagonal packing of spheres and increased thickness of aligned backbone domains increases the effective side chain density, and deters interdigitation.

While we do not observe interdigitation due to decreasing side chain density, we do observe interdigitation due to increasing side chain attraction, where side chain attraction can be tuned using solvent quality and side chain functionalization as discussed earlier. Moderately attractive side chains (PXa,b) are more interdigitated relative to weakly attractive side chains (PXc,d). Snapshots of isolated adjacent layers for P1 and P2 *a*, *b*, *c*, and *d* are shown in Figure 4.5, where more space is observed between lamellae of the weakly attractive side chains than between lamellae of moderately attractive side chains. The visual observation of slight interdigitation is confirmed by the feature spacing differences summarized in Figure 4.4, which show that the lamellar spacing for PXa,b at a given side chain length is generally smaller than for PXc,d with the same side chain length. Thus, our model captures correctly the dependence of interdigitation on side chain interactions, but not a dependence on side chain density.

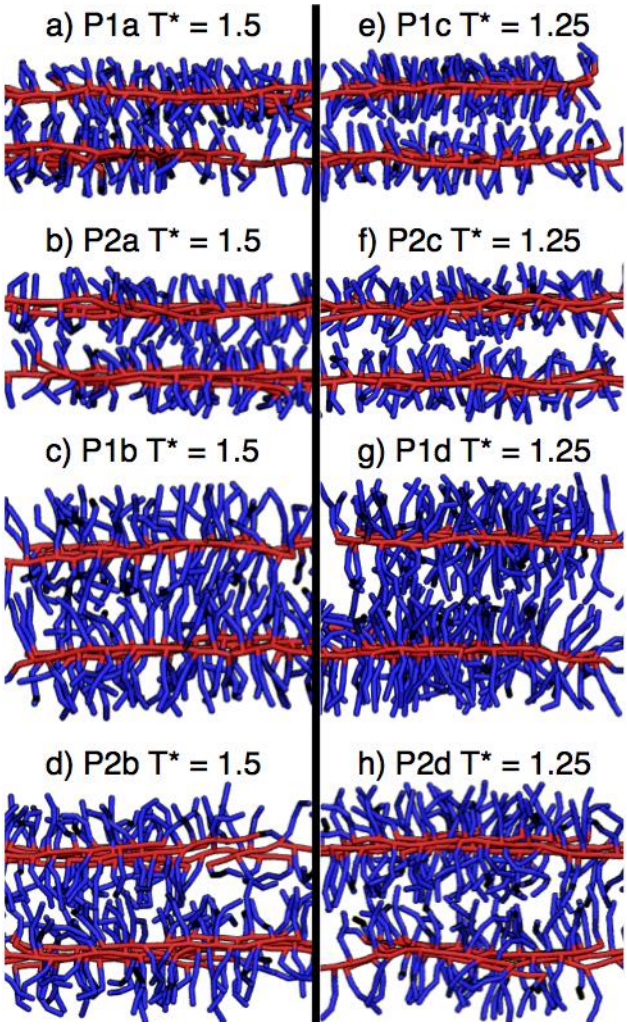

FIGURE 4.5: Snapshots of isolated adjacent lamellae for P1 and P2 oligomers at specific temperatures as denoted. Side chains with weak attraction (ε_{SS} = 0.1, right column) are less interdigitated than side chains with moderate attraction (ε_{SS} = 1.0, left column).

So far, we have presented general trends in structure and thermodynamics in melts of oligomers as a function of oligomer architecture (side chain length, density and orientation) and side chain interactions. Next, we show the thermodynamic underpinnings of many of the above trends in morphologies, using specific examples.

4.3.3 Thermodynamics Underlying Trends in Transitions and Morphologies

In this section we determine how intermolecular interactions and side chain architecture influence which morphologies are formed at given thermodynamic state point. First we examine

how the dihedral angle potentials imposing *–syn* vs. *–anti* architectures affect morphology at constant temperature. We then study how temperature impacts the thermodynamically stable morphologies for *–syn* oligomers that undergo a secondary order-order transition.

To determine why oligomers with the same number of side chains but different architectures give rise to different morphologies at a particular state point, we compare the components of the total potential energy, U_{total}, for *–anti* and *–syn* oligomers. For example, oligomers of P2b and P3b, have the same density of long, moderately attractive side chains, but differ in *–anti* vs. *–syn* architecture, respectively. At T* = 2.0, P2b forms lamellae while P3b forms cylinders. Since melts of P2b and P3b have the same number of coarse-grained beads of each type, any differences in morphology at this temperature must arise due to *anti*-versus-*syn* induced differential arrangement of the constituents in the system. The arrangement of the constituent coarse-grained beads determines the potential energy, U, and we find that $U_{total,\,P3b} < U_{total,\,P2b}$ at T* = 2.0, which shows the cylinders of P3b are energetically more favorable than P2b lamellae (See per-bead U values in Table 4.2). We note that the U_{total} of P3b and P2b in the disordered states are more positive than the U_{total} of P3b and P2b in these ordered states (i.e. $\Delta U_{Disorder \rightarrow order}$ is negative), thus driving the transition to these ordered states. The $U_{non\text{-}bonded}$ of P3b cylinders at T* = 2.0 is lower (more favorable) than $U_{non\text{-}bonded}$ of P2b lamellae. In contrast to the differences in $U_{non\text{-}bonded}$ for P3b and P2b, the differences in U_{bond}, U_{angle} and $U_{dihedral}$ potential energies are less significant, where U_{bond} denotes 2-body potentials, U_{angle} is the contribution from 3-body angle potentials and $U_{dihedral}$ is the contribution from 4-body dihedral angle potentials. A comparison of $g_{BB}(r)$ and $g_{SS}(r)$ contact peaks for P2b and P3b at T* = 2.0 shows that P3b has more backbone – backbone contacts than does P2b, but side chain – side chain contacts are similar between the two systems, indicating that the more favorable $U_{non\text{-}bonded}$ for

P3b compared to P2b comes from the higher number of backbone – backbone contacts rather than a change in side chain – side chain contacts (Figure 4.6a and b) in P3b than P2b. Thus, the cylindrical morphology of P3b allows for more backbone – backbone contacts than does the lamellar P2b morphology. The question that arises next is why P3b energetically prefers the cylindrical morphology while P2b the lamellar morphology.

TABLE 4.2: Total potential energy **per-bead**, U_{total}, (in units of ε) and its comprising components for the equilibrium ensembles of P2b at T* = 2.0, P2c at T* = 1.75, and P1b at T* = 1.75 which form lamellae, and P3b at T* = 2.0, P3c at T* = 1.75, and P4b at T* = 1.75 which form cylinders. U_{bond} denotes 2-body potentials, U_{angle} is the contribution from 3-body angle potentials and $U_{dihedral}$ is the contribution from 4-body dihedral angle potentials.

	U_{total}	$U_{non\text{-}bonded}$	U_{bond}	U_{angle}	$U_{dihedral}$
P2b T* = 2.0 (Lamellae)	0.48(3)	-2.08(3)	1.03(2)	1.40(1)	0.13(0)
P3b T* = 2.0 (Cylinders)	0.32(5)	-2.22(3)	1.02(1)	1.40(2)	0.13(0)
P2c T* = 1.75 (Lamellae)	0.75(3)	-1.56(2)	0.92(1)	1.18(1)	0.20(1)
P3c T* = 1.75 (Cylinders)	0.20(3)	-2.00(2)	0.90(1)	1.12(1)	0.19(1)
P1b T* = 1.75 (Lamellae)	0.14(3)	-2.13(2)	0.91(1)	1.26(1)	0.10(0)
P4b T* = 1.75 (Cylinders)	-0.18(2)	-2.42(2)	0.88(1)	1.25(1)	0.12(0)
P2b T* - 2.5 (Disordered)	2.72(5)	-0.71(1)	1.30(2)	1.92(2)	0.21(1)
P3b T* - 2.5 (Disordered)	2.54(6)	-0.89(4)	1.30(2)	1.89(2)	0.23(1)

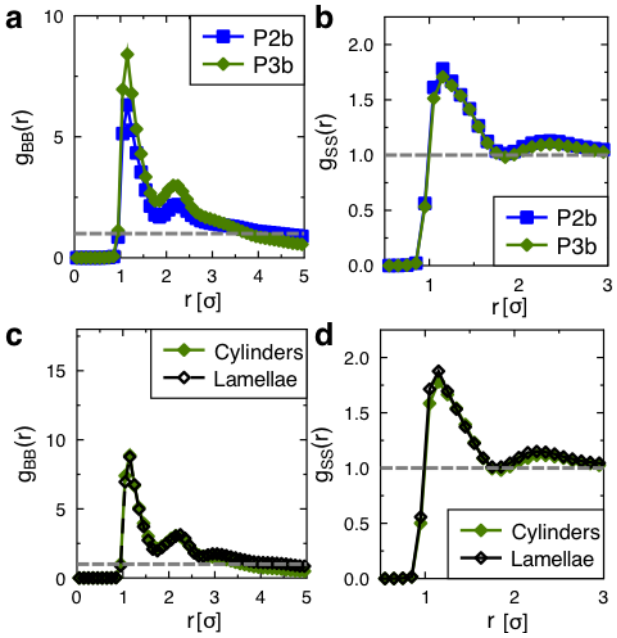

FIGURE 4.6: (a) At T* = 2.0, the contact peaks of the backbone radial distribution functions, $g_{BB}(r)$, show increased backbone contacts in P3b cylinders relative to P2b lamellae, while (b) the side chain radial distribution functions, $g_{SS}(r)$, show similar side-chain structure for both oligomers. (c) The difference in backbone structure between P3b cylinders and lamellae at T* = 1.8 as measured by $g_{BB}(r)$ is negligible, as is the difference in side chain structure measured by the side chain radial distribution function, $g_{SS}(r)$ (d).

The lower U_{total} of P3b cylinders relative to P2b lamellae suggests that the *–anti* orientation of P2b side chains inhibits the formation of a more energetically favorable cylindrical morphology. This leads to the question that if the dihedral angle constraints are removed from stable P2b lamellae at T* = 2.0, will the oligomers rearrange into cylinders? We perform this computational experiment by continuing the equilibrated simulation of P2b at T* = 2.0 with the dihedral angle bond constants set to 0, or in other words allowing neighboring side chains to assume any dihedral orientation without energetic penalty. Within 5e7 time steps, the P2b lamellae transition to cylinders with side chains assuming *–syn* conformations (Supporting Movie SM1). Thus, the architecture (*–syn* vs. *–anti* side chain orientations) of oligomers determines which morphology is thermodynamically stable at a state point. We perform the same test on P2c oligomers, which have weak side chain – side chain attraction and short, two

coarse-grained bead side chains. P2c forms lamellae at T* = 1.75, but rearranges into cylinders when the dihedral angle constraints are removed, confirming that the *–anti* architecture prevents cylinder formation for P2 oligomers of every side chain length studied here. Comparisons of potential energies and contact peak heights for the P2c and P3c oligomers are included in Table 2 and Figure 4.11.

Similarly, the *–syn* vs. *–anti* architectural dependence of cylinders vs. lamellae can be studied with oligomers P1 and P4 as well. At T* = 1.75, P1a,b form lamellae while P4a,b form cylinders. P4 cylinders have lower U_{total} than P1 lamellae, derived from P4b having lower $U_{non\text{-}bonded}$ than P1b because P4b cylinders have more energetically favorable backbone-backbone contacts than do P1b lamellae. See Table 4.2 for values of U, and Figure 4.11 for P1b and P4b contact peaks. Simulations beginning with the equilibrated P1b lamellar morphology at T* = 1.75 transition into cylinders when the dihedral side chain constraints are removed. Thus, the transition of stable lamellae into cylinders upon removal of the *–anti* side chain constraints proves the *–anti* architecture prevents the formation of more energetically favorable cylinders accessible to *–syn* architectures at the same temperature.

Effect of temperature on –syn oligomer morphology: In the previous section we showed how oligomer architecture dictated whether cylinders or lamellae formed at a given state point. In this section we describe how the temperature, and the competition between energy and entropy, dictates whether cylinders or lamellae are formed for *–syn* oligomers. Oligomers with *–syn* oriented, moderately attractive side chains (P3a,b and P4a,b) form cylinders at high temperature ($2.0 \leq T^* \leq 2.25$) and undergo a secondary order-order phase transition to lamellae or ribbons at lower temperatures. In order to investigate the driving forces that determine the cylinder to lamellae order-order transition, we simulate P3b oligomers at T* = 1.8 where cylinders are

observed to be locally stable for 32.2 nanoseconds before transitioning into lamellae, providing an approximation of phase coexistence. At T* = 1.8 the U_{total} of the lamellae is lower than that of the cylinders, indicating that $\Delta U_{cylinder \rightarrow lamellae}$ is negative (Table 4.3). This means, that for cylinders to be the stable morphology at $1.8 < T^* < 2.25$ the lamellar morphology is less entropically favorable than cylinders (i.e. $T\Delta S_{cylinder \rightarrow lamellae}$ is negative). In other words, the oligomers likely sacrifice their conformational entropy to gain more energetically favorable contacts in the lamellar morphology at temperatures T*<1.8.

The more favorable $U_{non\text{-}bonded}$ for the lamellae is accompanied by only subtle changes in average structure: the radial distribution functions $g_{BB}(r)$ and $g_{SS}(r)$ are nearly identical before (in lamellar phase) and after (in cylindrical phase) the transition (Figure 4.6c and d). However, the lower U_{angle} and $U_{dihderal}$ for the P3b lamellar phase compared to the P3b cylindrical phase at T* = 1.8 (Table 4.3) demonstrates that on average the side chains are accessing smaller free volumes in the lamellar phase. In the case of cylinders, side chains explore larger free volumes compared to lamellae and strain their angle and dihedral constraints, increasing the potential energy. We quantify the change in entropy, *S*, between P3b cylinders and P3b lamellae by equating the Gibbs free energy, *G,* at the coexistence temperature. Assuming $G_{cylinder} = G_{lamellae}$ at T* = 1.8, where we found cylinders transition to lamellae, we calculate the *per-bead* $T\Delta S_{cylinder \rightarrow lamellae} = -0.28\ \varepsilon$. That is, on average each bead sacrifices entropy corresponding to 3.8 kcal/mol in exchange for relieving strained bonds, three-body angles, and dihedral constraints in the transition from cylinders to lamellae. The fact that the transition from cylinders to lamellae shifts to lower temperature with increasing side chain length (T* = 2.0 for short P3a vs. T* = 1.75 for long P3b) suggests that short side chains lose less conformational entropy upon the transition to lamellae than do long side chains.

TABLE 4.3: Total potential energy **per-bead**, U_{total}, (in units of ε) and its comprising components for cylinders, lamellar, and ribbon-like morphologies at the coexistence temperatures for P3b (T* = 1.8), P4b (T* = 1.5), P3a (T* = 2.08), and P4a (T* = 1.5). U_{bond} denotes 2-body potentials, U_{angle} is the contribution from 3-body angle potentials and $U_{dihedral}$ is the contribution from 4-body dihedral angle potentials. For all cylinder-lamellae and cylinder-ribbon coexistence pairs, the lower U_{total} of the lamellae or ribbons relative to cylinders arises primarily from the $U_{non\text{-}bonded}$, U_{angle} and $U_{dihedral}$ contributions.

	U_{total}	$U_{non\text{-}bonded}$	U_{bond}	U_{angle}	$U_{dihedral}$
P3b T* = 1.8 (Cylinders)	-0.22(5)	-2.51(3)	0.91(1)	1.27(2)	0.11(1)
P3b T* = 1.8 (Lamellae)	-0.68(3)	-2.85(2)	0.89(2)	1.19(1)	0.09(0)
P4b T* = 1.5 (Cylinders)	-0.83(2)	-2.78(2)	0.74(1)	1.10(1)	0.11(0)
P4b T* = 1.5 (Ribbons)	-1.22(2)	-3.09(1)	0.74(1)	1.04(1)	0.09(0)
P3a T* = 2.08 (Cylinders)	0.23(4)	-2.44(3)	1.09(2)	1.34(2)	0.23(1)
P3a T* = 2.08 (Lamellae)	-0.42(6)	-2.95(4)	1.09(2)	1.26(2)	0.17(1)
P4a T* = 1.5 (Cylinders)	-1.53(2)	-3.22(2)	0.70(1)	0.84(1)	0.16(0)
P4a T* = 1.5 (Ribbons)	-1.77(1)	-3.42(2)	0.69(1)	0.82(1)	0.14(0)

The transition from cylinders to ribbons observed for P4b is also characterized by lowering of U_{total} and reduced straining of angle and dihedral constraints (lower U_{angle} and $U_{dihedral}$). At the cylinder-ribbon coexistence temperature T* = 1.5 there is no significant difference in $g_{BB}(r)$ or $g_{SS}(r)$ before and after the transition (Figure 4.12), while the U_{total} decreases in the transition to ribbons (Table 4.3). The per-particle change in entropy from P4b cylinders to lamellae at T* = 1.5 is $TS_{cylinder \rightarrow ribbon} = -0.26\ \varepsilon$. As is the case for the P3b cylinder-lamellae transition, the lower angle and dihedral potentials for P4b ribbons show that on average oligomers lose conformational entropy (Table 4.3). Table 4.3 and Figure 4.12 show that these trends are consistent for the P3a transition from cylinders to lamellae at T* = 2.08 and the

P4a transition from cylinders to ribbons at T* = 1.5. Thus, the secondary order – order transition from cylinders to lamellae or ribbons is energetically driven and the cylindrical phase has higher entropy than the lamellae or ribbon phases for oligomers P3 and P4.

Lastly, the side chain-side chain attractions impact ODT and also govern whether or not order-order transitions occur at temperatures below ODT. The phase transitions between cylinders and lamellae or ribbons for oligomers P3 and P4 with *–syn* oriented side chains are only observed for oligomers with moderate side chain attractions, and not for oligomers with weak side chain attractions. Oligomers with weak side chain attraction (P3c,d and P4c,d) do not form lamellae or ribbons at low temperatures because they lack the energetic driving force for side chain aggregation. For example, P3d differs from P3b only in side chain interaction strength, and a comparison of their side chain contacts at temperatures below the ODT shows that the number of side chain bead contacts increases for P3b but not for P3d as temperature is decreased (Figure 4.7a and 7b).

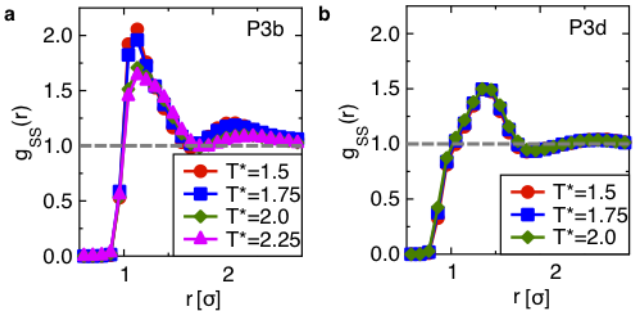

FIGURE 4.7: (a) Radial distribution functions, $g_{SS}(r)$, for moderately attractive P3b side chains show increased order as temperature is decreased. (b) Radial distribution function, $g_{SS}(r)$, for weakly attractive P3d side chains show no temperature-dependent change in structure.

Of particular note is the significant increase in side chain contacts at the transition between P3b cylinders T* = 2.0 and P3b lamellae at T* = 1.75, while the P3d side chain contacts do not change with temperature. The differences in side chain aggregation behavior between P3b (moderate side chain attraction) and P3d (weak side chain attraction) are representative of the

other –*syn* oriented oligomers (P3a vs. P3c, P4a vs. P4c, and P4b vs. P4d), which are included in Figure 4.13. For oligomers with –*anti* oriented side chains, side chain attraction does not significantly affect the morphologies formed except in the case of P1b vs. P1d and P2b vs. P2d. At low T*, P1d and P2d form perforated lamellae, while P1b and P2b form lamellae suggesting that long side chains with weak side chain – side chain attraction disrupt lamellar order. The difference in how temperature impacts morphology between systems with weak side chain attraction (*c* and *d*) and strong side chain attraction (*a* and *b*) demonstrates the importance of solvent and of side chain chemistry in achieving a desired morphology. Side chain chemistry or choice of solvent can be used to experimentally tune the relative attractions between side chains and backbones[37-39], and can therefore be used to select the formation of cylinders or lamellae/ribbons for a particular oligomer.

4.4 CONCLUSIONS

Using a coarse-grained model implemented with GPU-accelerated molecular dynamics software, we have studied melts of thiophene-based conjugated oligomers with varying architectures. We have determined how alkyl side chain length, orientation, placement, and molecular interactions affect the self-assembly of conjugated thiophene-based oligomers, the order disorder transition (ODT) and the equilibrated morphologies at the various temperatures below ODT. Architecture, specifically -*anti* vs. –*syn* oriented alkyl side chains, plays a large role in determining ODT because it dictates how neighboring oligomers pack and the amount of exposed backbone in the oligomers. Oligomers with more exposed backbone (e.g. –*syn* architectures) are shown to have higher ODT. Side chain – side chain attraction also affects ODT. Oligomers with moderately attractive side chains have higher ODTs than do oligomers with weakly attractive side chains. The effect of side chain length on ODT depends on side chain

– side chain attraction strength. Oligomer architecture determines the morphology assembled below the ODT, with *–syn* oligomers forming cylinders and *-anti* oligomers forming lamellar morphologies at the ODT. Side chain – side chain attraction governs whether a secondary order - order phase transition is possible at lower temperatures. Oligomers with *–syn* architecture and moderate side chain attraction transition from cylinders to lamellae or ribbons at low temperatures while oligomers with *–syn* architecture and weak side chain attraction do not. The sensitivity of the aforementioned cylinder to lamellae and cylinder to ribbon transitions to side chain attraction exemplifies the balance of entropic and energetic driving forces governing order-disorder, order – order transitions and these various morphologies. We find that conformation entropy arising from the relatively flexible side chains is key to the stabilization of cylinder morphologies relative to lamellae or ribbons, which can be assembled by oligomers with *–syn* architecture and moderate side chain attraction.

With the design rules presented here experimentalists can infer how the side chains extending from conjugated thiophene backbones impact the thermodynamic stability of lamellar and cylindrical morphologies, which can in turn help identify whether the morphologies observed in experiments are nearing equilibrium or are arrested in kinetically trapped configurations.

4.5 ACKNOWLEDGEMENTS

This work was supported by Department of Energy under Grant No. DE-SC0003912. The majority of this research used GPU resources of the National Energy Research Scientific Computing Center, which is supported by the Office of Science of the U.S. Department of Energy under Contract No. DE-AC02-05CH11231. Portions of this work utilized the Janus supercomputer, which is supported by the National Science Foundation (award number CNS-

0821794) and the University of Colorado Boulder. The Janus supercomputer is a joint effort of the University of Colorado Boulder, the University of Colorado Denver and the National Center for Atmospheric Research. Janus is operated by the University of Colorado Boulder. We thank Michael Engel, whose visualization software provided the basis for our diffraction pattern routines.

4.6 REFERENCES

1. McCulloch, I.; Heeney, M.; Chabinyc, M. L.; DeLongchamp, D.; Kline, R. J.; Coelle, M.; Duffy, W.; Fischer, D.; Gundlach, D.; Hamadani, B.; Hamilton, R.; Richter, L.; Salleo, A.; Shkunov, M.; Sporrowe, D.; Tierney, S.; Zhong, W. *Advanced Materials* **2009,** 21, (10-11), 1091-1109.

2. Singh, C. R.; Gupta, G.; Lohwasser, R.; Engmann, S.; Balko, J.; Thelakkat, M.; Thurn-Albrecht, T.; Hoppe, H. *Journal of Polymer Science Part B-Polymer Physics* **2013,** 51, (12), 943-951.

3. Ong, B. S.; Wu, Y. L.; Li, Y. N.; Liu, P.; Pan, H. L. *Chemistry-a European Journal* **2008,** 14, (16), 4766-4778.

4. Shen, X. B.; Duzhko, V. V.; Russell, T. P. *Advanced Energy Materials* **2013,** 3, (2), 263-270.

5. Gadisa, A.; Oosterbaan, W. D.; Vandewal, K.; Bolsee, J. C.; Bertho, S.; D'Haen, J.; Lutsen, L.; Vanderzande, D.; Manca, J. V. *Advanced Functional Materials* **2009,** 19, (20), 3300-3306.

6. Vakhshouri, K.; Kozub, D. R.; Wang, C. C.; Salleo, A.; Gomez, E. D. *Physical Review Letters* **2012,** 108, (2), 5.

7. Kozub, D. R.; Vakhshouri, K.; Orme, L. M.; Wang, C.; Hexemer, A.; Gomez, E. D. *Macromolecules* **2011,** 44, (14), 5722-5726.

8. Schmidt-Hansberg, B.; Sanyal, M.; Klein, M. F. G.; Pfaff, M.; Schnabel, N.; Jaiser, S.; Vorobiev, A.; Muller, E.; Colsmann, A.; Scharfer, P.; Gerthsen, D.; Lemmer, U.; Barrena, E.; Schabel, W. *Acs Nano* **2011,** 5, (11), 8579-8590.

9. Treat, N. D.; Brady, M. A.; Smith, G.; Toney, M. F.; Kramer, E. J.; Hawker, C. J.; Chabinyc, M. L. *Advanced Energy Materials* **2011,** 1, (1), 82-89.

10. Tashiro, K.; Ono, K.; Minagawa, Y.; Kobayashi, M.; Kawai, T.; Yoshino, K. *Journal of Polymer Science Part B-Polymer Physics* **1991,** 29, (10), 1223-1233.

11. Chen, S. A.; Ni, J. M. *Macromolecules* **1992,** 25, (23), 6081-6089.

12. Causin, V.; Marega, C.; Marigo, A.; Valentini, L.; Kenny, J. M. *Macromolecules* **2005,** 38, (2), 409-415.

13. Kline, R. J.; DeLongchamp, D. M.; Fischer, D. A.; Lin, E. K.; Richter, L. J.; Chabinyc, M. L.; Toney, M. F.; Heeney, M.; McCulloch, I. *Macromolecules* **2007,** 40, (22), 7960-7965.

14. Gallazzi, M. C.; Castellani, L.; Marin, R. A.; Zerbi, G. *Journal of Polymer Science Part a-Polymer Chemistry* **1993,** 31, (13), 3339-3349.

15. Koch, F. P. V.; Heeney, M.; Smith, P. *Journal of the American Chemical Society* **2013,** 135, (37), 13699-13709.

16. Prosa, T. J.; Winokur, M. J.; McCullough, R. D. *Macromolecules* **1996,** 29, (10), 3654-3656.

17. Brinkmann, M. *Journal of Polymer Science Part B-Polymer Physics* **2011,** 49, (17), 1218-1233.

18. Ma, X. J.; Guo, Y.; Wang, T.; Su, Z. H. *Journal of Chemical Physics* **2013,** 139, (1).

19. Ko, S. W.; Hoke, E. T.; Pandey, L.; Hong, S. H.; Mondal, R.; Risko, C.; Yi, Y. P.; Noriega, R.; McGehee, M. D.; Bredas, J. L.; Salleo, A.; Bao, Z. A. *Journal of the American Chemical Society* **2012,** 134, (11), 5222-5232.

20. Shinozaki, A.; Jasnow, D.; Balazs, A. C. *Macromolecules* **1994,** 27, (9), 2496-2502.

21. Stepanyan, R.; Subbotin, A.; Knaapila, M.; Ikkala, O.; ten Brinke, G. *Macromolecules* **2003,** 36, (10), 3758-3763.

22. Borisov, O. V.; Zhulina, E. B. *Macromolecules* **2005,** 38, (6), 2506-2514.

23. Ho, V.; Boudouris, B. W.; Segalman, R. A. *Macromolecules* **2010,** 43, (19), 7895-7899.

24. Salammal, S. T.; Mikayelyan, E.; Grigorian, S.; Pietsch, U.; Koenen, N.; Scherf, U.; Kayunkid, N.; Brinkmann, M. *Macromolecules* **2012,** 45, (13), 5575-5585.

25. Malik, S.; Nandi, A. K. *Journal of Polymer Science Part B-Polymer Physics* **2002,** 40, (18), 2073-2085.

26. McCulloch, I.; Heeney, M.; Bailey, C.; Genevicius, K.; Macdonald, I.; Shkunov, M.; Sparrowe, D.; Tierney, S.; Wagner, R.; Zhang, W. M.; Chabinyc, M. L.; Kline, R. J.; McGehee, M. D.; Toney, M. F. *Nature Materials* **2006,** 5, (4), 328-333.

27. Melis, C.; Colombo, L.; Mattoni, A. *Journal of Physical Chemistry C* **2011,** 115, (2), 576-581.

28. Adachi, T.; Brazard, J.; Ono, R. J.; Hanson, B.; Traub, M. C.; Wu, Z. Q.; Li, Z. C.; Bolinger, J. C.; Ganesan, V.; Bielawski, C. W.; Bout, D. A. V.; Barbara, P. F. *Journal of Physical Chemistry Letters* **2011,** 2, (12), 1400-1404.

29. Schwarz, K. N.; Kee, T. W.; Huang, D. M. *Nanoscale* **2013,** 5, (5), 2017-2027.

30. Carrillo, J.-M. Y.; Kumar, R.; Goswami, M.; Sumpter, B. G.; Brown, W. M. *Physical Chemistry Chemical Physics* **2013,** 15, (41), 17873-17882.

31. Jankowski, E.; Marsh, H. S.; Jayaraman, A. *Macromolecules* **2013**, 46, (14), 5775-5785.

32. Alexiadis, O.; Mavrantzas, V. G. *Macromolecules* **2013,** 46, (6), 2450-2467.

33. Huang, D. M.; Faller, R.; Do, K.; Moule, A. J. *Journal of Chemical Theory and Computation* **2010,** 6, (2), 526-537.

34. Huang, D. M.; Moule, A. J.; Faller, R. *Fluid Phase Equilibria* **2011,** 302, (1-2), 21-25.

35. Verlet, L. *Physical Review* **1967,** 159, (1), 98-103.

36. Weeks, J. D.; Chandler, D.; Andersen, H. C. *Journal of Chemical Physics* **1971,** 54, (12), 5237-5247.

37. Zhao, K.; Xue, L.; Liu, J.; Gao, X.; Wu, S.; Han, Y.; Geng, Y. *Langmuir* **2010,** 26, (1), 471-477.

38. Keum, J. K.; Xiao, K.; Ivanov, I. N.; Hong, K.; Browning, J. F.; Smith, G. S.; Shao, M.; Littrell, K. C.; Rondinone, A. J.; Payzant, E. A.; Chen, J.; Hensley, D. K. *Crystengcomm* **2013,** 15, (6), 1114-1124.

39. Kesters, J.; Kudret, S.; Bertho, S.; Van den Brande, N.; Defour, M.; Van Mele, B.; Penxten, H.; Lutsen, L.; Manca, J.; Vanderzande, D.; Maes, W. *Organic Electronics* **2014,** 15, (2), 549-562.

40. Anderson, J. A.; Lorenz, C. D.; Travesset, A. *Journal of Computational Physics* **2008,** 227, (10), 5342-5359.

41. Humphrey, W.; Dalke, A.; Schulten, K. *Journal of Molecular Graphics & Modelling* **1996,** 14, (1), 33-38.

42. Schmidt-Rohr, K. *Journal of Applied Crystallography* **2007,** 40, 16-25.

43. Frenkel, D. *European Physical Journal Plus* **2013,** 128, (1).

44. Adams, M.; Dogic, Z.; Keller, S. L.; Fraden, S. *Nature* **1998,** 393, (6683), 349-352.

45. Dogic, Z.; Fraden, S. *Physical Review Letters* **1997,** 78, (12), 2417-2420.

46. Vrij, A. *Pure and Applied Chemistry* **1976,** 48, (4), 471-483.

47. Bates, F. S. *Science* **1991,** 251, (4996), 898-905.

48. Stadler, R.; Auschra, C.; Beckmann, J.; Krappe, U.; Voigtmartin, I.; Leibler, L. *Macromolecules* **1995,** 28, (9), 3080-3097.

49. Wu, Y. L.; Liu, P.; Gardner, S.; Ong, B. S. *Chemistry of Materials* **2005,** 17, (2), 221-223.

50. Winokur, M. J.; Spiegel, D.; Kim, Y.; Hotta, S.; Heeger, A. J. *Synthetic Metals* **1989,** 28, (1-2), C419-C426.

51. Prosa, T. J.; Winokur, M. J.; Moulton, J.; Smith, P.; Heeger, A. J. *Macromolecules* **1992,** 25, (17), 4364-4372.

52. Koppe, M.; Scharber, M.; Brabec, C.; Duffy, W.; Heeney, M.; McCulloch, I. *Advanced Functional Materials* **2007,** 17, (8), 1371-1376.

4.7 SUPPORTING INFORMATION

4.7.1 Model and Simulation

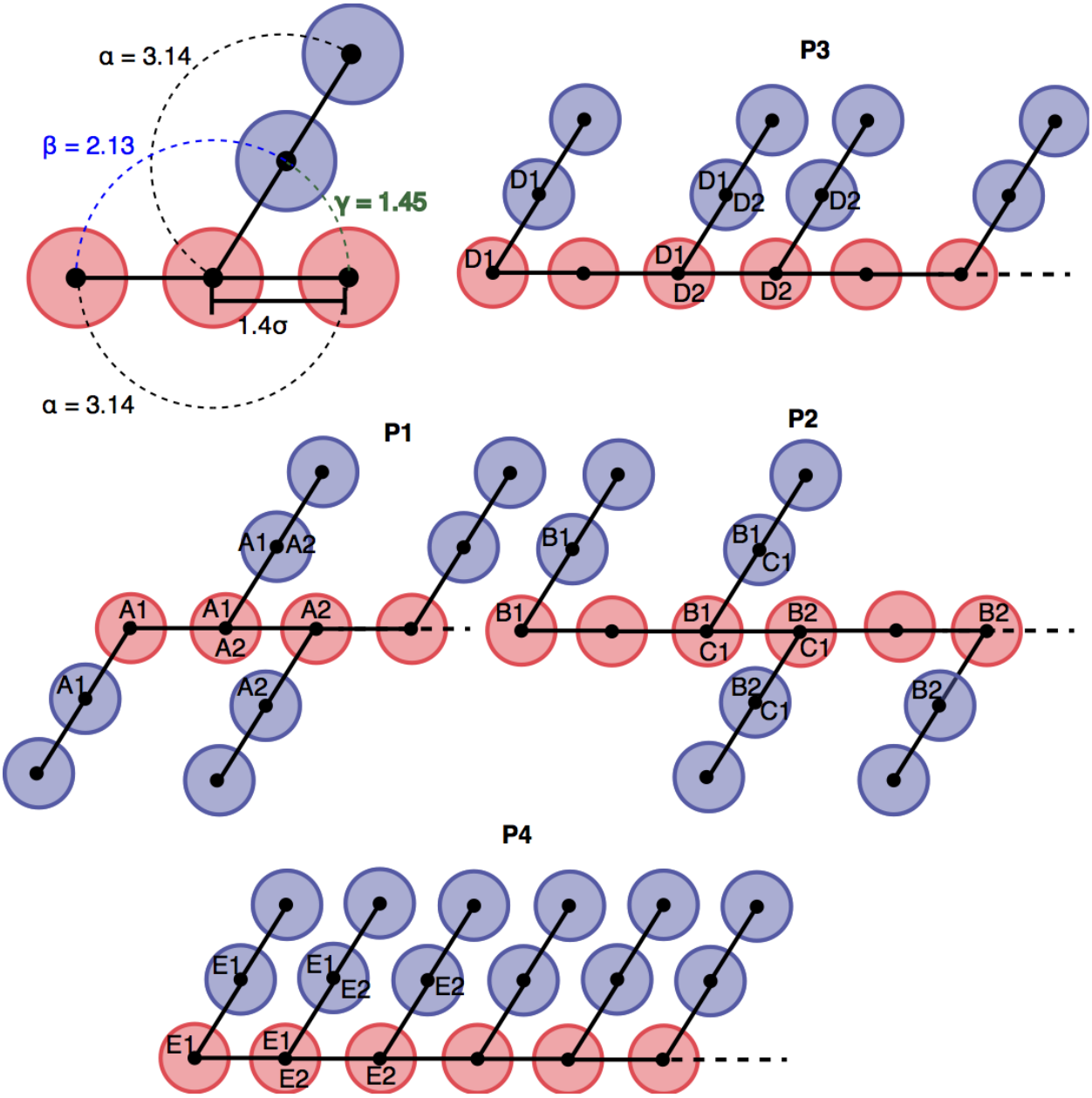

FIGURE 4.8: Connectivity of coarse-grained beads and the associated angle and dihedral constraints for oligomers P1, P2, P3, and P4.

The four oligomers differ in the number of side chains and the dihedral angle constraints imposed to maintain their respective architectures. Five different dihedral angle types are

denoted by the letters A-E. Examples of four beads comprising a dihedral angle constraint are indicated with a letter and number (e.g., A1 beads are all part of a type A dihedral angle constraint, and A2 beads are part of a different type A dihedral angle constraint). Dashed lines indicate where additional monomers are added to the shown schematics to complete the 15-bead oligomers.

Of the four oligomer architectures used in this work, P1, P2, and P3 are identical to those used in Jankowski, Marsh, and Jayaraman, *Macromolecules 46, 14 (2013),* and are shown In Figure 4.8. Oligomer P4 is similar to oligomer P3 in that each side chain extends along the same side of the backbone, but P4 has side chains extending from each backbone bead. Harmonic potentials model bond stretching constraints ($U_{bond} = k_{bond}(l - l_0)^2$), angle bending constraints ($U_{angle} = k_{angle}(\theta - \theta_0)^2$), and dihedral angle twisting constraints ($U_{di} = k_{di}(\phi - \phi_0)^2$), as in Jankowski, Marsh, and Jayaraman, *Macromolecules 46, 14 (2013)*, with the same spring constants: $k_{bond} = 50\ \varepsilon/\sigma^2$ for all bonded pairs, $k_{angle} = 6\ \varepsilon/\text{radian}^2$ for three body angle potentials with equilibrium angles $\beta = 2.13$ and $\gamma = 1.45$, and is $30\ \varepsilon/\text{radian}^2$ for angle $\alpha = 3.14$. The side chains of P1 are constrained only with dihedral angle A, which has equilibrium angle 3.14 (e.g., the four A1's or the four A2's in Figure 4.8.) and spring constant $10\ \varepsilon/\text{radian}^2$. The topology of P2 is maintained by dihedral angles B (equilibrium angle 0, spring constant $50\ \varepsilon/\text{radian}^2$) and C (equilibrium angle 3.14, spring constant $50\ \varepsilon/\text{radian}^2$). The topology of P3 is maintained by dihedral angle D (equilibrium angle 0, spring constant $10\ \varepsilon/\text{radian}^2$). The topology of P4 is maintained by dihedral angle E (equilibrium angle 0, spring constant $10\ \varepsilon/\text{radian}^2$).

4.7.2 Criteria for Choosing Snapshots for Data Analysis

Three criteria must be met for snapshots from a simulation trajectory to be used as statistically independent, equilibrated snapshots for data analysis. These are as follows:

The first criterion, that at least 20 **snapshots from the end of a trajectory are statistically independent**, is determined by using the autocorrelation time of the potential energy time series as a proxy for the autocorrelation time of structure. The potential energy autocorrelation time *a* is measured by identifying the first zero of

$$C(dt) = \frac{\langle (PE(t) - A)(PE(t+dt) - A) \rangle}{\sigma^2}$$

where *PE(t)* is the instantaneous potential energy at time *t*, with average *A* and variance σ^2 (not to be confused with particle diameter σ) over a subset of full potential energy time series. The first criterion is satisfied if there exists a subset of the potential energy time series with range $(t_{max} - t_{min}) > 20a$.

The second criterion, that the **structure observed is not dependent upon the shape of the simulation box**, is satisfied through the use of secondary simulations in which the periodic box axes are allowed to vary independently and as determined by the diagonal components of the pressure tensor. These "orthorhombic" simulations either show that the structure from the simulations with cubic boxes are stable under anisotropic box deformations, or allow the periodic spacing of features to relax slightly (typically a few 0.1 σ). The autocorrelation time criterion mentioned above is imposed on the orthorhombic simulation trajectories.

The third and final criterion that must be met is that no periodic box axis is short enough (22.1 σ) to allow for an oligomer to interact with itself through a periodic boundary. For three systems, P1b T* = 1.5, P4b T* = 1.5 and P4b T* = 1.75, we observed one box axis becoming shorter than 22.1 σ before 20 independent configurations were achieved in the orthorhombic runs. For these systems, we performed additional simulations for each system, using non-cubic

boxes from the orthorhombic runs as initial conditions in NPT simulations with isotropic pressure integration.

4.7.3 Additional Results

TABLE 4.4: Exposed backbone area calculated using the solvent available surface area method averaged over 20 snapshots for oligomers P1, P2, P3, and P4 at T* = 1.5. The average exposed backbone areas, A_E, plotted in Figure 4.3 in the main manuscript are the average of the exposed backbone areas of the four side chain types, *a*, *b*, *c*, and *d*, for each oligomer P1, P2, P3, and P4 at T* = 1.5 shown in this table.

	Backbone Area [σ^2]	+/-
P1a	151.4	44.3
P1b	132.1	60.1
P1c	148.9	44.7
P1d	127.4	32.8
P2a	236.3	48.9
P2b	239.0	42.2
P2c	259.1	52.0
P2d	225.1	58.0
P3a	286.9	50.4
P3b	277.0	51.1
P3c	265.9	56.0
P3d	277.5	50.1
P4a	257.7	47.7
P4b	237.0	55.4
P4c	281.9	52.0
P4d	239.0	59.7

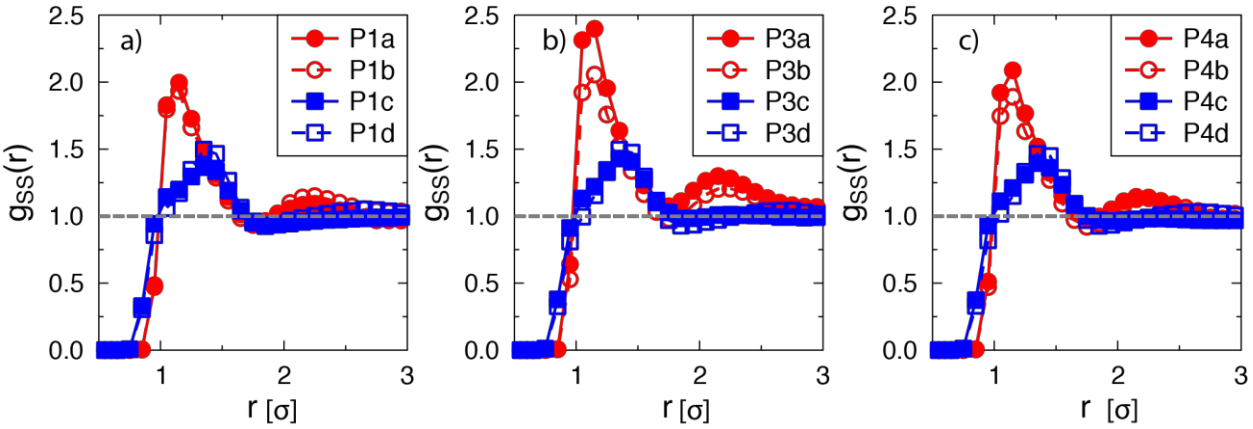

FIGURE 4.9: Side chain – side chain radial distribution function, $g_{SS}(r)$, as a function of reduced distance, r, for a) P1, b) P3, and c) P4 for side chain types *a*, *b*, *c*, and *d*, at T* = 1.5.

The plot of $g_{SS}(r)$ for P2 is found in the main manuscript, Figure 4.3. As for oligomer P2, the $g_{SS}(r)$ plots for oligomers P1, P3, and P4 show that at a given temperature, moderately attractive side chains are highly aggregated at the separation distance at the Lennard-Jones potential minimum ($r\sim=1.15\ \sigma$), and weakly attractive side chains show relatively less coordination at peak distance $r\sim=1.4\ \sigma$. The peak distance of $r \sim= 1.4\ \sigma$ matches the equilibrium bond length between side chain beads of 1.4 σ, demonstrating that there is negligible side chain aggregation due to non-bonded attractive interactions for all four oligomers at weak side chain – side chain attraction.

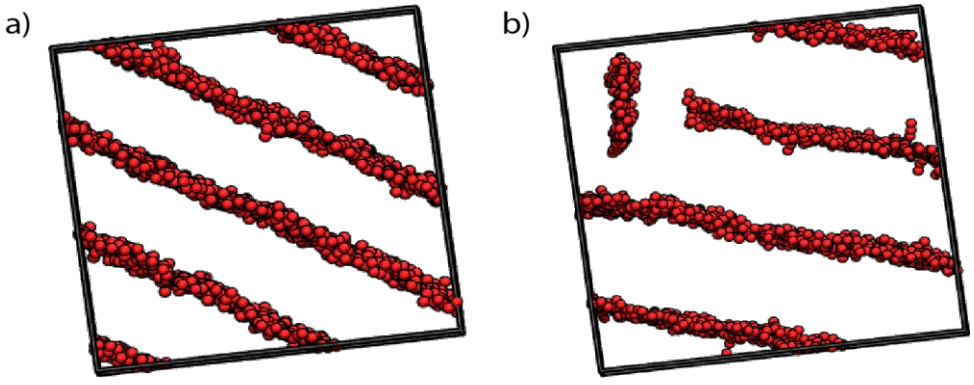

FIGURE 4.10: a) Snapshot of equilibrated P1b (ε_{SS} = 1.0) lamellae T* = 1.5. b) Snapshot of simulation at T* = 1.25 with the starting configuration shown in part (a) after transformation to P1d (setting ε_{SS} = 0.1) and equilibration.

Lamellae transform into perforated lamellae with the introduction of weak side chain – side chain interaction potentials (ε_{SS} = 0.1) suggesting that the perforated lamellar phase is stable for P1d at T* = 1.25.

TABLE 4.5: Widths of backbone lamellae for systems of oligomers P1 and P2 at temperatures T* ≤ T^*_{ODT}. Lamellar widths are not reported at temperatures where the oligomer is disordered, denoted by, D, or at temperatures where simulations were not performed, denoted by "--".

	P1		**P2**	
	Width [σ]	**+/-**	**Width [σ]**	**+/-**
a T* = 1.5	0.68	0.06	0.90	0.04
a T* = 1.75	0.85	0.12	0.89	0.05
b T* = 1.5	0.53	0.19	0.96	0.02
b T* = 1.75	0.63	0.09	0.91	0.05
b T* = 2.0	D	D	0.90	0.02
c T* = 1.25	0.52	0.09	--	--
c T* = 1.5	D	D	0.81	0.05
c T* = 1.75	D	D	0.87	0.02
d T* = 1.25	0.62	0.18	--	--
d T* = 1.5	D	D	0.97	0.06
d T* = 1.75	D	D	0.85	0.10

The widths of the backbone lamellae are greater for P2 than for P1. Spherical backbone beads in our model are able to hexagonally pack and the decreased side chain density for P2 compared to P1 promotes this packing and increases lamellar thickness for P2 compared to P1.

Supporting Movie SM1: To determine whether the *–anti* orientation of P2b side chains inhibits the formation of the cylinders that form for P3b with *–syn* oriented side chains, we continue the equilibrated simulation of P2b at T* = 2.0 with the dihedral angle bond constants set to 0. Within 5e7 time steps, the P2b lamellae transform into cylinders with oligomer side chains in the *-syn* orientation. Thus, oligomer architectures with side chains in the *–anti* orientation prevent the formation of the energetically favorable cylindrical phase.

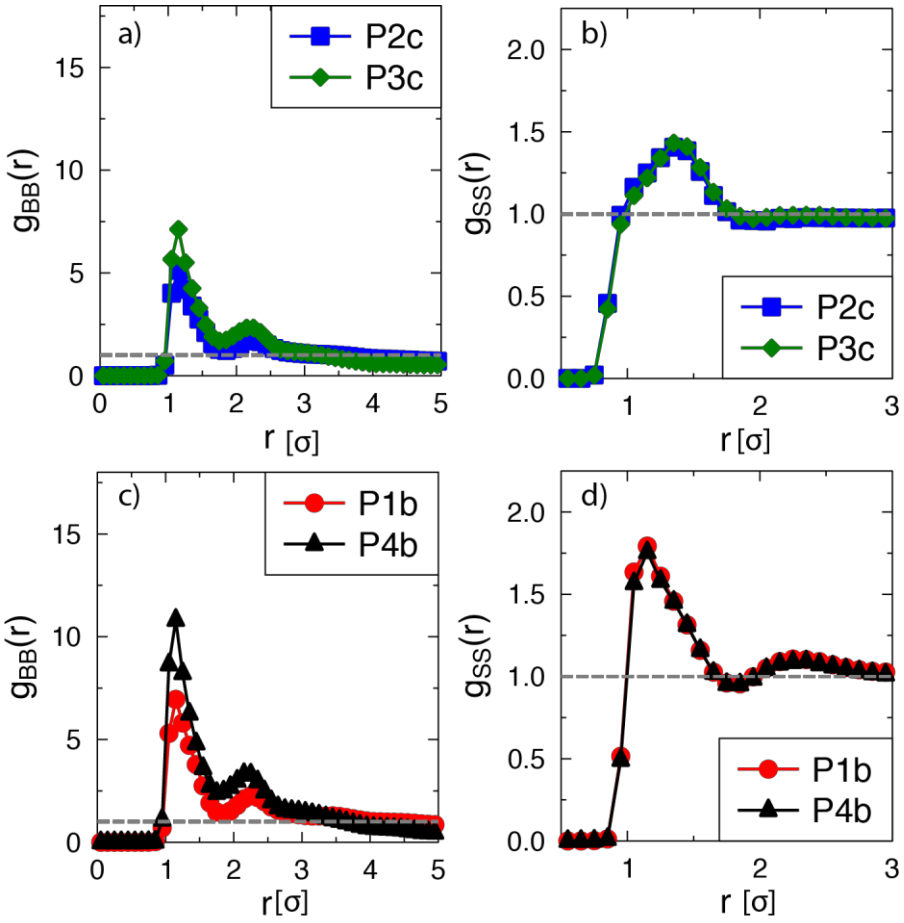

FIGURE 4.11: a) Backbone- backbone radial distribution function, $g_{BB}(r)$, and b) side chain – side chain radial distribution function, $g_{SS}(r)$, as a function reduced distance, r, for oligomers P2c and P3c at T* = 1.75. c) $g_{BB}(r)$, and d) $g_{SS}(r)$ for oligomers P1b and P4b at T* = 1.75.

P1 and P2 have side chains in the *–anti* orientation and form lamellae at T* = 1.75 while P3 and P4 have side chains in the *–syn* orientation and form cylinders at T* = 1.75. P2 and P3 have the same density of side chains and P1 and P4 have the same density of side chains so these systems with equal side chain density are compared to isolate the effect of side chain orientation on morphology. In both cases, the cylindrical phase (P3c or P4b) is energetically favorable and allows for more backbone-backbone contacts than does the lamellar phase (P2c or P1b, respectively) (Figure 4.10a and c). $g_{SS}(r)$ does not change significantly between P2c and P3c, or

between P1b and P4b (Figure 4.10b and d, respectively). Thus, side chain orientation and equilibrium morphology do not impact the number of side chain – side chain contacts. These trends match those for the comparison of P2b and P3b shown in the main manuscript.

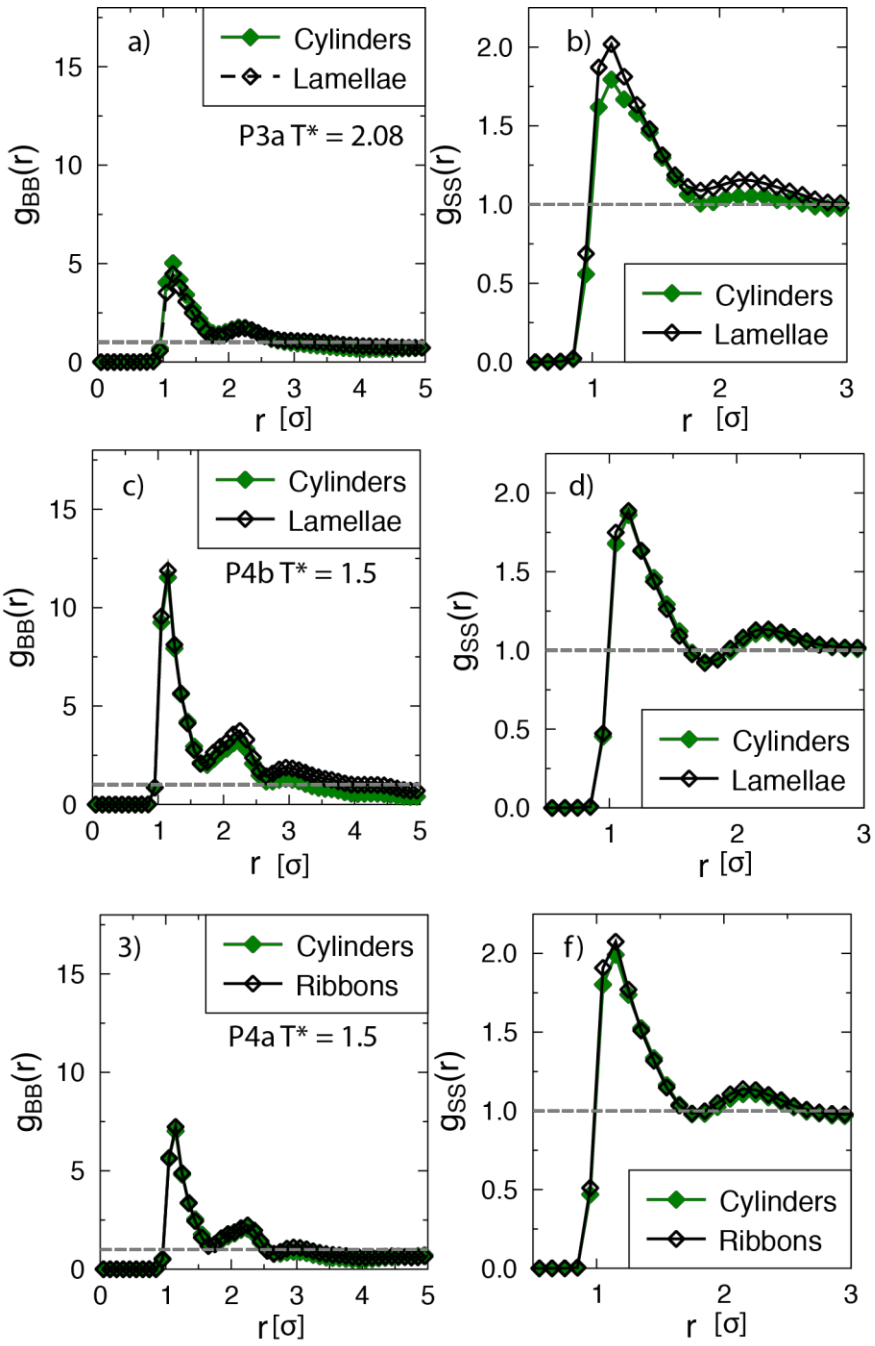

FIGURE 4.12: a) Backbone - backbone radial distribution function, $g_{BB}(r)$, and b) side chain – side chain radial distribution function, $g_{SS}(r)$, as a function reduced distance, r, for oligomer P3a at T* = 2.08 before the and after the phase transition from cylinders to lamellae. c) $g_{BB}(r)$, and d) $g_{SS}(r)$ for oligomer P4b T* = 1.5 before the and after the phase transition from cylinders to lamellae. e) $g_{BB}(r)$ and f) $g_{SS}(r)$, for oligomer P4a T* = 1.5 before the and after the phase transition from cylinders to ribbons.

The $g_{BB}(r)$ and $g_{SS}(r)$ plots show that there is little change in the number of backbone – backbone and side chain – side chain contacts at the transition temperature for P4b and P4a and this trend is consistent with the data shown for P3b in the main manuscript. P3a cylinders have slightly more backbone – backbone contacts and slightly fewer side chain contacts than do P3a lamellae after the transition.

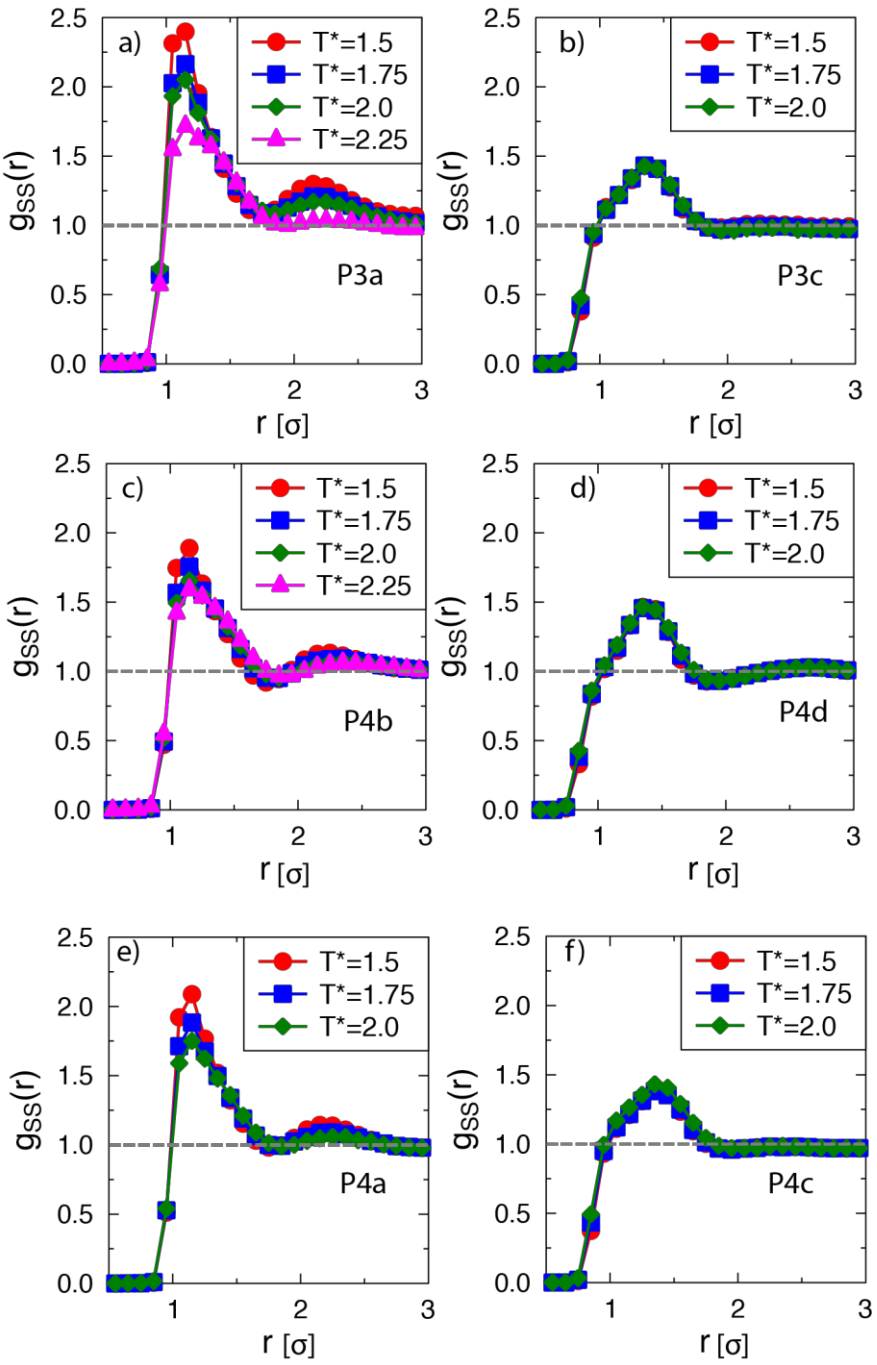

FIGURE 4.13: a) Side chain – side chain radial distribution function, $g_{SS}(r)$, as a function reduced distance, r, for oligomer P3a at T* = 1.5, 1.75, 2.0 and 2.25. b) $g_{SS}(r)$ for oligomer P3c at T* = 1.5, 1.75 and 2.0. c) $g_{SS}(r)$ for oligomer P4b at T* = 1.5, 1.75, 2.0 and 2.25. d) $g_{SS}(r)$ for oligomers P4d at T* = 1.5, 1.75 and 2.0. e) $g_{SS}(r)$ for oligomer P4a at T* = 1.5, 1.75, and 2.0. f) $g_{SS}(r)$ for oligomer P4c at T* = 1.5, 1.75 and 2.0.

Oligomers with moderate side chain – side chain attraction P3a, P4b, and P4a (left column) show increased side chain – side chain aggregation as temperature decreases, while oligomers with weak side chain – side chain attraction P3c, P4d, and P4c (right column) show little side chain – side chain aggregation and no change in side chain – side chain aggregation with temperature. These trends are consistent with those of P3b and P3d shown in the main manuscript and indicate that side chain – side chain attraction is a key driving force for the transition from cylinders at high temperature to lamellar morphologies at low temperature for oligomers with side chains in the *–syn* orientation.

Chapter 5

Effect of Additive Length and Chemistry on the Morphology of Blends of Conjugated Thiophenes and Fullerene Derivative Acceptor Molecules

Adapted from: *J. Polym. Sci., Part B: Polym. Phys.* **2015**, *in press.*

5.1 INTRODUCTION

Blends of electron donating thiophene-based conjugated polymers and electron accepting fullerene derivatives are used in active layers of bulk heterojunction organic solar cells. Since the morphology of the donor-acceptor blends within the active layer strongly influences device efficiency, significant scientific effort has gone towards finding routes for tuning the morphology of these blends. It has been shown that architecture and chemistry of donors and acceptor molecule, casting solvent, and processing conditions influence the donor-acceptor morphology[1-5]. Typical electron donor thiophene-based polymers are poly(3-alkylthiophene)s (**P3*A*T**)s, poly(2,2′:5′,2″-3,3″-dialkyl-terthiophene)s (**PTTTs**) and (2,5-bis(3-alkylthiophen-2-yl)thieno[3,2-b]thiophene)s (**PBTTT**). Electron acceptor molecules are typically functionalized fullerene derivatives such as [6,6]-phenyl-C_{61}-butyric acid methyl ester ($PC_{61}BM$) and [6,6]-phenyl-C_{71}-butyric acid methyl ester ($PC_{71}BM$). In recent work, a third component additive, such as diiodooctane (**DIO**), octanedithiol, and chloronapthalene (**CN**), has been introduced into the donor-acceptor blend with the goal of altering morphology and significantly increasing device efficiency[6-19]. The motivation behind using a third component additive lies in the fact that the majority of the additives have a higher boiling point than the solvent used in the blend (such as chlorobenzene, 1,2-dichlorobenzene, or chloroform), and thus the additive continues to modulate the blend morphology even after the solvent has evaporated[6]. In addition, one could choose the additives so as to selectively solubilize one of the blend components, altering the crystallization and diffusion of the donor and acceptor molecules[6, 13, 16, 19, 20].

Recent studies have suggested that additives, such as CN, facilitate polymer aggregation in solution [6, 13, 14], creating many nucleation sites and leading to the formation of a fibril polymer network with the PCBM filling the spaces in that polymer network[13]. For PBDTTPD (poly(di(2-ethylhexyloxy)benzo[1,2-b:4,5-b′]dithiophene-co-octylthieno[3,4-c]pyrrole-4,6-dione):$PC_{70}BM$ blends with highly phase segregated as-cast morphologies, domain sizes shrink with additive-induced polymer nucleation creating a more interconnected morphology with high interfacial area that is thought to be better for device efficiency than large phase separated domains[13]. When the as-cast morphology is intermixed, additive-induced polymer nucleation allows for more polymer-acceptor phase separation, creating more donor-acceptor interfacial area and increasing device efficiency[13]. Other work suggests that the relative affinity of additives such as DIO or octanedithiol for the fullerene derivative acceptor drives changes in donor-acceptor morphology[7, 9, 12, 16]. For example, recent work by Buchaca-Domingo *et al.* has shown that alkanoic acid methyl ester additives with varying alkyl segment lengths are capable of tuning the morphology of blends of the thiophene-based polymer pBTTT (poly(2,5-bis(3-alkyl-thiophene-2-yl)thieno[3,2-b] thiophene)) and the acceptor molecule $PC_{61}BM$[21]. Alkanoic acid ethyl ester additives were chosen with the hypothesis that the methyl ester head group of the additive is attractive to the PCBM molecule. In the absence of additives, 1:1 blends of PBTTT and $PC_{61}BM$ form bimolecular crystals with the fullerene derivatives intercalated between side chains of the PBTTT. In ternary blends with the additive heptanoic acid methyl ester (ME7), pure fullerene domains are formed with some acceptor molecules remaining in the intercalated phase, creating pure domains to facilitate charge transport and maintaining interfacial area between the donor and acceptor domains for charge dissociation. Alkanoic methyl esters with longer alkyl segments (ME12) remove more of the $PC_{61}BM$ from the intercalated phase compared to the ME7 case,

reducing donor-acceptor interfacial area and device efficiency compared to the ME7 case. The location of the additives in the ternary blend and the mechanism underlying this demixing of the conjugated polymer and fullerene derivative are however not well understood.

The above studies demonstrate that certain additives increase device efficiency and control morphology, but thus far, there is little work that systematically relates a range of additive features to their effects on donor-acceptor blend morphology[14]. In this regard, molecular simulations provide the ability to systematically vary additive features one feature at a time, and to characterize how the additive length and chemistry dependent location of these additives in the blend before evaporation affect effective donor-acceptor interactions, which is difficult to resolve experimentally. To the best of our knowledge, there has been no such simulation work investigating the effect of additive features on thoiphene-based polymer-acceptor blend morphology.

In this paper we use the coarse-grained models, presented and validated in our previous work[22,23,24], to simulate effect of additives of varying size and chemistry (Figure 5.1), mimicking methyl ester, DIO, and alkanethiol–like additives, on morphology of blends of conjugated thiophene-based oligomer (donor) and fullerene derivatives (acceptor). We study two different oligomer architectures: PTTT-like oligomers, denoted as **P1** oligomers in this paper, in which acceptors intercalate in the absence of additives, and P3DDT-like oligomers, denoted as **P2** oligomers, where acceptor intercalation is prohibited by the high side chain density along the backbone. We find that additive length and chemistry affect the extent of donor-acceptor phase separation in blends of conjugated thiophene-based oligomers and acceptor molecules. Additive functional end groups that are attracted to acceptor molecules are necessary to induce macrophase separation of acceptors from the oligomers. Blends with additives having long alkyl

segments are less macrophase separated than those with additives having shorter alkyl segments because the long alkyl segments sterically prevent the formation of large acceptor aggregates. Oligomer architecture also affects the degree of additive-induced phase separation. Blends with oligomers that are less crystalline (P2 oligomers) are less macrophase separated than blends with oligomers that are more crystalline (P1 oligomers) which have higher driving force for oligomer backbone ordering. In blends of P1 oligomers where acceptors are intercalated in the absence of additives, the addition of additives with functional end groups attracted to the acceptor molecules reduces the extent of intercalation in the blend.

The organization of the paper is as follows. We first describe in Section II: Approach, our coarse-grained model for conjugated thiophene-based oligomers, acceptor molecules, and additives. We then discuss the simulation method and techniques used to analyze simulation results. In Section III: Results, we present: A) the effect of additives on P1 oligomer blend morphology, B) the effect of additives on P2 oligomer blend morphology, and C) a comparison of P1 and P2 oligomer blend morphologies in the presence of additives. Finally we conclude with a summary of results and applications of this work.

5.2 APPROACH

5.2.1 Model

We use the coarse-grained (CG) model of thiophene oligomers and fullerene derivatives that we developed based on some earlier work by Huang *et al.* in refs [25], [26] and [27]), and we validated through comparison with experiments in refs [22], [23] and [24]. Using these CG models, in this paper we simulate blends of thiophene-based conjugated oligomers, acceptor molecules mimicking fullerene derivatives, and third minority component additives. Figure 5.1a shows the two different oligomer architectures simulated in this work: i) oligomers mimicking

poly(2,2′:5′,2″-3,3″-dialkyl-terthiophene), termed **P1** oligomers, and ii) oligomers mimicking poly(3-dodecylthiophene), termed **P2** oligomers; Figure 5.1b shows the corresponding chemical structures of PTTT and P3DDT. We model conjugated thiophene-based oligomers as shown in Figure 5.1c with each backbone thiophene ring represented with one spherical bead, 'B', and alkyl side chains as a chain of beads, 'S', with each bead representing three alkyl groups. In this study 15mer oligomers with dodecyl side chains (4 'S' beads per monomer) are simulated. Acceptor molecules, mimicking fullerene derivatives are modeled as a rigid body of 13 'A' beads (Figure 5.1d). Additives, mimicking methyl ester, DIO, and alkanethiol–like additives, are modeled using 'E' beads, representing alkyl groups and 'F' beads, representing end groups on the additive that are attracted to acceptor molecules (Figure 5.1e). We study five types of additives to systematically understand effect of varying lengths and end group functionalities. These five types of additives are denoted as EX, where $X \in [1,2,3,4,5]$ as shown in Figure 5.1e. Additives E1 and E2 have three beads: E1 has three 'E' beads and E2 has two 'E' beads and one functional end bead, 'F'. Additives E3, E4, and E5 have five beads: E3 has five 'E' beads, E4 has four 'E' beads and one functional 'F' bead, and E5 has three 'E' beads and two functional ends, 'F', one on each end of the additive. Simulating additives E1 and E3 without functionalized ends allows us to determine purely steric repulsion driven effects of additives, while simulating additives with varying number of number of functionalized ends allows us to determine effects of acceptor-additive attractions on the overall blend morphology. All coarse grained beads have diameter of one unit σ which corresponds to $3\dot{A}$, and all distances in this paper are denoted in units of σ.

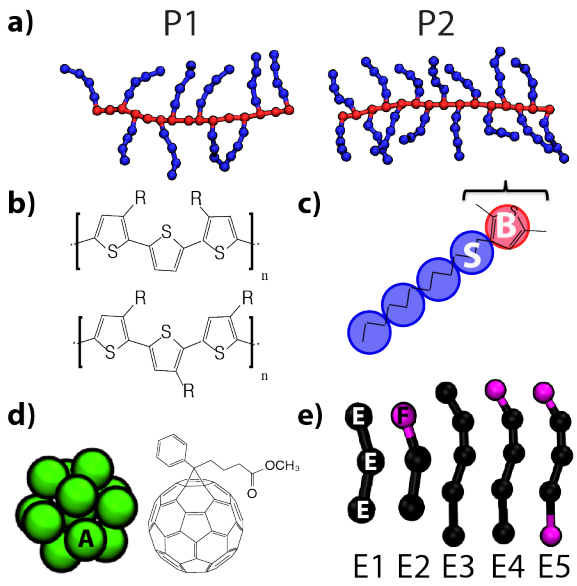

FIGURE 5.1: a) Coarse-grained model of **P1** and **P2** oligomers mimicking b) poly(2,2′ :5′ ,2 ″ -3,3″ -dialkyl-terthiophene)s or PTTT (top) and poly(3-alkylthiophene) or P3AT (bottom), specifically with dodecyl side chains. c) Coarse-grained bead representation of thiophene-based backbone ('B' bead) and alkyl side chains ('S' beads representing three alkyl groups each), d) acceptor molecule represented as a rigid body of 13 type 'A' coarse-grained beads arranged in an icosahedral pattern mimicking a fullerene derivative, like [6,6']-phenyl-C_{61}-butyric acid methyl ester ($PC_{61}BM$) (bottom) and e) additives of varying length and chemistry, denoted by EX, X ∈ [1,2,3,4,5], composed of 'E' beads and end groups, 'F' that are attracted to the acceptor beads.

As described in detail in refs [22] and [23], the oligomer and acceptor molecular structures are enforced using bond, angle, and dihedral potentials. Bonds have a harmonic spring constant of 50 ε/σ^2 and the equilibrium distance between bonded beads is 1.4σ. The backbone angle spring constant of 30 ε/σ^2 imparts to the conjugated oligomer backbones semi-flexibility, while alkyl side chains and additive molecules are relatively flexible with a spring constant of 6 ε/σ^2. The equilibrium bond distances, bead sizes, and equilibrium three and four body potential angles in our model are inspired by the coarse-grained model in ref [25] which was mapped from atomistic simulations of P3HT decamers and 40mers at 353 K in anisole solvent. The chemical interaction between pairs of coarse-grained beads in our model is given by Lennard-Jones[28] (LJ) potentials with ε_{ij} denoting the LJ potential well depth between beads of type i and type j. The

energy unit ε is 2.7 x 10^{-21} J and the LJ well depths for all pairs of bead types in units of ε are listed in Table 1. As in refs [22] and [23], the backbone-backbone bead LJ well depth is the strongest among the pairs listed in Table 1, to mimic the dominant π-π interactions (attractive) between conjugated backbone thiophene rings. The pair-wise interaction between backbone beads 'B' and the chemically different beads 'S' and 'E', representing alkyl groups is purely repulsive, and modeled by Weeks-Chandler-Andersen (WCA) potential[29]. The beads representing alkyl groups have a weak attraction with LJ well depth of $\varepsilon_{SS} = \varepsilon_{ES} = 0.1\varepsilon$. Type 'S' and type 'E' beads are indistinguishable except for their respective locations in either an oligomer alkyl side chain ('S') or additive's alkyl segment ('E') respectively. In ref [23] we found that the $\varepsilon_{SS} = 0.1\varepsilon$ side chain – side chain bead attraction best reproduced experimental trends in P3AT-like oligomer melting temperatures and lamellar spacing. Attraction between pairs of acceptor CG beads on different acceptors is $\varepsilon_{AA} = 0.1\varepsilon$, which cumulatively would lead to an effective attraction between acceptor-acceptor molecule higher than 0.1ε, as each acceptor is made up of 13 beads. The acceptor-backbone pair-wise attraction strength is $\varepsilon_{AB} = 1.0\varepsilon$ and we found that acceptor backbone attraction is necessary to induce intercalation in P1 oligomer blends in refs [22], as seen in experiments[30, 31]. The attraction between acceptor molecules and 'S' and 'E' beads representing alkyl groups is $\varepsilon_{AS} = \varepsilon_{AE} = 0.1\varepsilon$ Additive end beads, 'F', which represent the functionalized end groups of additives such as alkanoic methyl esters, DIO or alkylthiols, are selectively attracted to other additive end functional beads, $\varepsilon_{FF} = 1.0\varepsilon$, and to acceptor molecule beads $\varepsilon_{AF} = 1.0\varepsilon$.

TABLE 5.1: Lennard Jones pair-wise interaction well depths in units of ε (where ε = 2.7 x 10^{-21} J), between acceptor (type 'A'), backbone (type 'B'), side chain (type 'S'), additive (type 'E') and additive end group (type 'F') coarse-grained beads. The purely repulsive pair-wise interactions are modeled using Weeks-Chandler-Andersen (WCA) and denoted as such.

.

	A (acceptor)	B (backbone)	S (side chain)	E (additive)	F (end group)
A	0.1ε	1ε	0.1ε	0.1ε	1ε
B		2ε	*WCA*	*WCA*	*WCA*
S			0.1ε	0.1ε	0.1ε
E				0.1ε	0.1ε
F					1ε

As stated above, this coarse-grained model for conjugated thiophene-based oligomers and fullerene derivatives is validated through comparison to experimental morphologies in ref [22-24]. In ref [22] we show that the simulated morphologies of oligomers mimicking P3HT and PDHBT *qualitatively* match experimental morphologies and quantitatively match feature spacings[32]. Additionally, in ref [22] we also demonstrate the self-assembled intercalated structures depend on side chain spacing and acceptor – backbone attraction in the same manner as suggested by experiments[30, 31]. Recently in ref [24], we present simulations using the above models to complement experiments by Briseno and coworkers on blends of 2,5-bis(3-alkylthiophen- 2-yl)thieno[3,2-b]thiophene (BTTT) oligomers ranging in length 1-20 monomers and fullerene derivatives used in the active layer of organic solar cells. In agreement with experiments, our simulations show that oligomer order is higher in BTTT dimer-fullerene derivative acceptor blends compared to neat BTTT dimers (no acceptors), and that acceptors intercalate in between BTTT donor side chains in the same manner suggested by experimental x-ray diffraction data.

Having noted the above qualitative and some quantitative agreement with experimental morphologies, we also present a brief discussion of some features of this model that could be perceived as limitations. Our model described above is built mainly for oligomers with lengths comparable to or less than persistence lengths of conjugated polymers. While this has worked

really well when studying oligomeric systems as in ref [24], in polymer systems our model will likely not capture the folding seen in crystalline polymer domains. That said, the molecular-level packing between adjacent crystalline polymers or between monomers and acceptors (e.g. interaction) should be similar to that between aligned oligomers and is captured correctly with our model. As discussed in ref [23], despite the spherical representation of the thiophene rings, which could be thought of as a limitation, we note that through a combination of the side chain constraints (through bonded 3-body and 4-body potentials) we capture the conjugated backbone planarity and P3HT lamellar spacing in quantitative agreement with experiments[22, 23]. We direct the reader to ref [23] for a complete discussion. Lastly, we note that our model and simulation approach does not explore the dynamics of explicit solvent or additive evaporation. Keeping in mind the merits of this coarse-grained model that captures relevant features of the blend and polymer morphology, and appropriate disorder-to-order transition fairly well[22, 23], in this paper we connect the chemical and physical features of additives to their effects on donor-acceptor morphology.

5.2.2 Simulation Method

Using the above coarse-grained model we perform molecular dynamics simulations of blends of thiophene-based oligomers, acceptor molecules, and additives using HOOMD-Blue[33, 34] on graphics processing units. Molecules are placed in a cubic box with periodic boundary conditions and simulations are run in the isothermal-isobaric (NPT) ensemble where the pressure is equal to 0.1 ε/σ^3 as in ref [22] and [23] and reduced temperature, T*, ranges from 4.0 to 1.0. Ternary blends of oligomers, acceptor molecules and additives are formulated in the following manner. Blends are made up of 150 oligomer molecules and with the 632 or 862 acceptor molecules (for P1 oligomer and P2 oligomer blends, respectively) to make a 1:1

oligomer:acceptor ratio by volume. The number of additives is scaled so that the volume fraction of additives (defined as volume of additive beads divided by total occupied volume) in the ternary blend is 0.1, making the volume fraction of oligomers in the blend ~0.45 and that of acceptors ~0.45. The cubic simulation box lengths range from 30 σ to 40 σ, which is 90$\dot{A}$ to 120 $\dot{A}$ in real units.

All systems are simulated at an initial reduced temperature T* = 4.0 to ensure that molecules are well mixed. The temperature is then reduced to T* = 2.5, where we ensure that all blends remain disordered despite the quench from T* = 4.0 to 2.5. Systems are then cooled by reducing T* in decrements of 0.25, after equilibration is achieved, and at least 20 statistically independent snapshots are generated at the each temperature. We follow the same procedure as described in ref [22] and ref [23] to ensure that our simulations are equilibrated and that snapshots used for data analysis are statistically independent. The lowest temperature simulated is T* = 1.0, where all blends form ordered morphologies. Quantitative analysis, as described in the next section, is then performed on the systems at T* = 1.0 using at least 20 statistically independent snapshots.

5.2.3 Analysis

Visualization of the simulated blends is performed using the Visual Molecular Dynamics (VMD) package[35]. Analyses are performed using a combination of scripts written for VMD and in-house Python routines. The positional order of molecules in the blends is quantified using radial distribution functions $g_{i,j}(r)$[36] between beads of type *i* and type *j* as a function of reduced distance r. Acceptor radial distribution functions are calculated for acceptor centers of mass, while radial distribution functions for the other bead types are calculated for individual beads. Comparison of the magnitude at contact distance in the radial distribution function allows us to

compare relative number of bead-bead contacts between systems. For example, the contact peak of $g_{AB}(r)$ is used to quantify the relative number of acceptor-backbone bead contacts.

We also compute the acceptor-acceptor structure factor, $S_{AA}(k)$, by performing a Discrete Sine Transform (DST) on the acceptor-acceptor radial distribution function, $g_{AA}(r)$:

$$s_{AA}(k) = 1 + \frac{4\pi N}{L^3} \int_0^\infty r \cdot g_{AA}(r) \cdot \sin(kr)\, dr \qquad (1)$$

where N is the number of acceptor molecules and L is the length of the cubic simulation box. A divergence in $s_{AA}(k \rightarrow 0)$ indicates macrophase separation. The divergence of a partial structure factors at $k \rightarrow 0$, has been shown to signify macrophase separation; for example theoretical studies of macrophase separation in polymer-nanoparticle composites/blends showing agreement with experiments ref [37]. We use $s_{AA}(k)$ only to quantify the extent of macrophase separation that is visually evident in simulation snapshots. We note that, like most simulations, the lowest k we can access is limited by the simulation box size. Due to this limitation, we use $s_{AA}(k \rightarrow 0)$ simply to compare the extent of macrophase separation between systems. We note that in the $s_{AA}(k)$ plots the standard error are within ± 0.5 units, with the error calculated from five block averaged snapshots (10 snapshots per block) after equilibration.

The orientational order parameter, $P_2(r)$, is calculated to determine the orientational order between oligomer backbones with the following formula[38]:

$$P_2(r) = \frac{1}{2}(3 * \cos^2(\theta_{ij}) - 1) \qquad (2)$$

where r is the distance between the center of mass of backbone *i* and backbone *j* and θ_{ij} is the angle between backbones *i* and *j*. $P_2(r)$ is plotted as a histogram of the P_2 values at every center of mass-center of mass distance r in bins of 0.5. The error bar for each bin is calculated as the standard deviation of the average P_2 value for that bin at each frame after equilibration divided

by the square root of the number of frames. $P_2(r)$ value of near 0 indicates low orientational order while a $P_2(r)$ value of near 1.0 indicates that backbones are aligned.

5.2.4 Parameters Varied

In this work we simulate blends with two different oligomer architectures: P1 oligomers, with sufficient spacing in between the side chains for acceptors to intercalate, and P2 oligomers which prevent acceptors from intercalating because of the higher density of side chains compared to P1[22, 30, 39], to determine the impact of oligomer architecture on acceptor-oligomer blend morphology in the presence of additives. We simulate ternary blends with five types of additives, EX, where $X \in [1,2,3,4,5]$ (Figure 5.1e), to elucidate the effect of additive length and chemistry on acceptor and oligomers morphology. Additives E1 and E2 have a length of three additive beads, while additives E3, E4, and E5 have a length of five additive beads. Additives E2, E4, and E5 have additive end groups, type 'F', that are attracted to acceptor molecules and to other end groups. E2 and E4 each have one attractive end group and E5 has two attractive additive end groups, one on each end of the additive. The number of additives in the blend is varied, either to maintain a constant volume fraction of additives or a constant number of attractive additive end groups.

5.3 RESULTS

In this section, we demonstrate how additive characteristics affect the morphology of blends of thiophene-based oligomers and acceptor molecules. First, in section A, we report how the morphology of blends comprising P1 oligomers and fullerene derivative acceptors is impacted by additives of varying length and end functionalization (E1, E2, E3, E4, and E5). In section B, we show how the same additives affect the morphology blends of P2 oligomers and acceptors. Finally, in section C, we compare the morphologies of blends containing P1 and P2

oligomers in the presence of additives to elucidate how the effect of additives is modulated by oligomer architecture.

5.3.1 Effect of additives on P1 oligomer blend morphology

In blends of P1 oligomers and acceptors in the absence of additives, the P1 oligomers themselves form lamellae to maximize enthalpically favorable backbone-backbone contacts; the backbone-backbone attraction mimicking π-π stacking, is the dominant driving force for oligomers ordering in the blend. Acceptors intercalate in between oligomer side chains to maximize enthalpically favorable acceptor-backbone contacts ($\varepsilon_{AB} = 1.0\varepsilon$), while maintaining the lamellar oligomer structure which maximizes backbone-backbone contacts. This intercalated morphology is shown in simulation snapshots in Figure 5.2a.

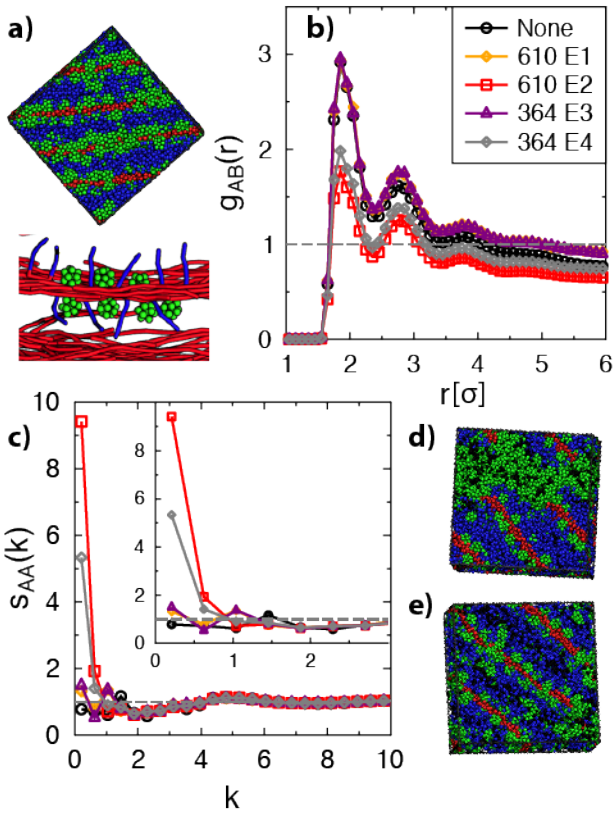

FIGURE 5.2: a) Simulation snapshot of P1 oligomer-acceptor blend in the absence of additives (top) and a zoomed-in view of P1 oligomers with intercalated acceptors at T* = 1.0 with only a select few side chains and acceptors shown, and others hidden for clarity. b) Acceptor-oligomer

backbone radial distribution function, $g_{AB}(r)$ and c) acceptor-acceptor structure factor, $s_{AA}(k)$, for the P1 oligomer binary blend with no additives (denoted as "None"), and with 10 volume percent additives E1, E2, E3, and E4. The oligomer-acceptor-additive ternary blends are denoted by the number of additive molecules in the blend and the type of additive EX, X ∈ [1,2,3,4,5]. Simulation snapshots of the d) 610 E2, and e) 610 E1 P1 oligomer-acceptor-additive blends are shown to visually confirm the $s_{AA}(k)$ trends.

To demonstrate impact of additives, Figure 5.2b presents a comparison of $g_{AB}(r)$ for the blend in the absence of additives (labeled "None") and oligomer-acceptor-additive (**ternary)** blends with 10 volume % additives, denoted in the key by the number of additive molecules in the blend and the type of additive EX, X ∈ [1,2,3,4]. In the absence of additives, the peak in $g_{AB}(r)$ is high, indicating that there are many A-B contacts and that acceptors are intercalated, as described above and shown in Figure 5.2a. Oligomer-acceptor blends with additives with no attractive end groups and additive lengths of three (E1) or five (E3) beads, have the same number of A-B contacts as the binary oligomer-acceptor blend. Additives of length three beads with one attractive end 'F' bead (E2) or length five beads with one attractive end bead (E4) significantly reduce the number of A-B contacts in the blend. This indicates that additives having attractive end groups (E2 or E4) reduce acceptor intercalation in P1 oligomers better than additives having no attractive end groups (E1 or E3).

In order to test our hypothesis that it is the attraction between the additive end group and the acceptor that drives the reduction in acceptor intercalation in oligomer-acceptor-additive blends, we simulate ternary blends with E2* additives. The E2* additives are identical to E2 in architecture but with weakened end group attraction to acceptors ($\varepsilon_{AF} = 0.1\varepsilon$, $\varepsilon_{FF} = 1.0\varepsilon$). We compare the results of E2* ternary blend to the intercalated E1 ($\varepsilon_{AE} = 0.1\varepsilon$, $\varepsilon_{EE} = 0.1\varepsilon$) ternary blend and to the E2 ($\varepsilon_{AF} = 1.0\varepsilon$, $\varepsilon_{FF} = 1.0\varepsilon$) ternary blend (Section 5.7: Figure 5.7). For E2* ternary blend, the number of blend A-B contacts is the same as for the E1 ternary blend in which

additives are composed only of weakly attractive 'E' beads, indicating that the additive-acceptor attraction is necessary to decrease intercalation. Forming A-F contacts in the place of A-B contacts is favorable despite equal strength in attraction ($\varepsilon_{AF} = \varepsilon_{AB} = 1.0\varepsilon$) because acceptors that are not intercalated are able to make contacts with multiple additive end groups and have larger translation entropy, while intercalated acceptors are confined (low translational entropy) and are prevented by the oligomer side chains from forming multiple A-B or A-F contacts. This confinement is confirmed by the acceptor-side chain radial distribution function in Section 5.7: Figure 5.8 showing that highly intercalated ternary blends and the binary oligomer-acceptor blend have more acceptor – side chain contacts than less intercalated ternary blends.

Acceptors that are not intercalated, phase separate from the oligomers domain due to energetically favorable contacts with additives having attractive end groups. Figure 5.2c shows that the E2 containing ternary blend has the highest $s_{AA}(k\rightarrow 0)$ value of the four ternary blends simulated, followed by the E4 ternary blend; an upturn in the $s_{AA}(k)$ as $k\rightarrow 0$ indicates macrophase separation of acceptors from oligomers[37, 40]. Figures 2d shows a snapshot of the E2 ternary blend and confirms the presence of macrophase separated acceptor domains in addition to some acceptors that remain intercalated in the oligomer domains of the E2 ternary blend. Ternary blends with the weakly attractive E1 and E3 additives show minimal macrophase separation as shown by a low $s_{AA}(k\rightarrow 0)$ value and by the simulation snapshot of the E1 ternary blend in Figure 5.2e. No acceptor phase separation occurs for the binary oligomer-acceptor blend as evidenced by lack of upturn in $s_{AA}(k\rightarrow 0)$ and visually in the simulation snapshot in Figure 5.2a. Additives with end groups attracted only to additive end groups and not to acceptor molecules, E2* additive, do not show macrophase separation, like E1, proving that additive –

acceptor attraction is necessary to drive acceptor phase separation in addition to acceptor intercalation (Section 5.7: Figure 5.7).

In Figure 5.2 we refrain from comparing ternary blends with E2 and ternary blends with E4 because even though these systems have the same volume fraction of additive coarse-grained beads (10 volume%), the ternary blend with the E4 additive has fewer attractive additive end 'F' beads (364 additives x 1'F' bead/additive = 364 'F' beads) than the ternary blend with the E2 additives (610 additives x 1 'F' bead/additive = 610 'F' beads). Both of these should affect trends in $g_{AB}(r)$ and $s_{AA}(k)$. In Figure 5.3, we maintain equal number of 'F' beads (610), and present the extent of intercalation and phase separation for ternary blends with E2, E4, and E5 additives. To maintain a constant number of attractive 'F' end groups, ternary blends with E5 have 305 additives, while ternary blends with E2 and E4 have 610 additives. Thus, the blend with E4 has more total additive beads than the E2 and E5 ternary blends because only one out of five additive beads is an attractive end group. The contact peaks of the $g_{AB}(r)$ curves in Figure 5.3a for ternary blends with E2, E4, and E5 are similar indicating that intercalation is reduced by approximately the same amount when the number of acceptor-attracting end 'F' groups are the same, irrespective of 2 'F' beads/additive or 1 'F' bead/additive and of additive length. While additive length and placement of end groups do not significantly affect the extent of acceptor intercalation, the extent of acceptor aggregation and macrophase separation are affected by additive length and number of end 'F' bead per additive. Figure 5.3b shows that the 610 E2 and 305 E5 ternary blends show more macrophase separation than the 610 E4 ternary blend.

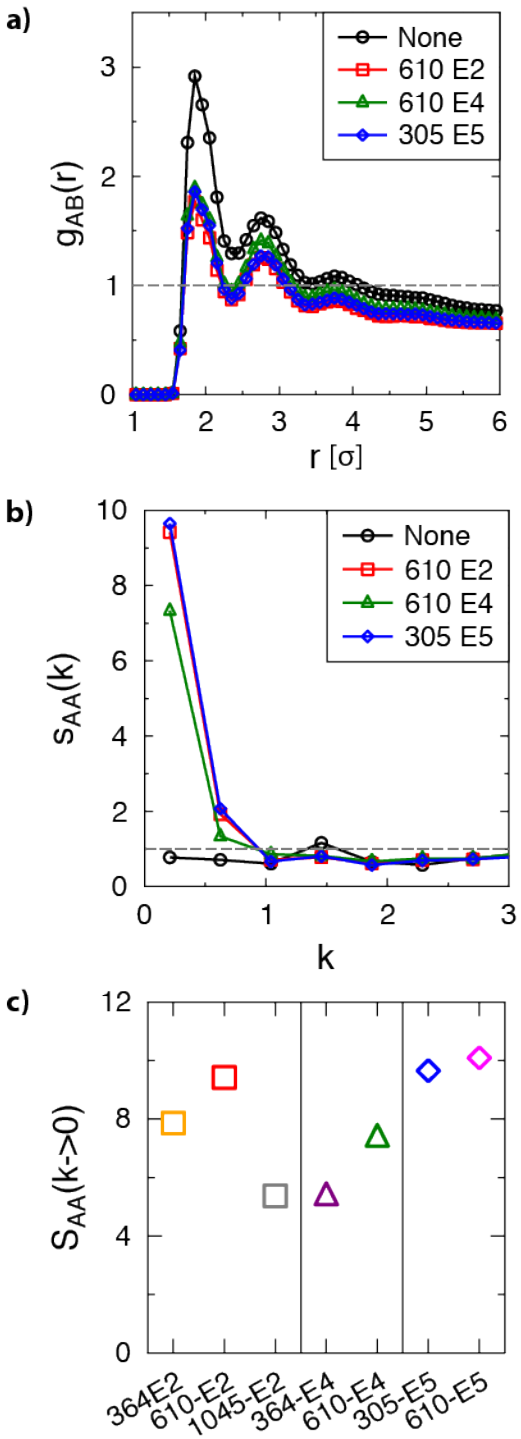

FIGURE 5.3: a) Acceptor-oligomer backbone bead radial distribution function, $g_{AB}(r)$, and b) acceptor-acceptor structure factor, $s_{AA}(k)$, for P1 oligomer-acceptor-additive ternary blends with additives E2, E4, and E5 where the total number of attractive additive end beads is constant at 610. These ternary blends are denoted by the number of additive molecules in the blend and the type of additive EX, X ∈ [1,2,3,4,5], with "None" corresponding to binary oligomer-acceptor

blends with no additives c) Plot of $s_{AA}(k \rightarrow 0)$ for oligomer-acceptor-additive blends with varying number of additives EX, X ∈ [1,2,3,4,5].

We examine the environment of the acceptor and additive molecules in the blend to understand why the E2 and E5 ternary blends are more macrophase separated than the E4 ternary blend. The E2, E4, and E5 blends have approximately the same number of A-A, F-A and F-F contacts, as shown by $g_{AA}(r)$, $g_{FA}(r)$, and $g_{FF}(r)$ in Section 5.7: Figure 5.9, indicating that at contact distance, the environments of the acceptor and the attractive additive end groups are similar. Snapshots of additives positioned around a single acceptor molecule in each ternary blend (Section 5.7: Figure 5.10) suggest that the degree of phase separation depends on the amount of steric hindrance imparted to the acceptors by the alkyl parts ('E' beads) of the different additives. We find that ternary E4 blend, which is less phase separated than the E2 and E5 blends, despite the same number of 'F' beads, has a higher number of weakly attractive type 'E' beads in the vicinity of each acceptor molecule compared to ternary E2 and E5 blends (Section 5.7: Figure 5.10). The presence of many 'E' beads, which have only a weak attraction to acceptors and other additives, in the vicinity of acceptors likely deters formation of large acceptor aggregates. The E2 additive is short (contains 2 'E' beads and 1 'F' bead), so the presence of this additive in proximity to the acceptors has low steric hindrance for the aggregation of acceptors. In contrast, E4 additives are longer than E2 additives, with four out of the five beads being an 'E' bead. Thus, in the E4 ternary blend, while the acceptors make F-A contacts similar to E2 and E5 ternary blends, as shown by $g_{FA}(r)$ in Section 5.7: Figure 5.9, the acceptors in E4 ternary blends are surrounded by many weakly attractive 'E' beads, sterically hindering the addition of acceptor molecules to the aggregate. The E5 additive is as long as E4, but only three out of five beads are 'E' beads and two are 'F' attractive additive end beads, making E5 as effective as E2 in facilitating macrophase separation.

Figure 5.3c shows that increasing the number of E2 and E4 additives in ternary blends from 364 to 610 and the number of E5 additives from 305 to 610 increases extent of acceptor macrophase separation. As the number of E5 additives increases acceptor intercalation decreases, leading to higher macrophase separation for increasing additives (Section 5.7: Figure 5.11). This is because in ternary blends with more attractive end groups, there is higher enthalpic drive for F-A and F-F contacts, facilitating acceptor aggregation and macrophase separation compared to the ternary blends with fewer additive end groups. However, when the number of E2 additives is increased from 610 to 1045, despite decreased intercalation, overall tendency for macrophase separation decreases likely because an overabundance of additives sterically hinders acceptor aggregation.

To further test this steric hinderance based reasoning behind why the E4 ternary blends are less phase separated than E2 and E5 blends, we simulate ternary blends with additives E2, E4, and E5 with the bond between the additive 'F' end group and the 'E' beads broken, creating free 'F' additive ends and shorter additives of 'E'. Separating the 'F' beads from the remaining additive beads allows enthalpically favorable F-A and F-F contacts to form without the steric hindrance imparted by the weakly attractive 'E' segments. Simulation snapshots in Section 5.7: Figure 5.12 show that large aggregates of acceptors and free 'F' beads form, and the remaining 'E' segments mix with side chains and are phase separated from the 'F' bead/acceptor aggregates. The extent of acceptor intercalation in the ternary blends with free 'F' beads, as estimated from $g_{AB}(r)$, is similar to the case of the regular E2, E4, and E5 additives (Section 5.7: Figure 5.13). The oligomer-acceptor phase separation, however, is increased in the case of free 'F' additive ends compared to the fully connected additives, especially for E4, the additive with the most steric hindrance to acceptor aggregation (Section 5.7: Figure 5.13). Macrophase

separation is increased in the cases with free 'F' beads because there is no steric hindrance from 'E' beads for the formation of large aggregates. The reduction of steric hindrance also allows for more F-A, F-F and A-A contacts in the ternary blends with free 'F' additive ends compared to ternary blends with fully connected additives (Section 5.7: Figure 5.13). Thus, the alkyl chains in the additive sterically prevents the formation of large acceptor aggregates induced by the end-functional groups that are chemically attractive to the acceptor, and together they tune the degree of phase separation in the oligomer-acceptor additive blend.

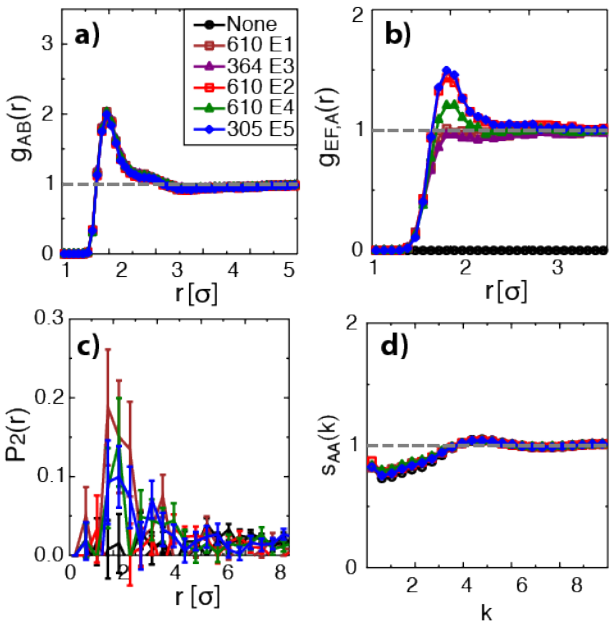

FIGURE 5.4: a) Acceptor-oligomer backbone radial distribution function, $g_{AB}(r)$, b) additive ('E' or 'F')-acceptor radial distribution function $g_{EF,A}(r)$, c) orientational order parameter, $P_2(r)$, and d) acceptor-acceptor structure factor, $s_{AA}(k)$, at T* = 2.0 for P1 binary oligomer-acceptor blends ("None") and for ternary blends with additives EX, X ∈ [1,2,3,4,5]. The legend in part (a) applies to all parts of this figure; oligomer-acceptor-additive blends are denoted by the number of additives of type EX, X ∈ [1,2,3,4,5].

Now that we understand the effect of additive characteristics on acceptor intercalation and blend macrophase separation at T* = 1.0, our next goal is to understand the mechanism of the additive-induced acceptor-oligomer phase separation. We first examine the blends at a temperature T* = 2.0 above the order-disorder transition (ODT) temperature of the blends. At T*

= 2.0, in the disordered state there is no difference in the A-B radial distribution function, $g_{AB}(r)$, of binary oligomer-acceptor blends and ternary blends with additives EX, X ∈ [1,2,3,4,5]. This suggests that additives are minimally intercalated at T* = 2.0, above ODT (Figure 5.4a). The A-A, F-A, and F-F radial distribution functions at T* = 2.0 show no difference between ternary blends with additives EX, X ∈ [1,2,3,4,5] or the oligomer-acceptor blend (Section 5.7: Figure 5.14). The length and chemistry of the additive does, however, affect number of contacts between acceptors and additive beads ('E' and 'F') in the blend as shown by $g_{E/F,A}(r)$, at T* = 2.0 (Figure 5.4b). Additives with attractive 'F' end groups, E2, E4, and E5, have a higher number of acceptor-additive contacts than the additives without attractive 'F' end groups, E1 and E3. This suggests that the reduction of A-B contacts (reduction in intercalation) in ternary blends with E2, E4, and E5 additives seen at T*=1.0 compared to the binary oligomer acceptor blend at T*=1.0, occurs because the additive - acceptor contacts at high temperature prevent acceptors from intercalating in between oligomer side chains upon cooling. E2 and E5 ternary blends have a higher number of additive-acceptor contacts at T* = 2.0 because the additives have a higher ratio of attractive 'F' beads to 'E' beads, compared to the E4 additive. We note that at T* = 2.0, oligomers are disordered in all blends as shown by the low $P_2(r)$ values in Figure 5.4c. Although ternary blends with different additives show varying amounts of additive-acceptor contacts at T* = 2.0, acceptors are not phase separated at T* = 2.0, as shown by the absence of divergence in $s_{AA}(k \rightarrow 0)$ for all blends (Figure 5.4d). Additionally, there is no difference in $s_{AA}(k)$ comparing ternary blends with additives to the binary oligomer-acceptor blend.. Thus, additive-acceptor contacts form at a higher temperature than acceptor-acceptor aggregation. Thus, the formation of additive-acceptor contacts is a precursor for acceptor-acceptor aggregation and the reduction of acceptor intercalation within the P1 oligomer domain.

So far we have shown that additives affect the acceptor phase separation from oligomers, and intercalation of acceptor molecules within the P1 oligomers. Next we show how additives affect P1 oligomer backbone ordering and alignment. Figure 5.5a shows the backbone bead – backbone bead radial distribution function, $g_{BB}(r)$ indicating that the presence of additives increases the number of backbone bead-backbone bead contacts. The presence of weakly attractive 'E' beads produce a weak confinement-like effect on the oligomer backbone, facilitating oligomer backbones to order. Ternary blends with attractive additive end groups E2, E4, and E5 have the highest backbone positional order because acceptors in these blends are more macrophase separated compared to ternary blends with E1 and E3 additives, further facilitating backbone order within the oligomer macrophase separated domain. In addition, the plot of the order parameter, $P_2(r)$, shows that backbones have more orientational order (evidenced by $P_2(r) \sim 1$) in the presence of end-functionalized additives (E2, E4, E5) or additives with large number of weakly attractive 'E' beads (E3) than in the case in the absence of additives (Figure 5.5b). We think that the lack of attractive end 'F' bead and fewer number of weakly attractive 'E' beads makes E1 unique, where instead of improving backbone alignment, E1 serves to deter backbone-backbone orientational order. Experiments with P3HT:PCBM blends and DIO or alkanethiol additives similarly show an increase in P3HT crystallinity in ternary blends with additives compared to binary oligomer-acceptor blends [12, 41]. In agreement, our simulation results show that additives increase backbone positional and orientational order compared to the case in the absence of additives, but interestingly, this high order is maintained even for ternary blends with larger additives, E3, that do not have attractive end groups.

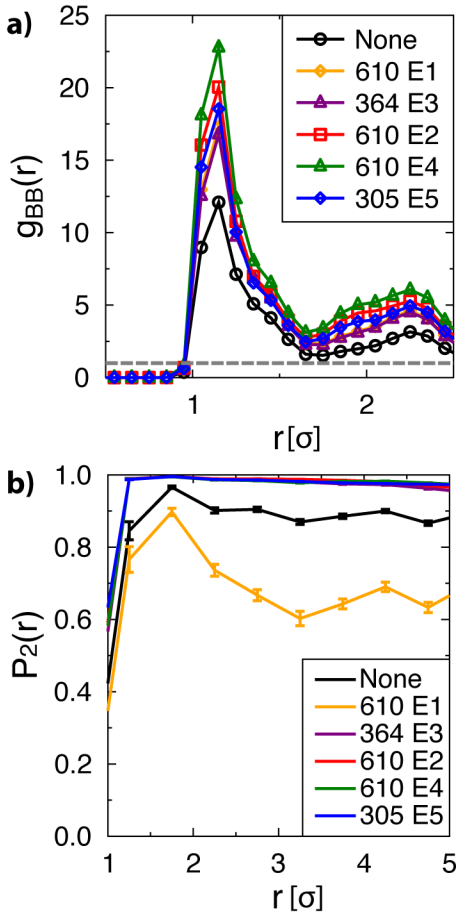

FIGURE 5.5: a) Oligomer backbone- oligomer backbone radial distribution function, $g_{BB}(r)$, and b) orientational order parameter, $P_2(r)$, for P1 oligomer-acceptor-additive blends in the absence of additives and with additives EX, X ∈ [1,2,3,4,5].

The key results so far are that the additive length and chemistry control blend macrophase separation and acceptor intercalation in the ternary blends of P1 oligomers with acceptor molecules and additives. Additives with attractive end groups decrease acceptor intercalation and increase acceptor phase separation compared to the binary oligomer-acceptor blend, with this effect increasing with the number of (acceptor) attractive additive end groups and in general decreasing with increasing additive length. Our simulation results qualitatively agree with experimental work by Buchaca-Domingo *et al.* which showed reduction in intercalation of $PC_{61}BM$ with the thiophene-based conjugated polymer PBTTT in the presence of methyl ester

additives, which are hypothesized to be attracted to the $PC_{61}BM$[21]. In experiments, however, the methyl ester additive with the longer alkyl segment decreased intercalation more than the additive with the shorter alkyl segment which is the opposite of what is found in this work. The experimental trend may be caused by higher boiling point of the longer additive (262 °C) compared to that of the shorter additive (172 °C), which would allow the longer additive to remain in the film longer, leaving more attractive additive end groups to interact with the acceptor molecules and sterically prevent intercalation. This explanation agrees with our simulation results which show that increasing the number of attractive additive ends decreases the extent of intercalation in P1 ternary blends for blends with >1000 additives end groups compared to blends with 364-610 additive end groups (Section 5.7: Figure 5.11).

5.3.2 Effect of additives on P2 oligomer blend morphology

In the previous section, we discussed P1 oligomers, which have sufficient spacing between side chains for acceptors to intercalate. We now move to P2 oligomers to examine the effect of additives on blends that do not exhibit intercalation. P3DDT backbone has alkyl side chains on every backbone thiophene ring and this high side chain density prevents acceptors from intercalating both in experiments and in our coarse-grained simulations[22, 30, 39].

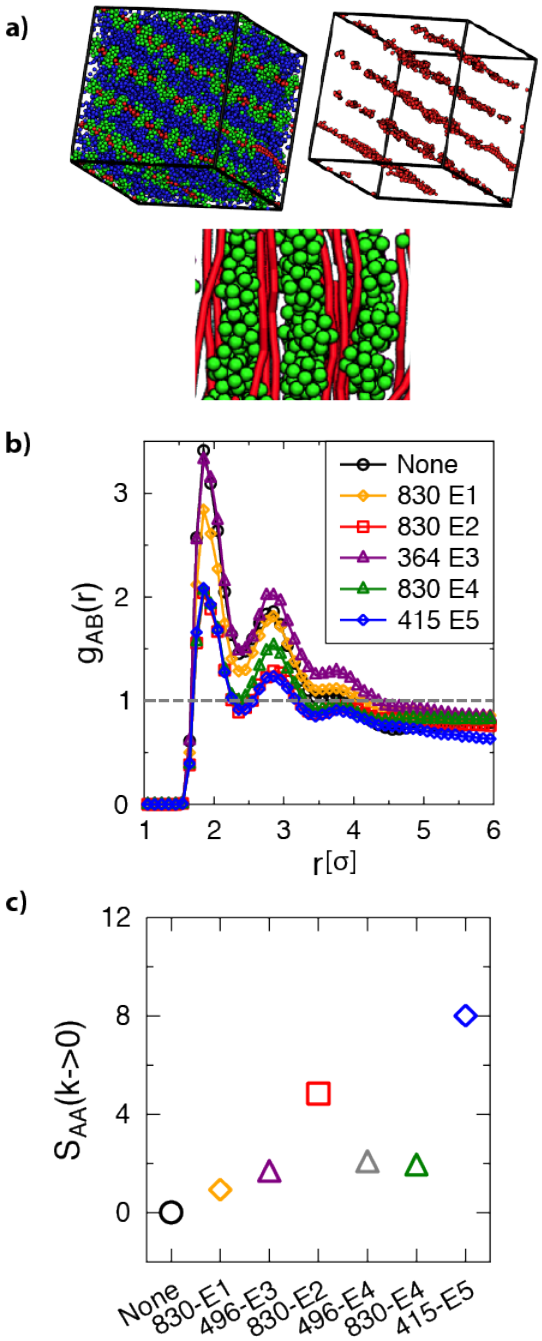

FIGURE 5.6: a) Simulation snapshot of P2 oligomer-acceptor blend in the absence of additives (top right), showing only backbone beads (top left) and a view of P2 oligomers with acceptors occupying regions between ordered P2 oligomer backbones (bottom). b) Acceptor-backbone radial distribution function, $g_{AB}(r)$, for the P2 oligomer-acceptor binary oligomer-acceptor blend ("None") and ternary blends with E2, E4, and E5 additives holding the number of attractive additive end 'F' beads constant at 830. Blends are denoted by the number of additive molecules in the ternary blend and the type of additive EX, X ∈ [1,2,3,4,5]. c) Plot of $s_{AA}(k\rightarrow 0)$ for oligomer-acceptor-additive blends of additives EX, X ∈ [1,2,3,4,5], with varying number of additives.

Figure 5.6a shows that in the absence of additives, acceptors blended with P2 oligomers do not intercalate but instead form layers of acceptors in between strips of oligomer backbone to maximize acceptor-backbone and backbone-backbone contacts. In the presence of additives, this morphology is disrupted and the number of enthalpically favorable acceptor (A) - backbone (B) contacts is reduced. Figure 5.6b shows that the contact peaks in the $g_{AB}(r)$ for ternary P2 blends with weakly attractive additives E1 has a lower magnitude than in the absence of additives, indicating that the number of A-B contacts is reduced by adding E1 additives. In ternary blends with additives E2, E4, and E5 with attractive 'F' end groups, the number of A-B contacts is reduced further compared to the binary oligomer-acceptor blend. In ternary blends with additives with attractive end groups, enthalpically favorable F-A contacts compete with A-B contacts, reducing the number of A-B contacts compared to E1 and E3 ternary blends and to the binary oligomer-acceptor blend. The contact peaks in the $g_{AB}(r)$ curves are similar for the E2, E4, and E5 ternary blends, indicating that number of A-B contacts is not sensitive to the variations in length and chemistry of the E2, E4, and E5 additives.

While the number A-B contacts does not vary with the placement of attractive additive end groups, the plot of $s_{AA}(k\rightarrow 0)$ in Figure 5.6c shows that additive identity affects the degree phase separation in P2 oligomer blends. Ternary blends with additives E1, E3 and E4 have a low $s_{AA}(k\rightarrow 0)$ value indicating low acceptor-oligomer phase separation, while the E2 ternary blend is moderately phase separated and the E5 ternary blend is highly phase separated. To understand why the E2 and E5 additives cause more acceptor macrophase separation than the E4 additives and why E4 additives have the same low degree of macrophase separation as ternary blends with weakly attractive additives E1 and E3, we do the following analyses. We first visually examine the equilibrated structures. In the macrophase separated P2-E5 and P2-E2 ternary blends,

backbones form ordered lamellae, while in P2-E4 ternary blends, which are less phase separated, backbones assemble into disordered strips of aligned backbones (Section 5.7: Figure 5.15). The snapshots suggest that the disordered backbone domains in P2 E4 ternary blends likely prevent the formation of large acceptor aggregates. More weakly attractive additive type 'E' beads in ternary blends with E4 additives cause more disruption to backbone order hindering macrophase separation in E4 ternary blends compared to E2 and E5 ternary blends. In addition, E4 additives have more steric hindrance to acceptor aggregation (as discussed in section A), which also contributes to lower macrophase separation in E4 blends compared to ternary blends with E2 and E5 additives.

To determine the mechanism of ordering in each P2 blend, we calculate $P_2(r)$ and $s_{AA}(k)$ for the E2, E4, and E5 ternary blends as a function of simulation of temperature, T* (Section 5.7: Figure 5.16). We find that for the E5 ternary blend, acceptor molecules aggregate (evidenced by $s_{AA}(k)$) at the same temperature, T* = 1.25, as the onset of backbone orientational order (evidenced by $P_2(r)$), allowing for the formation of large acceptor aggregates and facilitating backbone lamellar order. In contrast, for the E2 and E4 ternary blends, the onset of backbone orientational order occurs at T* = 1.25 which is above the temperature of acceptor aggregation (T* = 1.0), giving acceptors less mobility at the aggregation temperature and reducing acceptor phase separation. We hypothesize that if the additive–induced driving force for acceptor aggregation is large enough, as in the case of the E5 ternary blend, acceptors and additives have higher mobility and form large aggregates as backbones order, which leads to larger extent of oligomer-acceptor phase separation and allows ordered backbone lamellae to form.

5.3.3 Comparison of P1 and P2 oligomer blend morphologies in the presence of additives

For ternary blends of both P1 and P2 oligomers, additives with attractive end groups reduce the number acceptor-backbone (A-B) contacts. The possibility for multiple acceptor-additive end group (A-F) contacts makes it enthalpically favorable for acceptors to aggregate with additives and other acceptor molecules, instead of being intercalated between backbone side chains (in case of P1 oligomers) or being adjacent to oligomer backbones (in case of P2 oligomers) where attractive contacts are sterically limited by the oligomer backbone and side chains. Due to this acceptor aggregation, oligomer-acceptor macrophase separation is increased in the presence of additives with attractive end groups. The extent of acceptor macrophase separation in general increases with increasing number of end-functional groups that attract to acceptors and/or decreasing size of the alkyl group. In addition, at T* = 2.0, acceptors and additive additives are aggregated in both P1 and P2 ternary blends, indicating that high temperature acceptor-additive aggregation enhances acceptor macrophase separation by sterically preventing acceptor – backbone contacts (Section 5.7: Figure 5.17).

There are some differences in the way additives affect ternary blends with P1 and P2 oligomers because of the difference in oligomer architecture. The ternary blends with P1 oligomers are generally more macrophase separated than ternary blends with P2 oligomers. Oligomer backbones have slightly lower orientational order in blends with P2 oligomers than blends with P1 oligomers (Section 5.7: Figure 5.18). Backbone order is higher for P1 oligomers because the P1 has a lower density of side chains, exposing more strongly attractive backbone beads. The backbone-backbone bead attraction is the strongest attractive interaction in these systems at $\varepsilon_{BB} = 2.0\varepsilon$, and with more exposed backbone beads due to lower side chain density, the P1 oligomers have a stronger driving force for oligomer backbone alignment and the

formation of lamellae than do P2 oligomers. Higher backbone disorder in the P2 blends prevents formation of large acceptor aggregates.

To compare the mechanism of additive influence on morphology we compare backbone orientational order in P1 and P2 blends using the order parameter $P_2(r)$, and oligomer-acceptor phase separation using the acceptor-acceptor structure factor, $s_{AA}(k)$, as a function of temperature for P1 and P2 ternary blends with E2, E4 and E5 additives (Section 5.7: Figure 5.16 and 5.19). The order-disorder transition temperature (ODT) is $T^*_{ODT} \approx 1.5$ for P1 E2, P1 E4, and P1 E5 ternary blends (Section 5.7: Figure 5.16), while $T^*_{ODT} \approx 1.0$ for P2 E2 and P2 E4 ternary blends, and $T^*_{ODT} \approx 1.25$ for P2 E5 blends (Section 5.7: Figure 5.19). The P1 blends have higher ODTs because of the higher enthalpic driving force for P1 backbone ordering compared to P2 as discussed above. We note that if there is simultaneous backbone alignment and acceptor aggregation at the ODT it allows for higher acceptor molecule mobility during the transition (especially at higher ODTs), increasing acceptor macrophase separation. This happens at $T^* = 1.5$, for P1 E2, P1 E4 and P1 E5 blends, all of which show significant acceptor macrophase separation. In the P2 case the simultaneous backbone alignment and acceptor aggregation only occurs for E5-based ternary blend at $T^*=1.25$ (leading to the largest macrophase separation of all P2 blends) and not E2- and E4-based ternary blends.

5.4 CONCLUSION

Our simulations of conjugated thiophene oligomer and fullerene derivative (acceptor) based blends with additives of varying length and chemistry show how additive features control oligomer-acceptor blend morphology and extent of donor (oligomer)-acceptor phase separation as a function of oligomer architecture. We study two types of oligomers PTTT-like, denoted as P1 and P3DDT-like, denoted as P2. The additives are small alkyl chains varying in length from

nine to fifteen alkyl groups (three to five coarse-grained beads), with one or two end functional groups that are selectively attractive to the fullerene derivative acceptor molecule.

We find that attraction between additive functional end groups and acceptor molecules is needed to induce acceptor macrophase separation from the oligomers, and to reduce acceptor-oligomer backbone contacts (reduction in intercalation in the case of P1 oligomers) compared to the no additive blends. While extent of reduction of number of acceptor-backbone contacts does not vary significantly with additive length and chemistry, these additive features significantly modulate the extent of acceptor-oligomer phase separation. For example, in the case of P1 oligomer blends, macrophase separation is higher in ternary blends with additives with shorter alkyl segments compared to ternary blends with additives having longer alkyl segments because shorter alkyl segments present less steric hindrance towards formation of large acceptor aggregates than additives with longer alkyl segments. The P1 ternary blends are more macrophase separated than P2 ternary blends because P1 oligomers have a higher order-disorder temperature than P2. And, at this order-disorder temperature if the acceptor aggregation occurs simultaneously with the ordering of backbones, it provides mobility to the acceptors, especially at higher temperatures, to form large acceptor aggregates. This happens for P1 ternary blends with all end-functionalized additives, while it only occurs in P2 blends with bi-functionalized additives.

We note that while we provide design rules for additives and systematically link additive features to various aspects of donor-acceptor morphology, we do not attempt to determine the best or optimal additive for organic photovoltaic device performance. The key design rules we have produced in this work are as follows. To achieve intermediate donor oligomer-acceptor phase separation, an additive with an attractive end group and long alkyl segment should be

used. To achieve high donor oligomer-acceptor phase separation, additives with attractive additive end groups and short alkyl segments or additives with two attractive additive end groups should be used, depending on the oligomer architecture.

5.5 ACKNOWLEDGEMENTS

We would like to thank Department of Energy for project funding under Grant DE-SC0003912. Simulations were run on GPU resources of the National Energy Research Scientific Computing Center, which is supported by the Office of Science of the U.S. Department of Energy under Contract DE-AC02- 05CH11231.

5.6 REFERENCES

1. Slota, J. E.; He, X. M.; Huck, W. T. S. *Nano Today* **2010,** 5, (3), 231-242.
2. Ruderer, M. A.; Muller-Buschbaum, P. *Soft Matter* **2011,** 7, (12), 5482-5493.
3. Brady, M. A.; Su, G. M.; Chabinyc, M. L. *Soft Matter* **2011,** 7, (23), 11065-11077.
4. Deibel, C.; Dyakonov, V. *Rep. Prog. Phys.* **2010,** 73, (9), 39.
5. Zhou, H. X.; Yang, L. Q.; You, W. *Macromolecules* **2012,** 45, (2), 607-632.
6. Shin, N.; Richter, L. J.; Herzing, A. A.; Kline, R. J.; DeLongchamp, D. M. *Advanced Energy Materials* **2013,** 3, (7), 938-948.
7. Yao, Y.; Hou, J.; Xu, Z.; Li, G.; Yang, Y. *Advanced Functional Materials* **2008,** 18, (12), 1783-1789.
8. Ramani, R.; Alam, S. *Polymer* **2013,** 54, (25), 6785-6792.
9. Chang, L.; Jacobs, I. E.; Augustine, M. P.; Moule, A. J. *Organic Electronics* **2013,** 14, (10), 2431-2443.
10. Thomas, A.; Elsa Tom, A.; Rao, A. D.; Varman, K. A.; Ranjith, K.; Vinayakan, R.; Ramamurthy, P. C.; Ison, V. V. *Journal of Applied Physics* **2014,** 115, (10), 104302.
11. Cho, S.; Nho, S.-H.; Eo, M.; Lee, M. H. *Organic Electronics* **2014,** 15, (5), 1002-1011.
12. Salim, T.; Wong, L. H.; Brauer, B.; Kukreja, R.; Foo, Y. L.; Bao, Z. N.; Lam, Y. M. *Journal of Materials Chemistry* **2011,** 21, (1), 242-250.

13. Bartelt, J. A.; Douglas, J. D.; Mateker, W. R.; Labban, A. E.; Tassone, C. J.; Toney, M. F.; Fréchet, J. M. J.; Beaujuge, P. M.; McGehee, M. D. *Advanced Energy Materials* **2014**, 4, 1301733.

14. Schmidt, K.; Tassone, C. J.; Niskala, J. R.; Yiu, A. T.; Lee, O. P.; Weiss, T. M.; Wang, C.; Fréchet, J. M. J.; Beaujuge, P. M.; Toney, M. F. *Advanced Materials* **2014,** 26, (2), 300-305.

15. Su, M.-S.; Kuo, C.-Y.; Yuan, M.-C.; Jeng, U. S.; Su, C.-J.; Wei, K.-H. *Advanced Materials* **2011,** 23, (29), 3315-3319.

16. Lee, J. K.; Ma, W. L.; Brabec, C. J.; Yuen, J.; Moon, J. S.; Kim, J. Y.; Lee, K.; Bazan, G. C.; Heeger, A. J. *Journal of the American Chemical Society* **2008,** 130, (11), 3619-3623.

17. Peet, J.; Kim, J. Y.; Coates, N. E.; Ma, W. L.; Moses, D.; Heeger, A. J.; Bazan, G. C. *Nature Materials* **2007,** 6, (7), 497-500.

18. Cha, H.; Baek, J. Y.; An, T. K.; Kim, S.-O.; Kwon, S.-K.; Kim, Y.-H.; Park, C. E. *Organic Electronics* **2014,** 15, (12), 3558-3567.

19. Kim, C. S.; Tinker, L. L.; DiSalle, B. F.; Gomez, E. D.; Lee, S.; Bernhard, S.; Loo, Y.-L. *Advanced Materials* **2009,** 21, (30), 3110-3115.

20. Richter, L. J.; DeLongchamp, D. M.; Bokel, F. A.; Engmann, S.; Chou, K. W.; Amassian, A.; Schaible, E.; Hexemer, A. *Advanced Energy Materials* **2015,** 5, (3), 1400975.

21. Buchaca-Domingo, E.; Ferguson, A. J.; Jamieson, F. C.; McCarthy-Ward, T.; Shoaee, S.; Tumbleston, J. R.; Reid, O. G.; Yu, L.; Madec, M. B.; Pfannmoller, M.; Hermerschmidt, F.; Schroder, R. R.; Watkins, S. E.; Kopidakis, N.; Portale, G.; Amassian, A.; Heeney, M.; Ade, H.; Rumbles, G.; Durrant, J. R.; Stingelin, N. *Materials Horizons* **2014,** 1, (2), 270-279.

22. Jankowski, E.; Marsh, H. S.; Jayaraman, A. *Macromolecules* **2013,** 46, (14), 5775-5785.

23. Marsh, H. S.; Jankowski, E.; Jayaraman, A. *Macromolecules* **2014,** 47, (8), 2736-2747.

24. Zhang, L.; Liu, F.; Diao, Y.; Marsh, H. S.; Colella, N. S.; Jayaraman, A.; Russell, T. P.; Mannsfeld, S. C. B.; Briseno, A. L. *Journal of the American Chemical Society* **2014,** 136, (52), 18120-18130.

25. Schwarz, K. N.; Kee, T. W.; Huang, D. M. *Nanoscale* **2013,** 5, (5), 2017-2027.

26. Huang, D. M.; Faller, R.; Do, K.; Moule, A. J. *J. Chem. Theory Comput.* **2010,** 6, (2), 526-537.

27. Huang, D. M.; Moule, A. J.; Faller, R. *Fluid Phase Equilibria* **2011,** 302, (1-2), 21-25.

28. Verlet, L. *Physical Review* **1967,** 159, (1), 98-103.

29. Weeks, J. D.; Chandler, D.; Andersen, H. C. *Journal of Chemical Physics* **1971,** 54, (12), 5237-+.

30. Miller, N. C.; Cho, E.; Gysel, R.; Risko, C.; Coropceanu, V.; Miller, C. E.; Sweetnam, S.; Sellinger, A.; Heeney, M.; McCulloch, I.; Bredas, J. L.; Toney, M. F.; McGehee, M. D. *Advanced Energy Materials* **2012,** 2, (10), 1208-1217.

31. Miller, N. C.; Cho, E.; Junk, M. J. N.; Gysel, R.; Risko, C.; Kim, D.; Sweetnam, S.; Miller, C. E.; Richter, L. J.; Kline, R. J.; Heeney, M.; McCulloch, I.; Amassian, A.; Acevedo-Feliz, D.; Knox, C.; Hansen, M. R.; Dudenko, D.; Chmelka, B. F.; Toney, M. F.; Bredas, J. L.; McGehee, M. D. *Advanced Materials* **2012,** 24, (45), 6071-6079.

32. Ko, S. W.; Hoke, E. T.; Pandey, L.; Hong, S. H.; Mondal, R.; Risko, C.; Yi, Y. P.; Noriega, R.; McGehee, M. D.; Bredas, J. L.; Salleo, A.; Bao, Z. A. *Journal of the American Chemical Society* **2012,** 134, (11), 5222-5232.

33. Anderson, J. A.; Lorenz, C. D.; Travesset, A. *Journal of Computational Physics* **2008,** 227, (10), 5342-5359.

34. Nguyen, T. D.; Phillips, C. L.; Anderson, J. A.; Glotzer, S. C. *Computer Physics Communications* **2011,** 182, (11), 2307-2313.

35. Humphrey, W.; Dalke, A.; Schulten, K. *Journal of Molecular Graphics & Modelling* **1996,** 14, (1), 33-38.

36. Leach, A. E., *Molecular Modelling: Principles and Applications* 1ed.; Longman: Essex, 1996.

37. Hall, L. M.; Anderson, B. J.; Zukoski, C. F.; Schweizer, K. S. *Macromolecules* **2009,** 42, (21), 8435-8442.

38. Yankova, T. S.; Bobrovsky, A. Y.; Vorobiev, A. K. *Journal of Physical Chemistry B* **2012,** 116, (20), 6010-6016.

39. Mayer, a. C.; Toney, M. F.; Scully, S. R.; Rivnay, J.; Brabec, C. J.; Scharber, M.; Koppe, M.; Heeney, M.; McCulloch, I.; McGehee, M. D. *Advanced Functional Materials* **2009,** 19, (8), 1173-1179.

40. Schweizer, K. S.; Curro, J. G. *Atomistic Modeling of Physical Properties* **1994,** 116, 319-377.

41. Fan, X.; Zhao, S.; Yue, C.; Yang, Q.; Gong, W.; Chen, Y.; Wang, H.; Jia, Q.; Xu, Z.; Xu, X. *Journal of Nanoscience and Nanotechnology* **2014,** 14, (5), 3592-3596.

5.7 SUPPORTING INFORMATION

5.7.1 P1 oligomer blends

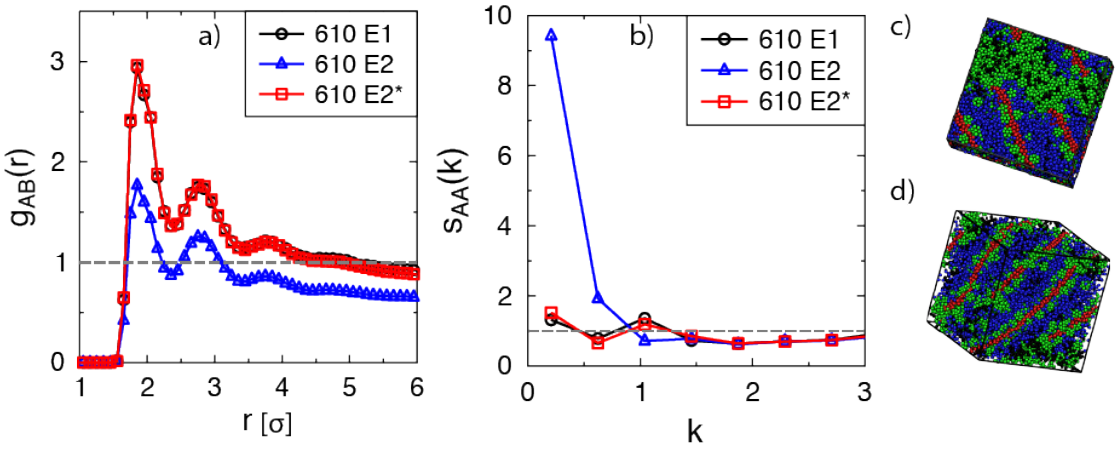

FIGURE 5.7: a) Acceptor-backbone radial distribution function $g_{AB}(r)$, and b) Acceptor-acceptor structure factor, $s_{AA}(k)$, for P1 oligomer-acceptor-additive (**ternary**) blends with additives E1, E2, and with E2* with reduced A-F attraction ($\varepsilon_{AF} = 0.1$, $\varepsilon_{FF} = 1.0$). c) Simulation snapshot of the ternary E2 blend with high phase separation. c) Simulation snapshot of the ternary E2* blend showing that acceptors are intercalated and that this blend has low phase separation.

In order to elucidate the mechanism of additive induced oligomer-acceptor phase separation, we simulate PTTT-like (**P1**) oligomer-acceptor-additive (**ternary**) blends with additives that have end groups that are attracted to other additive end groups but not to acceptor molecules and compare the results to the E1 and E2 ternary blends. In effect, this additive, here denoted E2*, is the additive E2 with reduced F-A attraction, $\varepsilon_{AF} = 0.1$. Figures S.1a and S.1b show that the ternary blend with E2* has a high number of A-B contacts and reduced phase separation, similar to the ternary blends with the E1 additive. In contrast the E2 additive with the additive end group attracted to acceptor molecules has fewer A-B contacts (reduced intercalation) and higher phase separation. Thus, **Figure 5.7 shows that additive end group – acceptor attraction is necessary to reduce intercalation and to induce macrophase separation for ternary blends of P1 oligomers**.

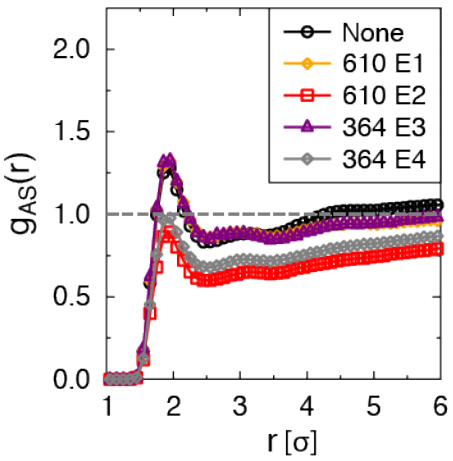

FIGURE 5.8: Acceptor-side chain, $g_{AS}(r)$, radial distribution function for the P1 oligomer-acceptor blend (denoted as "None") and ternary blends with ten percent volume fraction of additives EX, X ∈ [1,2,3,4].

Figure 5.8 shows that the number of A-S contacts is reduced in ternary blends with additives (E2 and E4) with attractive end type 'F' groups compared to oligomer-acceptor blends with no additives (denoted as "None") or ternary blends with E1 or E3. The reduction in A-S contacts provides further evidence for reduction of intercalation in ternary blends with additives having attractive end groups (E2 and E4) compared to binary oligomer-acceptor blend or ternary blends with additives E1 or E3. The increased number of acceptor-side chain contacts for intercalated blends suggests that intercalated acceptors are sterically hindered by side chain beads from making enthalpically favorable contacts with additional type 'A' or type 'F' beads.

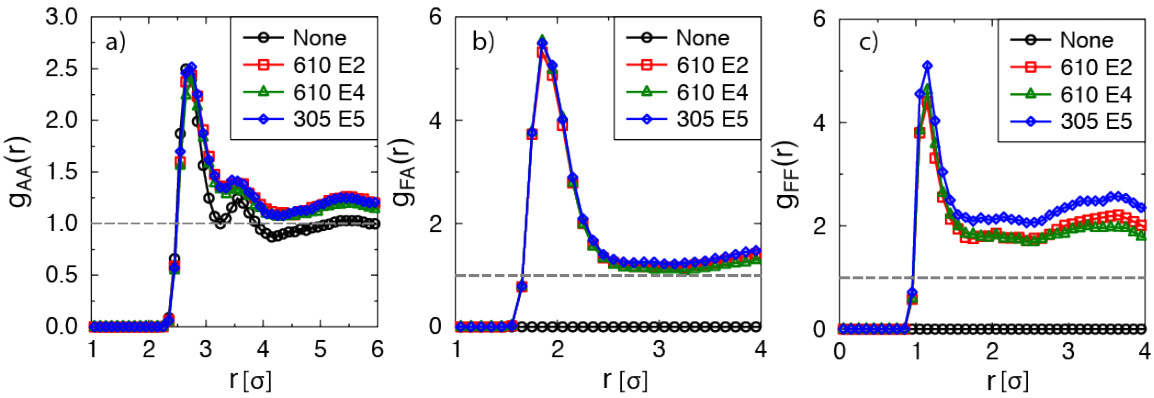

FIGURE 5.9: a) Acceptor-acceptor, $g_{AA}(r)$, b) additive end-acceptor, $g_{FA}(r)$, and c) additive end-additive end, $g_{FF}(r)$, radial distribution functions for the binary P1 oligomer-acceptor blend (denoted as "None") and ternary blends with additives E2, E4, and E5 maintaining 610 attractive additive end beads per blend.

The $g_{AA}(r)$ plot shows that the number of acceptor-acceptor contacts is the same for the binary oligomer-acceptor blend compared to the ternary blends and it is the same regardless of additive identity (Figure 5.9a). The number of F-A and F-F contacts also do not change significantly for ternary blends with additives E2, E4, and E5 (Figure 5.9b and c).

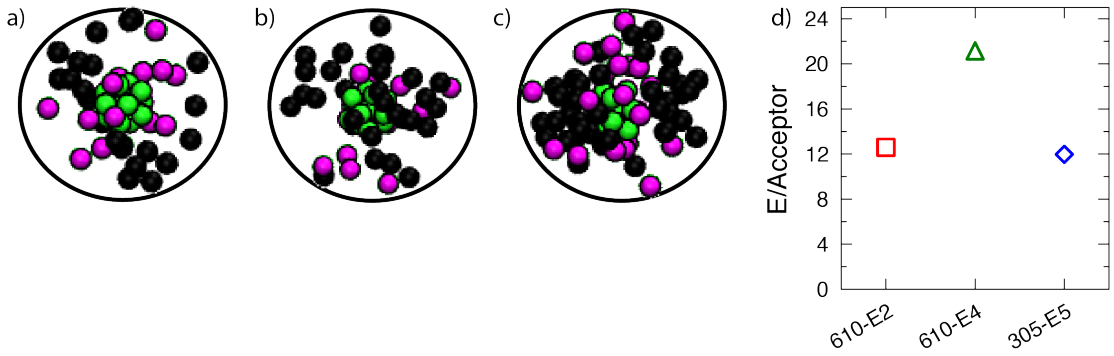

FIGURE 5.10: Snapshots of single acceptor molecules showing all additive beads in a radius of 4σ from the acceptor center for the P1 ternary blend with a) 610 E2, b) 610 E4, and c) 305 E5 additives. Oligomers and other acceptor molecules are not shown in the snapshots. Type 'E' beads are black, type 'F' beads are pink and type 'A' acceptor beads are green. d) Average number of 'E' beads within 4σ of an acceptor molecule center beads for the ternary 610 E2, 610 E4 and 305 E5 ternary blends at T* = 1.0. The average number of 'E' beads is computed for all acceptor centers using the final 20 statistically independent simulation snapshots at T*=1.0. The error bars computed using these 20 snapshots are smaller than the size of the symbols.

The snapshots in Figures 5.10a-c show that there are more type 'E' beads surrounding a representative acceptor for the E4 ternary blend compared to the E2 and E5 ternary blends. When we compare the average number of 'E' beads in E2, E4 and E5 ternary blends in Figure 5.10d we find that the E4 blend has a higher average number of 'E' beads within 4σ of acceptor centers than the E2 and E5 blends, in agreement with the snapshots. The presence of 'E' beads in the vicinity of an acceptor molecule sterically hinders additional acceptor molecules from joining the aggregate thus reduces the size of the acceptor aggregates formed, decreasing blend phase separation. Thus, E4 additives have higher steric hindrance, reducing the size of acceptor aggregates in E4 blends. The composition of the additive modulates number of 'E' beads in the vicinity of the acceptor and the degree of steric hindrance.

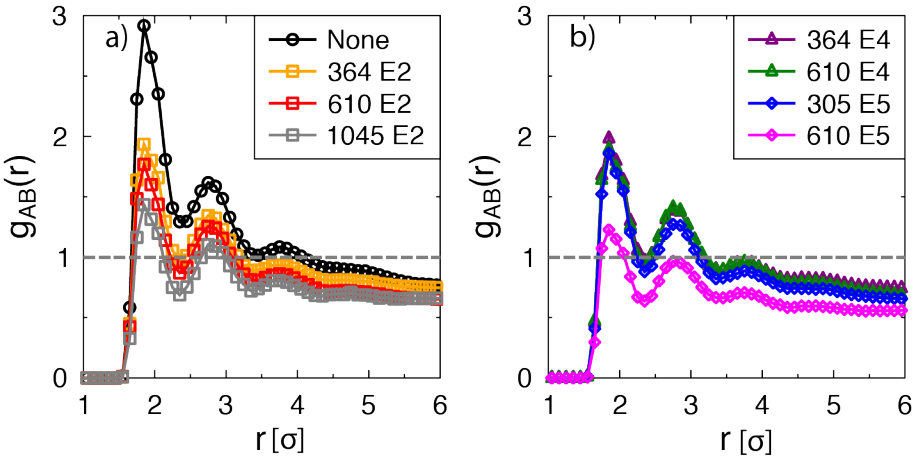

FIGURE 5.11: a) Acceptor-backbone radial distribution function, $g_{AB}(r)$, for P1 ternary blends with varying numbers of E2 additives and b) Acceptor-backbone radial distribution function, $g_{AB}(r)$, for P1 ternary blends with varying numbers E4 and E5 additives.

The number of acceptor-backbone contacts decreases (indicating reduced intercalation) as the number of attractive additive end groups is increased from 364 or 610 additive end groups to >1000 additive end groups (eg. 1045 E2 and 610 E5 ternary blends). Ternary blends with a higher number of attractive additive end groups, as in E5, have a higher enthalpic driving force

for acceptor-additive aggregation which reduces intercalation significantly with increasing number of E5 additives.

5.7.2 P1 oligomer blends with additives with free 'F' end groups

In order to elucidate the affect of the additive alkyl segment on P1 ternary blend morphology, we simulate ternary blends with additives E2, E4, and E5 with the bond between the attractive additive end group ('F' bead) and the weakly attractive 'E' beads removed. We denote these additives as '*Free*' additives. Separating the 'F' bead from the remaining 'E' additive beads eliminates steric hindrance from 'E' beads for enthalpically favorable F-A and F-F contacts.

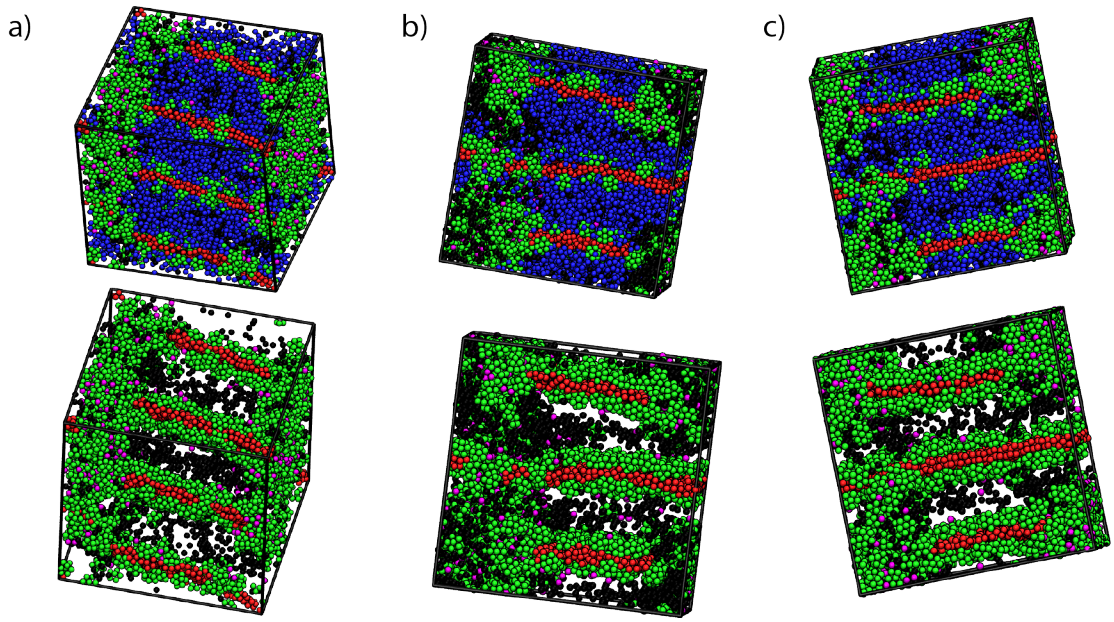

FIGURE 5.12: Snapshots of P1 ternary blends with additives: a) "Free E2", b) "Free E4", and c) "Free E5". Side chains are hidden in the bottom image for clarity. Backbone beads are colored red, side chain are colored beads blue, acceptor beads are colored green, additive type 'E' beads are colored black, and additive attractive end beads, type 'F', are colored pink.

Figure 5.12 shows the morphology of the "Free E2", "Free E4" and "Free E5" ternary blends with 610 additives. Free attractive additive end beads (pink) mix with acceptors and phase

separate from the oligomers. Type 'E' beads mix with chemically identical alkyl side chain beads and show some phase separation in the E4 blend.

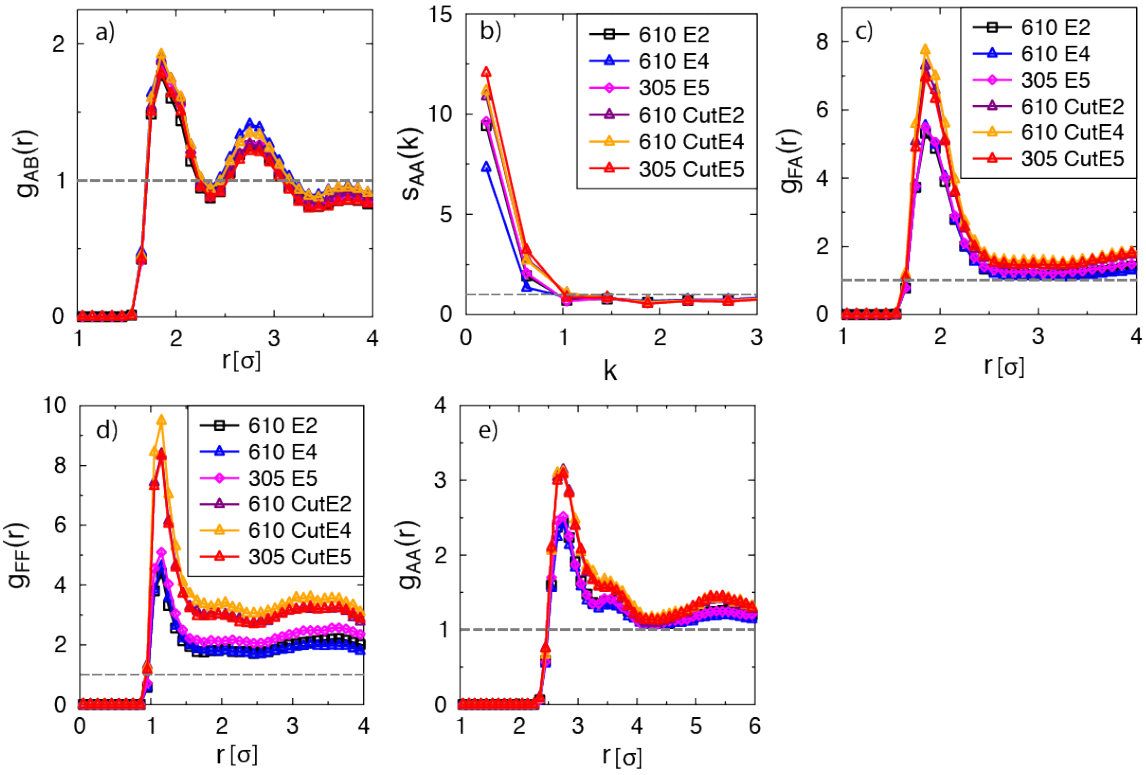

FIGURE 5.13: a) Acceptor-backbone radial distribution function, $g_{AB}(r)$, b) acceptor-acceptor structure factor, $s_{AA}(k)$, c) acceptor-additive end radial distribution function, $g_{FA}(r)$, d) additive end-additive end radial distribution function, $g_{FF}(r)$, and e) acceptor-acceptor radial distribution function, $g_{AA}(r)$,for P1 ternary blends with additives E2, E4, and E5 and with additives E2, E4, and E5 where the bond connecting the attractive additive end bead to the additive alkyl segment has been removed. These 'Free E2', 'Free E4', and 'Free E5' additives are denoted as 'CutE2', 'CutE4', and 'CutE5' in the legends. All blends contain 610 attractive additive end groups.

The acceptor-backbone radial distribution function shows that the connectivity of the additive end group and the alkyl segment does not significantly affect the number of acceptor-backbone contacts in the P1 ternary blends. This indicates that acceptors are intercalated to a similar extent in ternary blends with 'Free' additives as in ternary blends with regular additives. However, the acceptor-acceptor structure factor shows that the ternary blends with free additive end beads have higher phase separation than blends with regular additives where the end groups

are attached to the alkyl segments. Breaking the bond between the additive attractive end group ('F' beads) and the alkyl segment ('E' beads) eliminates the steric hindrance from the 'E' beads for acceptor aggregation and for enthalpically favorable F-A and F-F contacts. Figures 5.13c and 5.13d show that removing the bond between the attractive additive end and weakly attractive 'E' beads does indeed increase the number of F-A and F-F contacts in the ternary blend. The reduction in steric hindrance caused by removing the bond between the attractive end group and the weakly attractive additive segment is further evidenced in the $g_{AA}(r)$ plot (Figure 5.13). Ternary blends with 'Free' additives have a higher number of acceptor-acceptor contacts than in the case of the regular additives because there are fewer weakly attractive 'E' beads in the acceptor aggregates that sterically hinder acceptor-acceptor contacts.

5.7.3 P1 oligomer blends at T* = 2.0

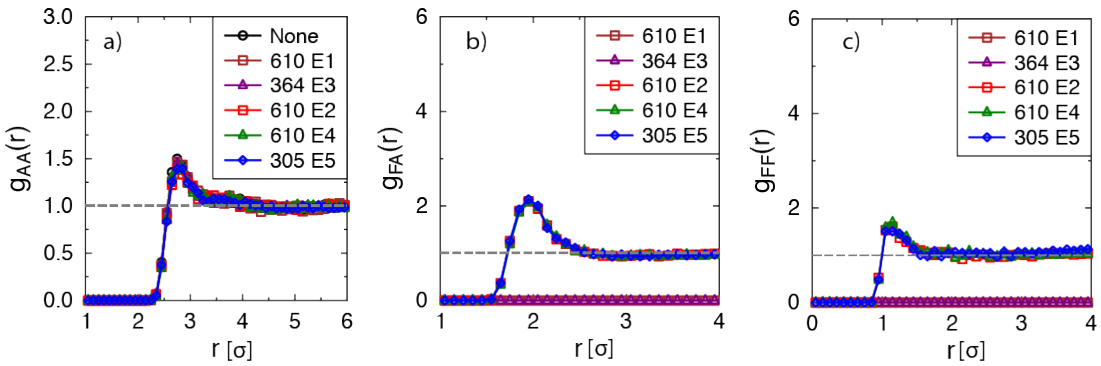

FIGURE 5.14: a) Acceptor-acceptor, $g_{AA}(r)$, b) additive end-acceptor, $g_{FA}(r)$, and c) additive end-additive end, $g_{FF}(r)$, radial distribution functions for ternary blends of P1 oligomers with additives EX, X ∈ [1,2,3,4,5] at T* = 2.0.

The acceptor-acceptor, $g_{AA}(r)$, additive end-acceptor, $g_{FA}(r)$, and additive end-additive end, $g_{FF}(r)$, radial distribution functions show that at T* = 2.0, above the disorder-to-order transition temperature, there is no difference in the number of A-A, F-A, or F-F contacts comparing ternary blends with the different additives and the binary oligomer-acceptor blend.

5.7.4: P2 oligomer blends

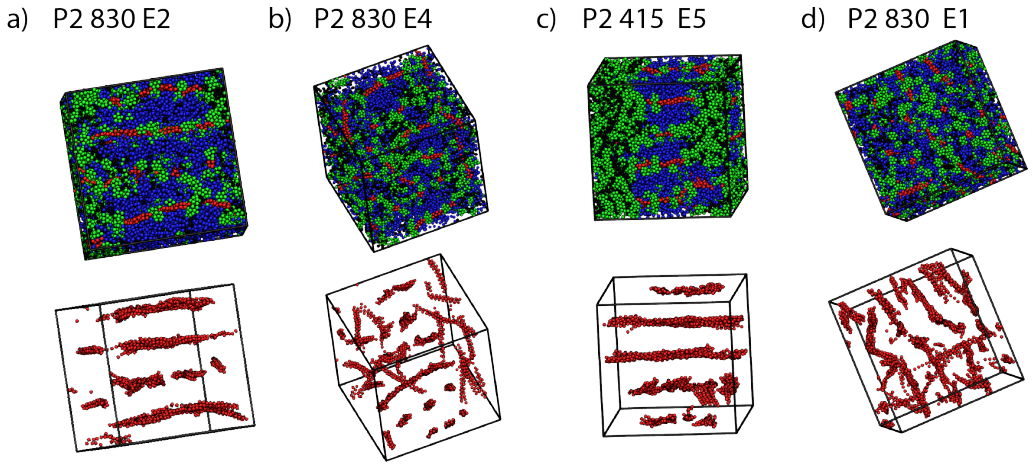

FIGURE 5.15: Simulation snapshots of a) P3DDT-like (**P2**) 830 E2, b) P2 830 E4, c) P2 415 E5, and d) P2 830 E1 ternary blends. Bottom images show only backbone beads.

Figure 5.15 shows that in the **P2** based E2 and E5 ternary blends with high phase separation the oligomer backbones are aligned. The backbone disorder in the 830 E4 ternary blend likely decreases acceptor phase separation. The E1 ternary blend also has disordered backbone domains.

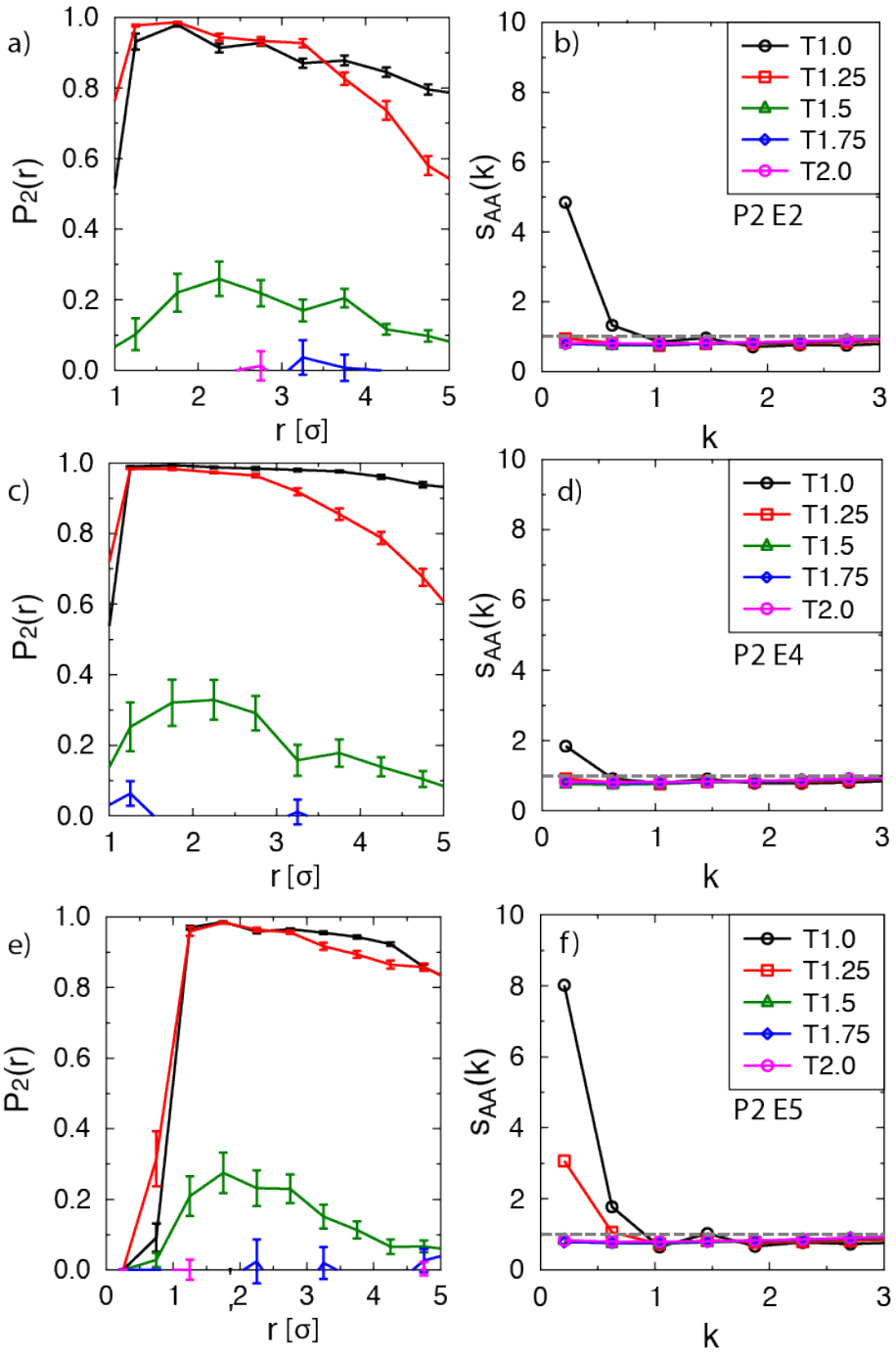

FIGURE 5.16: a) Order parameter, $P_2(r)$, and b) acceptor-acceptor structure factor, $s_{AA}(k)$, for the P2 ternary blend with E2 as a function of simulation temperature, T*. c) Order parameter, $P_2(r)$, and d) acceptor-acceptor structure factor, $s_{AA}(k)$, for the P2 ternary blend with E4 as a function of simulation temperature, T*. e) Order parameter, $P_2(r)$, and f) acceptor-acceptor structure factor, $s_{AA}(k)$, for the P2 ternary blend with E5 as a function of simulation temperature, T*.

The $P_2(r)$ and $s_{AA}(k)$ plots in Figure 5.16 show that oligomer backbone orientational alignment occurs at temperatures above the temperature of blend macrophase separation for P2 E2 and E4 ternary blends while backbone orientational alignment occurs at the same temperature (T* = 1.25) as macrophase separation for the E5 ternary blend. Backbone orientational order is indicated by a $P_2(r)$ value of near 1.0. We think macrophase separation is facilitated for the P2 E5 ternary blend because the additive induced driving force for acceptor aggregation is strong enough that acceptor aggregation occurs at a temperature above that of backbone alignment, allowing for higher acceptor mobility and increased aggregation.

5.7.5: Comparison of P1 and P2 oligomer blends

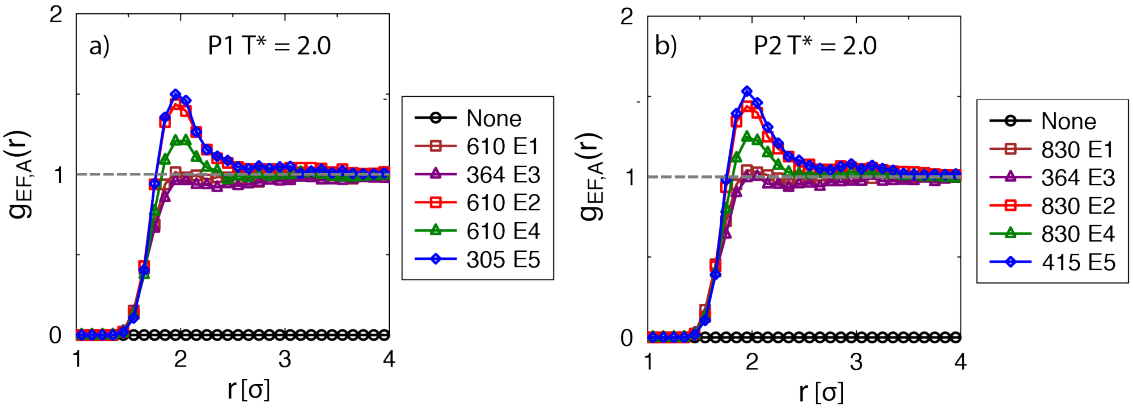

FIGURE 5.17: Additive-acceptor bead radial distribution function $g_{EF,A}(r)$ for ternary blends of a) P1 oligomers and b) P2 oligomers with varying numbers of additives EX, X ∈ [1,2,3,4,5] at T* = 2.0.

Figure 5.17 shows that additive-acceptor contacts are similar comparing P1 ternary blends to P2 ternary blends. Thus, additive-acceptor aggregation at T*=2.0 does not depend on oligomer architecture and additives and acceptors aggregate to the same extent at high temperature.

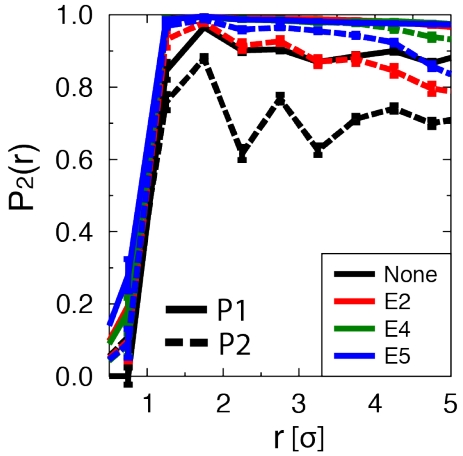

FIGURE 5.18: Orientational order parameter, $P_2(r)$, for ternary and binary oligomer-acceptor P1 (solid) and P2 (dashed) blends.

Figure 5.18 shows that P1 ternary and binary oligomer-acceptor blends have higher local orientational order than the corresponding P2 blends.

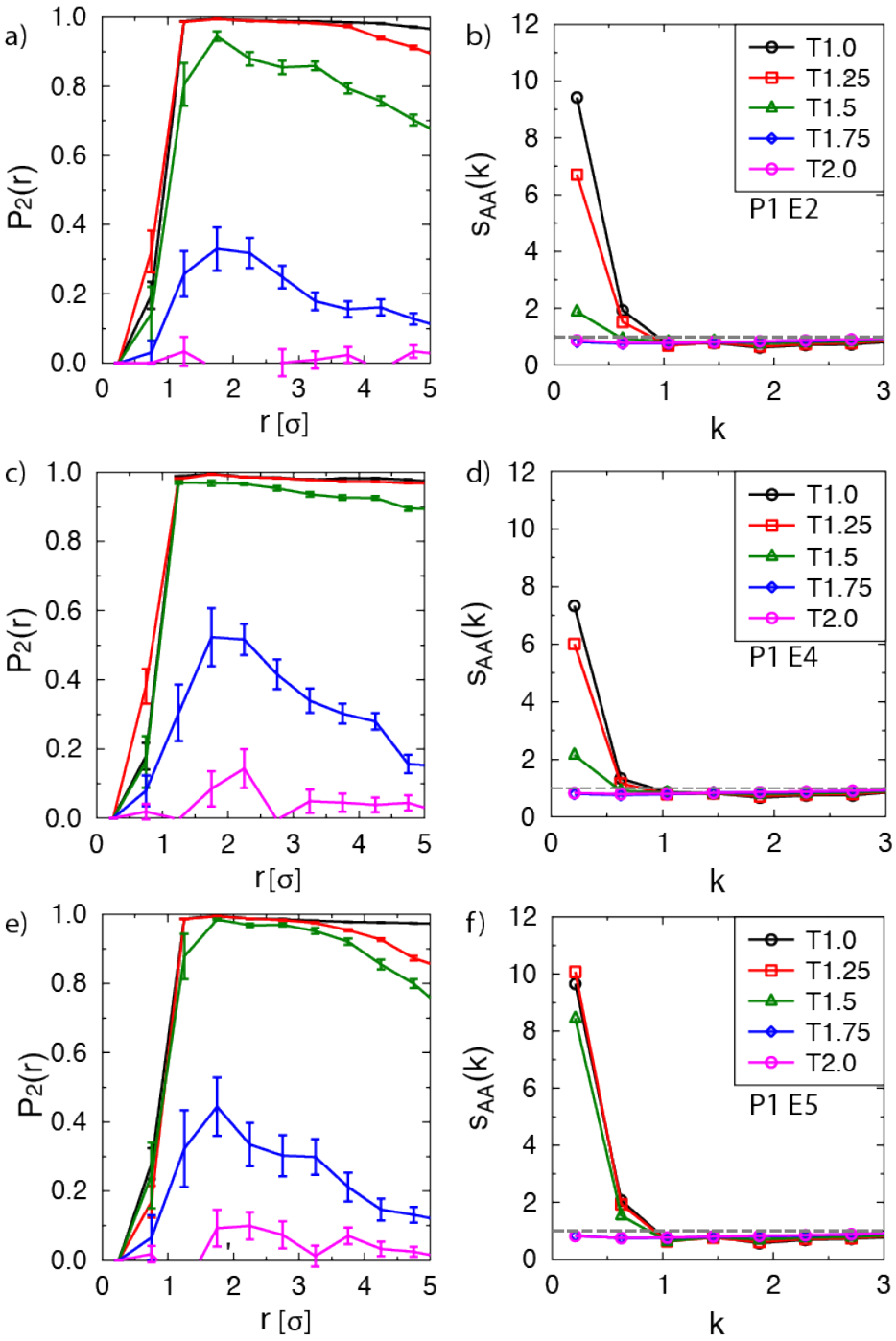

FIGURE 5.19: a) Order parameter, $P_2(r)$, and b) acceptor-acceptor structure factor, $s_{AA}(k)$, for the P1 ternary blend with E2 as a function of simulation temperature, T*. c) Order parameter, $P_2(r)$, and d) acceptor-acceptor structure factor, $s_{AA}(k)$, for the P1 ternary blend with E4 as a function of simulation temperature, T*. e) Order parameter, $P_2(r)$, and f) acceptor-acceptor structure factor, $s_{AA}(k)$, for the P1 ternary blend with E5 as a function of simulation temperature, T*.

Figure 5.19 shows that P1 ternary blends have an ODT of T* = 1.5. Both oligomer backbone ordering and acceptor phase separation occur at T* = 1.5 as evidenced by the $P_2(r)$ and $s_{AA}(k)$ plots. Simultaneous backbone and acceptor ordering in the P1 blends facilitates oligomer-acceptor phase separation compared to the P2 case where backbone alignment happens at temperatures above the temperature of acceptor aggregation. Backbone order occurs at a higher temperature for P1 compared to P2 because P1 has more exposed attractive backbone beads which facilitate alignment.

Chapter 6

2,5-bis(3-alkylthiophen-2-yl)thieno[3,2-b]thiophene (BTTT) Oligomer Morphology for Organic Electronics Applications

Adapted from: *Journal of the American Chemical Society, 136* (52), 18120–18130, **2014.**

6.1 INTRODUCTION

While polythiophenes are more commonly used in organic electronic devices, oligothiophenes consisting of several monomer units are also of interest because they have significant charge carrier mobility, and their synthesis and film morphology are more easily controlled compared to polythiophenes[1-3]. In addition, oligothiophenes serve as useful models to study the assembly and crystalline packing of polythiophenes without the formation of amorphous domains that complicate polythiophene structural characterization[1, 4]. For example, short oligomers form single crystals suitable for X-ray diffraction analysis while polymers typically do not[1].

Poly(2,5-bis(3-alkylthiophen-2-yl)thieno[3,2-b]thiophene), PBTTT, is a polythiophene typically used in transistors and organic photovoltaic devices because of its high charge carrier mobility and three-dimensional order[5-7]. In blends with fullerene derivative acceptors used in bulk heterojunction solar cells, acceptors intercalate between the alkyl side chains of PBTTT because there is sufficient space for the molecule to fit and acceptor-backbone attraction makes intercalation energetically favorable[8-10]. Recently, Zhang *et al.* synthesized BTTT oligomers of length 1-5 monomer units, and studied single crystals, neat polymer films, and films of 1:1 blends of BTTT with [6,6]-phenyl-C_{71}-butyric acid methyl ester ($PC_{71}BM$) fullerene derivative molecules to understand the affect of oligomer length on oligomer morphology, electronic

properties, and device performance[1]. They found that acceptors intercalate in blends with BTTT oligomers of length 2-5 monomer units (BTTT-2 to BTTT-5), but not in the case BTTT-1. X-Ray Diffraction results showed that blends had higher crystallinity than neat BTTT. BTTT-2:$PC_{71}BM$ blends a formed cocrystal with well-ordered, 1D channels of acceptors. Figures 6.1a and b from ref [1] show the packing of BTTT-2 oligomers in the 1:1 blends, and Figures 6.1c and d show the ordered PCBM sublattice and 1D channels. Acceptors intercalated in blends with the longer oligomers did not form the highly ordered $PC_{71}BM$ sublattice and BTTT-5 oligomers exhibited properties that approached that of the polymer PBTTT[1]. Photovoltaic devices were made with these blends and devices containing BTTT-2 blends were the most efficient out of the oligomers BTTT-1 to BTTT-5.

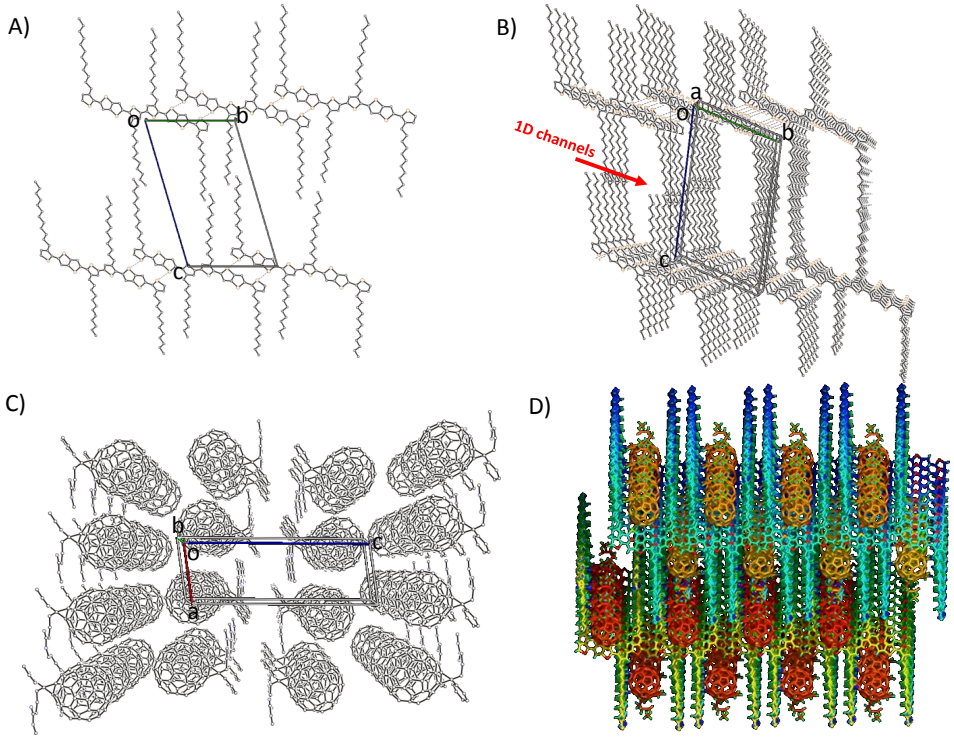

FIGURE 6.1. A) The crystal packing of BTTT-2 "catalyzed" by $PC_{71}BM$, B) the 1D channels formed by BTTT-2 side chains, C) the crystal packing of $PC_{71}BM$, and D) the bimolecular co-crystal packing of BTTT-2/$PC_{71}BM$ (the channels host $PC_{71}BMs$)[1]. Figure and caption from ref [1].

In this work, published within ref [1], we perform molecular dynamics simulations on neat BTTT oligomers and 1:1 blends of BTTT oligomers with fullerene derivative acceptor molecules to compare with the morphologies hypothesized from experimental X-ray diffraction results in ref [1] and to create a foundation for future work to predict the effect of BTTT alkyl side chain length on neat and blend BTTT morphology. We find that acceptor molecules intercalate in blends with BTTT-2 oligomers but not in blends of BTTT-1 oligomers, as in experiments. BTTT-2 1:1 blends show higher crystallinity than neat BTTT-2, and acceptors form ordered channels as suggested by the experimental results. This work demonstrates that our simulations of conjugated oligothiophenes model well morphologies of oligothiophenes that are directly applicable in organic photovoltaic devices.

6.2 MOLECULAR DYNAMICS SIMULATION APPROACH

6.2.1 Simulation Model and Method

The coarse-grained BTTT-2 oligomer model is an extension of the generalized thiophene oligomer model that was developed in our recent work[11, 12]. In this work, as in the previous studies, the backbone thiophene rings are modeled with one coarse-grained bead, 'type B', and side chains are modeled with 'type S' beads representing three alkyl groups each (Figure 6.2). Figure 6.2b shows a single BTTT-2 model oligomer isolated from a simulation snapshot. Each PCBM molecule is modeled as a rigid collection of 13 'type A' beads (6.2c).

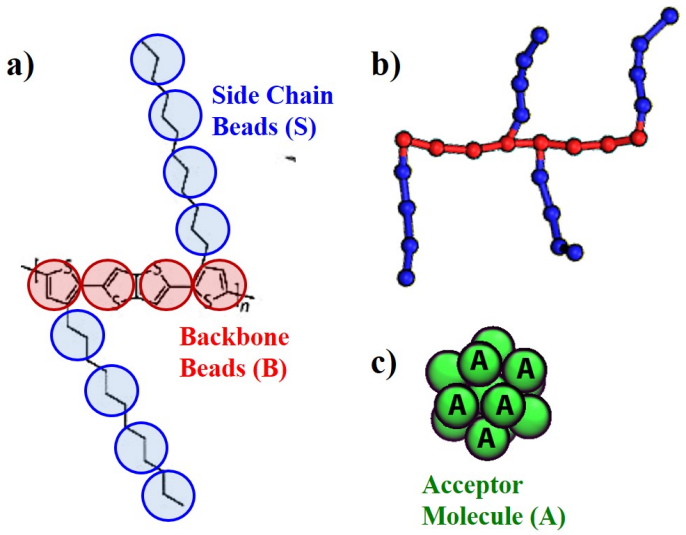

FIGURE 6.2: a) Coarse-grained model of a BTTT monomer unit with backbone thiophene rings modeled as 'type B' beads and side chains modeled with 'type S' beads representing 3 alkyl groups each. b) Coarse-grained BTTT-2 oligomer isolated from a simulation snapshot. c) PCBM molecule represented as a rigid body of 13 'type A' beads. The physical details and the bonded and non-bonded interaction potentials used in the coarse-grained model are presented in detail in our recent work[11, 12].

The diameter of these CG beads is 1.0σ, where $\sigma = 3\times10^{-10}$m. The bond, angle, and dihedral potentials enforcing the architecture (e.g. side chain orientation with respect to the backbone) and flexibility (e.g. stiffer backbone versus side chains) of these oligomers are described in detail in refs [11, 12]. The non-bonded interactions between the coarse-grained beads are described by Lennard-Jones potentials[13] as in refs [11, 12], where σ_{ij} is the distance between the centers of mass of beads i and j and ε_{ij} is the well depth of the potential for beads of 'type i' and 'type j'. The energy unit is $\varepsilon = 2.7 \text{ X } 10^{-21}$ J. The backbone bead-backbone bead interaction, ε_{BB}, is the most strongly attractive interaction in the system to mimic π-π interactions. The potential well depths are: $\varepsilon_{BB} = 2.0\varepsilon$, $\varepsilon_{BS} = 0\varepsilon$ (modeled by the Weeks-Chandler-Andersen potential[14]), $\varepsilon_{SS} = 0.1\varepsilon$, $\varepsilon_{AA} = 0.1\varepsilon$, $\varepsilon_{AS} = 0.1\varepsilon$ and $\varepsilon_{AB} = 1.0\varepsilon$, as described in refs [11, 12]. This model was able to reproduce experimentally observed backbone-backbone spacing in the ordered structure of poly(3-hexyl thiophene) (P3HT), different morphologies for

varying polymer architecture (e.g. P3HT vs poly(3,4-dihexyl-2,2′-bithiophene) (PDHBT)), and PCBM intercalation between oligomer side chains for polymers with larger side chain spacing.

We conduct molecular dynamics simulations of a) 350 oligomers of neat BTTT-2, and b) 1:1 (weight) BTTT-2:PCBM blends (350 oligomers and 435 PCBM molecules) using the HOOMD-blue[15] package on graphical processing units (GPUs). The simulation boxes are cubic with periodic boundary conditions and are run in the isothermal-isobaric ensemble (NPT) and the resulting volume fraction (defined as volume of all beads/volume of simulation box) of these neat and blend systems, at the temperature and pressure of interest, are 0.20 and 0.29, respectively. We followed the same simulation protocol as described, in detail, in our recent work[11, 12]. Briefly, simulations begin at high temperature where the BTTT-2 (in case of neat systems) and the BTTT-2 and PCBM (in case of blends) are well mixed and completely disordered. The systems are then cooled slowly, and equilibrated at each temperature. The systems go through a disorder to order transition, and the equilibrated ordered configurations at reduced temperature T*=1.0 are analyzed.

6.2.3 Analysis

Aside from the simulation snapshots visualized using VMD package[16], we also quantify the positional ordering of the structure within the neat and blend systems using a combination of pair correlation functions and structure factors, as done in our recent work[11, 12]. Orientational ordering between oligomer backbones is quantified using the order parameter, $P_2(r)$, calculated using the following formula[17]:

$$P_2(r) = \frac{1}{2}(3 * \cos^2(\theta_{ij})$$

where r is the distance between centers of mass of any two BTTT-2 backbones i and j, and θ_{ij} is the angle between backbones i and j. A P_2 value of 1 indicates perfect backbone orientational

order (e.g. two aligned rods would have a P_2 at contact equal to 1) and lower P_2 values indicates reduced orientational order.

6.3 RESULTS

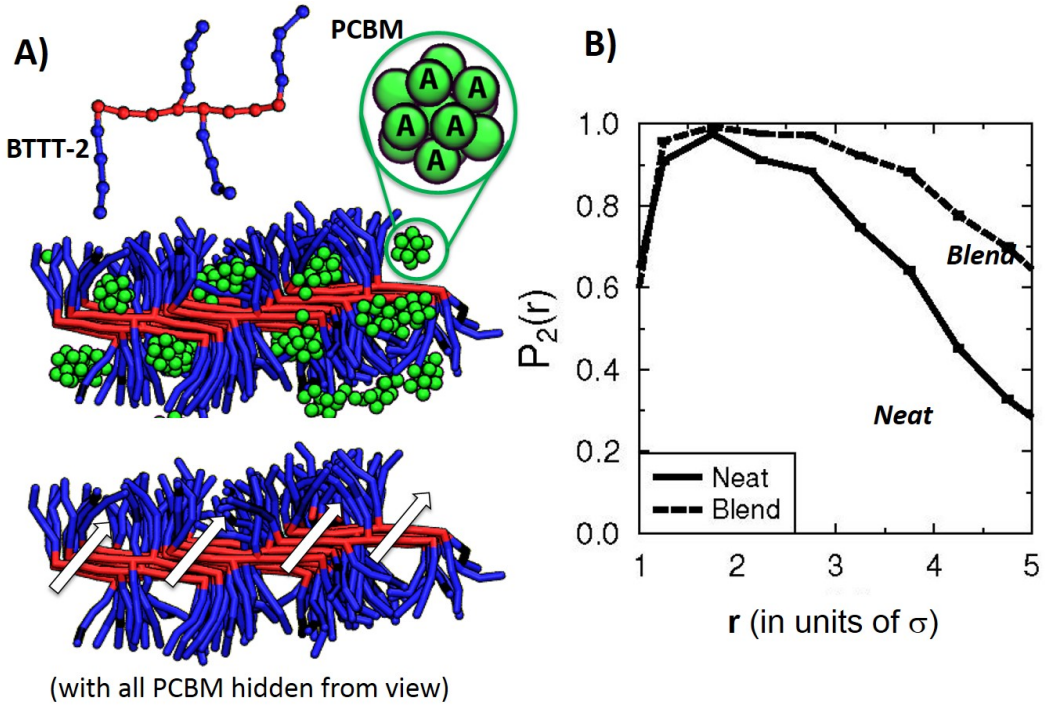

FIGURE 6.3. a) Simulation snapshot of a section of the simulation box showing the PCBM molecules (inset showing a single PCBM molecule, modeled as the green icosahedral collection of coarse-grained 'type A' spheres) intercalating amidst the side chains of BTTT-2. Bottom image shows the same snapshot as above with the PCBM molecules hidden from view to present clearly the channels formed by side chains to host the PCBM, as suggested in experiments. b) Orientational order parameter between BTTT-2 backbones, P_2, as a function of r, defined as the distance between centers of mass of BTTT-2 backbones in reduced units of σ (where σ=0.3nm) show higher orientational order (higher P_2) of BTTT-2 in blends versus neat systems especially at larger r.

The calculated structures of BTTT-2/PCBM blends and of neat BTTT-2 as obtained from molecular simulations also show an increased orientational ordering of BTTT-2 in the presence of PCBM as compared to pristine BTTT-2 with no PCBM (Figure 6.3). We note that the generic coarse-grained models used in these molecular dynamics (MD) simulations were validated in earlier work on thiophene-based oligomers[11, 12] and were *not* customized to reproduce any of the

experimental data in ref [1]. Therefore, it is striking that, in agreement with the experimental results, these independently validated MD simulations also predict higher orientational order. This is quantified by the orientational order parameter, $P_2(r)$, of BTTT-2 backbone-backbone distances which is larger in the blends with PCBM than in pristine systems in the absence of PCBM (Figure 6.3b). The PCBM molecules are found to intercalate between the side chains of the BTTT-2 in the ordered state. The favorable enthalpic interactions between the PCBM and BTTT-2, in addition to the favorable attractive (stacking) interactions between the (red) beads of orientationally aligned BTTT-2 backbones, and the favorable topology of BTTT-2 that allows the PCBMs to intercalate, together lower the total energy of the ordered states of BTTT-2/PCBM over the neat BTTT-2 systems at similar temperature and pressure. Such PCBM intercalation was not observed with this model in blends of PCBM with oligomers of poly(3-hexyl thiophene)[47] or with BTTT-1/PCBM blends, the latter showing a different packing motif compared to BTTT-2/PCBM blends (data not shown).

6.4 CONCLUSION

Our coarse-grained simulations of neat BTTT-2 and 1:1 blends of BTTT-2 with fullerene derivative acceptor molecules predict molecular-level packing in agreement with the experimental X-ray diffraction results in ref [1]. BTTT-2 blends have higher oligomer backbone order than systems of neat BTTT-2, and acceptor molecules form ordered channels in BTTT-2 blends in simulation and experiment. Thus, our model reproduces well oligothiophene morphology and is relevant in the field of organic electronics where both oligomers and polymers are used. With this experimentally validated model, in future work, we will predict morphologies of BTTT oligomers with varying alkyl side chain (length 6-15 alkyl groups) and oligomer backbone lengths (BTTT-2 and BTTT-4).

6.5 AKNOWLEDGEMENTS

We thank U.S. Department of Energy, Office of Basic Energy Sciences, grant (DE-SC0003912) for financially supporting the simulations presented in this work, and acknowledge the use of supercomputing resources at National Energy Research Scientific Computing Center supported by the Office of Science of the U.S. Department of Energy under Contract DE-AC02-05CH11231.

6.6 REFERENCES

1. Zhang, L.; Liu, F.; Diao, Y.; Marsh, H. S.; Colella, N. S.; Jayaraman, A.; Russell, T. P.; Mannsfeld, S. C. B.; Briseno, A. L. *Journal of the American Chemical Society* **2014,** 136, (52), 18120-18130.

2. Zhang, L.; Colella, N. S.; Liu, F.; Trahan, S.; Baral, J. K.; Winter, H. H.; Mannsfeld, S. C. B.; Briseno, A. L. *Journal of the American Chemical Society* **2013,** 135, (2), 844-854.

3. Ahmed, M. O.; Wang, C.; Keg, P.; Pisula, W.; Lam, Y.-M.; Ong, B. S.; Ng, S.-C.; Chen, Z.-K.; Mhaisalkar, S. G. *Journal of Materials Chemistry* **2009,** 19, (21), 3449-3456.

4. Koch, F. P. V.; Heeney, M.; Smith, P. *Journal of the American Chemical Society* **2013,** 135, (37), 13699-13709.

5. Wang, C. C.; Jimison, L. H.; Goris, L.; McCulloch, I.; Heeney, M.; Ziegler, A.; Salleo, A. *Advanced Materials* **2010,** 22, (6), 697-701.

6. Cho, E.; Risko, C.; Kim, D.; Gysel, R.; Miller, N. C.; Breiby, D. W.; McGehee, M. D.; Toney, M. F.; Kline, R. J.; Bredas, J. L. *Journal of the American Chemical Society* **2012,** 134, (14), 6177-6190.

7. Miller, N. C.; Gysel, R.; Miller, C. E.; Verploegen, E.; Beiley, Z.; Heeney, M.; McCulloch, I.; Bao, Z. N.; Toney, M. F.; McGehee, M. D. *Journal of Polymer Science Part B-Polymer Physics* **2011,** 49, (7), 499-503.

8. Miller, N. C.; Cho, E.; Gysel, R.; Risko, C.; Coropceanu, V.; Miller, C. E.; Sweetnam, S.; Sellinger, A.; Heeney, M.; McCulloch, I.; Bredas, J. L.; Toney, M. F.; McGehee, M. D. *Advanced Energy Materials* **2012,** 2, (10), 1208-1217.

9. Miller, N. C.; Cho, E.; Junk, M. J. N.; Gysel, R.; Risko, C.; Kim, D.; Sweetnam, S.; Miller, C. E.; Richter, L. J.; Kline, R. J.; Heeney, M.; McCulloch, I.; Amassian, A.; Acevedo-Feliz, D.; Knox, C.; Hansen, M. R.; Dudenko, D.; Chmelka, B. F.; Toney, M. F.; Bredas, J. L.; McGehee, M. D. *Advanced Materials* **2012,** 24, (45), 6071-+.

10. Mayer, a. C.; Toney, M. F.; Scully, S. R.; Rivnay, J.; Brabec, C. J.; Scharber, M.; Koppe, M.; Heeney, M.; McCulloch, I.; McGehee, M. D. *Advanced Functional Materials* **2009,** 19, (8), 1173-1179.

11. Marsh, H. S.; Jankowski, E.; Jayaraman, A. *Macromolecules* **2014,** 47, (8), 2736-2747.

12. Jankowski, E.; Marsh, H. S.; Jayaraman, A. *Macromolecules* **2013,** 46, (14), 5775-5785.

13. Verlet, L. *Physical Review* **1967,** 159, (1), 98-103.

14. Weeks, J. D.; Chandler, D.; Andersen, H. C. *Journal of Chemical Physics* **1971,** 54, (12), 5237-5247.

15. Anderson, J. A.; Lorenz, C. D.; Travesset, A. *Journal of Computational Physics* **2008,** 227, (10), 5342-5359.

16. Humphrey, W.; Dalke, A.; Schulten, K. *Journal of Molecular Graphics & Modelling* **1996,** 14, (1), 33-38.

17. Yankova, T. S.; Bobrovsky, A. Y.; Vorobiev, A. K. *Journal of Physical Chemistry B* **2012,** 116, (20), 6010-6016.

Chapter 7

Control of Polythiophene Film Microstructure and Charge Carrier Dynamics Through Crystallization Temperature

Adapted from: *J. Polym. Sci., Part B: Polym. Phys*. 52 (10) 700-707, **2014**

7.1 INTRODUCTION

Blends of conjugated polymers, such as poly(3-hexylthiophene) (P3HT), with high electron affinity molecules show great promise as active layers for inexpensive, flexible solar cells. The polymer serves as the electron donating and primary light absorbing material, while molecular species such as fullerene derivatives act as the electron acceptors.[1-4] Much work has focused on the putative two-phase morphology formed by these donor/acceptor blends, and on how structure correlates with performance.[1, 4-7] More recently, it has become evident that the microstructural evolution of the polymer component – by itself complex – can play a crucial role in determining the ultimate phase morphology of these blends.[8] Such blended films are now known to be composed of at least three phases: domains of amorphous polymer (mixed with electron acceptor molecules), domains of crystalline polymer, and domains of pure electron acceptors.[8-13]

Previously, we proposed that photogeneration of long-lived charge carriers in neat P3HT is dominated by its solid-state microstructure and that charge separation occurs at the boundary between amorphous and crystalline regions (generally found in high molecular weight materials only).[14] Recent photovoltage spectroscopy studies also suggest that free charge carriers are generated at the interfaces between the amorphous and crystalline regions in P3HT films.[15] In addition, charge carrier recombination is thought to occur at this interface.[16] Thus, manipulation

of the size of the amorphous and crystalline domains can be expected to have a strong influence on the yield and lifetime of free photogenerated charges, as such changes determine the interfacial area between amorphous and crystalline domains for a given degree of crystallinity.

Here, we demonstrate control over the microstructure in neat films of two closely related polythiophene derivatives, poly(3-hexylthiophene) (P3HT) and poly[(3,3''-didecyl[2,2':5',2''-terthiophene]-5,5''-diyl) (PTTT-10) (Figure 7.1a). PTTT is a structural analogue of P3HT in which every third thiophene unit in the polymer backbone is unsubstituted and the regiochemistry of the side chains is changed from head-to-tail to tail-to-tail. As a result of the reduction in overall alkyl chain density compared to P3HT, longer side chains, in this case decyl, are required to ensure similar levels of solubility. The reduction in alkyl side chain density alters the crystallization behavior of PTTT compared to P3HT, with PTTT forming ordered lamellae in which side chains of adjacent backbones interdigitate. Such changes result in a reduction of interlamellar distance compared to P3HT, even for identical side chain lengths.[17]

We study conjugated polythiophenes due to the semi-flexible nature of the polymer backbone, which renders its solidification and crystallization behavior similar to that of polyolefins and leading, in materials of higher $M_{w,}$ to a semicrystalline morphology composed of folded-chain crystals, amorphous inter-crystalline zones and interconnecting tie molecules.[18-22] According to classical polymer physics studies, the thickness (fold length) of lamellar crystals in flexible polymers (e.g. polyethylene) crystallized from solution is controlled by solvent quality and crystallization temperature. Both of these influences are captured by a single parameter: the supercooling during crystal formation (i.e. the difference between the crystallization temperature and dissolution temperature of the polymer in a given solvent).[23-25]

Fold-length control is kinetic in origin: starting with an extended polymer chain in solution, there is a finite probability that it will fold back on itself through random thermal motion, with longer folds being less probable than shorter ones. A fold is stabilized if the temperature and fold length-dependent Gibbs energy reduction from increasing inter-chain contacts (crystallization) balances the Gibbs energy gain associated with creating a fold edge and a sharp bend in the polymer backbone. At higher temperatures, a longer fold length is needed to achieve this balance because the Gibbs energy of crystallization per unit crystal volume becomes more positive with increasing temperature. Thus, polymers crystallized from solution at a higher temperature form structures composed of thicker crystals, i.e. larger fold lengths.[24]

Other researchers have shown that this understanding of flexible polymers like polyethylene can be applied to P3HT. For example, the lamellar crystal thickness (or fold length) of P3HT nanowiskers and nanoribbons crystallized from solution has been shown to depend on temperature in precisely the way that traditional polymer crystallization theory predicts.[26] However, little is known about how such changes in the structural features of neat conjugated polymer films control electronic processes such as charge carrier dynamics.

In this work, we control the crystalline domain size and lamellar crystal thickness of PTTT and P3HT through judicious choice of crystallization temperature, T_c, and find that these structural features affect the charge carrier yield and lifetime probed with time-resolved microwave conductivity (TRMC). Films cast at high temperatures, with larger crystalline domains and thicker lamellae than those deposited at lower temperatures, produce longer-lived photogenerated carriers. Similarly, charge carrier yield depends on the crystallite surface area available for exciton dissociation, generally decreasing with increasing crystalline domain size.

7.2 EXPERIMENTAL

7.2.1 Thin Film Fabrication

Poly[(3,3"-didecyl[2,2':5',2"-terthiophene]-5,5"-diyl) (PTTT-10) of weight-average molecular weight $M_w \approx$ 41 kg/mol (PDI = 1.7) and $M_w \approx$ 18 kg/mol (PDI 1.5) were synthesized by the Stille polymerization of 2,5-bis(trimethylstannyl)thiophene and 5,5'-dibromo-4,4'-didecyl-2,2'-bithiophene according to the previously published procedure.[27] The lower molecular weight polymer was prepared by using a slight excess (10%) of the 2,5-bis(trimethylstannyl)-thiophene monomer. Number-average (M_n) and weight-average (M_w) molecular weights were determined by Agilent Technologies 1200 series GPC running in chlorobenzene at 80 ˚C, using two PL mixed B columns in series, and calibrated against narrow polydispersity polystyrene standards. Poly(3-hexylthiophene) (P3HT) of $M_w \approx$ 48 kg/mol and 20 kg/mol were purchased from Merck and used for the TRMC and XRD experiments presented in this manuscript. P3HT from Rieke Metals 4002-EE of 50-70 kg/mol was used for DSC and annealing experiments. Comparison of the Merck and Rieke Metals P3HT shows that the two batches have similar properties (Section 7.7.1). Thin film fabrication was conducted under nitrogen atmosphere (<1 ppm O_2, <0.1 PPM H_2O) in a glovebox. Films were drop cast onto quartz substrates using 100 µL of a 7.5 mg/mL solution in chlorobenzene. Substrate temperature or crystallization temperature, T_c, was controlled with a hot plate and varied between 26 and 150 ˚C measured independently. Thin film microstructure was found to be independent of solution temperature 60 ˚C $\leq T \leq$ 100 ˚C (see Section 7.7.2), which is to be expected as the small volume of initially deposited solution will thermally equilibrate quite rapidly with the substrate. Identical experiments using 1,2-dichlorobenzene, chloroform, and p-xylene as the solvent in place of chlorobenzene show that the polymer microstructure is dominated by crystallization temperature,

and is not related to the evaporation rate of the solvent (Section 7.7.2). Samples were loaded into the sealed TRMC sample cavity in a glovebox under Nitrogen.

7.2.2 Flash-Photolysis Time-Resolved Microwave Conductivity (TRMC)

Flash-photolysis TRMC is a contactless transient absorption technique sensitive to the yield and lifetime of mobile charge carriers. The full description of the TRMC method and experimental set up can be found in other publications[28-30] and in Section 7.7.3. Neat PTTT and P3HT films were placed at the point of maximum electric field in an X-band TE_{102} microwave resonance cavity tuned to 9 GHz. Samples were excited with a ~ 4 ns 550 nm pulse (OPO-Continuum Panther pumped with the third harmonic of Nd:YAG laser: Continuum Powerlite) generating excitons that dissociate into free charge carriers. The change in microwave absorption induced by the photoinduced charges is measured to obtain the high frequency photoconductance, ΔG, as a function of time.

7.2.3 X-Ray Diffraction

X-ray diffraction experiments were conducted in air with a Rigaku DMAX X-Ray Diffractometer. Each sample was aligned and the edges of the drop cast polythiophene films were removed with a razor blade. $\theta/2\theta$ scans were conducted from 3˚ to 13˚ at a scan rate of 0.5˚ per minute at 40 kV and 250 mA. The coherence length, L_c, along the lamellar stacking direction (the (100)-direction) was calculated from the diffraction data using Scherrer's formula[31]. See Section 7.7.4 for calculation details and representative diffraction data. Determination of crystallite size for polymer samples is difficult due to disorder in the polymer crystallites[32]. Thus, L_c values presented here are reported to compare crystallite sizes between samples, and are not intended as a quantitative measure of the size of the polymer crystallites. Additionally, the data we report is not corrected for instrument broadening. These caveats should not, however, impact

the qualitative trends we observe. Instrument broadening should not change significantly between samples because all data is measured under the same conditions[33] and the diffraction peaks for the polymers studied here fall within a narrow 2θ range. In Section 7.7.4, we show that correcting the XRD data with an approximate instrument broadening value determined from a lanthanum hexaboride standard does not affect trends in coherence length data.

7.2.4 Differential Scanning Calorimetry (DSC)

Differential Scanning Calorimetry was performed on samples of high-M_w PTTT and P3HT (Rieke Metals P3HT) films cast at 26 °C and at 100 ˚C using a TA Q Series DSC 2000 instrument. Films were cast on microscope slides, using the procedure described above, and removed using a razor blade. Samples were weighed in air, and packed into measurement crucibles under nitrogen atmosphere before measurement in the TA Q Series DSC 2000. A scanning rate of 10 °C/min was employed. Melting temperatures, T_m, are deduced from the peak of the melting endotherms, and the enthalpies of fusion, ΔH_f, are obtained from the integral of melting endotherms and the sample mass.

7.3 RESULTS

The crystallization of polymers is strongly affected by the crystallization temperature, T_c, (here, the substrate temperature) providing a tool to manipulate features such as the size and thickness of crystalline domains.[34] We demonstrate how T_c controls crystalline domain size, using the coherence length, L_c, (Figure 7.1b) along the lamellar stacking direction (the (100)-direction) as our measure of structural change. Figure 7.1c shows the dependence of L_c on casting temperature for P3HT and PTTT samples of both low and high-M_w, calculated from the XRD data using Scherrer's formula. Data points for all samples measured are plotted in Figures 1b and 1c and thus we do not show error bars. Fewer data points are needed for P3HT because

behavior is less complex. Representative XRD data and analysis method are presented in Section 7.7.4. At low casting temperatures, i.e. large supercooling, the crystalline domains in low and high-M_w PTTT films have a coherence length of about 200 Å, while films cast at temperatures between 70 and 120 ˚C (small supercooling) show a longer coherence length of approximately 400 Å. Note that using $T_c \geq 125$ ˚C for PTTT leads to a decrease in L_c, likely due to the proximity to the melting/dissolution temperature of PTTT which is ≤ 160 ˚C (depending on the extent to which the melting point of PTTT is depressed in the presence of the solvent).[13] Indeed, the film cast at 125 ˚C was observed turn orange in color, suggesting melting/dissolution of the polymer. For P3HT, L_c continues to increase at $T_c \geq 125$ ˚C, which is expected, as the melting point of P3HT is substantially higher than that of PTTT[35].

In addition to the general trend of increasing L_c with increasing crystallization temperature, two qualitatively different effects are evident in Figure 7.1c. For P3HT there is a gradual increase in L_c as a function of increasing crystallization temperature for both molecular weights. However, at first glance, the PTTT samples appear to behave in a completely different manner: there is a sharp transition in L_c at $T_c = 65$ ˚C. However, careful examination of the data shows that PTTT also exhibits a slow increase in L_c as a function of temperature with a very similar slope to P3HT, with the additional stepwise change imposed on top of this more general trend.

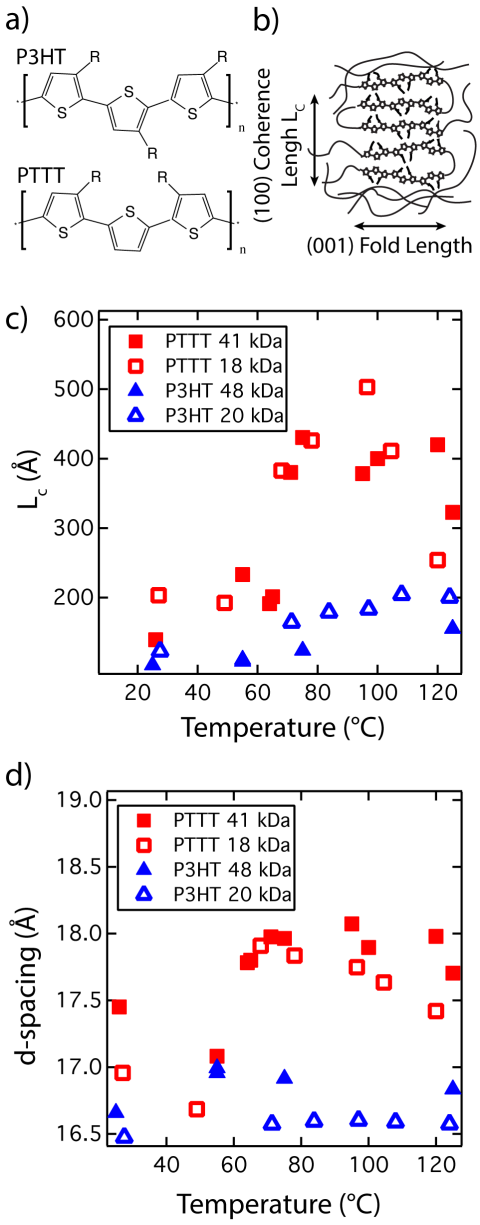

FIGURE 7.1: a) Chemical structures of poly(3-hexylthiophene) (P3HT) (top) and poly[(3,3"-didecyl[2,2':5',2"-terthiophene]-5,5"-diyl) (PTTT) (bottom). **b)** Schematic of the thin-film microstructure of the PTTT and P3HT samples showing both amorphous and crystalline regions. Coherence length, L_c, in the (100)-direction was calculated from XRD data, while with DSC we obtained information on the fold length or lamellar crystal thickness (i.e. the (001)-direction along the polymer backbone). **c)** Coherence length, L_c, along the (100)-direction and **d)** d-spacing, along the (100)-direction determined from XRD measurements plotted as a function of casting temperature for thin films of low and high-M_w PTTT and P3HT. If a PTTT film contains crystallites of both the low and high d-spacing polymorphs, coherence length and d-spacing are reported as an average for the two polymorphs, weighted by the XRD peak area for each polymorph.

We can understand the stepwise increase in L_c observed for the PTTT samples, and the lack of any similar behavior in P3HT, when the d-spacing derived from XRD peak position is examined (Figure 7.1d). A step change very similar to that for L_c occurs for the lamellar d-spacing of PTTT, suggestive of polymorphism in these samples. At low temperature, primarily a structure with a d-spacing of approximately 17 Å is formed, while at high temperatures, a higher d-spacing arrangement (18 Å) is induced. Additionally, low-M_w PTTT samples cast at 75, 85, 100, and 110 ˚C and high-M_w PTTT samples cast at 125 ˚C contain a mixture of both of these polymorphs, evident from the two distinct peaks observed in the corresponding XRD data. Coherence length and d-spacing values for samples made up of both polymorphs are reported in Figure 7.1c and d, taken as an average of the values calculated for each of the two populations weighted by the XRD peak areas (see Section 7.7.4 for details). In contrast, the P3HT samples exhibit no such obvious polymorphism, and thus provide a clearer demonstration of the gradual increase of L_c with crystallization temperature.

Although we only observe polymorphism in PTTT here, this type of behavior has previous precedent in P3HT. For example, P3HT typically forms the Form I polymorph, but P3HT oligomers can form a lower d-spacing Form II polymorph under certain processing conditions [36-38]. The d-spacing measured for our P3HT samples is consistent with the Form I polymorph: 16.7 Å[39 40 41].

We argue that the increase in crystalline domain size with increasing crystallization temperature, excluding the particulars of polymorphism, can be understood in terms of classical polymer crystallization theory as described in our introduction. Thus, a crucial control experiment is the demonstration that crystallization at elevated temperatures is not equivalent to thermally annealing samples deposited at low temperature; and, indeed, we find that thermally

annealing PTTT and P3HT samples drop cast at 26 ˚C does not have the same effect on L_c and lamellar d-spacing as does drop casting at elevated temperature. For example, annealing high-M_w PTTT and P3HT samples crystallized at 26 ˚C at 100 ˚C does not significantly increase L_c. The high-M_w PTTT sample cast at 26 ˚C has an L_c of 139 Å while a PTTT sample cast at 26 ˚C and annealed at 100 ˚C for 20 minutes has approximately the same L_c (130 Å). This coherence length of 130 Å is quite small compared to the coherence length of 400 Å found for the PTTT sample drop cast at 100 ˚C. Similarly, the P3HT sample cast at 26 ˚C and the 26 ˚C sample annealed at 100 ˚C have low coherence lengths, 109 Å and 131 Å respectively, compared with that of the P3HT sample cast at 100 ˚C (192 Å).

We predict, however, that such polymer samples that are melted and subsequently crystallize will be subject to the same rules of crystallite size control as a sample crystalized form solution. For example, when a PTTT sample cast at 26 ˚C is exposed to temperatures above its melting temperature (we selected 180 ˚C, 10 min) and subsequently allowed to crystallize at 100 ˚C, L_c is found to be 345 Å, which is similar to coherence length of 400 Å measured for the sample crystallized from solution at 100 ˚C. Thus, crystallite size control is conferred through the process of polymer crystallization; whether crystallization takes place from solution or the melt is of little importance. Plots comparing high-M_w PTTT and P3HT L_c and lamellar d-spacing values for annealed and as cast samples can be found in Section 7.7.5.

Further information on the structural changes induced by variation of T_c is obtained using DSC, which provides qualitative information on the lamellar crystal thickness, or fold length, essentially corresponding to the crystallite thickness along the polymer backbone perpendicular to the π-stacking direction and the coherence length measured by XRD (Figure 7.1c). A higher

melting temperature indicates a larger lamellar thickness.[24, 34, 42, 43] Additionally, the enthalpy of fusion can be used to compare the molecular order between systems.[34]

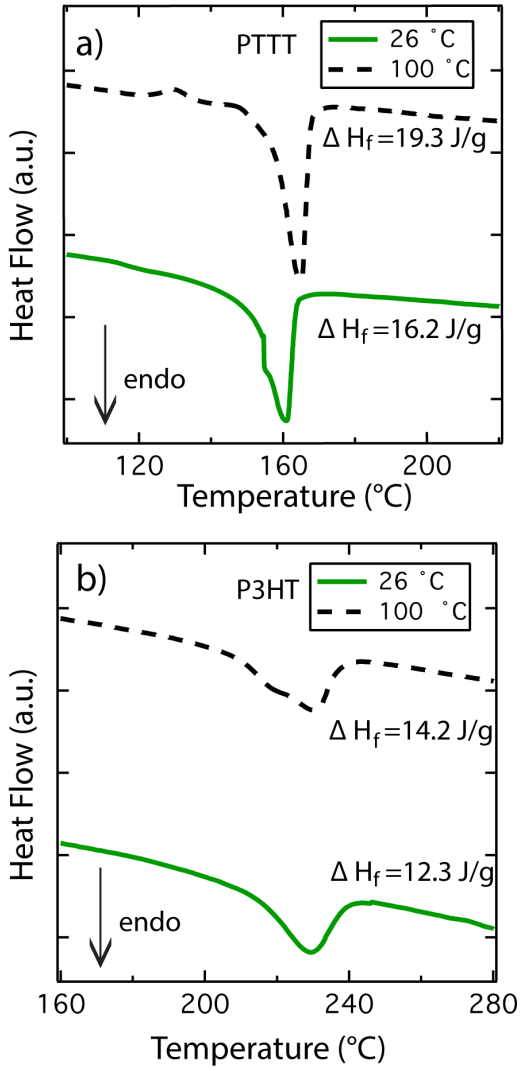

FIGURE 7.2: a) DSC thermograms shown between 100 and 220 ˚C for high-M_w PTTT samples cast at 26 ˚C and 100 ˚C. **b)** DSC thermograms shown between 160 and 280 ˚C for Rieke Metals P3HT samples cast at 26 ˚C and 100 ˚C. Full DSC thermograms for all four samples are shown in Section 7.7.6.

Figure 7.2a shows the DSC thermograms of two films prepared with high-M_w PTTT, cast at 26 °C and 100 ˚C. Full DSC thermograms taken between 25 and 225 °C for the two PTTT samples are shown in Section 7.7.6. We find that the melting point of the film cast at 100 ˚C is

approximately 3 ˚C higher than that of the film cast at 26 °C, indicating a thickening of the lamellae at higher casting temperatures. In addition, we observe an increase in the enthalpy of fusion, ΔH_f, from 16.2 J/g to 19.3 J/g for films cast at 26 ˚C and 100 ˚C, respectively. This observation suggests that the high-temperature cast PTTT films have a higher degree of crystallinity than those cast at lower temperature.

DSC thermorgrams for the Rieke Metals P3HT for samples cast at 26 °C and 100 ˚C are shown in Figure 7.2b, with full thermograms measured between 25 and 300 ˚C shown in Section 7.7.6. The melting temperatures and heats of fusion for the two samples show the same trends with casting temperature as PTTT, but the differences between the 26 °C and 100 ˚C cast P3HT samples are smaller than the differences between the 26 °C and 100 ˚C cast PTTT samples. The P3HT samples studied here exhibit only one polymorph and the increase in L_c with temperature is modest compared to PTTT, so it is expected that the DSC thermograms for the two P3HT samples are similar. Thus, L_c along the (100)-direction, the lamellar crystal thickness, and the degree of crystallinity are all tuned by T_c for both PTTT and P3HT, allowing us now to establish how these features affect the charge carrier dynamics in neat conjugated polymer films.

We find that the processing-induced microstructural changes in the polythiophene films have a strong influence on the dynamics of photogenerated charges probed using TRMC. Figure 7.3 shows typical normalized TRMC photoconductance transients at multiple light intensities (~10^{12} to 10^{14} photons/cm^2) for films of high-M_w PTTT and high-M_w P3HT, cast at 26 °C and 100 ˚C, leading to architectures of small and large crystalline domains and lamellar crystal thicknesses, respectively. The black traces in Figure 7.3 are fits to the experimental data using a sum of two exponentials (Section 7.7.3).

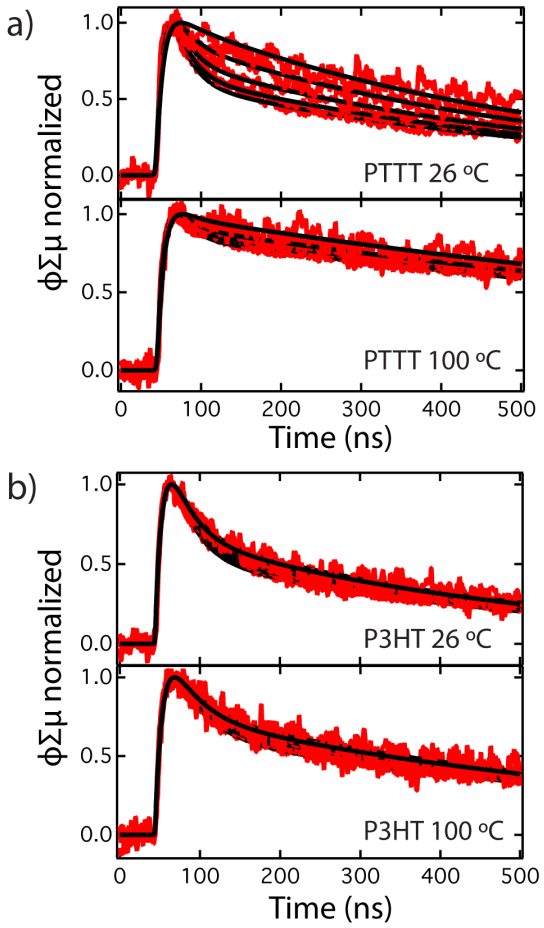

FIGURE 7.3: Photoconductance decay transients at light intensities between 10^{12} and 10^{14} photons/cm^2 for **(a)** high-M_w PTTT samples and **(b)** high-M_w P3HT samples, cast at 26 ˚C, with small crystalline domains and short photoconductance lifetimes (top), and films cast at 100 ˚C, with large crystalline domains and long photocounductance lifetimes (bottom). Black lines are fits to the experimental data using the sum of two exponential functions (Section 7.7.3).

Clear differences between the photoconductance decay transients of the two high-M_w PTTT samples are evident: the film cast at 26 °C exhibits a more rapid decay of the photoconductance signal and a greater dependence of the decay rate on light intensity relative to the film cast at 100 ˚C. Similarly, for P3HT, the 26 °C cast sample shows a more rapid decay of the photoconductance signal compared to the 100 ˚C sample, indicating that charge carriers are longer lived for both PTTT and P3HT for the cast 100 ˚C samples compared to the 26 °C cast

samples. Note that the transients for the P3HT samples cast at different temperatures do not show a discernable difference in light intensity dependence.

The differences in lifetime and intensity dependence of the photoconductance transients are related to two connected, but distinct, changes in carrier dynamics: the reestablishment of the equilibrium between trapped-mobile holes, and the recombination rate. We have previously attributed a strong dependence of the decay rate on light intensity to a low density of dark carriers (dopants) which modify effective recombination order.[44] Thus, the transition from the apparent second-order decay of the photoconductance transients for low temperature processed PTTT samples to predominantly first-order decay for the high temperature processed PTTT samples suggests an increasing dark carrier density with processing temperature. P3HT samples exhibit primarily first-order decay, suggesting a relatively high dark carrier density in these films.

We obtain values for the average photoconductance lifetime of each sample using the sum of two exponentials to fit the photoconductance transients. The weighted average of the time constants in the fit function is taken to represent the photoconductance lifetime for a particular incident light intensity. Figure 7.4a shows the average photoconductance lifetime at the lowest measured light intensity common to all samples, 1.62×10^{13} photons/cm^2, as a function of L_c for films of low and high-M_w PTTT and P3HT. For PTTT, data from samples drop cast at high temperatures ~ T $\geq$ 120 °C is not shown if there was evidence of melting. Photoconductance lifetime increases with L_c for all four polymers and the trend is unified across the samples. We hypothesize that larger crystallites have a lower surface area to volume ratio than do small crystallites, providing fewer recombination and/or trapping sites and enabling charge carriers to have longer lifetimes in films with large crystallites compared to in films with small crystallites.

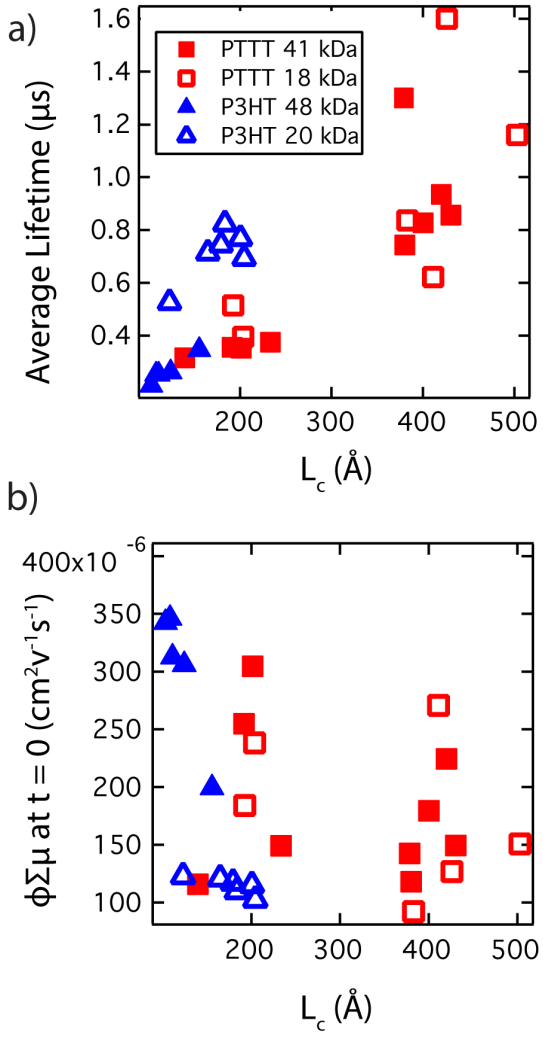

FIGURE 7.4: a) Photoconductance lifetimes for films made from low and high-M_w PTTT and P3HT, plotted as a function of (100)-coherence length, L_c. Lifetimes are calculated from double exponential fits to photoconductance data and an interpolation is performed to obtain values for the photoconductance lifetime at the lowest measured light intensity common to all samples, 1.62×10^{13} photons/cm^2. **b)** $\phi\sum\mu$ at t = 0 at 10^{12} photons/cm^2 plotted as a function of L_c for the same PTTT and P3HT samples calculated from fitting procedures shown in Section 7.7.3.

The crystalline domain size and lamellar crystal thickness also affect the yield of mobile charges in P3HT. The initial photoconductance (transient signal extrapolated to t = 0, or beginning of the laser pulse), is proportional to the yield of free charges in the film, ϕ, multiplied by the sum of the mobilities of free photoinduced charges, $\sum\mu$ (Section 7.7.3). We denote this

quantity as the yield mobility product, $\phi\sum\mu(t = 0)$, which is simply the sum of the exponential pre-factors from our double exponential fit.

The yield mobility product at low light intensity, 10^{12} photons/cm^2 (360 nJ cm^{-2}), (calculated using the fitting procedure in Section 7.7.3) is plotted as a function of L_c in Figure 7.4b. We interpret the trends observed as being due primarily to a variation in charge carrier yield, as the local GHz mobility in P3HT has been shown to be remarkably insensitive to microstructure. For example, Dicker et al. demonstrated that the local GHz mobility sum did not change between films of substantially differing regioregularity P3HT or between films made with different processing methods, despite large changes in microstructure evidenced by absorption spectra and large charges in thin-film transistor mobilities.[45] Similarly, varying the molecular weight of P3HT from 2.5-35 kg/mol was demonstrated to have minimal impact on the GHz hole mobility, despite a change in bulk (transistor) mobility of four orders of magnitude for the same samples.[46] Furthermore, recent work by some of the present authors has demonstrated that even substantially different polymer backbone structures show very similar GHz hole motilities.[47] Thus, we interpret charges in $\phi\sum\mu(t = 0)$ observed for this set of samples as being dominated by changes in charge carrier yield.

Figure 7.4b shows that charge carrier yield decreases with increasing L_c for both high and low-M_w P3HT. The dominant downward trend in yield with L_c is consistent with our previous work, which showed that solid-state processed films of larger lamellar crystallite thicknesses had lower yields of charge carriers compared to films of small lamellar crystallite thicknesses.[14] In that work, we argued that the yield of free photogenerated charge is correlated with the interfacial area between amorphous and crystalline domains of the polymer. Per unit crystallite volume, large crystalline domains have less interfacial area between crystalline and amorphous

regions than small crystalline domains do, resulting in a lower carrier yield.[14] The general decrease in yield with increasing L_c observed in this work is clearly consistent with this hypothesis. In contrast to the P3HT samples, the PTTT samples in Figure 7.4b show no clear trend in yield as a function of L_c. We think it plausible to suggest a general downward trend with increasing L_c for PTTT, but the data are too scattered for any strong interpretation. We believe that the presence of multiple polymorphs in these films complicates the yield data and obscures any trends in yield with crystallite size. Moreover, the argument that increasing crystallite size should result in lower charge carrier yield depends on the assumption that total crystallinity does not change substantially; we cannot rule out changing crystallinity as a competing factor that obscures the predicted relationship between crystallite size and carrier yield. Future work with better control of film thickness and uniformity will allow quantitative determination of total crystallinity along with crystal size.

In order to demonstrate that the above trends did not arise because of solvent properties such as evaporation rate at the casting temperatures used, samples made from solutions of high-M_w PTTT in chloroform ($T_b \approx 61$ ˚C), 1,2-dichlorobenzene ($T_b \approx 180$ ˚C) and p-xylene ($T_b \approx 138$ ˚C) were tested over a similar temperature range (see Section 7.7.2). Trends in coherence length, charge carrier lifetime and charge carrier yield were found to be independent of solvent identity and were dependent only on temperature of the sample during casting. In the present case, the fold length is independent of solvent identity because the solvent quality and, thus the degree of supercooling of the polymer, is similar for all solvent systems chosen.

7.4 CONCLUSION

We demonstrate that the classical interpretation of polymer crystallization from solution can be used to understand the mechanism of microstructure formation in polymer films such as those used in active layers of organic photovoltaic devices. Crystalline domain size and lamellar crystal thickness in neat PTTT and P3HT films can be manipulated by selection of the deposition temperature (crystallization temperature) during film preparation. Coherence length along the (100)-direction and changes in the lamellar crystal thickness modulate the yield and decay dynamics of photogenerated charge carriers. Films with larger crystallite coherence lengths, measured by XRD, and longer crystallite fold lengths, measured by DSC, have longer photoconductance lifetimes than those films with crystallites of shorter coherence and fold lengths. Charge carrier yield is correlated with the size of crystalline domains for P3HT samples. Yield decreases as crystallite coherence length and processing temperature increase for low and high-M_w P3HT, suggesting that charge carrier yield is limited by crystallite surface area to volume ratio for the samples studied. The presence of multiple polymorphs for low and high-M_w PTTT obscures trends in charge carrier yield with crystallite coherence length.

7.5 AKNOWLEDGEMENTS

The TRMC system described here was funded by the Solar Photochemistry Program, Division of Chemical Sciences, Geosciences, and Biosciences, Office of Basic Energy Sciences, U.S. Department of Energy. The experimental development for controlling polymer crystalline domain size was supported by the Laboratory Directed Research and Development (LDRD) Program at the National Renewable Energy Laboratory under task number 06RF1201. This work was supported by the U.S. Department of Energy under Contract No. DE-AC36-08-GO28308 with the National Renewable Energy Laboratory.

We also acknowledge Nikos Kopidakis from the National Renewable Energy Laboratory, Neil Treat from Imperial College, London and Alex Ayzner and Mike Toney from the Stanford Synchrotron Radiation Lightsource (SSRL) for helpful discussions. Dr. Alan Sellinger's group at Colorado School of Mines is acknowledged for the use of the TA Q Series DSC 2000 instrument.

This work was also supported by a KAUST Global Collaborative Research Academic Excellence Alliance (AEA) grant. NS is in addition supported by a European Research Council (ERC) Starting Independent Research Fellowship under the grant agreement No. 279587. We acknowledge EPRSC grant EP/G037515/1 for funding the polymer synthesis portion of this work.

7.6 REFERENCES

1. Hoppe, H.; Sariciftci, N. S. *Journal of Materials Chemistry* **2006,** 16, (1), 45-61.
2. Ruderer, M. A.; Muller-Buschbaum, P. *Soft Matter* **2011,** 7, (12), 5482-5493.
3. Deibel, C.; Dyakonov, V. *Reports on Progress in Physics* **2010,** 73, (9), 39.
4. Shaheen, S. E.; Brabec, C. J.; Sariciftci, N. S.; Padinger, F.; Fromherz, T.; Hummelen, J. C. *Applied Physics Letters* **2001,** 78, (6), 841-843.
5. Ma, W. L.; Yang, C. Y.; Gong, X.; Lee, K.; Heeger, A. J. *Advanced Functional Materials* **2005,** 15, (10), 1617-1622.
6. Campoy-Quiles, M.; Ferenczi, T.; Agostinelli, T.; Etchegoin, P. G.; Kim, Y.; Anthopoulos, T. D.; Stavrinou, P. N.; Bradley, D. D. C.; Nelson, J. *Nature Materials* **2008,** 7, (2), 158-164.
7. Groves, C.; Reid, O. G.; Ginger, D. S. *Accounts of Chemical Research* **2010,** 43, (5), 612-620.
8. Kozub, D. R.; Vakhshouri, K.; Orme, L. M.; Wang, C.; Hexemer, A.; Gomez, E. D. *Macromolecules* **2011,** 44, (14), 5722-5726.
9. Yin, W.; Dadmun, M. *Acs Nano* **2011,** 5, (6), 4756-4768.

10. Pfannmoller, M.; Flugge, H.; Benner, G.; Wacker, I.; Sommer, C.; Hanselmann, M.; Schmale, S.; Schmidt, H.; Hamprecht, F. A.; Rabe, T.; Kowalsky, W.; Schroder, R. R. *Nano Letters* **2011,** 11, (8), 3099-3107.

11. Schmidt-Hansberg, B.; Sanyal, M.; Klein, M. F. G.; Pfaff, M.; Schnabel, N.; Jaiser, S.; Vorobiev, A.; Muller, E.; Colsmann, A.; Scharfer, P.; Gerthsen, D.; Lemmer, U.; Barrena, E.; Schabel, W. *Acs Nano* **2011,** 5, (11), 8579-8590.

12. Jamieson, F. C.; Domingo, E. B.; McCarthy-Ward, T.; Heeney, M.; Stingelin, N.; Durrant, J. R. *Chemical Science* **2012,** 3, (2), 485-492.

13. Stingelin, N. *Polymer International* **2012,** 61, (6), 866-873.

14. Reid, O. G.; Malik, J. A. N.; Latini, G.; Dayal, S.; Kopidakis, N.; Silva, C.; Stingelin, N.; Rumbles, G. *Journal of Polymer Science Part B-Polymer Physics* **2012,** 50, (1), 27-37.

15. Osterloh, F. E.; Holmes, M. A.; Chang, L.; Moulé, A. J.; Zhao, J. *The Journal of Physical Chemistry C* **2013**.

16. Paquin, F.; Latini, G.; Sakowicz, M.; Karsenti, P. L.; Wang, L. J.; Beljonne, D.; Stingelin, N.; Silva, C. *Physical Review Letters* **2011,** 106, (19).

17. Koppe, M.; Scharber, M.; Brabec, C.; Duffy, W.; Heeney, M.; McCulloch, I. *Advanced Functional Materials* **2007,** 17, (8), 1371-1376.

18. Mena-Osteritz, E.; Meyer, A.; Langeveld-Voss, B. M. W.; Janssen, R. A. J.; Meijer, E. W.; Bäuerle, P. *Angewandte Chemie* **2000,** 112, (15), 2791-2796.

19. Lim, J. A.; Liu, F.; Ferdous, S.; Muthukumar, M.; Briseno, A. L. *Materials Today* **2010,** 13, (5), 14-24.

20. Liu, J. H.; Mikhaylov, I. A.; Zou, J. H.; Osaka, I.; Masunov, A. E.; McCullough, R. D.; Zhai, L. *Polymer* **2011,** 52, (10), 2302-2309.

21. Malik, S.; Nandi, A. K. *Journal of Polymer Science Part B-Polymer Physics* **2002,** 40, (18), 2073-2085.

22. Keg, P.; Lohani, A.; Fichou, D.; Lam, Y. M.; Wu, Y. L.; Ong, B. S.; Mhaisalkar, S. G. *Macromolecular Rapid Communications* **2008,** 29, (14), 1197-1202.

23. Wunderlich, B.; Kashdan, W. H. *Journal of Polymer Science* **1961,** 50, (153), 71-&.

24. Keller, A. *Rep. Prog. Phys.* **1968**, 623-704.

25. Keller, A.; Kawai, T. *Philosophical Magazine* **1965,** 11, (114), 1165-1177.

26. Liu, J. H.; Arif, M.; Zou, J. H.; Khondaker, S. I.; Zhai, L. *Macromolecules* **2009,** 42, (24), 9390-9393.

27. Tierney, S.; Heeney, M.; McCulloch, I. *Synthetic Metals* **2005,** 148, (2), 195-198.

28. Ferguson, A. J.; Kopidakis, N.; Shaheen, S. E.; Rumbles, G. *Journal of Physical Chemistry C* **2008,** 112, (26), 9865-9871.

29. Kroeze, J. E.; Savenije, T. J.; Vermeulen, M. J. W.; Warman, J. M. *Journal of Physical Chemistry B* **2003,** 107, (31), 7696-7705.

30. Dehaas, M. P.; Warman, J. M. *Chemical Physics* **1982,** 73, (1-2), 35-53.

31. Cullity, B. D.; Stock, S. R., *Elements of X-Ray Diffraction*. 3 ed.; Prentice Hall: Upper Saddle River, 2001.

32. Rivnay, J.; Noriega, R.; Kline, R. J.; Salleo, A.; Toney, M. F. *Physical Review B* **2011,** 84, (4).

33. Roehling, J. D.; Arslan, I.; Moule, A. J. *Journal of Materials Chemistry* **2012,** 22, (6), 2498-2506.

34. Wunderlich, B., *Macromolecular Physics Vol. 2: Crystal Nucleation, Growth, Annealing*. Academic Press: New York, 1976.

35. Ho, V.; Boudouris, B. W.; Segalman, R. A. *Macromolecules* **2010,** 43, (19), 7895-7899.

36. Koch, F. P. V.; Heeney, M.; Smith, P. *Journal of the American Chemical Society* **2013,** 135, (37), 13699-13709.

37. Prosa, T. J.; Winokur, M. J.; McCullough, R. D. *Macromolecules* **1996,** 29, (10), 3654-3656.

38. Brinkmann, M. *Journal of Polymer Science Part B-Polymer Physics* **2011,** 49, (17), 1218-1233.

39. Winokur, M. J.; Spiegel, D.; Kim, Y.; Hotta, S.; Heeger, A. J. *Synthetic Metals* **1989,** 28, (1-2), C419-C426.

40. Prosa, T. J.; Winokur, M. J.; Moulton, J.; Smith, P.; Heeger, A. J. *Macromolecules* **1992,** 25, (17), 4364-4372.

41. Tashiro, K.; Ono, K.; Minagawa, Y.; Kobayashi, M.; Kawai, T.; Yoshino, K. *Journal of Polymer Science Part B-Polymer Physics* **1991,** 29, (10), 1223-1233.

42. Ungar, G.; Stejny, J.; Keller, A.; Bidd, I.; Whiting, M. C. *Science* **1985,** 229, (4711), 386-389.

43. Buckley, C. P.; Kovacs, A. J. *Colloid and Polymer Science* **1976,** 254, (8), 695-715.

44. Ferguson, A. J.; Kopidakis, N.; Shaheen, S. E.; Rumbles, G. *Journal of Physical Chemistry C* **2011,** 115, (46), 23134-23148.

45. Dicker, G. Photogeneration And Dynamics Of Charge Carriers In The Conjugated Polymer Poly(3-hexylthiophene). Delt University, IOS Press, 2004.

46. Pingel, P.; Zen, A.; Abellon, R. D.; Grozema, F. C.; Siebbeles, L. D. A.; Neher, D. *Advanced Functional Materials* **2010,** 20, (14), 2286-2295.

47. Dicker, G.; de Haas, M. P.; Siebbeles, L. D. A.; Warman, J. M. *Physical Review B* **2004,** 70, (4).

48. Rivnay, J.; Mannsfeld, S. C. B.; Miller, C. E.; Salleo, A.; Toney, M. F. *Chemical Reviews* **2012,** 112, (10), 5488-5519.

7.7. SUPPORTING INFORMATION

7.7.1 Comparison of Merck P3HT and the Rieke Metals P3HT used in annealing and DSC experiments

P3HT from Rieke Metals 4002-EE listed as 50-70 kg/mol was used for the DSC and annealing experiments because our supply of the 48 kDa Merck P3HT used in the main manuscript was exhausted. Thus it is necessary to show that these two batches of polymer exhibit qualitatively identical microstructural and photophysical changes with processing conditions. Figure 7.5 shows a comparison of XRD and TRMC results for samples made with these two different batches of P3HT. Both batches of P3HT show a similar increase in L_c as processing temperature increases (Figure 7.5a) and Figure 7.5b shows that the samples have similar lamellar d-spacings, indicating that the two batches of P3HT respond similarly to processing temperature when drop cast. Photoconductance lifetime increases as L_c increases for both samples, and lifetime values are similar, indicating that the two batches of P3HT also have similar charge carrier dynamics (Figure 7.5c). Charge carrier yields, however, are different for the two batches (Figure 7.5d). The Merck P3HT samples show a significantly higher charge carrier yield than those from Rieke Metals. The origin of the decreased yield of charges in the Rieke vs. the Merck samples is not clear, but may be related to the higher polydispersity for the Rieke sample, as this is the only quantitatively known systematic difference between the two batches.

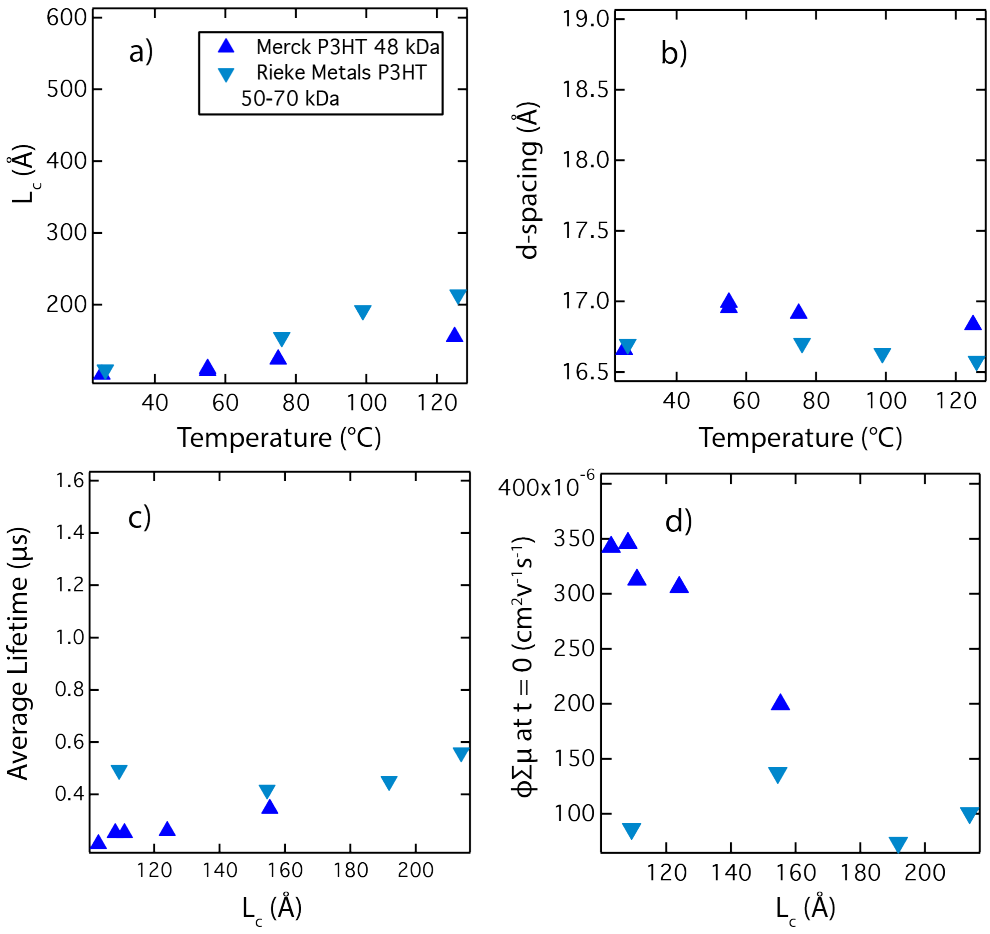

FIGURE 7.5: a) Coherence length, L_c, determined from XRD measurements plotted as a function of drop casting temperature, b) lamellar d-spacing, determined from XRD measurements plotted as a function of drop casting temperature, c) photoconductance lifetime interpolated at 1.62×10^{13} photons/cm^2 plotted as a function of L_c and d) $\phi\sum\mu$ at t = 0 extrapolated to 10^{12} photons/cm^2 plotted as a function of L_c for samples drop cast at 26 – 125 ˚C from Merck 48 kDa P3HT and Rieke Metals 50-70 kDa P3HT.

7.7.2 Dependence of Microstructure and Decay Dynamics on Solvent Properties

Figure 7.6 shows that L_c, lamellar d-spacing, charge carrier lifetime, and charge carrier yield are independent of the solution temperature prior to drop casting. Samples of high-M_w PTTT drop cast at a *substrate* temperature of 26, 75, 100, and 125 ˚C with the initial *solution* temperature at 60 ˚C (open symbols) are compared with samples cast with the solution at the

temperature of the substrate for T ≤ 100 ˚C and with the solution temperature fixed at T = 100 ˚C for samples cast with a substrate temperature T > 100 ˚C (solid symbols). In all cases, the substrate temperature determines the ultimate microstructure of the sample, and thus its photoconductance dynamics. This is to be expected, as a small drop of solution will thermally equilibrate with the substrate and heating plate rapidly.

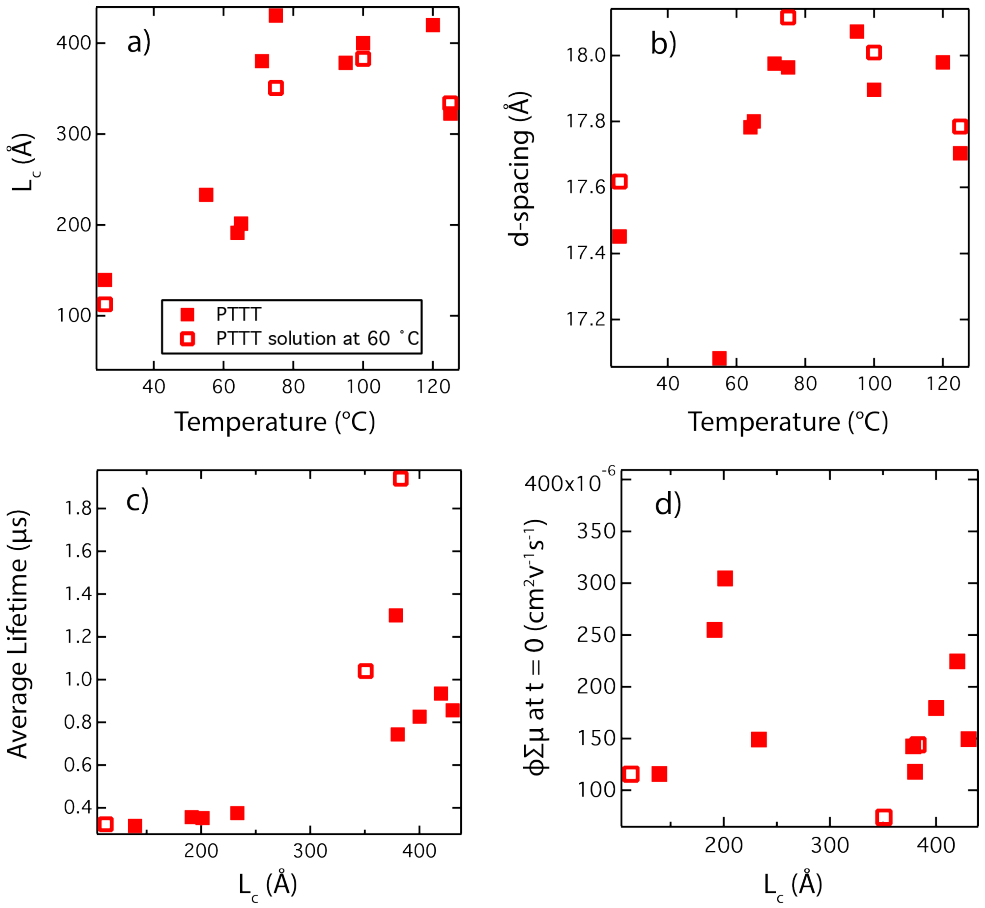

FIGURE 7.6: a) Coherence length, L_c, determined from XRD measurements, plotted as a function of drop casting temperature, b) lamellar d-spacing, determined from XRD measurements, plotted as a function of drop casting temperature, c) photoconductance lifetime at 1.62×10^{13} photons/cm^2 plotted as a function of L_c and d) $\phi\sum\mu$ at t = 0 extrapolated to 10^{12} photons/cm^2 plotted as a function of L_c for high-M_w PTTT samples drop cast with the solution at the temperature of the substrate for samples cast at T ≤ 100 ˚C and solution at T = 100 ˚C for samples cast at T > 100 ˚C (solid symbols), and high-M_w PTTT samples drop cast with solution at 60 ˚C (open symbols). Trends in coherence length, lamellar d-spacing, photoconductance lifetime and charge carrier yield do not change with solution temperature.

Samples made from solutions of high-M_w PTTT in chloroform ($T_b \approx 61$ ˚C), 1,2-dichlorobenzene ($T_b \approx 180$ ˚C) and p-xylene ($T_b \approx 138$ ˚C) were tested to ensure that differences in solvent evaporation rate did not affect crystallite coherence lengths. PTTT has a similar solubility in these solvents as it does in chlorobenzene ($T_b \approx 132$ ˚C) but the solvents have considerably different boiling points. The trends in PTTT coherence length and lamellar d-spacing as a function of crystallization temperature and trends in charge carrier yield and photoconductance lifetime as a function of coherence length were found to be independent of choice of solvent and solvent boiling point (Figure 7.7). Samples were made only at 26 °C and 55 ˚C from the chloroform solution because of the low boiling point of this solvent.

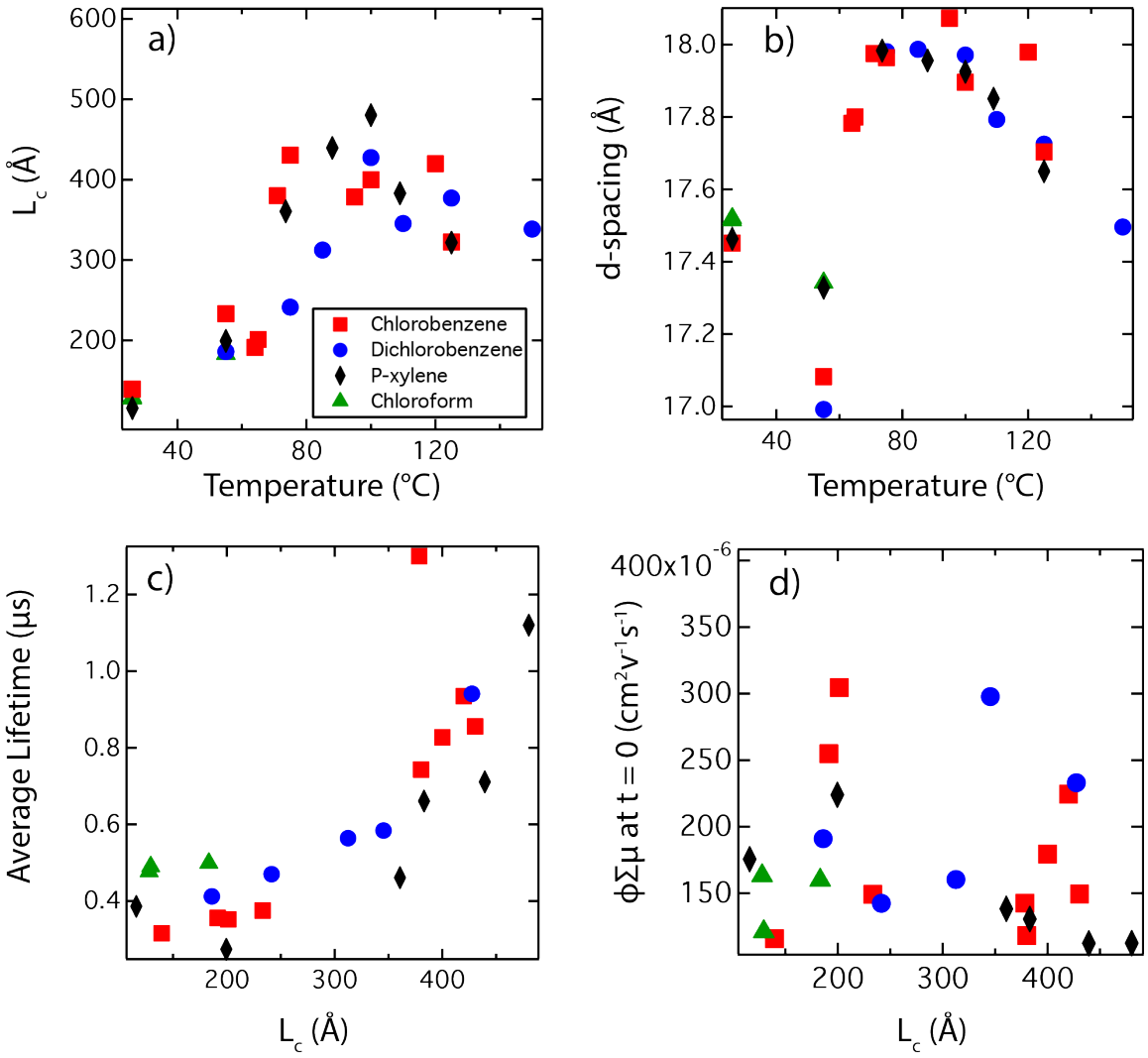

FIGURE 7.7: a) Coherence length, L_c, determined from XRD measurements plotted as a function of drop casting temperature, b) lamellar d-spacing, determined from XRD measurements plotted as a function of drop casting temperature, c) photoconductance lifetime at 1.62×10^{13} photons/cm^2 plotted as a function of L_c and d) $\phi\sum\mu$ at t = 0 extrapolated to 10^{12} photons/cm^2 plotted as a function of L_c for samples made from high-M_w PTTT in chlorobenzene (red squares), 1,2-dichlorobenzene (blue circles), p-xylene (black diamonds), and chloroform (green triangles).

7.7.3 Time-Resolved Microwave Conductivity (TRMC) Experimental Details

PTTT and P3HT samples are placed in a microwave cavity at the position of maximum electric field. Samples are then excited with a 4 ns 550 nm laser pulse, generating excitons that dissociate into free charge carriers, which absorb microwave energy. The change in microwave

power reflected form the cavity after excitation as a function of time, ΔP(t), is proportional the photoconductance of the sample, ΔG(t). ΔP(t) and ΔG(t) are related by the following equation where K is a sensitivity factor associated with the known properties and dimensions of the microwave cavity and sample.

$$\frac{\Delta P}{P_0} = -K \cdot \Delta G(t) \tag{S1}$$

The experimental photoconductance data, $\Delta G_{exp}(t)$, is the convolution of the instrument response function (IRF), representative of the cavity response time and laser pulse width, F(t), and the photoconductance of the sample, ΔG(t). The IRF function is itself formed by a convolution of the Gaussian laser pulse with the known single-exponential response time of the cavity.

$$\Delta G_{\text{exp}}(t) = F(t) \otimes G(t) \tag{S2}$$

The K factor and cavity time constant, τ, were calculated for 12 samples drop cast at various temperatures. The set of samples tested included at least two samples from each batch of polymer used in this work. The average K factor was found to be 54,900 with a standard deviation of 5% and the average cavity time constant, τ, was found to be 9.03×10^{-9} s with a standard deviation of 5%. Thus, the K factor and cavity time constants did not change significantly between samples and K was set to 55,000 and the cavity time constant were set to $9 * 10^{-9}$ s for all samples. Furthermore, we have measured the K factor and cavity time constant for other conjugated polymer samples and have found that the values are independent of sample properties, such as thickness or polymer chemistry, for these relatively thin, weakly conducting samples.

To calculate the K factor and time constant of the cavity, we rely on the fact that the cavity can be modeled as a damp-driven harmonic oscillator following a previously reported

method[30, 45]. We measure the microwave power reflection coefficient, R, as a function of frequency: the ratio of the power reflected by the cavity to that reflected by a shorting plate. Figure 7.8 shows a representative plot of *R* as a function of microwave frequency, *f*, where black circles are collected data points and the red line is a Lorentzian fit to the curve. The Lorentzian fit is used to determine the full width half maximum (FWHM), depth (R_o), and frequency (f_o) of the resonance. Using these experimentally determined values, the following formulas are used to calculate the cavity time constant, τ, and the sensitivity (K) factor[45].

The quality factor of this cavity is given with the following formula:

$$Q = \frac{f_o}{FWHM} \qquad \text{S3}$$

The response time of the cavity, τ, is:

$$\tau = \frac{Q}{\pi \cdot f_o} \qquad \text{S4}$$

Equation S5 relates the cavity K factor to Q, where ε_r is the dielectric constant of the sample, *a* and *b* are dimensions of the waveguide, and *d* is the thickness of the sample at which 90% of incident light as been absorbed. The value of *d* is ~100 nm for P3HT at 2.38 eV excitation, corresponding to a characteristic absorption coefficient of 0.01 nm^{-1}. The drop cast films are all optically thick, absorbing > 99% of incident light at our excitation wavelength of 550 nm. Total film thickness is estimated to be several microns. However, since the microwave experiment only probes photoexcited portion of the film, we assume an effective sample thickness, *d*, of 100 nm that is constant for all films.

$$\frac{2Q\left(1 \pm \frac{1}{\sqrt{R_o}}\right)}{f_o \varepsilon_r \varepsilon_o d \frac{a}{b} \pi} = -K \qquad \text{S5}$$

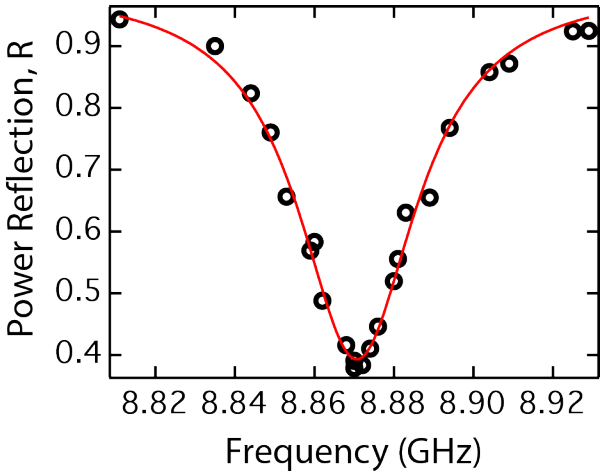

FIGURE 7.8: Representative plot of power reflection coefficient, *R*, plotted as a function of microwave frequency. The red curve is a Lorentzian fit to the values of power reflection coefficient (black circles) as a function of frequency.

We fit ΔG(t) as a double exponential decay in order to approximately account for carriers that are trapped or recombine within the response time of the system and to quantify the average rate of photoconductance decay. The function has no physical significance, and was chosen because it provides adequate fits to the experimental data with a minimum number of variable parameters. The function is:

$$\Delta G(t) = A_1 \exp\left(\frac{-t}{\tau_1}\right) + A_2 \exp\left(\frac{-t}{\tau_2}\right) \tag{S6}$$

where $A_{1,2}$, are pre-exponential factors and $t_{1,2}$ are time constants that are allowed to vary during the fitting procedure. A data set is made up of the photoconductance transients collected at multiple light intensities between approximately 10^{12} and 10^{14} photons/cm^2 for a given sample. The incident light intensity is controlled using neutral density filters. All of the transients in a data set are fit simultaneously using scripted procedures in IGOR pro. The values of $A_{1,2}$ are allowed to vary between transients in a data set but t_1 and t_2 are linked between transients in a data set. Other parameters in the fit, including the laser pulse width and cavity response time, are

fixed at their experimentally measured values (4 ns, and 9 ns, respectively). The lifetime of the photconductance at a given light intensity is represented by the average of the time constants, $t_{1,2,}$ weighted by the pre-exponential factors, $A_{1,2,}$ in Equation S6. Figure 7.9 shows average photoconductance lifetime plotted as a function of light intensity for high-M_w PTTT samples drop cast at temperatures between 26 and 120 ˚C. The lifetimes plotted in the main manuscript are the interpolated values of the lifetime for each sample at a light intensity of 1.62×10^{13} photons/cm^2, the lowest light intensity common to all data sets.

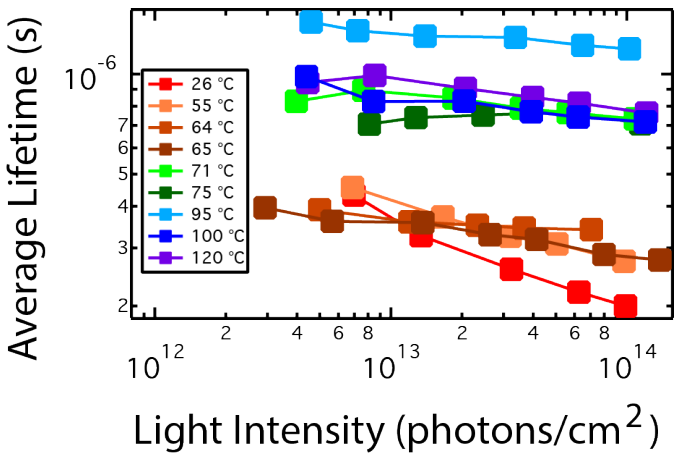

FIGURE 7.9: a) Photoconductance lifetime in seconds plotted as a function of light intensity for high-M_w PTTT samples drop cast at temperatures 26 to 120 ˚C.

The photoconductance, ΔG, is related to the yield mobility product, $\phi\sum\mu$, by the following equation:

$$\phi\Sigma\mu = \frac{\Delta G}{\beta q_e I_o F_A} \tag{S7}$$

Here, β is equal to 2.2 which is the ratio of the short to long dimensions of the waveguide cavity cross-section, q_e, is the charge of an electron, I_o is the incident photon flux and F_A is the fraction of light absorbed by the film. F_A is assumed to be 1 for all samples because the drop cast P3HT

and PTTT films are thick and opaque. We calculate $\phi\sum\mu$ at time = 0, or the beginning of the laser pulse, from the double exponential fits to the photoconductance data (Equation S6) at each light intensity where data was collected. The value of ΔG at t = 0 (which is related to $\phi\sum\mu(t = 0)$, the yield mobility product, by Equation S7, is the sum of the pre-exponential factors in Equation S6. Figure 7.10a shows $\phi\sum\mu(t = 0)$ plotted as a function of light intensity for high-M_w PTTT samples drop cast at temperatures between 26 and 120 ˚C.

The values of $\phi\sum\mu(t = 0)$ at each light intensity are then fit using a procedure developed originally by Dicker et al.[47] which allows us to extrapolate the data to low light intensities that we cannot probe experimentally. This equation models the fact that at low light intensities, $\phi\sum\mu(t = 0)$ does not depend on light intensity, while at higher light intensities processes such as the annihilation of excitons by holes causes $\phi\sum\mu(t = 0)$ to be related to intensity sub-linearly. The fit equation we use is shown below:

$$\phi\Sigma\mu = \frac{A}{1 + \sqrt{B \cdot \frac{I_o F_A}{d}}} \tag{S8}$$

where *d* is the length of the sample where light is absorbed and A and B are fitting coefficients. *d* is the depth at which 90% of incident light as been absorbed, which is ~100 nm for P3HT at 2.38 eV excitation. The drop cast films are optically thick so *d* is assumed to be the same for all films. Using the fit function in Eq. S8, we extrapolate to a low light intensity of 10^{12} photons/cm^2. Figure 7.10b shows fits to the $\phi\sum\mu(t = 0)$ data for high-M_W PTTT samples calculated from Eq. S8 with the fits shown as black lines.

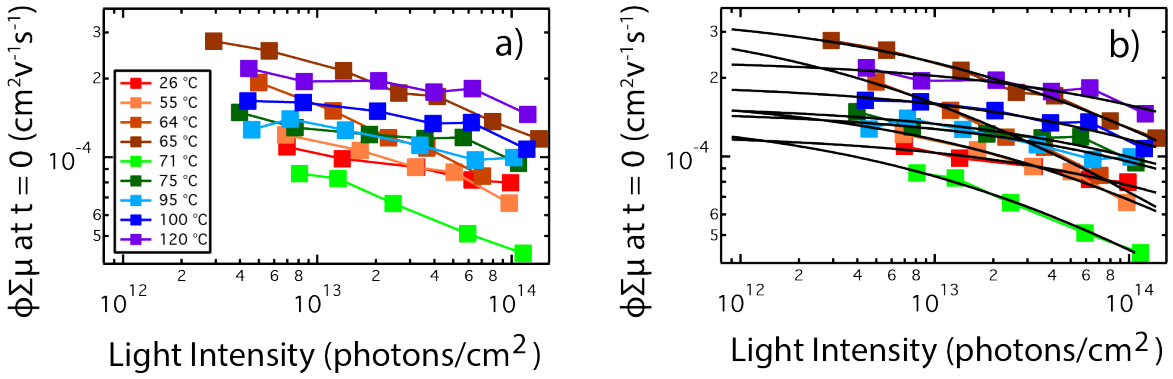

FIGURE 7.10: a) $\phi\sum\mu(t = 0)$ plotted as a function of light intensity for high-M_w PTTT samples drop cast at temperatures 26 to 120 ˚C. b) $\phi\sum\mu(t = 0)$ plotted as a function of light intensity for high-M_w PTTT with the fits given by Eq. S8 shown as black lines.

Figure 7.11 shows a comparison of $\phi\sum\mu(t = 0)$ for high-M_w PTTT samples drop cast at temperatures 26 - 120 ˚C extrapolated to 10^{12} photons/cm^2 using Eq. S8 and $\phi\sum\mu$ at t = 0 interpolating to $1.62\text{x}10^{13}$ photons/cm^2 (the light intensity used for lifetime values) plotted as a function of coherence length. Trends in the data are the same for both methods, but values of $\phi\sum\mu$ at t = 0 are slightly lower when the interpolation method is used because the light intensity is higher and more excitons are annihilated by holes.

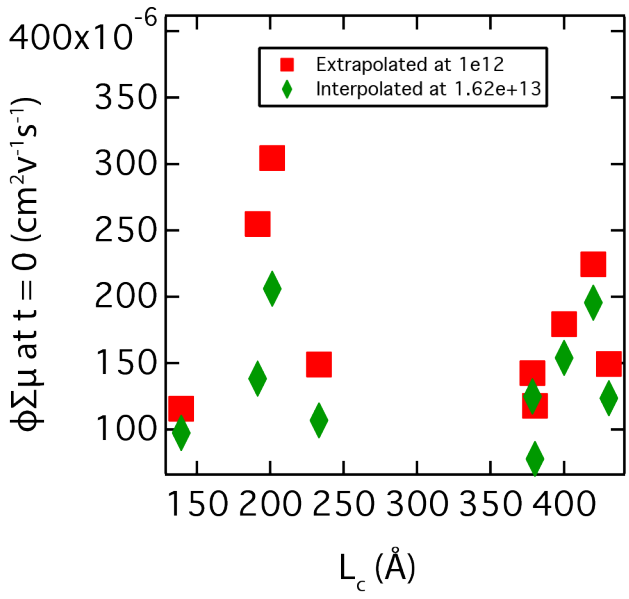

FIGURE 7.11: $\phi\sum\mu$ at t = 0 extrapolated to 10^{12} photons/cm^2 calculated using Eq. S8 and $\phi\sum\mu$ at t = 0 interpolated to $1.62\text{x}10^{13}$ photons/cm^2 plotted as a function of coherence length for high-M_w PTTT samples drop cast at temperatures 26 - 120 ˚C. Trends in $\phi\sum\mu$ at t = 0 are the same for both methods.

7.7.4 X-Ray Diffraction

Data Analysis Procedure

For all samples, the first-order diffraction peak at approximately 5˚ in the x-ray diffraction data is fit using a double peak Lorentzian function corresponding to the $K_{\alpha 1}$ and $K_{\alpha 2}$ x-ray wavelengths emitted by the rotating Cu K alpha anode source in the Rigaku DMAX X-Ray Diffractometer. The Lorentzian function is used to obtain the full width half maximum (FWHM) of the peak. We use a background function of the form:

$$y = A + B\left(\frac{1}{\frac{1}{x}-\frac{1}{D}}\right) + C\left(\frac{1}{\frac{1}{x}-\frac{1}{D}}\right)^2 \qquad \text{S9}$$

Data from several PTTT samples show two distinct diffraction peaks, indicating the presence of two polymorphs with slightly different d-spacing. The two peaks are fully resolved in the second order diffraction line, but overlap in the first-order line (because the difference

between the peak 2θ values is halved). Where two diffraction peaks are present, two Lorentzian functions are used to fit the first order diffraction line and extract the FWHM of each component for use in the Scherrer analysis. For samples with both polymorphs, the coherence length and d-spacing for each sample are reported as averages weighted by the peak areas found from the Lorentzian fits of the two diffraction peaks near 5˚.

The coherence length, L_c , (Figure 7.1c) along the lamellar stacking direction (the 100-direction) was calculated from Scherrer's formula[31] using the FWHM calculated from the Lorentzian fits:

$$L_c = \frac{0.9\lambda}{B\cos(\theta_B)} \qquad \text{S10}$$

where B is the FWHM of the Lorentzian curve fit to the diffraction data. θ_B is the value of theta at the maximum of the Lorentzian curve and λ is the wavelength of the x-rays, here 1.54 Å. Determination of crystallite size for polymer samples is difficult due to disorder in the polymer crystallites[48]. Thus, L_c values presented here are reported to compare crystallite sizes between samples, not to report the precise size of the polymer crystallites.

The d-spacing of the polymer lamellae is calculated with the following formula:

$$d = \frac{\lambda}{2\sin(\theta_B)} \qquad \text{S11}$$

Alignment tests were performed to ensure that the background signal at low 2θ did not interfere with determination of the peak width and position. Figure 7.12 shows XRD data from the high-M_w PTTT cast at 55 ˚C measured between 3 and 7˚. Tilting the sample along the θ axis by 0.1 or 0.2˚ reduced the background signal but did not change the peak shape, calculated L_c or calculated d-spacing significantly (Table 7.1). Thus, the background signal at low 2θ does not affect the calculated d-spacings or L_c values.

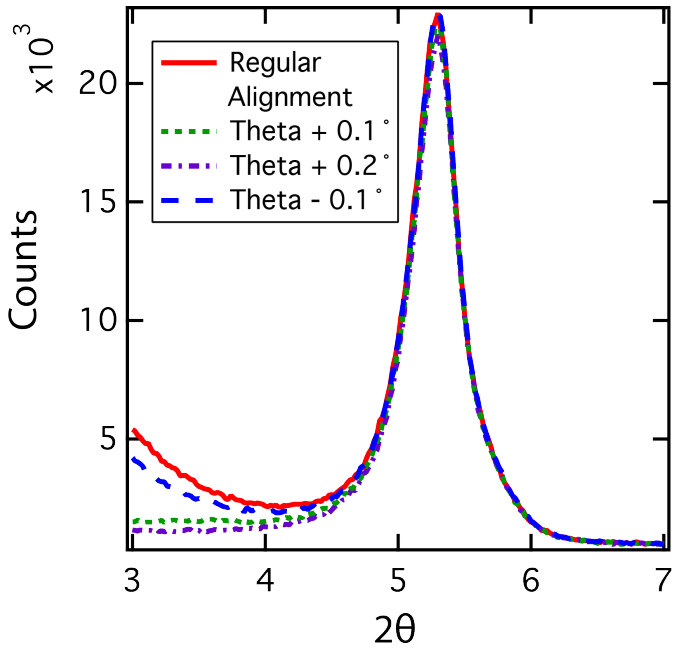

FIGURE 7.12: XRD data from the high-M_w PTTT sample cast at 55 ˚C measured from 3 to 7˚. The sample was tilted along the θ-axis by 0.1 or 0.2˚.

TABLE 7.1: L_c and lamellar d-spacing calculated for the high-M_w PTTT sample cast at 55 ˚C for automatic alignment and when the sample was tilted the θ-axis by 0.1 or 0.2˚.

	Automatic	**Theta + 0.1˚**	**Theta + 0.2˚**	**Theta - 0.1˚**
L_c [Å]	187.8	191.8	189.3	188.8
d-spacing [Å]	16.7	16.7	16.7	16.7

An approximation for instrument broadening and the lower limit of FWHM detectable by the Rigaku DMAX X-Ray Diffractometer was determined by measuring a lanthanum hexaboride standard, number 660, obtained from NIST using the same experimental conditions used for the polymer samples. The FWHM of the thirteen lanthanum hexaboride peaks are obtained from curve fits using the Lorentzian function described above. The average of the FWHM for these peaks is used as the approximate instrument broadening and as the lower limit of the FWHM detectable by the Rigaku DMAX X-Ray Diffractometer. Lanthanum hexaboride has does not

have diffraction peaks below 20˚, which precludes the use of this number as an accurate value for instrument broadening at 5˚. An accepted standard for low values of 2θ was not available. However, as we are primarily interested in trends in coherence length rather than absolute values, we do not correct the data in the manuscript for instrument broadening. If we do correct using the instrument broadening determined from the lanthanum hexaboride standard (Figure 7.13), trends in coherence length as a function of temperature and trends in photoconductance lifetime and charge carrier yield do not change compared to what is reported in the main manuscript. Figure 7.14 shows that the FWHM for the polymer samples fall well above the instrument broadening determined from the lanthanum hexaboride standard.

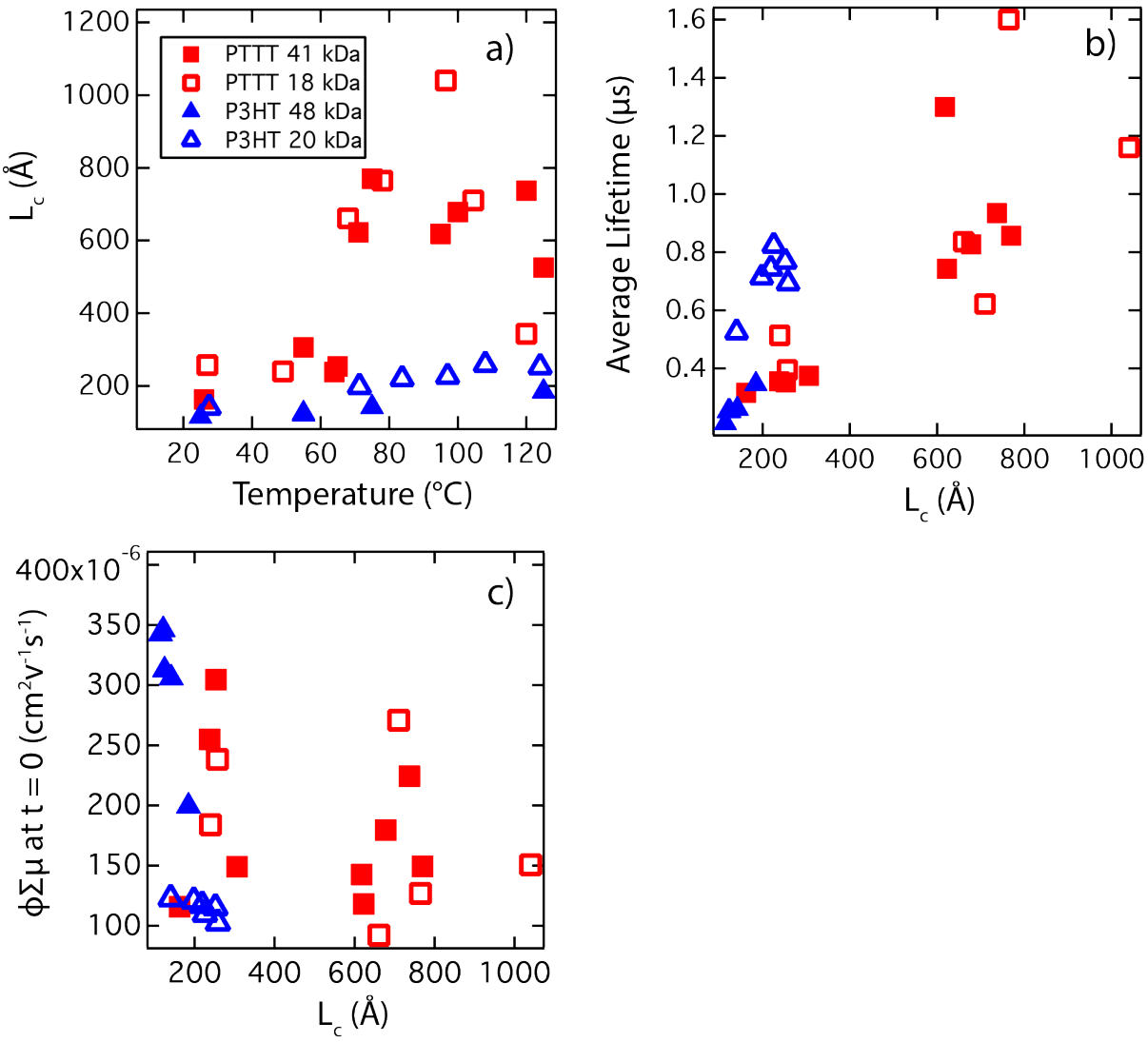

FIGURE 7.13: a) Coherence length, L_c, along the (100)-direction determined from XRD measurements plotted as a function of casting temperature for thin films of low and high-M_w PTTT and P3HT corrected with a constant instrument broadening determined by measuring lanthanum hexaboride, standard number 660, obtained from NIST. b) Photoconductance lifetime at 1.62×10^{13} photons/cm^2 plotted as a function of corrected coherence length, L_c, and c) $\phi\sum\mu$ at t = 0 extrapolated to 10^{12} photons/cm^2 plotted as a function of corrected coherence length for low and high-M_w PTTT and P3HT samples.

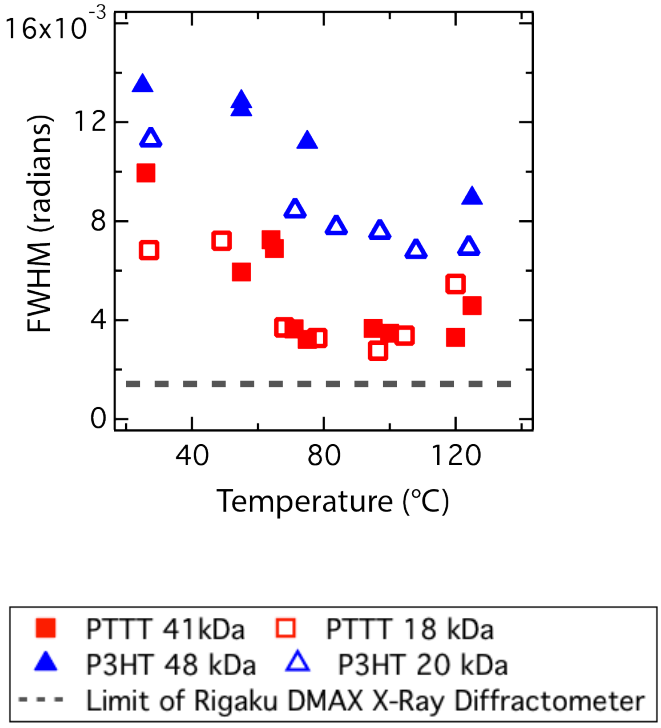

FIGURE 7.14: FWHM of XRD data in radians plotted as a function of drop casting temperature. The dashed gray line indicates approximate instrument broadening or the lower limit of the FWHM detectable by the Rigaku DMAX X-Ray Diffractometer determined by measuring lanthanum hexaboride standard, number 660 obtained from NIST.

Representative XRD Data

XRD data for high-M_w PTTT samples cast at 26 ˚C and 100 ˚C is shown in Figure 7.15. The XRD peak for the 100 °C cast sample is narrower than that of the 26 °C cast sample indicating a higher coherence length for the sample cast at a higher temperature. The peak also shifts to lower 2θ for the 100 °C sample compared to the 26 °C sample which means that the d-spacing for the sample cast at 100 °C is slightly larger than that of the sample cast at 26 °C. These two samples are representative of the two different polymorphs found for PTTT samples, one with low d-spacing (~17 Å), termed "low-d polymorph", formed at low casting temperature and the other with high d-spacing (~18 Å), termed "high-d polymorph", formed at high casting temperature.

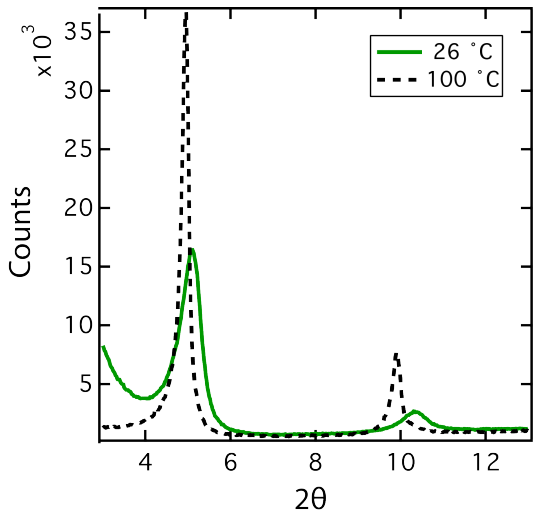

FIGURE 7.15: XRD data for high-M_w PTTT samples cast at 26 ˚C and 100 ˚C (black dashed and green solid lines, respectively).

Figure 7.16a shows XRD data for high-M_w PTTT samples cast at 26, 55, 65, 75, and 95 ˚C, each having only one peak. Samples cast at 26 and 55 ˚C form the low-d polymorph, while the samples cast at 65, 75, and 95 ˚C form the high-d polymorph. XRD data for several PTTT samples show two XRD peaks, one for the low-d polymorph and one for the high-d polymorph, indicating the presence of two populations of crystallites in these films. Figure 7.16b shows the XRD data for the high-M_w PTTT sample cast at 125 ˚C which has two distinct peaks. The following samples exhibited two diffraction peaks indicating the presence of both polymorphs: high-M_w PTTT in cholorobenzene cast at 125 ˚C, high-M_w PTTT in p-xylene cast at 125 ˚C, high-M_w PTTT in dicholorobenzene cast at 110, 125, and 150 ˚C, and low-M_w PTTT in cholorobenzene cast at 75, 85, 100, and 110 ˚C.

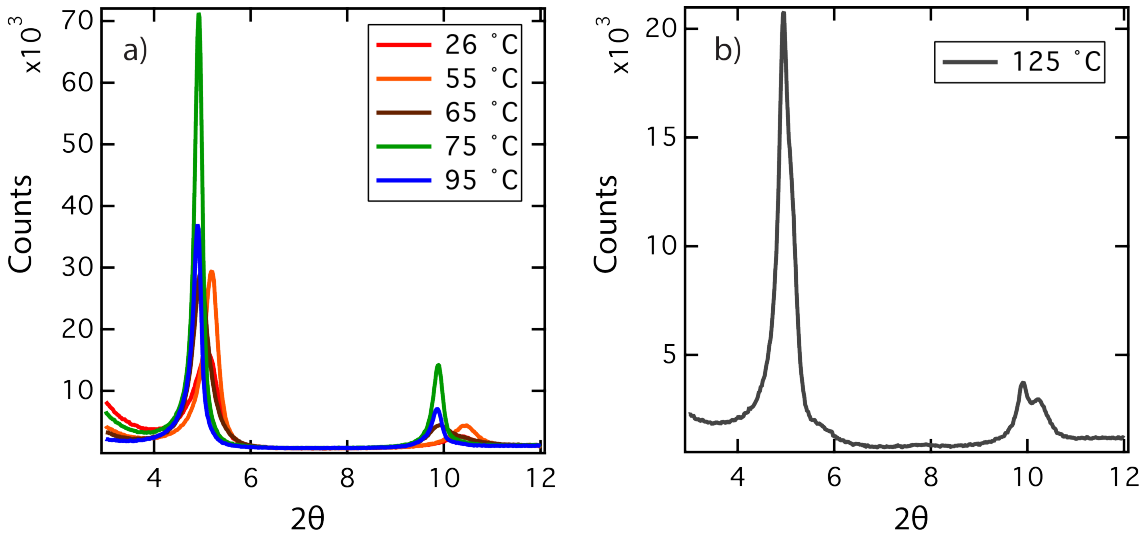

FIGURE 7.16: XRD data for a) high-M_w PTTT samples cast at 26 ˚C - 95 ˚C which form only one polymorph and b) high-M_w PTTT sample cast at 125 ˚C which has two XRD peaks, indicating the presence of both the low and high-d polymorphs in the sample.

P3HT samples exhibit only one polymorph as shown by the XRD data for high-M_w P3HT cast at 26 ˚C, 55 ˚C, 75 ˚C, and 125 ˚C (Figure 7.17). P3HT peaks are broader than those for PTTT, indicating that P3HT crystallites have smaller coherence lengths than do PTTT crystallites. P3HT peaks are shifted to slightly higher 2θ compared to PTTT peaks indicating that P3HT crystallites have a smaller d-spacing. One reason for the smaller d-spacing of P3HT crystallites compared to PTTT crystallites is that P3HT has six alkyl groups in the side chain compared to 10 alkyl groups in the side chain for the PTTT used in this work.

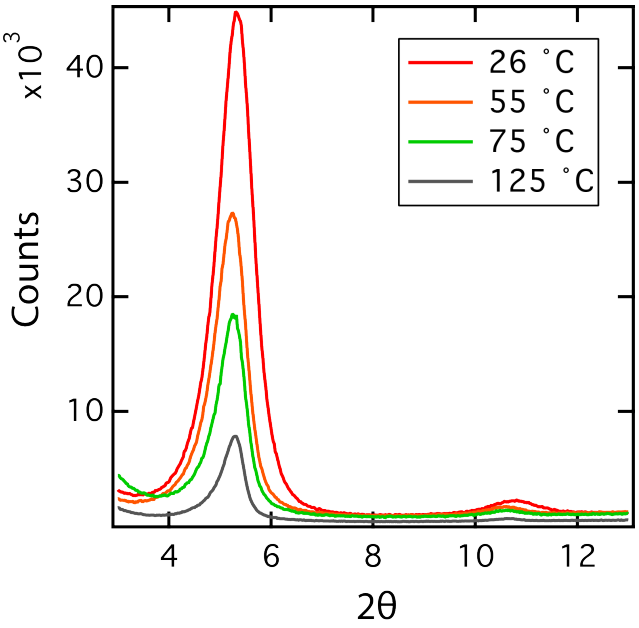

FIGURE 7.17: XRD data for high-M_w P3HT samples cast at 26 ˚C - 125 ˚C.

7.7.5 Annealing Experiments

Films of high-M_w PTTT and Rieke Metals P3HT cast at 26 ˚C were thermally annealed under various conditions to determine the effect of annealing on crystallite size and on charge carrier dynamics. Figure 7.18 shows L_c, lamellar d-spacing, average lifetime, and charge carrier yield for the annealed samples in comparison with the data for samples drop cast at various temperatures.

We find that thermal annealing at 100 ˚C, below the melting point of the polymer, for 20 minutes does not significantly change L_c or lamellar d-spacing from that of the 26 ˚C cast samples. Annealing PTTT at 180 ˚C (above the melting point of the polymer) for 10 minutes and then cooling to 26 ˚C increases L_c but not to the extent of the 100 ˚C drop cast sample. When the PTTT 26 ˚C sample is annealed at 180 ˚C for 10 minutes and cooled to 100 ˚C, the crystallite size is similar to that of the sample drop cast at 100 ˚C. Thus, annealing below the melting temperature of the polymer does not allow sufficient mobility for the polymer chains to form

larger crystallites at higher temperatures, while when crystallization takes place from solution or from the melt and proceeds at higher temperatures, larger crystallites are formed. Annealing is shown to have a varying affect on photoconductance lifetime and yield.

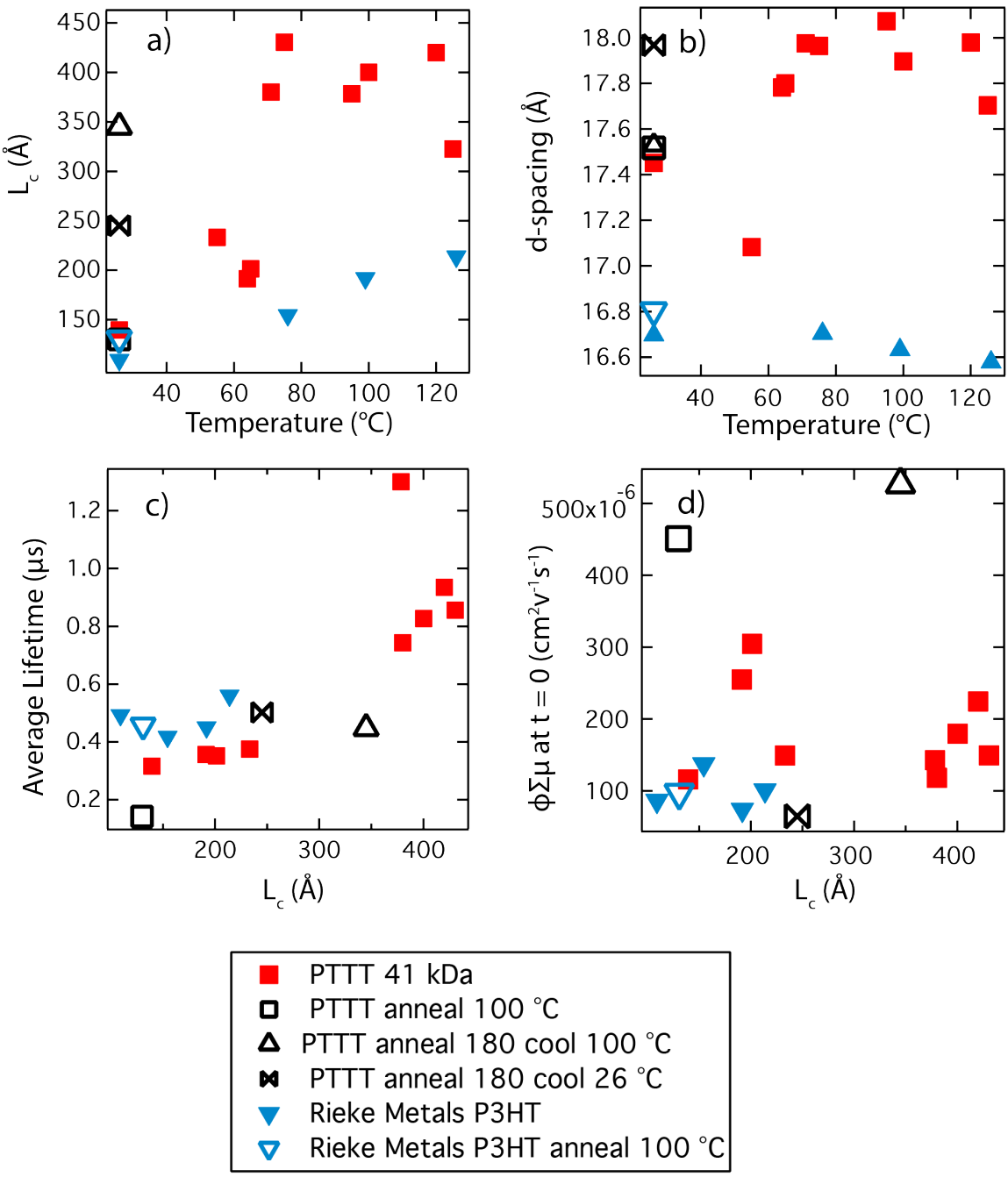

FIGURE 7.18: a) Coherence length as a function of drop casting temperature, b) lamellar d-spacing as a function of drop casting temperature, c) photoconductance lifetime at 1.62×10^{13} photons/cm^2 for plotted as a function of coherence length, L_c, and d) $\phi\sum\mu$ at t = 0 extrapolated to 10^{12} photons/cm^2 plotted as a function of coherence length for samples drop cast from 26 – 125 ˚C from high-M_w PTTT and Rieke Metals P3HT (solid symbols) and samples drop cast at 26 ˚C and annealed at various conditions (open black symbols).

3) Differential Scanning Calorimetry (DSC)

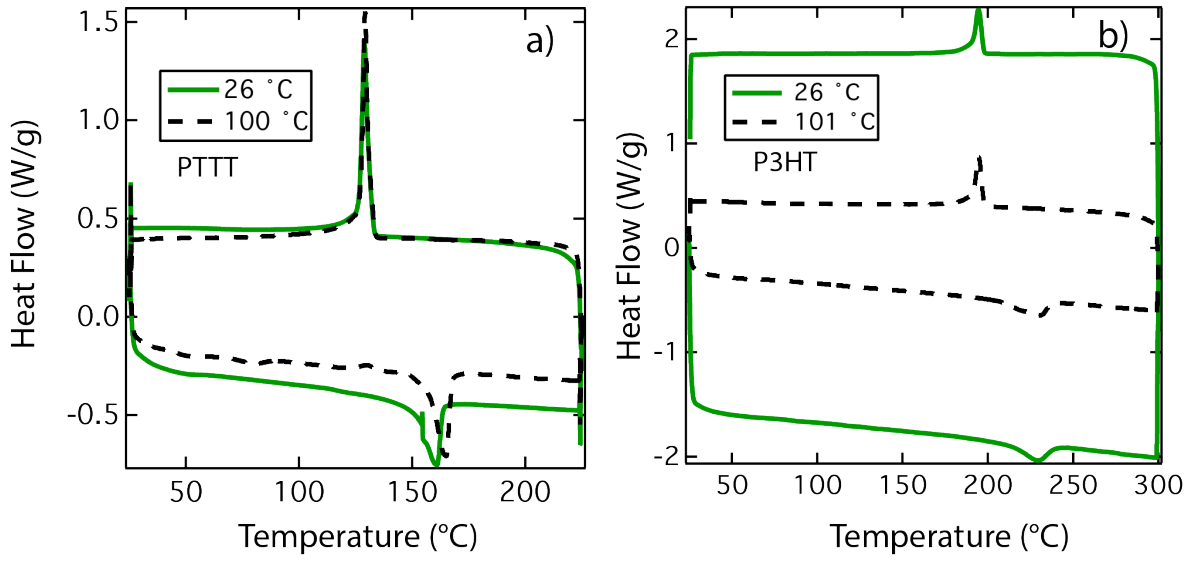

FIGURE 7.19: a) Full DSC thermograms for high-M_w PTTT samples cast at 26 ˚C and 100 ˚C. b) Full DSC thermograms for high-M_w P3HT samples cast at 26 ˚C and 100 ˚C (black dashed and green solid lines).

Chapter 8

Probing Polythiophene Film Microstructure and Charge Carrier Dynamics with Phthalocyanine Dye Molecules

8.1 INTRODUCTION

Polythiophenes such as poly(3-hexylthiophene) (P3HT), poly(2,5-bis(3-alkylthiophen-2-yl)thieno[3,2-b]thiophene) (PBTTT), and poly(2,2′:5′,2″-3,3″-dihexyl-terthiophene) (PTTT) are used in organic photovoltaics, light emitting diodes and field effect transistors to generate and transport charge carriers[1-6]. The morphology of the polythiophene significantly influences both the generation of charge carriers from excitons and the transport of charges in films[6-9]. Thus, an understanding of the complexities of polythiophene morphology is important for improving device efficiency and performance.

Polythiophenes are conjugated polymers which form amorphous and crystalline domains in films[7]. We showed previously that polythiophene crystalline domain size is controlled with processing temperature as in classical polymer physics studies of flexible polymers such as polyethylene: films cast at high temperatures have larger crystallites than films cast at lower temperatures[10]. Crystalline domain size is important because it modulates the amount of amorphous-crystalline interface where free charge carrier generation and recombination are thought to occur in neat polymer films[11, 12]. Excitons dissociate at this interface in low yield because there is a small difference in energy between the amorphous and crystalline regions[11, 13, 14]. We expect holes to go to lower energy crystalline regions while electrons remain trapped at the amorphous-crystalline interface[14]. Our previous results using Time Resolved Microwave Conductivity (TRMC) showed that photoinduced holes had longer lifetimes in neat

polythiophene films with large crystallites than in films with small crystallites. The holes mobile in a large crystallite have longer lifetimes because they have a higher crystallite volume to surface area ratio and thus have a lower probability of recombination with an electron at the amorphous-crystalline interface compared to a hole in a smaller crystallite[10]. In this previous study, charge carriers were generated in the neat polymer, but the question remains whether crystallite size would affect charge carrier dynamics in more device-relevant contexts, when charge carriers are generated at the interface between a polythiophene donor and an electron acceptor molecule and when more charge carriers are present in the film.

We answer this question by incorporating probe molecules into polythiophene films. Probe molecules report information about the surrounding microenvironment and are present at low concentration so as not to disrupt the local morphology. We add electron accepting phthalocyanine (PC) dye molecules ("Molecule 2" synthesized by Bergkamp et al. in ref [15]) in low concentration to P3HT films (Figure 8.1) to determine whether the lifetime of holes generated from excitons on probe molecules depends on polythiophene crystalline domain size in the same way as holes generated in neat polymer. The PC molecule is an electron acceptor relative to P3HT because it has a larger electron affinity[15]. The PC dye molecule was chosen because it can be selectively excited at 760 nm, a wavelength where polythiophenes do not significantly absorb. In addition, PCs are of interest as a minority component in organic photovoltaic active layers, specifically, in ternary blends with polythiophenes and fullerene derivative acceptor molecules[16-18]. In ternary blends, the PC extends the portion of the visible spectrum absorbed by the film. It is hypothesized that PCs facilitate electron transfer from P3HT to PCBM if the PC energy levels are between those of the donor and acceptor molecules but this mechanism is not agreed upon[16, 18].

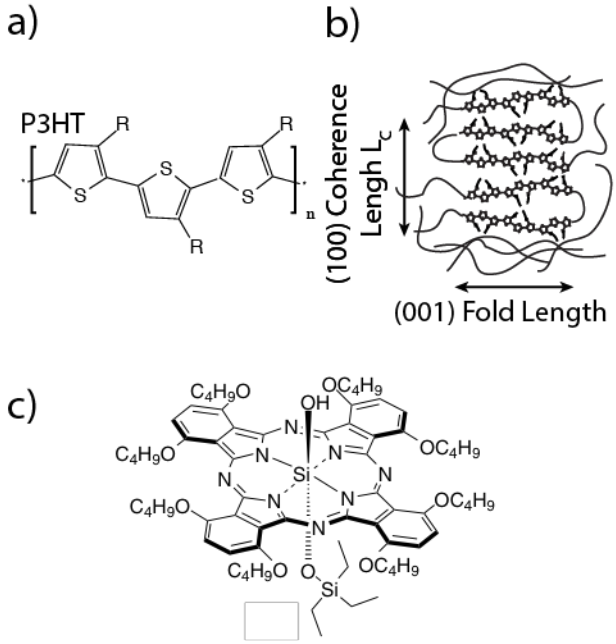

FIGURE 8.1: a) Chemical structure of poly(3-hexylthiophene) (P3HT). b) Schematic showing a polythiophene crystalline domain in amorphous polymer from ref [10]. c) Phthalocyanine dye used as a probe molecule in P3HT films from ref [15].

Preliminary results in this work show that PC molecules can be used to probe the crystallite size in polythiophene films. Holes generated from selective excitation of the probe molecules have longer lifetimes in films with large crystallites than in films with small crystallites as in the case of polymer excitation in neat films. Additionally, PC excitation generates a higher yield of charge carriers than is generated in neat films, demonstrating that the lifetime of holes in polymer crystallites depends on crystallite size with charge carrier densities approaching those in organic photovoltaic devices.

8.2 EXPERIMENTAL

8.2.1 Thin Film Fabrication

Poly(3-hexylthiophene) (P3HT) from Rieke Metals 4002-EE of 50-70 kg/mol and 91-94% regioregularity was used for the films in this work. PC molecules are “Molecule 2” from ref

[15] and were prepared as described therein. Films of neat P3HT or of P3HT with PC probe molecules are drop cast onto quartz substrates in a glove box under nitrogen atmosphere using 100 μL of a 7.5 mg/mL polythiophene solution in chlorobenzene. Solutions containing PC probe molecules have a molar ratio of 0.001 moles PC to 1 mole polythiophene monomer (0.1 mol% PC). Deposition occurs at room temperature, ~26 °C, to produce films with smaller crystalline polymer domains, and at ~100 °C (97-99 °C) to produce films with larger crystalline domains. Temperatures are measured independently of the hotplate setting.

In addition to drop cast films for TRMC, films are prepared for absorption measurements on quartz substrates using a blade coater (Zehntner ZAA 2300 Automatic Film Applicator Coater). The drop cast films are opaque ~ 400-620 nm, while the blade-coated films are thinner and more uniform, allowing absorption to be measured at all wavelengths used in this study. Films are coated at 10 mm/s with the blade set 40 μm above the sample surface. Solutions for bladed coated films are prepared in the same manner as those for drop cast films and 10 μL was deposited at room temperature and 15 μL at 100 °C. The absorption measurements of these films are used to calculate the absorption cross-section of each material at the wavelengths used for TRMC and the thickness of the films was measured using a Dektak8 profilometer.

8.2.2 Flash-Photolysis Time-Resolved Microwave Conductivity (TRMC)

TRMC is a pump-probe technique used to quantify the yield and lifetime of mobile charge carriers in films in the absence of electrical contacts. Our TRMC technique and analysis are described in detail in previous publications[10, 14, 19-21] and in Chapter 7. Films are placed in an X-band TE_{102} microwave resonance cavity tuned to 9 GHz in nitrogen atmosphere at the position of maximum electric field. A Nd:YAG laser: Continuum Powerlite is used to excite the samples at wavelengths of 430, 550, 610, and 760 nm using ~4 ns pulses which generates excitons in the

polymer or probe molecules (depending on wavelength), that then dissociate into free electrons and holes. The change in microwave power in the sample cavity due to the absorption of microwaves by the photoinduced charges is proportional to the yield of charge carriers in the film. Microwave power is measured as a function of time to obtain high frequency photoconductance (ΔG) transients. We measure ΔG transients at multiple light intensities controlled by neutral density filters, and measure the power at each light intensity before data collection.

8.2.3 X-Ray Diffraction (XRD)

We use X-Ray Diffraction (XRD) data, as in Chapter 7, to compare the crystalline domain size in polythiophene films. Measurements are conducted in air using Rigaku DMAX X-Ray Diffractometer and an alignment procedure was conducted before each measurement. The $\theta/2\theta$ scans are conducted from 2.5˚ to 13˚ at a scan rate of 0.5˚ per minute at 40 kV and 250 mA. Sherrer's formula[22] was used to calculate the coherence length, L_c, which is the crystallite dimension along the lamellar stacking diffraction (Figure 8.1b). We do not attempt to quantitatively measure crystallite size, but instead qualitatively compare crystallite size in similar samples. See 7.7.4 for more information on XRD procedure and analysis.

8.2.4 Absorption Measurements

A Shimadzu UV-3600 UV-VIS-NIR spectrophotometer equipped with an integrating sphere is used to measure the fraction of light absorbed by the polythiophene films as a function of wavelength. Absorption spectra are used to obtain the fraction of light absorbed at the TRMC excitation for data analysis. Absorption measurements of blade coated films are used in the calculation of absorption cross section, which is used to normalize the TRMC data for constant

excitation density. The absorption spectrum of the dilute PC solution was measured with a Cary 500 Scan UV-VIS-NIR Spectrometer.

8.3 RESULTS

Figure 8.2a shows the fraction of light absorbed by a blade coated P3HT film (black) compared to a spectrum of dilute PC in solution (green). It is evident that the absorption spectra in Figure 8.2 are complimentary and that the PC is be selectively excited at 760 nm.

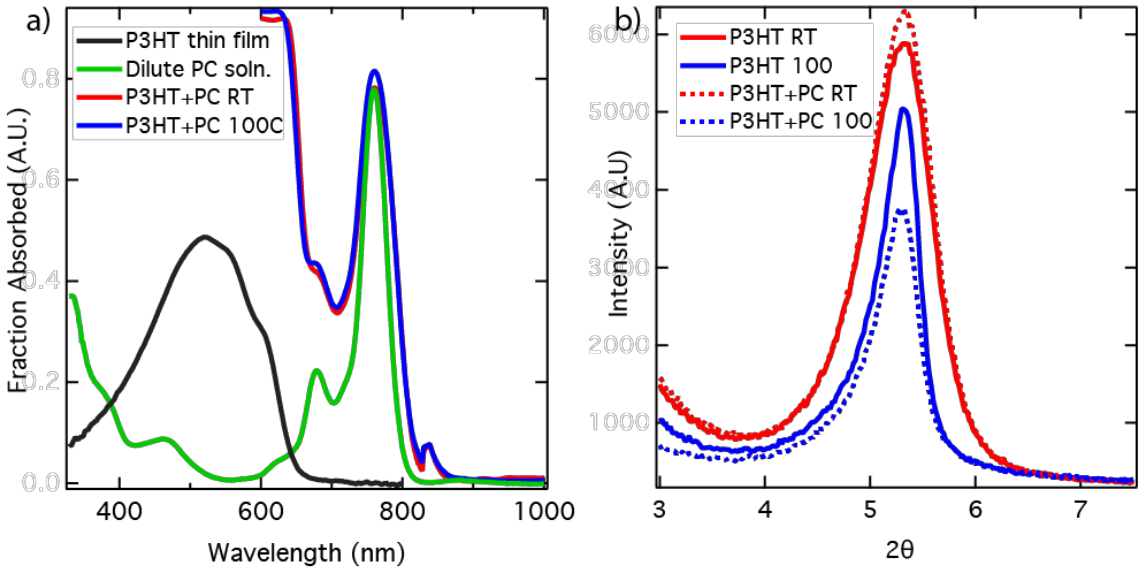

FIGURE 8.2: a) Fraction of light absorbed in arbitrary units for comparison of the P3HT absorption spectrum (black) to the PC absorption spectrum in dilute solution (green). The red and blue curves are the absorption spectra of drop cast P3HT films with 0.1 mol% PC cast at room temperature (RT) and 100 °C, respectively. The small anomaly in the spectra of the P3HT films at ~830 nm is the result of the Shimadzu spectrometer grating change. b) X-ray diffraction data for neat P3HT films (solid) and P3HT with 0.1 mol% PC films (dashed) cast at room temperature and 100 °C.

P3HT films in this study are drop cast at room temperature (smaller crystalline domains) and ~100 °C (larger crystalline domains) from 7.5 mg/mL chlorobenzene solution. Films are either neat (no PC) or contain PC molecules in a molar ratio of 0.001 PC to 1 polythiophene monomer (0.1 mol% PC). Probe molecule concentration is dilute to ensure that polymer microstructure is not disrupted and that probe molecules do not aggregate. Thus, we expect that

PC absorption in films will be similar to that in dilute solution. Figure 8.2a shows the absorption spectra of P3HT films with 0.1 mol% PC drop cast at room temperature and at 100 °C. The overlaid spectrum of dilute PC in solution shows that the PC peak at 760 nm does not shift in the drop cast films, indicating that it is valid to assume that PC molecules are not aggregating in the films and behaving as PC molecules in dilute solution. The small anomaly in the spectra of the P3HT films at ~830 nm is the result of a spectrometer grating change. The solution spectrum was measured with a different spectrometer (Cary 500) and thus does not contain the anomaly.

To demonstrate that the PC probe molecules do not disrupt polythiophene morphology, we show XRD data of neat P3HT drop cast films and films with 0.1 mol% PC in Figure 8.2b. The FWHM and position of the XRD peaks do not differ significantly for the neat P3HT film and the P3HT film with PC probe molecules, indicating that the probe molecules do not affect the crystallite size or lamellar spacing in the polythiophene films.

Now that we have established the validity of PC a candidate probe molecule, we perform TRMC experiments on films of neat P3HT and P3HT with 0.1 mol% PC, exciting at 430, 550, 610, and 760 nm. Wavelengths of 430 and 610 nm are chosen to primarily excite the amorphous and crystalline regions of the polymer, respectively, and thus elucidate the location of probe molecules in the films, since charge carrier yield would be higher when the region containing the probe molecules is excited. We also excite the samples at 550 nm to compare to previous results in ref [10] and, most importantly, at 760 nm to selectively excite PC probe molecules. We assume that only holes are detected in the polymer and polymer/probe molecule samples because TRMC is sensitive only to mobile charge carriers. Holes are mobile in polymer crystallites while electrons are trapped at the interface between amorphous and crystalline regions of polymer or on isolated probe molecules.

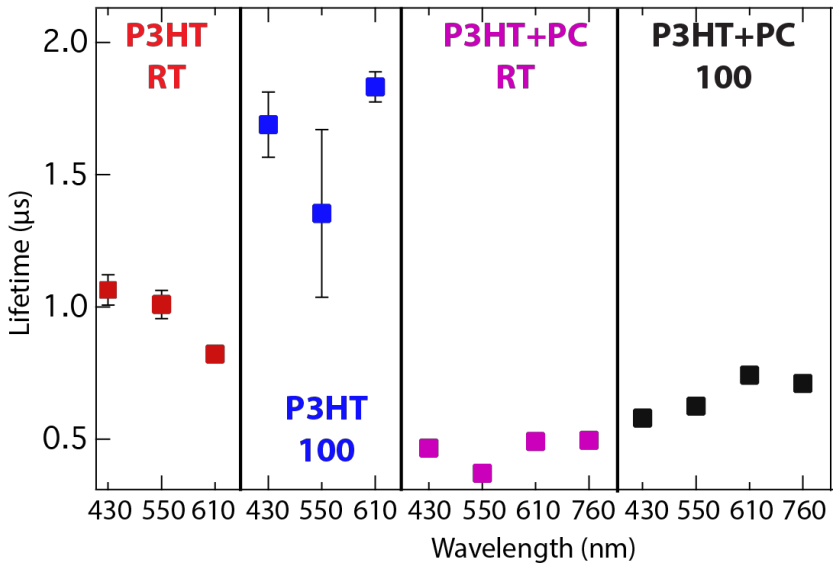

FIGURE 8.3: Photoconductance lifetime at a constant excitation density of $1.22*10^{17}$ photons/cm^3 for neat P3HT films and films with 0.1 mol% PC drop cast at room temperature and 100 °C as a function of excitation wavelength.

Figure 8.3 shows the average photoconductance lifetime of charge carriers in P3HT films cast at room temperature and 100 °C, both neat and with 0.1 mol% PC, as a function of excitation wavelength and a constant excitation density of $1.22*10^{17}$ photons/cm^3. Photoconductance lifetime data points were obtained for each data set (a data set is composed of photoconductance measurements taken at multiple light intensities as a function of time for a given sample at a given wavelength) by first fitting the set of TRMC transients using a double exponential function as described 7.7.3. The lifetime at each light intensity is taken as the weighted average of the time constants in the exponential fit. Light intensity is normalized by the absorption cross section of each material so that samples excited at different wavelengths are compared fairly at a constant excitation density. Absorption cross section is calculated at 430, 550, 610, and 760 nm from absorption and thickness measurements of thin, blade coated films as described in 8.2.1. The lifetime data as a function of excitation density is then fit as shown in supporting information 8.7.1 to obtain a lifetime value interpolated at the lowest excitation

density measured common to all samples, $1.22*10^{17}$ photons/cm^3. Error bars are calculated by using 68% confidence intervals on fitting parameters as described in 8.7.1. We focus on low excitation density because at high excitation density, the high density of charge carriers causes exciton-hole annihilation and obscures true charge carrier dynamics.

The most significant result in Figure 8.3 is that the photoinduced lifetime at each wavelength is longer in films cast at 100 °C (larger crystallites) compared to films cast at room temperature (smaller crystallites) when comparing the two neat films and when comparing the two 0.1 mol% PC films. Thus, the trend seen in the neat polymer case is valid with more charge carriers in the system and if charge carriers are generated by the probe molecule and not by the polymer (excitation at 760 nm). Thus, PC serves as a probe molecule for the polythiophene microstructure. Neat polymer does not absorb at 760 nm as shown by the small TRMC signal (on the order of a blank substrate, see 8.7.2) indicating that the TRMC signal at 760 nm comes only from holes generated via PC excitation not from polymer excitation. The PC films have much shorter charge carrier lifetimes than the neat films because there are more photoinduced charge carriers in 0.1 mol% PC films (see Figure 8.4), increasing the probability of recombination of the mobile holes in the polymer with electrons on PC molecules.

The yield of free charge carriers, holes in this case, is proportional to the initial photoconductance (transient signal extrapolated to t = 0, or beginning of the laser pulse), ϕ, multiplied by the sum of the local mobilities of free photoinduced charges, $\sum\mu$ (see 7.7.3 for a detailed explanation). The yield mobility product ($\phi\sum\mu$) at the lowest excitation density common to all samples ($1.22*10^{17}$ photons/cm^3), obtained using the fitting procedure used for lifetime data (8.7.1 and 7.7.3), is plotted as a function of wavelength for films cast at room temperature and 100 °C in Figure 8.4. We assume that changes in $\phi\sum\mu$ are due predominantly to changes in

charge carrier yield because local charge carrier mobility has been shown to be independent of neat polythiophene morphology[23, 24]. Yield is higher in films with PC in contrast to neat films in the absence of PC due to an increased number of dissociation sites. There is no significant difference in yield between PC films excited at 430 nm (primarily exciting amorphous P3HT) and 610 nm (primarily exciting crystalline P3HT), indicating that this yield data is not sufficient to determine the location of the probe molecules in the films. Exciting the PC molecules at 760 nm yields a similar number of charge carriers as exciting the polymer in samples with probe molecules.

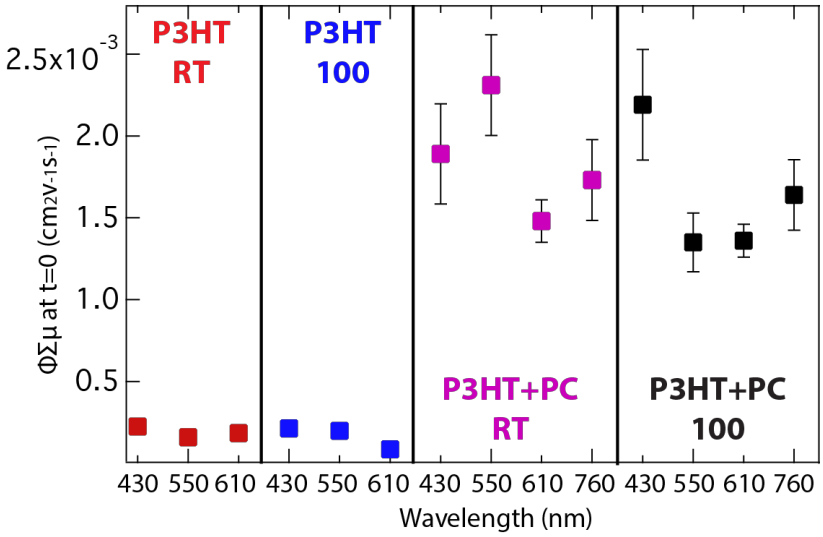

FIGURE 8.4: Relative Yield, $\phi\Sigma\mu$, at t=0 with a constant excitation density of $1.22*10^{17}$ photons/cm^3, for neat P3HT films and films with 0.1 mol% PC drop cast at room temperature and 100 °C as a function of excitation wavelength.

8.4 CONCLUSION

From preliminary data we conclude that: 1) Crystallite size affects lifetime and yield of charge carriers in neat polythiophene and in films with PC molecules, and 2) PC shows potential as a probe molecule for polythiophene microenvironments. Future work will be to repeat this experiment for P3HT, PTTT, and regiorandom P3HT films with PC. Regiorandom P3HT is

completely amorphous and will serve as a control experiment to see if crystalline domains are necessary to generate free charge carriers upon excitation of PC. In addition, we will use $PC_{71}BM$ as a second probe molecule because fullerene derivatives are more relevant acceptor molecules in organic solar cells. The absorption coefficient of $PC_{71}BM$ outside the range of polythiophene absorption is much lower than that of PC, however, making it a less effective probe molecule. We will study PTTT in addition to the more commonly used P3HT because in our previous work, ref [10], we found PTTT had a larger difference in crystallite size and photoinduced charge carrier lifetime compared to P3HT.

8.5 AKNOWLEDGEMENTS

The TRMC system described here was funded by the Solar Photochemistry Program, Division of Chemical Sciences, Geosciences, and Biosciences, Office of Basic Energy Sciences, U.S. Department of Energy. The experimental development for controlling polymer crystalline domain size was supported by the Laboratory Directed Research and Development (LDRD) Program at the National Renewable Energy Laboratory under task number 06RF1201.

8.6 REFERENCES

1. McCulloch, I.; Heeney, M.; Chabinyc, M. L.; DeLongchamp, D.; Kline, R. J.; Coelle, M.; Duffy, W.; Fischer, D.; Gundlach, D.; Hamadani, B.; Hamilton, R.; Richter, L.; Salleo, A.; Shkunov, M.; Sporrowe, D.; Tierney, S.; Zhong, W. *Advanced Materials* **2009,** 21, (10-11), 1091-1109.

2. Ong, B. S.; Wu, Y. L.; Li, Y. N.; Liu, P.; Pan, H. L. *Chemistry-a European Journal* **2008,** 14, (16), 4766-4778.

3. McCulloch, I.; Heeney, M.; Bailey, C.; Genevicius, K.; Macdonald, I.; Shkunov, M.; Sparrowe, D.; Tierney, S.; Wagner, R.; Zhang, W. M.; Chabinyc, M. L.; Kline, R. J.; McGehee, M. D.; Toney, M. F. *Nature Materials* **2006,** 5, (4), 328-333.

4. Koppe, M.; Scharber, M.; Brabec, C.; Duffy, W.; Heeney, M.; McCulloch, I. *Advanced Functional Materials* **2007,** 17, (8), 1371-1376.

5. Parmer, J. E.; Mayer, A. C.; Hardin, B. E.; Scully, S. R.; McGehee, M. D.; Heeney, M.; McCulloch, I. *Applied Physics Letters* **2008,** 92, (11).

6. Ma, W. L.; Yang, C. Y.; Gong, X.; Lee, K.; Heeger, A. J. *Advanced Functional Materials* **2005,** 15, (10), 1617-1622.

7. Brinkmann, M. *Journal of Polymer Science Part B-Polymer Physics* **2011,** 49, (17), 1218-1233.

8. Shen, X. B.; Duzhko, V. V.; Russell, T. P. *Advanced Energy Materials* **2013,** 3, (2), 263-270.

9. Kozub, D. R.; Vakhshouri, K.; Orme, L. M.; Wang, C.; Hexemer, A.; Gomez, E. D. *Macromolecules* **2011,** 44, (14), 5722-5726.

10. Marsh, H. S.; Reid, O. G.; Barnes, G.; Heeney, M.; Stingelin, N.; Rumbles, G. *Journal of Polymer Science Part B-Polymer Physics* **2014,** 52, (10), 700-707.

11. Osterloh, F. E.; Holmes, M. A.; Chang, L.; Moulé, A. J.; Zhao, J. *The Journal of Physical Chemistry C* **2013,** 117, (51), 26905-26913.

12. Paquin, F.; Latini, G.; Sakowicz, M.; Karsenti, P. L.; Wang, L. J.; Beljonne, D.; Stingelin, N.; Silva, C. *Physical Review Letters* **2011,** 106, (19).

13. Sweetnam, S.; Graham, K. R.; Ndjawa, G. O. N.; Heumuller, T.; Bartelt, J. A.; Burke, T. M.; Li, W. T.; You, W.; Amassian, A.; McGehee, M. D. *Journal of the American Chemical Society* **2014,** 136, (40), 14078-14088.

14. Reid, O. G.; Malik, J. A. N.; Latini, G.; Dayal, S.; Kopidakis, N.; Silva, C.; Stingelin, N.; Rumbles, G. *Journal of Polymer Science Part B-Polymer Physics* **2012,** 50, (1), 27-37.

15. Bergkamp, J. J.; Sherman, B. D.; Marino-Ochoa, E.; Palacios, R. E.; Cosa, G.; Moore, T. A.; Gust, D.; Moore, A. L. *Journal of Porphyrins and Phthalocyanines* **2011,** 15, (9-10), 943-950.

16. Honda, S.; Yokoya, S.; Ohkita, H.; Benten, H.; Ito, S. *Journal of Physical Chemistry C* **2011,** 115, (22), 11306-11317.

17. Lim, B.; Bloking, J. T.; Ponec, A.; McGehee, M. D.; Sellinger, A. *Acs Applied Materials & Interfaces* **2014,** 6, (9), 6905-6913.

18. Honda, S.; Ohkita, H.; Benten, H.; Ito, S. *Advanced Energy Materials* **2011,** 1, (4), 588-598.

19. Ferguson, A. J.; Kopidakis, N.; Shaheen, S. E.; Rumbles, G. *Journal of Physical Chemistry C* **2008,** 112, (26), 9865-9871.

20. Kroeze, J. E.; Savenije, T. J.; Vermeulen, M. J. W.; Warman, J. M. *Journal of Physical Chemistry B* **2003,** 107, (31), 7696-7705.

21. Dehaas, M. P.; Warman, J. M. *Chemical Physics* **1982,** 73, (1-2), 35-53.

22. Cullity, B. D.; Stock, S. R., *Elements of X-Ray Diffraction*. 3 ed.; Prentice Hall: Upper Saddle River, 2001.

23. Dicker, G. Photogeneration And Dynamics Of Charge Carriers In The Conjugated Polymer Poly(3-hexylthiophene). Delt University, IOS Press, 2004.

24. Pingel, P.; Zen, A.; Abellon, R. D.; Grozema, F. C.; Siebbeles, L. D. A.; Neher, D. *Advanced Functional Materials* **2010,** 20, (14), 2286-2295.

25. Rubinson, K.; Rubinson, J., *Contemporary Instrumental Analysis*. Prentice-Hall: Upper Saddle River, 2000.

8.7 SUPPORTING INFORMATION

8.7.1 Procedure for Fitting Lifetime and $\phi\sum\mu$ Data as a function of Excitation Density

Photoconductance lifetime and $\phi\sum\mu$ data extracted from fits to photoconductance transients (as in 7.7.3) as a function of excitation density are fit using the following empirical formula where y is lifetime or $\phi\sum\mu$, x is excitation density, and A and B are fit parameters.

$$y = \frac{A}{1+\sqrt{(B \times x)}} \qquad (1)$$

Figure 8.5 shows photoconductance lifetime plotted as a function of excitation density for P3HT samples: Neat RT (red), Neat 100 °C (blue), P3HT-PC RT (pink), P3HT-PC 100 °C (black) excited at 430 nm (triangles), 550 nm (squares), 610 nm (diamonds), and 760 nm (circles) and fit with Equation 1. Equation 1 is an empirical formula chosen to fit the data to obtain interpolated values. The interpolated lifetime at $1.22*10^{17}$ photons/cm^3, the lowest excitation density common to all samples, is used to compare lifetime between samples and

wavelengths in Figures 8.3. The same procedure is used to fit $\phi\sum\mu$ as a function of excitation density and obtain the interpolated values at $1.22*10^{17}$ photons/cm^3 shown in Figure 8.4. The error on each coefficient with 68% confidence is calculated during fitting and the square root of the sum of the squares of these errors is used to calculate the error on each interpolated value as described in ref [25].

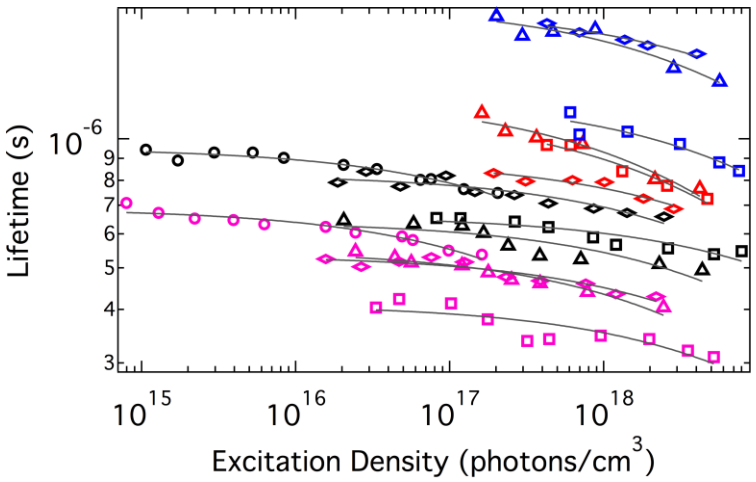

FIGURE 8.5: Photoconductance lifetime plotted as a function of excitation density for P3HT samples: Neat room temperature (RT) (red), Neat 100 °C (blue), P3HT-PC RT (pink), P3HT-PC 100 °C (black) excited at 430 nm (triangles), 550 nm (squares), 610 nm (diamonds), and 760 nm (circles). Gray lines are fits to the data using Equation 1.

8.7.2 Neat P3HT Samples Excited at 760 nm

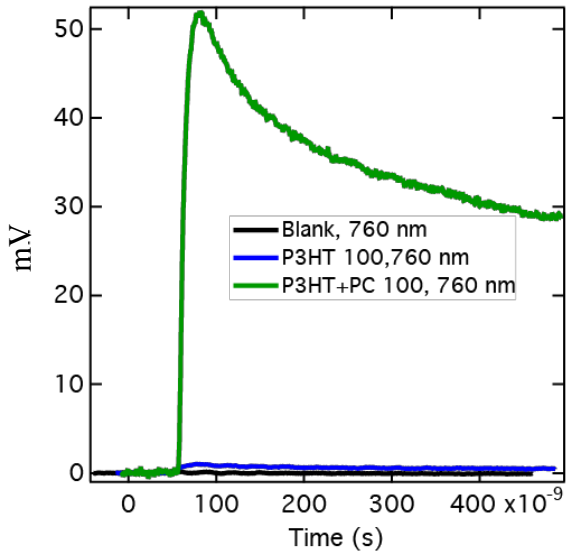

FIGURE 8.6: Photoconductance transients for a blank substrate, neat P3HT film cast at 100°C and P3HT film with 0.1 mol% PC (P3HT+PC) cast at 100 °C excited at 760 nm.

Figure 8.6 shows that the photoconductance signal for the neat P3HT film is on the order of the signal for the blank substrate indicating that the photoconductance signal data for P3HT films with 0.1 mol% PC comes only from PC excitation. The P3HT film with 0.1 mol% PC in Figure 8.6 is excited at a light intensity ~14 times lower than that used for the neat P3HT film and blank substrate, but has a much higher signal.

Chapter 9
Conclusion

In this thesis work we performed both simulations and experiments to study how the morphology and charge carrier dynamics of neat polythiophene and blends of polythiophene with acceptor molecules are affected by changing molecular features and processing conditions. This combined approach leads to a broader understanding of the morphology of thiophene-based materials for organic electronic applications than would be possible with either a computational or an experimental approach alone.

9.1 COMPUTATIONAL WORK

Summary of work in this thesis: In Chapters 2-6, we studied how the molecular features of conjugated thiophene-based oligomer and fullerene derivative acceptor molecules affect the equilibrium morphology of neat oligomers, oligomer-acceptor blends, and oligomer-acceptor blends with additives. Model oligomers mimicked commonly used thiophene polymers including poly(3-alkylthiophene) (P3AT), poly(2,2′:5′,2″-3,3″-dialkyl-terthiophene) (PTTT), poly(3,4-dihexyl-2,2′-bithiophene) (PDHBT), and (2,5-bis(3-alkylthiophen-2-yl)thieno[3,2-b]thiophene) (BTTT). Model acceptor molecules mimicked fullerene derivatives such as [6,6]-phenyl-C_{61}-butyric acid methyl ester (PCBM). Our goal was to provide guidelines to materials scientists about how the features of the polymer/acceptor/additive architecture and chemistry tune morphology, so as to enable the selection of materials that lead to desirable morphologies needed for high device efficiency.

In Chapter 2, we developed a coarse-grained model adapted from work by Huang et al.[1], to model oligomers with 10 monomer units (10-mers) and fullerene derivative acceptor

molecules. We modeled the oligomer backbones as rigid rods, and blends were simulated with varying side chain – side chain, backbone-backbone, side chain – backbone, acceptor-acceptor attraction and varying oligomer flexibility. Depending on the strength of side chain-side chain attraction, which can be tuned by solvent choice, the alkyl side chains on oligomer backbones increased or decreased the blend disorder-order transition temperature compared to the case of backbones without side chains,. We simulated blends with and without constraints on the rigidity of oligomer backbones and on the flexibility of alkyl side chains, and found that backbone rigidity drives oligomer ordering. When backbone-backbone interactions are strong, changing acceptor-acceptor attraction from high to low modulates morphology from highly macrophase separated domains to interconnecting domains. In Chapter 3, we increased the computational efficiency of our simulations by running the simulations on Graphics Processing Units (GPUs) using HOOMD-Blue software, which allowed us to simulate larger systems with more realistic coarse-grained models for the thiophene oligomers and fullerene derivatives. We validated our new intermediate-resolution coarse-grained model by comparing simulated diffraction patterns to experimental diffraction patterns. Then, with the validated model we explored the design parameters and created a phase diagram of blends with varying oligomer architecture and chemistry and acceptor molecule chemistry. Blend order-disorder transition temperature depended on oligomer alkyl side chain density and orientation, and on acceptor miscibility. Strongly miscible acceptors intercalated between donor oligomer side chains if there was sufficient space between donor side chains to fit acceptor molecules and if there was sufficient acceptor-backbone attraction, as seen in experiments. Finally, we found new morphologies in blends with high acceptor-backbone attraction that had high interfacial area and domain connectivity that could be beneficial for organic photovoltaic devices.

In Chapter 4, we extended the work in Chapter 3 to neat oligomers (no acceptors) to focus on the thermodynamic driving forces governing thiophene oligomer assembly. Oligomers with side chains on both sides of the backbone formed lamellae, while oligomers with side chains on one side of the backbone formed cylinders. An order-to-order transition involving cylindrical and lamellar morphologies was found in some cases depending on the strength of side chain – side chain attraction and on the balance of entropic and enthalpic driving forces for order. We characterized the thermodynamic driving forces by quantifying system potential energy and entropy. For oligomers with side chains on one side of the backbone, conformational entropy favored cylinder morphologies over lamellar morphologies at high temperature where entropic driving forces dominated. Enthalpically favorable side chain – side chain contacts stabilized lamellar morphologies at low temperatures.

In Chapter 5, we determined how minority component additive architecture and chemistry affected the morphology of PTTT-like and P3DDT-like oligomer-acceptor blends. Specifically additives mimicking diiodooctane, alkanedithiols, and methyl ester additives were studied as they have been used recently (experimentally) in the preparation of active layers for organic photovoltaic devices with increased device efficiency. We simulated blends of oligomers, acceptor molecules and additives with varying length and end functionalization to investigate the mechanism of the effect of additives on oligomer-acceptor morphology. We found that additive functional groups attracted to acceptor molecules are necessary to induce acceptor macrophase separation and reduction in acceptor intercalation in PTTT-like oligomers. We proposed the following design rules for experimentalists when synthesizing and selecting additives: 1) To achieve moderate oligomer-acceptor macrophase separation, use additives with

long alkyl segments. 2) To achieve high oligomer-acceptor phase separation, use additives with short alkyl segments or additives with functional groups on both ends of the additive.

Finally, in Chapter 6, motivated by experimental work by Briseño and coworkers, we simulated neat BTTT oligomers and blends of BTTT with fullerene derivative acceptor molecules. These oligomers were synthesized by Briseño *et al*. and used in organic solar cells. Simulation results using our coarse-grained model developed in Chapters 2-5 produced morphologies that agreed with the interpretation of experimental X-ray diffraction results. BTTT dimers formed lamellae with acceptors in ordered rows in between oligomer side chains in both our simulations and the experiments. Furthermore, oligomer backbone orientational order was higher in blends than in neat oligomers, both in simulations and experiments.

Future work: Processing, such as solvent-vapor annealing, plays a large role in determining the morphology of donor-acceptor blends for organic photovoltaic devices. Thus, it would be beneficial in simulations to explicitly model solvent molecules (modeled implicitly in this work), and enact a simulation protocol where solvent beads leave the polymer phase to mimic solvent evaporation. Examining how solvent chemistry and volatility affect polymer morphology, film thickness, and film dynamics during drying could be useful. Additionally, oligomer-acceptor-additive blends with explicit solvent molecules could be simulated in future work to mimic the evaporation of the majority-component solvent followed by that of the lower boiling point additive.

While work in this thesis has been purely on bulk morphology, one could also investigate the effect of a substrate surface on donor-acceptor morphology. Studies varying the interactions of the donor and acceptor molecules with the surface, patterning the surface, and functionalizing the surface with donor and acceptor molecules could be valuable.

A third direction for future work is thiophene-based star oligomers where three or more oligothiophenes are connected at a central core. Star oligomers are of interest for organic photovoltaics because these molecules have 2D charge carrier transport, good solubility and film quality and specific structure and energy levels[2]. Stars can form diverse morphologies[2] and the morphology of star oligomers has been found to differ from the linear case[3]. P3HT 3-arm[4] and 6-arm[5] stars have been synthesized but little is known about the morphology or thermodynamics of these molecules. Simulations of blends of oligothiophene stars with three or six oligothiophenes of varying architecture attached to the central core could be useful.

9.2: EXPERIMENTAL WORK

Summary of work in this thesis: The second section of the thesis, Chapters 7 and 8, describes our experimental studies of the morphology and charge carrier dynamics in neat polythiophene (P3HT and PTTT) films and polythiophene films with a low concentration of phthalocyanine acceptor molecules. Our goal was to understand how processing conditions, polymer architecture and polymer molecular weight affect polythiophene microstructure and charge carrier dynamics. We used Time-Resolved Microwave Conductivity (TRMC) to probe the lifetime and yield of free charge carriers (electrons and holes) in films, and X-Ray Diffraction (XRD) and Differential Scanning Calorimetry (DSC) to determine polythiophene crystallite size.

In Chapter 7, we found that the classical interpretation of polymer chain folding applies to the conjugated polythiophenes P3HT and PTTT of low and high molecular weights: polymer films cast at higher temperatures had larger crystalline domains than those cast at low temperatures. Our TRMC results suggested that tuning crystallite size modulated the amount amorphous-crystalline interface in the films, which is the hypothesized location of exciton dissociation into electrons and holes in neat polymer, and the location of charge carrier loss to

recombination. P3HT and PTTT films with larger crystallites had longer charge carrier lifetimes than those with smaller crystallites because charge carriers in the larger crystallites had a lower probability of encountering the amorphous-crystalline interface and recombining. P3HT films with larger crystallites had a lower yield of free charge carriers than those with smaller crystallites because there was less amorphous-crystalline interfacial area for excitons to dissociate into electrons and holes per crystallite volume, compared to films with smaller crystallites.

In Chapter 8, we investigated the effect of P3HT crystallite size on charge carrier lifetime and yield in films where charge carriers were generated on phthalocyanine acceptor molecules instead of in the polymer phase. These films had a low concentration of acceptor molecules so that polymer morphology was not disrupted, but charge carrier density was significantly higher than in the case of neat polymer, making these results more relevant to organic electronic device applications. Preliminary results showed that polythiophene crystalline domain size affected charge carrier lifetime regardless of whether charge carriers were generated on the phthalocyanine molecule or in the polythiophene. Charge carrier yield was higher in films with phthalocyanine compared to neat films.

Future work: Future work will directly follow the preliminary work described in Chapter 8. We will perform the same experiments with PTTT in addition to the P3HT investigated in Chapter 8 because PTTT showed a larger difference in crystallite size and charge carrier lifetime than P3HT in Chapter 7. We will also use regiorandom P3HT as a control experiment because this polymer is completely amorphous. This work will also include experiments with P3HT, PTTT, and regiorandom P3HT films containing a low concentration of PCBM, a fullerene derivative acceptor molecule more commonly used in bulk heterojunction active layers.

Polythiophene films are known to contain intrinsic charge carriers in the absence of excitation, termed "dark carriers", the origin of which is unknown. TRMC results in Chapter 7 suggested that PTTT films cast at high temperature had a higher density of dark carriers than did films cast at low temperature, but the dark carrier concentration was not quantified. Future work should include quantification of the dark carriers using Photothermal Deflection Spectroscopy. This technique measures sub-bandgap absorption and is sensitive to absorption at around 1.35 eV, which is characteristic of the intrinsic carriers[6].

Future work should also include an investigation of the mechanism of free charge carrier generation in neat polymer films, which is hypothesized to occur at the interface of amorphous and crystalline domains. A future study would carefully modulate the amount of amorphous-crystalline surface area and the amount of polymer folding by varying the concentration of pre-formed nanofibers of high molecular weight (chain-folded) or low molecular weight (not chain-folded) P3HT mixed in regiorandom P3HT which is completely amorphous. These films would then have known amounts of amorphous-crystalline interface either with folds or without folds and TRMC experiments would be performed to determine photoinduced charge carrier yield and lifetime in these films. PDS measurements would also be conducted to determine how dark carrier concentration is affected by chain folding and the amount of amorphous-crystalline interfacial area.

9.3 REFERENCES

1. Schwarz, K. N.; Kee, T. W.; Huang, D. M. *Nanoscale* **2013,** 5, (5), 2017-2027.
2. Kanibolotsky, A. L.; Perepichka, I. F.; Skabara, P. J. *Chemical Society Reviews* **2010,** 39, (7), 2695-2728.
3. Lorenzo, A. T.; Muller, A. J.; Lin, M.-C.; Chen, H.-L.; Jeng, U. S.; Priftis, D.; Pitsikalis, M.; Hadjichristidis, N. *Macromolecules* **2009,** 42, (21), 8353-8364.

4. Yuan, M.; Okamoto, K.; Bronstein, H. A.; Luscombe, C. K. *Acs Macro Letters* **2012,** 1, (3), 392-395.

5. Senkovskyy, V.; Beryozkina, T.; Bocharova, V.; Tkachov, R.; Komber, H.; Lederer, A.; Stamm, M.; Severin, N.; Rabe, J. P.; Kiriy, A. *Polymer Networks: Synthesis, Properties, Theory and Applications* **2010,** 291-292, 17-25.

6. Goris, L.; Haenen, K.; Nesladek, M.; Wagner, P.; Vanderzande, D.; De Schepper, L.; D'Haen, J.; Lutsen, L.; Manca, J. V. *Journal of Materials Science* **2005,** 40, (6), 1413-1418.

Bibliography

[1] Adachi, T.; Brazard, J.; Ono, R. J.; Hanson, B.; Traub, M. C.; Wu, Z. Q.; Li, Z. C.; Bolinger, J. C.; Ganesan, V.; Bielawski, C. W.; Bout, D. A. V.; Barbara, P. F. Journal of Physical Chemistry Letters 2011, 2, (12), 1400-1404.

[2] Adams, M.; Dogic, Z.; Keller, S. L.; Fraden, S. Nature 1998, 393, (6683), 349-352.

[3] Agarwal, U.; Escobedo, F. A. Nature Materials 2011, 10, (3), 230-235.

[4] Ahmed, M. O.; Wang, C.; Keg, P.; Pisula, W.; Lam, Y.-M.; Ong, B. S.; Ng, S.-C.; Chen, Z.-K.; Mhaisalkar, S. G. Journal of Materials Chemistry 2009, 19, (21), 3449-3456.

[5] Alexiadis, O.; Mavrantzas, V. G. Macromolecules 2013, 46, (6), 2450-2467.

[6] Anderson, J. A.; Lorenz, C. D.; Travesset, A. Journal of Computational Physics 2008, 227, (10), 5342-5359.

[7] Anderson, J.; Jankowski, E.; Grubb, T.; Engel, M.; Glotzer, S. 2012.

[8] Bartelt, J. A.; Douglas, J. D.; Mateker, W. R.; Labban, A. E.; Tassone, C. J.; Toney, M. F.; Fréchet, J. M. J.; Beaujuge, P. M.; McGehee, M. D. Advanced Energy Materials 2014, (4), 1301733.

[9] Bates, F. S. Science 1991, 251, (4996), 898-905.

[10] Bergkamp, J. J.; Sherman, B. D.; Marino-Ochoa, E.; Palacios, R. E.; Cosa, G.; Moore, T. A.; Gust, D.; Moore, A. L. Journal of Porphyrins and Phthalocyanines 2011, 15, (9-10), 943-950.

[11] Borisov, O. V.; Zhulina, E. B. Macromolecules 2005, 38, (6), 2506-2514.

[12] Brady, M. A.; Su, G. M.; Chabinyc, M. L. Soft Matter 2011, 7, (23), 11065-11077.

[13] Brinkmann, M. Journal of Polymer Science Part B-Polymer Physics 2011, 49, (17), 1218-1233.

[14] Brinkmann, M.; Rannou, P. Macromolecules 2009, 42, (4), 1125-1130.

[15] Brown, W. M.; Wang, P.; Plimpton, S. J.; Tharrington, A. N. Computer Physics Communications 2011, 182, (4), 898-911.

[16] Buchaca-Domingo, E.; Ferguson, A. J.; Jamieson, F. C.; McCarthy-Ward, T.; Shoaee, S.; Tumbleston, J. R.; Reid, O. G.; Yu, L.; Madec, M. B.; Pfannmoller, M.; Hermerschmidt, F.; Schroder, R. R.; Watkins, S. E.; Kopidakis, N.; Portale, G.; Amassian, A.; Heeney, M.; Ade, H.; Rumbles, G.; Durrant, J. R.; Stingelin, N. Materials Horizons 2014, 1, (2), 270-279.

[17] Buckley, C. P.; Kovacs, A. J. Colloid and Polymer Science 1976, 254, (8), 695-715.

[18] Campoy-Quiles, M.; Ferenczi, T.; Agostinelli, T.; Etchegoin, P. G.; Kim, Y.; Anthopoulos, T. D.; Stavrinou, P. N.; Bradley, D. D. C.; Nelson, J. Nature Materials 2008, 7, (2), 158-164.

[19] Carbonnier, B.; Egbe, D. A. M.; Birckner, E.; Grummt, U. W.; Pakula, T. Macromolecules 2005, 38, (18), 7546-7554.

[20] Carrillo, J.-M. Y.; Kumar, R.; Goswami, M.; Sumpter, B. G.; Brown, W. M. Physical Chemistry Chemical Physics 2013, 15, (41), 17873-17882.

[21] Cates, N. C.; Gysel, R.; Dahl, J. E. P.; Sellinger, A.; McGehee, M. D. Chemistry of Materials 2010, 22, (11), 3543-3548.

[22] Causin, V.; Marega, C.; Marigo, A.; Valentini, L.; Kenny, J. M. Macromolecules 2005, 38, (2), 409-415.

[23] Cha, H.; Baek, J. Y.; An, T. K.; Kim, S.-O.; Kwon, S.-K.; Kim, Y.-H.; Park, C. E. Organic Electronics 2014, 15, (12), 3558-3567.

[24] Chang, L.; Jacobs, I. E.; Augustine, M. P.; Moule, A. J. Organic Electronics 2013, 14, (10), 2431-2443.

[25] Chen, S. A.; Ni, J. M. Macromolecules 1992, 25, (23), 6081-6089.

[26] Cheung, D. L.; McMahon, D. P.; Troisi, A. Journal of Physical Chemistry B 2009, 113, (28), 9393-9401.

[27] Cho, E.; Risko, C.; Kim, D.; Gysel, R.; Miller, N. C.; Breiby, D. W.; McGehee, M. D.; Toney, M. F.; Kline, R. J.; Bredas, J. L. Journal of the American Chemical Society 2012, 134, (14), 6177-6190.

[28] Cho, S.; Nho, S.-H.; Eo, M.; Lee, M. H. Organic Electronics 2014, 15, (5), 1002-1011.

[29] Chu, T.; Lu, J.; Beaupre, S.; Zhang, Y.; Pouliot, J.; Jiayun, Z.; Najari, A.; Leclerc, M.; Tao, Y. Adv. Funct. Mater. 2012, 22, (11), 2345-2351.

[30] Cullity, B. D.; Stock, S. R., Elements of X-Ray Diffraction. 3 ed.; Prentice Hall: Upper Saddle River, 2001.

[31] Curtarolo, S.; Hart, G.; Nardelli, M.; Mingo, N.; Sanvito, S.; Levy, O. Nature Materials 2013, 12, 191-201.

[32] Dag, S.; Wang, L. W. Journal of Physical Chemistry B 2010, 114, (18), 5997-6000.

[33] Dehaas, M. P.; Warman, J. M. Chemical Physics 1982, 73, (1-2), 35-53.

[34] Deibel, C.; Dyakonov, V. Rep. Prog. Phys. 2010, 73, (9), 39.

[35] Dicker, G. Photogeneration And Dynamics Of Charge Carriers In The Conjugated Polymer Poly(3-hexylthiophene). Delt University, IOS Press, 2004.

[36] Dicker, G.; de Haas, M. P.; Siebbeles, L. D. A.; Warman, J. M. Physical Review B 2004, 70, (4).

[37] Dogic, Z.; Fraden, S. Physical Review Letters 1997, 78, (12), 2417-2420.

[38] Fan, X.; Zhao, S.; Yue, C.; Yang, Q.; Gong, W.; Chen, Y.; Wang, H.; Jia, Q.; Xu, Z.; Xu, X. Journal of Nanoscience and Nanotechnology 2014, 14, (5), 3592-3596.

[39] Ferguson, A. J.; Kopidakis, N.; Shaheen, S. E.; Rumbles, G. Journal of Physical Chemistry C 2008, 112, (26), 9865-9871.

[40] Ferguson, A. J.; Kopidakis, N.; Shaheen, S. E.; Rumbles, G. Journal of Physical Chemistry C 2011, 115, (46), 23134-23148.

[41] Frenkel, D. European Physical Journal Plus 2013, 128, (1).

[42] Gadisa, A.; Oosterbaan, W. D.; Vandewal, K.; Bolsee, J. C.; Bertho, S.; D'Haen, J.; Lutsen, L.; Vanderzande, D.; Manca, J. V. Advanced Functional Materials 2009, 19, (20), 3300-3306.

[43] Gallazzi, M. C.; Castellani, L.; Marin, R. A.; Zerbi, G. Journal of Polymer Science Part a-Polymer Chemistry 1993, 31, (13), 3339-3349.

[44] Glotzer, S. C.; Solomon, M. J. Nature Materials 2007, 6, (8), 557-562.

[45] Goris, L.; Haenen, K.; Nesladek, M.; Wagner, P.; Vanderzande, D.; De Schepper, L.; D'Haen, J.; Lutsen, L.; Manca, J. V. Journal of Materials Science 2005, 40, (6), 1413-1418.

[46] Gotz, A. W.; Williamson, M. J.; Xu, D.; Poole, D.; Le Grand, S.; Walker, R. C. Journal of Chemical Theory and Computation 2012, 8, (5), 1542-1555.

[47] Groves, C.; Reid, O. G.; Ginger, D. S. Accounts of Chemical Research 2010, 43, (5), 612-620.

[48] Haji-Akbari, A.; Engel, M.; Keys, A. S.; Zheng, X. Y.; Petschek, R. G.; Palffy-Muhoray, P.; Glotzer, S. C. Nature 2009, 462, (7274), 773-U91.

[49] Hall, L. M.; Anderson, B. J.; Zukoski, C. F.; Schweizer, K. S. Macromolecules 2009, 42, (21), 8435-8442.

[50] Heffner, G. W.; Pearson, D. S. Macromolecules 1991, 24, (23), 6295-6299.

[51] Ho, V.; Boudouris, B. W.; Segalman, R. A. Macromolecules 2010, 43, (19), 7895-7899.

[52] Honda, S.; Ohkita, H.; Benten, H.; Ito, S. Advanced Energy Materials 2011, 1, (4), 588-598.

[53] Honda, S.; Yokoya, S.; Ohkita, H.; Benten, H.; Ito, S. Journal of Physical Chemistry C 2011, 115, (22), 11306-11317.

[54] Hooper, J. B.; Schweizer, K. S. Macromolecules 2006, 39, (15), 5133-5142.

[55] Hoppe, H.; Sariciftci, N. S. Journal of Materials Chemistry 2006, 16, (1), 45-61.

[56] Huang, D. M.; Faller, R.; Do, K.; Moule, A. J. Journal of Chemical Theory and Computation 2010, 6, (2), 526-537.

[57] Huang, D. M.; Moule, A. J.; Faller, R. Fluid Phase Equilibria 2011, 302, (1-2), 21-25.

[58] Humphrey, W.; Dalke, A.; Schulten, K. Journal of Molecular Graphics & Modelling 1996, 14, (1), 33-38.

[59] Jamieson, F. C.; Domingo, E. B.; McCarthy-Ward, T.; Heeney, M.; Stingelin, N.; Durrant, J. R. Chemical Science 2012, 3, (2), 485-492.

[60] Jankowski, E.; Marsh, H. S.; Jayaraman, A. Macromolecules 2013, 46, (14), 5775-5785.

[61] Kamberaj, H.; Low, R. J.; Neal, M. P. Journal of Chemical Physics 2005, 122, (22).

[62] Kanibolotsky, A. L.; Perepichka, I. F.; Skabara, P. J. Chemical Society Reviews 2010, 39, (7), 2695-2728.

[63] Kastner, C.; Susarova, D. K.; Jadhav, R.; Ulbricht, C.; Egbe, D. A. M.; Rathgeber, S.; Troshin, P. A.; Hoppe, H. Journal of Materials Chemistry 2012, 22, (31), 15987-15997.

[64] Keg, P.; Lohani, A.; Fichou, D.; Lam, Y. M.; Wu, Y. L.; Ong, B. S.; Mhaisalkar, S. G. Macromolecular Rapid Communications 2008, 29, (14), 1197-1202.

[65] Keller, A. Rep. Prog. Phys. 1968, 623-704.

[66] Keller, A.; Kawai, T. Philosophical Magazine 1965, 11, (114), 1165-1177.

[67] Kesters, J.; Kudret, S.; Bertho, S.; Van den Brande, N.; Defour, M.; Van Mele, B.; Penxten, H.; Lutsen, L.; Manca, J.; Vanderzande, D.; Maes, W. Organic Electronics 2014, 15, (2), 549-562.

[68] Keum, J. K.; Xiao, K.; Ivanov, I. N.; Hong, K.; Browning, J. F.; Smith, G. S.; Shao, M.; Littrell, K. C.; Rondinone, A. J.; Payzant, E. A.; Chen, J.; Hensley, D. K. Crystengcomm 2013, 15, (6), 1114-1124.

[69] Kim, C. S.; Tinker, L. L.; DiSalle, B. F.; Gomez, E. D.; Lee, S.; Bernhard, S.; Loo, Y.-L. Advanced Materials 2009, 21, (30), 3110-3115.

[70] Kim, K. H.; Kang, H.; Kim, H. J.; Kim, P. S.; Yoon, S. C.; Kim, B. J. Chemistry of Materials 2012, 24, (12), 2373-2381.

[71] Kline, R. J.; DeLongchamp, D. M.; Fischer, D. A.; Lin, E. K.; Richter, L. J.; Chabinyc, M. L.; Toney, M. F.; Heeney, M.; McCulloch, I. Macromolecules 2007, 40, (22), 7960-7965.

[72] Kline, R. J.; McGehee, M. D.; Kadnikova, E. N.; Liu, J. S.; Frechet, J. M. J.; Toney, M. F. Macromolecules 2005, 38, (8), 3312-3319.

[73] Ko, S. W.; Hoke, E. T.; Pandey, L.; Hong, S. H.; Mondal, R.; Risko, C.; Yi, Y. P.; Noriega, R.; McGehee, M. D.; Bredas, J. L.; Salleo, A.; Bao, Z. A. Journal of the American Chemical Society 2012, 134, (11), 5222-5232.

[74] Koch, F. P. V.; Heeney, M.; Smith, P. Journal of the American Chemical Society 2013, 135, (37), 13699-13709.

[75] Koppe, M.; Scharber, M.; Brabec, C.; Duffy, W.; Heeney, M.; McCulloch, I. Advanced Functional Materials 2007, 17, (8), 1371-1376.

[76] Kozub, D. R.; Vakhshouri, K.; Orme, L. M.; Wang, C.; Hexemer, A.; Gomez, E. D. Macromolecules 2011, 44, (14), 5722-5726.

[77] Kroeze, J. E.; Savenije, T. J.; Vermeulen, M. J. W.; Warman, J. M. Journal of Physical Chemistry B 2003, 107, (31), 7696-7705.

[78] Leach, A. E., Molecular Modelling: Principles and Applications 1ed.; Longman: Essex, 1996.

[79] Lee, C. K.; Hua, C. C.; Chen, S. A. Macromolecules 2013, 46, (5), 1932-1938.

[80] Lee, C. K.; Pao, C. W. Journal of Physical Chemistry C 2012, 116, (23), 12455-12461.

[81] Lee, C. K.; Pao, C. W.; Chu, C. W. Energy & Environmental Science 2011, 4, (10), 4124-4132.

[82] Lee, J. K.; Ma, W. L.; Brabec, C. J.; Yuen, J.; Moon, J. S.; Kim, J. Y.; Lee, K.; Bazan, G. C.; Heeger, A. J. Journal of the American Chemical Society 2008, 130, (11), 3619-3623.

[83] Lim, B.; Bloking, J. T.; Ponec, A.; McGehee, M. D.; Sellinger, A. Acs Applied Materials & Interfaces 2014, 6, (9), 6905-6913.

[84] Lim, J. A.; Liu, F.; Ferdous, S.; Muthukumar, M.; Briseno, A. L. Materials Today 2010, 13, (5), 14-24.

[85] Liu, J. H.; Arif, M.; Zou, J. H.; Khondaker, S. I.; Zhai, L. Macromolecules 2009, 42, (24), 9390-9393.

[86] Liu, J. H.; Mikhaylov, I. A.; Zou, J. H.; Osaka, I.; Masunov, A. E.; McCullough, R. D.; Zhai, L. Polymer 2011, 52, (10), 2302-2309.

[87] Lorenzo, A. T.; Muller, A. J.; Lin, M.-C.; Chen, H.-L.; Jeng, U. S.; Priftis, D.; Pitsikalis, M.; Hadjichristidis, N. Macromolecules 2009, 42, (21), 8353-8364.

[88] Ma, W. L.; Yang, C. Y.; Gong, X.; Lee, K.; Heeger, A. J. Advanced Functional Materials 2005, 15, (10), 1617-1622.

[89] Ma, X. J.; Guo, Y.; Wang, T.; Su, Z. H. Journal of Chemical Physics 2013, 139, (1).

[90] Malgas, G. F.; Motaung, D. E.; Arendse, C. J. Journal of Materials Science 2012, 47, (10), 4282-4289.

[91] Malik, S.; Nandi, A. K. Journal of Polymer Science Part B-Polymer Physics 2002, 40, (18), 2073-2085.

[92] Marsh, H. S.; Jankowski, E.; Jayaraman, A. Macromolecules 2014, 47, (8), 2736-2747.

[93] Marsh, H. S.; Jayaraman, A. Journal of Polymer Science Part B: Polymer Physics 2013, 51, 64-77.

[94] Marsh, H. S.; Reid, O. G.; Barnes, G.; Heeney, M.; Stingelin, N.; Rumbles, G. Journal of Polymer Science Part B-Polymer Physics 2014, 52, (10), 700-707.

[95] Massip, S.; Oberhumer, P. M.; Tu, G.; Albert-Seifried, S.; Huck, W. T. S.; Friend, R. H.; Greenham, N. C. Journal of Physical Chemistry C 2011, 115, (50), 25046-25055.

[96] Mayer, a. C.; Toney, M. F.; Scully, S. R.; Rivnay, J.; Brabec, C. J.; Scharber, M.; Koppe, M.; Heeney, M.; McCulloch, I.; McGehee, M. D. Advanced Functional Materials 2009, 19, (8), 1173-1179.

[97] McCulloch, I.; Heeney, M.; Bailey, C.; Genevicius, K.; Macdonald, I.; Shkunov, M.; Sparrowe, D.; Tierney, S.; Wagner, R.; Zhang, W. M.; Chabinyc, M. L.; Kline, R. J.; McGehee, M. D.; Toney, M. F. Nature Materials 2006, 5, (4), 328-333.

[98] McCulloch, I.; Heeney, M.; Chabinyc, M. L.; DeLongchamp, D.; Kline, R. J.; Coelle, M.; Duffy, W.; Fischer, D.; Gundlach, D.; Hamadani, B.; Hamilton, R.; Richter, L.; Salleo, A.; Shkunov, M.; Sporrowe, D.; Tierney, S.; Zhong, W. Advanced Materials 2009, 21, (10-11), 1091-1109.

[99] Melis, C.; Colombo, L.; Mattoni, A. Journal of Physical Chemistry C 2011, 115, (2), 576-581.

[100] Mena-Osteritz, E.; Meyer, A.; Langeveld-Voss, B. M. W.; Janssen, R. A. J.; Meijer, E. W.; Bäuerle, P. Angewandte Chemie 2000, 112, (15), 2791-2796.

[101] Meredig, B.; Salleo, A.; Gee, R. Acs Nano 2009, 3, (10), 2881-2886.

[102] Miller, N. C.; Cho, E.; Gysel, R.; Risko, C.; Coropceanu, V.; Miller, C. E.; Sweetnam, S.; Sellinger, A.; Heeney, M.; McCulloch, I.; Bredas, J. L.; Toney, M. F.; McGehee, M. D. Advanced Energy Materials 2012, 2, (10), 1208-1217.

[103] Miller, N. C.; Cho, E.; Junk, M. J. N.; Gysel, R.; Risko, C.; Kim, D.; Sweetnam, S.; Miller, C. E.; Richter, L. J.; Kline, R. J.; Heeney, M.; McCulloch, I.; Amassian, A.; Acevedo-Feliz, D.; Knox, C.; Hansen, M. R.; Dudenko, D.; Chmelka, B. F.; Toney, M. F.; Bredas, J. L.; McGehee, M. D. Advanced Materials 2012, 24, (45), 6071-6079.

[104] Miller, N. C.; Gysel, R.; Miller, C. E.; Verploegen, E.; Beiley, Z.; Heeney, M.; McCulloch, I.; Bao, Z. N.; Toney, M. F.; McGehee, M. D. Journal of Polymer Science Part B-Polymer Physics 2011, 49, (7), 499-503.

[105] Nguyen, T. D.; Phillips, C. L.; Anderson, J. A.; Glotzer, S. C. Computer Physics Communications 2011, 182, (11), 2307-2313.

[106] Ong, B. S.; Wu, Y. L.; Li, Y. N.; Liu, P.; Pan, H. L. Chemistry-a European Journal 2008, 14, (16), 4766-4778.

[107] Osterloh, F. E.; Holmes, M. A.; Chang, L.; Moulé, A. J.; Zhao, J. The Journal of Physical Chemistry C 2013, 117, (51), 26905-26913.

[108] Osterloh, F. E.; Holmes, M. A.; Chang, L.; Moulé, A. J.; Zhao, J. The Journal of Physical Chemistry C 2013.

[109] Paquin, F.; Latini, G.; Sakowicz, M.; Karsenti, P. L.; Wang, L. J.; Beljonne, D.; Stingelin, N.; Silva, C. Physical Review Letters 2011, 106, (19).

[110] Parmer, J. E.; Mayer, A. C.; Hardin, B. E.; Scully, S. R.; McGehee, M. D.; Heeney, M.; McCulloch, I. Applied Physics Letters 2008, 92, (11).

[111] Peet, J.; Kim, J. Y.; Coates, N. E.; Ma, W. L.; Moses, D.; Heeger, A. J.; Bazan, G. C. Nature Materials 2007, 6, (7), 497-500.

[112] Pfannmoller, M.; Flugge, H.; Benner, G.; Wacker, I.; Sommer, C.; Hanselmann, M.; Schmale, S.; Schmidt, H.; Hamprecht, F. A.; Rabe, T.; Kowalsky, W.; Schroder, R. R. Nano Letters 2011, 11, (8), 3099-3107.

[113] Pingel, P.; Zen, A.; Abellon, R. D.; Grozema, F. C.; Siebbeles, L. D. A.; Neher, D. Advanced Functional Materials 2010, 20, (14), 2286-2295.

[114] Plimpton, S. Journal of Computational Physics 1995, 117, (1), 1-19.

[115] Prosa, T. J.; Winokur, M. J.; McCullough, R. D. Macromolecules 1996, 29, (10), 3654-3656.

[116] Prosa, T. J.; Winokur, M. J.; Moulton, J.; Smith, P.; Heeger, A. J. Macromolecules 1992, 25, (17), 4364-4372.

[117] Ramani, R.; Alam, S. Polymer 2013, 54, (25), 6785-6792.

[118] Reid, O. G.; Malik, J. A. N.; Latini, G.; Dayal, S.; Kopidakis, N.; Silva, C.; Stingelin, N.; Rumbles, G. Journal of Polymer Science Part B-Polymer Physics 2012, 50, (1), 27-37.

[119] Ren, G. Q.; Wu, P. T.; Jenekhe, S. A. Chemistry of Materials 2010, 22, (6), 2020-2026.

[120] Richter, L. J.; DeLongchamp, D. M.; Bokel, F. A.; Engmann, S.; Chou, K. W.; Amassian, A.; Schaible, E.; Hexemer, A. Advanced Energy Materials 2015, 5, (3), pages not assigned yet.

[121] Rivnay, J.; Mannsfeld, S. C. B.; Miller, C. E.; Salleo, A.; Toney, M. F. Chemical Reviews 2012, 112, (10), 5488-5519.

[122] Rivnay, J.; Noriega, R.; Kline, R. J.; Salleo, A.; Toney, M. F. Physical Review B 2011, 84, (4).

[123] Roehling, J. D.; Arslan, I.; Moule, A. J. Journal of Materials Chemistry 2012, 22, (6), 2498-2506.

[124] Rubinson, K.; Rubinson, J., Contemporary Instrumental Analysis. Prentice-Hall: Upper Saddle River, 2000.

[125] Ruderer, M. A.; Muller-Buschbaum, P. Soft Matter 2011, 7, (12), 5482-5493.

[126] Saba, M. I.; Melis, C.; Colombo, L.; Malloci, G.; Mattoni, A. Journal of Physical Chemistry C 2011, 115, (19), 9651-9655.

[127] Salammal, S. T.; Mikayelyan, E.; Grigorian, S.; Pietsch, U.; Koenen, N.; Scherf, U.; Kayunkid, N.; Brinkmann, M. Macromolecules 2012, 45, (13), 5575-5585.

[128] Salim, T.; Wong, L. H.; Brauer, B.; Kukreja, R.; Foo, Y. L.; Bao, Z. N.; Lam, Y. M. Journal of Materials Chemistry 2011, 21, (1), 242-250.

[129] Scharsich, C.; Lohwasser, R.; Sommer, M.; Asawapirom, U.; Scherf, U.; Thelakkat, M.; Neher, D.; Kohler, A. Journal of Polymer Science Part B: Polymer Physics 2011, 50, (6), 442-453.

[130] Schmidt-Hansberg, B.; Sanyal, M.; Klein, M. F. G.; Pfaff, M.; Schnabel, N.; Jaiser, S.; Vorobiev, A.; Muller, E.; Colsmann, A.; Scharfer, P.; Gerthsen, D.; Lemmer, U.; Barrena, E.; Schabel, W. Acs Nano 2011, 5, (11), 8579-8590.

[131] Schmidt-Rohr, K. Journal of Applied Crystallography 2007, 40, 16-25.

[132] Schmidt, K.; Tassone, C. J.; Niskala, J. R.; Yiu, A. T.; Lee, O. P.; Weiss, T. M.; Wang, C.; Fréchet, J. M. J.; Beaujuge, P. M.; Toney, M. F. Advanced Materials 2014, 26, (2), 300-305.

[133] Schwarz, K. N.; Kee, T. W.; Huang, D. M. Nanoscale 2013, 5, (5), 2017-2027.

[134] Schwarz, K. N.; Kee, T. W.; Huang, D. M. Nanoscale 2013.

[135] Schweizer, K. S.; Curro, J. G. Atomistic Modeling of Physical Properties 1994, 116, 319-377.

[136] Senkovskyy, V.; Beryozkina, T.; Bocharova, V.; Tkachov, R.; Komber, H.; Lederer, A.; Stamm, M.; Severin, N.; Rabe, J. P.; Kiriy, A. Polymer Networks: Synthesis, Properties, Theory and Applications 2010, 291-292, 17-25.

[137] Shaheen, S. E.; Brabec, C. J.; Sariciftci, N. S.; Padinger, F.; Fromherz, T.; Hummelen, J. C. Applied Physics Letters 2001, 78, (6), 841-843.

[138] Shen, X. B.; Duzhko, V. V.; Russell, T. P. Advanced Energy Materials 2013, 3, (2), 263-270.

[139] Shin, N.; Richter, L. J.; Herzing, A. A.; Kline, R. J.; DeLongchamp, D. M. Advanced Energy Materials 2013, 3, (7), 938-948.

[140] Shin, W. S.; Lee, J. C.; Kim, J. R.; Lee, H. Y.; Lee, S. K.; Yoon, S. C.; Moon, S. J. Journal of Materials Chemistry 2011, 21, (4), 960-967.

[141] Shinozaki, A.; Jasnow, D.; Balazs, A. C. Macromolecules 1994, 27, (9), 2496-2502.

[142] Singh, C. R.; Gupta, G.; Lohwasser, R.; Engmann, S.; Balko, J.; Thelakkat, M.; Thurn-Albrecht, T.; Hoppe, H. Journal of Polymer Science Part B-Polymer Physics 2013, 51, (12), 943-951.

[143] Sista, P.; Xue, B. F.; Wilson, M.; Holmes, N.; Kularatne, R. S.; Nguyen, H.; Dastoor, P. C.; Belcher, W.; Poole, K.; Janesko, B. G.; Biewer, M. C.; Stefan, M. C. Macromolecules 2012, 45, (2), 772-780.

[144] Slota, J. E.; He, X. M.; Huck, W. T. S. Nano Today 2010, 5, (3), 231-242.

[145] Stadler, R.; Auschra, C.; Beckmann, J.; Krappe, U.; Voigtmartin, I.; Leibler, L. Macromolecules 1995, 28, (9), 3080-3097.

[146] Steinhardt, P. J.; Nelson, D. R.; Ronchetti, M. Physical Review B 1983, 28, (2), 784-805.

[147] Stepanyan, R.; Subbotin, A.; Knaapila, M.; Ikkala, O.; ten Brinke, G. Macromolecules 2003, 36, (10), 3758-3763.

[148] Stingelin, N. Polymer International 2012, 61, (6), 866-873.

[149] Stone, J. E.; Phillips, J. C.; Freddolino, P. L.; Hardy, D. J.; Trabuco, L. G.; Schulten, K. Journal of Computational Chemistry 2007, 28, (16), 2618-2640.

[150] Su, M.-S.; Kuo, C.-Y.; Yuan, M.-C.; Jeng, U. S.; Su, C.-J.; Wei, K.-H. Advanced Materials 2011, 23, (29), 3315-3319.

[151] Sweetnam, S.; Graham, K. R.; Ndjawa, G. O. N.; Heumuller, T.; Bartelt, J. A.; Burke, T. M.; Li, W. T.; You, W.; Amassian, A.; McGehee, M. D. Journal of the American Chemical Society 2014, 136, (40), 14078-14088.

[152] Tashiro, K.; Ono, K.; Minagawa, Y.; Kobayashi, M.; Kawai, T.; Yoshino, K. Journal of Polymer Science Part B-Polymer Physics 1991, 29, (10), 1223-1233.

[153] Thomas, A.; Elsa Tom, A.; Rao, A. D.; Varman, K. A.; Ranjith, K.; Vinayakan, R.; Ramamurthy, P. C.; Ison, V. V. Journal of Applied Physics 2014, 115, (10), 104302.

[154] Tierney, S.; Heeney, M.; McCulloch, I. Synthetic Metals 2005, 148, (2), 195-198.

[155] Topham, P. D.; Parnell, A. J.; Hiorns, R. C. Journal of Polymer Science Part B-Polymer Physics 2011, 49, (16), 1131-1156.

[156] Treat, N. D.; Brady, M. A.; Smith, G.; Toney, M. F.; Kramer, E. J.; Hawker, C. J.; Chabinyc, M. L. Advanced Energy Materials 2011, 1, (1), 82-89.

[157] Treat, N. D.; Varotto, A.; Takacs, C. J.; Batara, N.; Al-Hashimi, M.; Heeney, M. J.; Heeger, A. J.; Wudl, F.; Hawker, C. J.; Chabinyc, M. L. Journal of the American Chemical Society 2012, 134, (38), 15869-15879.

[158] Triplett, D. A.; Fichthorn, K. A. Physical Review E 2008, 77, (1).

[159] Ungar, G.; Stejny, J.; Keller, A.; Bidd, I.; Whiting, M. C. Science 1985, 229, (4711), 386-389.

[160] Urakami, N.; Imai, M. The Journal of Chemical Physics 2003, 119, (4), 2463-2463.

[161] Vakhshouri, K.; Kozub, D. R.; Wang, C. C.; Salleo, A.; Gomez, E. D. Physical Review Letters 2012, 108, (2), 5.

[162] Verlet, L. Physical Review 1967, 159, (1), 98-103.

[163] Vrij, A. Pure and Applied Chemistry 1976, 48, (4), 471-483.

[164] Wang, C. C.; Jimison, L. H.; Goris, L.; McCulloch, I.; Heeney, M.; Ziegler, A.; Salleo, A. Advanced Materials 2010, 22, (6), 697-+.

[165] Weeks, J. D.; Chandler, D.; Andersen, H. C. Journal of Chemical Physics 1971, 54, (12), 5237-5247.

[166] Wignall, G. D.; Ballard, D. G. H.; Schelten, J. European Polymer Journal 1974, 10, (9), 861-865.

[167] Winokur, M. J.; Spiegel, D.; Kim, Y.; Hotta, S.; Heeger, A. J. Synthetic Metals 1989, 28, (1-2), C419-C426.

[168] Wu, P. T.; Ren, G. Q.; Jenekhe, S. A. Macromolecules 2010, 43, (7), 3306-3313.

[169] Wu, Y. L.; Liu, P.; Gardner, S.; Ong, B. S. Chemistry of Materials 2005, 17, (2), 221-223.

[170] Wunderlich, B., Macromolecular Physics Vol. 2: Crystal Nucleation, Growth, Annealing. Academic Press: New York, 1976.

[171] Wunderlich, B.; Kashdan, W. H. Journal of Polymer Science 1961, 50, (153), 71.

[172] Yang, L. Q.; Zhou, H. X.; You, W. Journal of Physical Chemistry C 2010, 114, (39), 16793-16800.

[173] Yankova, T. S.; Bobrovsky, A. Y.; Vorobiev, A. K. Journal of Physical Chemistry B 2012, 116, (20), 6010-6016.

[174] Yao, Y.; Hou, J.; Xu, Z.; Li, G.; Yang, Y. Advanced Functional Materials 2008, 18, (12), 1783-1789.

[175] Yiannourakou, M.; Economou, I. G.; Bitsanis, I. A. Journal of Chemical Physics 2010, 133, (22).

[176] Yin, W.; Dadmun, M. Acs Nano 2011, 5, (6), 4756-4768.

[177] Yuan, M.; Okamoto, K.; Bronstein, H. A.; Luscombe, C. K. Acs Macro Letters 2012, 1, (3), 392-395.

[178] Zhang, L.; Colella, N. S.; Liu, F.; Trahan, S.; Baral, J. K.; Winter, H. H.; Mannsfeld, S. C. B.; Briseno, A. L. Journal of the American Chemical Society 2013, 135, (2), 844-854.

[179] Zhang, L.; Liu, F.; Diao, Y.; Marsh, H. S.; Colella, N. S.; Jayaraman, A.; Russell, T. P.; Mannsfeld, S. C. B.; Briseno, A. L. Journal of the American Chemical Society 2014, 136, (52), 18120-18130.

[180] Zhang, Z.; Guo, H. The Journal of chemical physics 2010, 133, (14), 144911-144911.

[181] Zhao, K.; Xue, L.; Liu, J.; Gao, X.; Wu, S.; Han, Y.; Geng, Y. Langmuir 2010, 26, (1), 471-477.

[182] Zhou, H. X.; Yang, L. Q.; You, W. Macromolecules 2012, 45, (2), 607-632.